LES model for inhomogeneous wall-free turbulent flows and flow characteristics in laminar wall-free and wall-dominated viscoelastic fluid flows

A thesis submitted in partial fulfilment of the requirements for the degree of
Doctor of Philosophy in the Mechanical Engineering by

Saeed Parvar

Supervisor:

Professor Fernando Manuel Coutinho Tavares de Pinho

(Departamento de Engenharia Mecânica, Faculdade de Engenharia da Universidade do Porto)

Co-supervisor:

Professor Carlos Frederico Neves Bettencourt da Silva

(Departamento de Engenharia Mecânica, Instituto Superior Técnico, Universidade de Lisboa)

12/12/2020

قومی متفکرند اندر ره دین

قومی به گمان فتاده در راه یقین

میترسم از آن که بانگ آید روزی

کای بی خبران راه نه آنست و نه این

حکیم عمر خیام

Some are preoccupied with matters of religion

And some are beset by doubt on their course of conviction

I fear the day when a divine voice may call out

You ignorant people, true course is neither of your two ways

Omar Khayyam

(18 May 1048 – 4 December 1131)

A Persian mathematician, astronomer, philosopher, and poet

*To **my family**,*

for their eternal encouragement, support, and love.

With special thanks to

***Dr.** Rahman Maleki Maryan,*

***Dr.** Hossein Guilani Asl,*

*and **Dr.** Mojtaba Masalifar*

For helping me in the critical stage of my life

Abstract

Direct numerical simulations (DNS) and large-eddy simulations (LES) of turbulent planar jets are utilized to assess the distortion similarity (DSIM) model, recently developed by Ferreira et al. (P. O. Ferreira, F. T. Pinho, C. B. Silva, Large-eddy simulations of forced isotropic turbulence with viscoelastic fluids described by the FENE-P model. *Phys. Fluids*, 28 125104, 2016.) to describe the subgrid scale contribution to the distortion in the viscoelastic constitutive model known as FENE-P for homogeneous isotropic turbulence, in the simulation of turbulent viscoelastic planar jets. Both *a-priori* and *a-posteriori* tests of the DSIM model are performed, and show that the several assumptions used in the development of the DSIM model hold well in inhomogeneous wall-free turbulent viscoelastic flows e.g. i) the scale similarity of the subgrid-scale (SGS) polymer stretching, and ii) the local equilibrium of the elastic energy production and dissipation. The DSIM model for the SGS polymer stretching term, together with the dynamic Smagorinsky model for the SGS term in the momentum equation is able to reproduce well the flow structures and the classical one point statistics of turbulent viscoelastic planar jets, and the model should be equally able to simulate other free shear flows of viscoelastic fluids e.g. wakes and mixing layers.

A semi-analytical solution is also proposed for the laminar planar jet flow of viscoelastic FENE-P fluids. This semi-analytical solution not only helped validate the DNS code, but it also provided a tool to understand the corresponding laminar flow characteristics such as the laws of the decay of the centerline velocity and of the growth of the jet half-width and to ascertain the effects of the viscoelasticity upon the flow characteristics, before facing with the complexity of the studying the corresponding turbulent flow. The solution is obtained by performing an order of magnitude analysis and ensuing simplifications of the governing equations. Although we get inspiration from Olagunju's solution (D. O. Olagunju, Local similarity solutions for boundary layer flow of a FENE-P fluid, *Appl. Math. Comput.*, 173, 593–602, 2006a, D. O. Olagunju, A self-similar solution for forced convection boundary layer flow of a FENE-P fluid, *Appl. Math. Lett.*, 19, 432–436, 2006b.) for viscoelastic boundary layer flow, the performance of both the present solution and Olagunju's solution are assessed by comparing them with the results of RheoFoam module of the freeware OpenFoam code (F. Pimenta, M. Alves, Stabilization of an open-source finite-volume solver for viscoelastic fluid flows, *J. Non-Newt. Fluid Mech.*, 239, 85 – 104, 2017, F. Pimenta, M. A. Alves, RheoTool, https://github.com/fppimenta/rheoTool, (2016)).

This type of semi-analytical solution is also extended to two other classical laminar flows of viscoelastic fluids, namely the boundary layer and mixing layer flows, due to their wide range of scientific and industrial applications. It is observed that, at low elasticity levels, in all aforementioned flows the kinematic quantities collapse on the corresponding Newtonian flow curves, with the polymer characteristics exhibiting an asymptotic behavior if adequately normalized. However, with increasing levels of elasticity the semi-analytical solutions deviate from the asymptote curves. Through these semi-analytical solutions, we provide an extensive set of results, including profiles of polymer conformation and stress tensor components, laws of decay for peak stresses under low elasticity conditions and their location as well as the streamwise variations of boundary and mixing layer thicknesses as well as displacement and momentum thicknesses for both boundary and mixing layer flows.

Resumo

Simulação numérica direta (DNS) e de grandes escalas de turbulência (LES) de jatos planos, em regime turbulento, são utilizadas para avaliar o desempenho do modelo de semelhança de distorção (DSIM), recentemente desenvolvido por Ferreira et al. (P. O. Ferreira, F. T. Pinho, C. B. Silva, Large-eddy simulations of forced isotropic turbulence with viscoelastic fluids described by the FENE-P model. *Phys. Fluids*, 28 125104, 2016.) para descrever a contribuição residual do termo da distorção da equação constitutiva do fluido viscoelástico, conhecido como modelo FENE-P, em turbulência homogénea e isotrópica, aplicada agora à simulação de escoamentos de fluidos viscoelásticos em jatos planos. São realizados quer testes *a priori* quer *a posteriori* do modelo DSIM, dos quais se conclui que as hipóteses fundamentais que lhe são inerentes se mantêm válidas para escoamentos turbulentos, não-homogéneos e não-confinados de fluidos viscoelásticos. Essas hipóteses são: (i) a semelhança de escalas da contribuição residual (SGS) da extensão polimérica e (ii) o equilíbrio local entre produção e dissipação de energia elástica. O modelo DSIM para a contribuição residual da extensão polimérica, juntamente com o modelo dinâmico de Smagorinsky aplicado às tensões residuais da equação da quantidade de movimento, permitem reproduzir a estrutura do escoamento e as estatísticas clássicas locais de jatos viscoelásticos planos em regime turbulento. Espera-se que o modelo também seja capaz de simular outros escoamentos de corte sem efeitos de parede de fluidos viscoelásticos, de que são exemplo as esteiras e camadas de mistura.

Uma solução semi-analítica é ainda proposta para o escoamento laminar de jatos planos de fluidos descritos pelo modelo FENE-P. Esta solução foi usada na validação do código para DNS, mas também revelou-se uma ferramenta essencial para a compreensão das características intrínsecas do respetivo escoamento, tais como as leis de decaimento da velocidade axial, de crescimento da espessura do jato, e ainda da contribuição da viscoelasticidade para a sua dinâmica, antes de se enveredar pelo estudo do jato em regime turbulento. A solução é obtida através de uma análise de ordem de grandeza dos termos das equações governativas e sua simplificação para escoamento de corte de baixa espessura. Apesar de inspirada na solução de Olagunju (D. O. Olagunju, Local similarity solutions for boundary layer flow of a FENE-P fluid, *Appl. Math. Comput.*, 173, 593–602, 2006a, D. O. Olagunju, A self-similar solution for forced convection boundary layer flow of a FENE-P fluid, *Appl. Math. Lett.*, 19, 432–436, 2006b) para escoamento de camada limite de

fluidos viscoelásticos, a solução obtida não é idêntica à que se obteria a partir dos seus pressupostos. Assim, os desempenhos da solução do jato e da solução de Olagunju para jatos foram comparados com resultados de simulação numérica para as equações completas obtidos com o módulo RheoFoam da aplicação gratuita de mecânica de fluidos computacional OpenFOAM (F. Pimenta, M. Alves, Stabilization of an open-source finite-volume solver for viscoelastic fluid flows, *J. Non-Newt. Fluid Mech.*, 239, 85 – 104, 2017, F. Pimenta, M. A. Alves, RheoTool, https://github.com/fppimenta/rheoTool, (2016)).

Este tipo de solução semi-analítica é ainda estendida a dois escoamentos laminares clássicos de fluidos viscoelásticos, nomeadamente os escoamentos de camada limite e de camada de mistura, dadas as suas inúmeras aplicações científicas e industriais. Nestes escoamentos, para baixos níveis de elasticidade, as quantidades cinemáticas avaliadas registam uma evolução newtoniana e as características poliméricas apresentam um comportamento assintótico se normalizadas de forma adequada. No entanto, com o aumento da elasticidade do escoamento as soluções semi-analíticas afastam-se das curvas assíntotas. Para as soluções propostas apresentamos um vasto leque de resultados, incluindo perfis das componentes dos tensores de conformação polimérica e das tensões, leis de decaimento para picos de tensão em escoamentos a baixa elasticidade, as suas localizações, variações axiais da espessura das camadas limite e de mistura, e espessuras de deslocamento e de quantidade de movimento.

Acknowledgments

I would like to express my sincere gratitude to Professor Fernando Pinho, for giving me the opportunity to pursue my education under his supervision, and also his support, motivation, and guidance from developing an idea until reaching the final publication of the wok. I would like to appreciate his sharing of his profound knowledge of viscoelastic fluid, which was the main reason of fortifying and success of the present study.

I want to thank Prof. Carlos da Silva for making available the DNS code of viscoelastic fluid which was the main tool of present work. Furthermore, I want to thank him for hosting me in LASEF at the first year of my PhD and his suggestions and recommendations to improve and enhance the quality of present study especially in turbulent viscoelastic fluid topic.

Special thanks go to Prof. Alexandre Afonso, Dr. Francisco Galindo Rosales, Prof. Laura Campo-Deaño, Prof. Pedro Miguel Rebelo Resende, and Dr. Carlos Alberto Veiga Rodrigues, for providing warm environment in the laboratory and their teamwork support, I want to state that what a great pleasure it was collaborating with all of you, I will be forever thankful for that.

A very special gratitude goes out to Prof. D.O.A. Almeida Cruz and Prof. Hamidreza Anbarlooei for hosting me at UFRJ in Brazil and also giving me a user access to Gesualdo and Arquimedes supercomputers which were used for the performing main simulations of the present work.

I would also thank all of my colleagues in the CEFT research center, especially L401 room for their friendship and eternal support during my study at FEUP with a special thanks to Tomás Rodrigues, Ângela Ribau, Tomás Schuller, Artur Martins Ferreira, and Hugo Nóbrega.

Finally, I should acknowledge the financial support of project PTDC/EMS-ENE/2390/2014, POCI-01-0145-FEDER-016669 funded by Fundo Europeu de Desenvolvimento Regional, via COMPETE2020 - Programa Operacional Competitividade e Internacionalização (POCI) and Fundação para a Ciência e a Tecnologia. In addition, I would like to thank financial support provided by Centro de Estudos de Fenómenos de Transporte through projects UIDB/ 00532/2020 and UIDP/00532/2020 and through a protect of INEGI for the final 15 monthes.

Table of contents

List of figures

Chapter 4

Chapter 5

Chapter 6

Chapter 7

List of tables

Nomenclature

Latin symbols

C_D	The constant of Dynamic Smagorinsky
Cs	The constant of Classical Smagorinsky
C_K	Smagorinsky constant
$E(\kappa)$	Energy spectrum
H & D	Width of the inlet slot
κ	Wave number
L_x	Computational domain length in the x direction
L_y	Computational domain length in the y direction
L_z	Computational domain length in the z direction
n_x	Number of grid points in the x direction
n_y	Number of grid points in the y direction
n_z	Number of grid points in the z direction
P	Pressure
Re	Reynolds number
S_{ij}	Strain rate tensor
$\|S\|$	Norm of the strain rate tensor
T	time
u_i	The vector of velocity
U_J	Peak velocity at the inlet
U_∞^{in}	Co-flow velocity
U	Velocity in streamwise direction
V	Velocity in normal direction
w	Velocity in spanwise direction
x_i	i^{th} coordinate in space
X	Space Coordinate component in streamwise direction
Y	Space Coordinate component in normal direction
Z	Space Coordinate component in spanwise direction
C_{ij}	Components i, j of the Conformation tensors
$f(C_{kk})$	Peterlin function
$G_\Delta(x)$	Spatial filter

Greek symbols

δ_u	Mean flow thickness of the planar jet
δ_{ij}	Kronecker delta
Δ	Filter size
Δx	Grid spacing in the x direction
Δy	Grid spacing in the y direction
Δz	Grid spacing in the z direction
Δt	Time step
ε_s	Turbulent kinetic energy dissipation
η	Kolmogorov length micro-scale

υ_s	Solvent kinematic viscosity
υ_p	Polymer kinematic viscosity
υ_t	Turbulent kinematic viscosity
ρ	Fluid density
τ_{ij}^{S}	Solvent Stress tensor
τ_{ij}^{R}	Residual stress tensor
τ_{ij}^{P}	Polymer Stress tensor
ω	Vorticity vector
λ	Relaxation time of polymer
β	Polymer Concentration
ψ_{ij}	SGS polymer convection tensor
χ_{ij}	SGS Sink term tensor
γ_{ij}	SGS polymer stretching tensor

Acronyms

DNS	Direct Numerical Simulation
FFT	Fast Fourier Transform
LES	Large Eddy Simulation
MPI	Message Passing Interface
QUICK	Quadratic Upstream Interpolation for Convective Kinematics
RANS	Reynolds Averaged Navier-Stokes Equations
RK	Runge-Kutta
GS	Grid Scale
SGS	Subgrid scale
DR	Drag Reduction
FENE-P	Finitely Extensible Non-linear Elastic Peterlin model
HIT	Homogeneous Isotropic Turbulence
KT	Kurganov-Tadmor
PDF	Probability Density Function
JPDF	Joint Probability Density Function
SPD	Symmetric Positive Definite

Notation

X'	Fluctuation of X
$\overline{X}$	X low pass filtered in space
$\langle X \rangle_a$	Spatial averaging of X at a direction

Subscripts and superscripts

i, j, k	Computational indexes
rms	Root-mean-square
x,y,z	Cartesian components
$[p]$	Polymer
$[s]$	Solvent

Part I

Introduction

I've made the most important discovery of my life. It's only in the mysterious equation of love that any logical reasons can be found. I'm only here tonight because of you. You're the only reason I am...you're all my reasons.

- John Nash

(June 13, 1928 – May 23, 2015)

An American mathematician

Dedicated to G.A.D. A.L.A.R.A.M.

Chapter 1 : General introduction

1.1.Motivation

In 1949 Toms [1] found that adding a small number of long-chain polymeric molecules, such as polyethylene oxide (PEO), into Newtonian fluids induces severe drag reduction (DR), of up to 80%, in turbulent pipe flow, which also naturally leads to a concomitant reduction in heat transfer. Since then the use of viscoelastic fluids has been proposed in several industrial applications, in order of benefit from drag and heat transfer reductions under turbulent flow conditions such as in heating and cooling systems [2], transport of oil in pipelines and drilling wells in oil and gas industries [3]. The increment of the flow rate associated with drag reduction in sewage systems during floods [4]. Other fields of application include also the design of ships and submarines, since drag reduction leads to more efficient energy use [5], increasing the mixing rates in microfluidics [6] and biofluid [7,8] application due to the onset of viscoelastic instabilities, and reducing energy consumption rate in irrigation systems and in percolation through the soil [9]. Finally, some applications are encountered also in medicine during surgery, when blood analogs containing polymer are used [10,11].

Consequently, there has been considerable effort and competition for developing physical models as well as numerical techniques to precisely estimate the properties of viscoelastic turbulent flows. There are three main approaches to deal with the numerical calcualtion of turbulent flows namely the direct numerical Simulation (DNS) of the basic governing equaitons, the solution of the Reynolds-averaged Navier-Stokes equations (RANS) (for newtonian fluids), and finally large-eddy simulations (LES). However due to the high computational cost of DNS, RANS and LES approaches are preferred for engineering applications. Regarding turbulent flows of viscoelastic fluids, it is worth mentioning that the most common available turbulence models of viscoelastic fluids have been developed based on RANS and they have been calibrated for wall flows. However, RANS suffers from several well-known constraints in engineering applications such as when dealing with unsteady and transient flows, separation or rotation, among others, therefore, LES has been increasingly adopted due to its accuracy, acceptable computational cost, and capability of dealing with some of RANS shortcomings.

To overcome the shortcoming of the existing turbulence models for viscoelastic fluids and develop a proper LES model, the fundamental approach is to start studying and developing turbulence models for homogeneous isotropic turbulence (HIT), which was the topic of interest of earlier investigations [12-15]. However, the effects of both in-homogeneities and wall proximity are absent in HIT. Therefore, the next step is to study the effect of turbulent flow in-homogeneities in the absent of wall, a topic also correctly under way by our colleagues at Laboratory of Fluid Simulation in Energy and Fluids (LASEF) research group [16]. In this thesis, we pursue the road map by developing LES model for wall-free turbulent flow of viscoelastic fluid to consider the effect of turbulent flow in-homogeneity. For this purpose the planar jet flow is selected as a flow of interest, however the mixing layer and wake flows are other alternatives that can also be used for this goal.

Before studying planar turbulent jet flow of viscoelastic fluids and to develop any turbulent models, it is necessary to validate the code used for DNS and LES, which can be done by comparing their predictions with those using to RheoFoam module of the freeware OpenFoam code [17,18] as well as those from other solutions such as a semi-analytical solution for the corresponding laminar flow. For that purpose and by getting inspiration from Olagunju solution for boundary layer flow of FENE-P fluid [19,20], an approximate similarity solution is proposed for the laminar planar jet flow of viscoelastic fluid described by the same viscoelastic constitutive equation. Furthermore, since the laminar jet solution was developed on the basis of a set of simplified governing equations that are also valid for laminar boundary layer and mixing layer flows, semi-analytical solutions are also obtained for these flows, to be used the future studies and turbulent code validations. These semi-analytical solutions are appropriate tools to study and fully understand the effects of viscoelasticity on the corresponding laminar flow characteristics before dealing with the complexity of the study of their turbulent flows counterparts.

It is important at this stage to clarify that the main interest lies with dilute polymer solutions and that a rheological constitutive equation able to describe their main rheological behavior needs to be adopted for the purpose of this investigation. As will be explained and justified later, the model adopted is the finitely extensible non-linear elastic model with Peterlin's approximation, denoted henceforth as the FENE-P model.

1.2.Objectives

As a natural consequence of the motivation and background in the field and general objective, more specific objectives of this thesis are:

1) Proposing an approximate similarity solution for planar jet FENE-P fluid to verify the direct numerical simulation code for planar jet turbulent flow of FENE-P fluids;
2) Numerical simulation of laminar planar jet FENE-P fluid by utilizing RheoFoam to verify the corresponding DNS code;
3) Developing the post-processing tools for investigation of turbulent planar jet flows of FENE-P fluids;
4) Performing detailed DNS investigations of turbulent planar jet flows of FENE-P fluids as a function of the relevant dimensionless numbers (Weissenberg number, maximum polymer extensibility, and viscosity ratio) in order to understand its physics;
5) Doing *a-priori* tests on extracted data of turbulent planar jet flow of FENE-P fluids, which is required for developing LES closure of viscoelastic fluids;
6) Extending the distortion similarity model (DSIM) to use in in-homogenous wall-free turbulent flow and then, by performing *a-posteriori* tests, assessing the model performance through simulation of turbulent planar jets flow;
7) Proposing a semi-analytical solution for laminar boundary layer flow of viscoelastic fluids, studying the effects of viscoelasticity on flow properties, while verifying the results with RheoFoam to better establish its limits of validity;
8) Suggesting an approximate similarity solution for laminar mixing layer flow of FENE-P fluids and investigating its flow characteristics.

1.3.Thesis organization

This thesis is divided in four main parts and organized as follows.

Part I: After explaining the main motivation of the present study in chapter I, chapter II discusses the main theory and the necessary background. We start with introducing Newtonian and non-Newtonian fluids and then popular constitutive equations used for describing dilute polymer solution with special attention paid to the FENE-P model by discussing its pros and cons. Afterward, the main characteristics of turbulent flow, the main numerical approaches to deal with the numerical simulation of turbulent flows, as well as their limits, are briefly discussed. Viscoelastic turbulent flows is discussed next, by explaining the main proposed theories which shed light on the mechanisms of drag reduction phenomena. Subsequently, we explain what the main requirements are to develop a proper LES model for turbulent flows of non-Newtonian fluids and we review the available turbulent models for the corresponding flows fluids as well as their constrains.

Part II: In this part, the three classical laminar flows of viscoelastic fluid described by FENE-P model are investigated. This includes the derivation of the simplified form of the governing equations, the discussion of the numerical schemes used to solve them, and a comprehensive investigation and discussion of the results. An approximate similarity solution for laminar boundary layer flow FENE-P fluids is explained in chapter III, while chapters IV and V deal with the laminar planar mixing layer and jet flows respectively.

Part III: This part starts with section VI where after briefly describing the numerical method used in the DNS/LES code and in the RheoFoam module of OpenFoam, the planar jet turbulent flow viscoelastic fluid code is verified via the corresponding an approximate similarity solution and RheoFoam toolbox. Afterward, in Section VII, the main requirement for developing an SGS model for non-Newtonian fluids are explained. Chapter VII also performs the *a-priori* tests on statistical data extracted from the direct numerical simulation of viscoelastic fluids of Guimarães et al. [16]

and gets inspiration from Masoudian et al. [21] and Ferreira et al. [12] to assess the validity of the hypotheses needed to develop an LES model. In particular scale-similarity of the subgrid-scale polymer stretching and local equilibrium of the polymeric elastic energy and statistically stationary flow are assessed. Then the performance of the extended distortion similarity model (DSIM) implemented into the DNS/LES code is assessed, by carrying out *a-posteriori* tests. Furthermore, two turbulence models for the subgrid scale stress in the momentum equation, such as the Smagorinsky and the dynamic Smagorinsky models, are considered and their performances on instantaneous and statistical turbulent planar jet flow features are analyzed. At the end of section VII, the self-similar theory of viscoelastic turbulent planar jet flow proposed by Guimarães et al. [16] and the energy spectrum of the corresponding turbulent flow are also studied.

Part IV: Chapter VIII summarizes the main conclusions of the present thesis and proposes some topics proposal for future investigation in this area.

“I came to realize that exaggerated concern about what others are doing can be foolish. It can paralyze effort, and stifle a good idea. One finds that in the history of science almost every problem has been worked out by someone else. This should not discourage anyone from pursuing his own path.”

-Theodore von Kármán

(11 May 1881 – 6 May 1963)

A Hungarian-American mathematician, aerospace engineer.

Chapter 2 : Theory and background

2.1. Newtonian and non-Newtonian fluids

In Cambridge dictionary, fluid is defined as a substance that flows and is not solid [22], however, in scientific point of view fluid is defined as a material which cannot endure any shear stress applied to it and it continually deforms under that shear force [23,24]. Generally speaking, fluids are categorized in two main subcategories, Newtonian and non-Newtonian fluids, according to the relation between the stress and rate of deformation tensors. In Newtonian fluids, stress and rate of strain have a linear relation, meaning that imposing forces are linearly proportional to deformation rate, so due to the constant proportionality, the viscosity is constant and does not depend on strain rate [23,24]. However, non-Newtonian fluids do not obey the Newtonian law of viscosity, but instead follow a wide range of other relations of quasi-linear or non-linear nature between those two tensors or their derivatives. non-Newtonian fluids exhibit linear, quasilinear or non-linear between stress and rate of deformation [25,26]. Besides pure viscous non-Newtonian fluids, there are some types of non-Newtonian fluids which exhibit viscous and elastic behavior under shear flow, for example they may exhibit time-dependence of their properties, even when forced under stationary conditions, memory effects or the appearance of normal stresses in flows in which there is only a steady nonzero shear deformation. Such behavior is characteristic of viscoelasticity [25,26]. The viscoelastic effects can be obtained by adding small amount of long-chain polymeric molecules to an otherwise Newtonian solvent.

2.1.1. The constitutive equation of viscoelastic fluid

Despite of Newtonian fluids only required a single rheological constitutive equation to describe its characteristics, non-Newtonian fluids are characterized by a wide range of behaviors which described by a variety of rheological constitutive equations [27,28]. There are several debates about selecting a proper constitutive equation to describe the dilute polymer solutions [12,29]. One of the simplest is the Oldroyd-B model, a constitute equation for viscoelastic fluids named after James G. Oldroyd, a British mathematician and rheologist [30,31]. Although the Oldroyd-B model provide acceptable results for shear flow of viscoelastic fluid at low or moderate shear rate,

polymer molecules in the solution can infinitely extend at high strain rate, therefore in Oldroyd-B model may cause some unphysical results which is not correct.

Another popular constitutive equation used to describe dilute long-chained polymer solutions is the finitely extensible nonlinear elastic (FENE) model developed based on kinetic theory. Warner [32] was the first who used the FENE model. In the FENE model, polymers are described by beads connected with each other by a nonlinear spring. FENE model needs to perform a statistical average of dumbbells at each location in order to determine the polymer stress and therefore the model does not contain a closed-form constitutive equation for the polymer stress. Note that comparing to Oldroyd-B model, the extensibility of polymer molecule is finite in FENE model therefore it provides better physical results. Several versions of FENE models have been extended from the original version. There are various discussions about the proper FENE model in the literature, as discussed in follows.

Zhou and Akhavan [33] illustrated that if bead-spring parameters are selected properly, FENE dumbbell is appropriate model for simulating turbulent transient elongational flow. The most common used two-bead dumbbells closure of the FENE type model are the FENE-CR model which was introduced by Chilcott and Rallison [34] and the FENE-P model suggested by Peterlin [35]. FENE-CR model uses the Peterlin approximation, without considering the shear rate dependence of viscosity, it is utilized to describe Boger fluids[1] [36], However, FENE-P fluid has the minimum number of ingredients needed to describe the rheology of dilute polymer solutions, namely memory effects, shear-thinning of the shear viscosity and bounded elastic stresses. Furthermore, regarding FENE-P model, Zhou and Akhavan [33] also showed that the FENE-P dumbbell is a suitable constitute equation for steady state flow, but its accuracy decreases considerably if it is utilized for transient elongational flows.

Regarding other similar models of the FENE type, Zhou and Akhavan [33] concluded that FENE-LS closure proposed by Lielens et al. [37] and multi-mode models such as FENE-PM [38] and the adaptive length-scale model (FENE-ALS) proposed by Ghosh et al. [39] are appropriate models if a more sophisticated model than FENE-P is required. The main differnce of FENE-L and its simplified version FENE-LS with FENE-P is that they consider both the average dumbbell

1 -Boger fluid is a type of dilute polymer solution which is so dilute that its viscosity variation with shear rate is negligible.

configuration and its dispersion [37]. The decoupled distribution takes to the account by utilizing an extra scalar parameter and its evolution equation. Furthermore, in contrast to FENE-P model which developed based on Gaussian configuration distribution function, FENE-L and FENE-LS used Dirac/tail L-shaped distrobution and two-Dirac length distribution functions, respectively[37]. FENE-ALS model [39], developed based on Kramers chain since Ghosh et al. [39] noticed that it can capture the features of dilute polyer solution of fast varying extensional flow better than FENE dumbbell model, the model also required an evolution equation for representing the adaptive length scale that varies according to the kinematical history.

It should be noted that utilizing sophisticated models does not guarantee to considerably improve the results accuracy because in some cases such as the study of hysteretic behavior of dilute polymer solutions in extensional flow there is no significant difference in the accuracy of FENE-P and FENE-L, while the computational cost and complexity of FENE-L model are clearly distinguishable [40]. Because FENE-P is one of the lowest computaional cost and simplest constitutive equations in this type of family and can describe the main features of the rheology of dilute polymer solutions [25,26,35], it has been utilized in many studies of turbulent viscoelastic fluid flows [13,14,28,41]. As a result, in the present study FENE-P model is also utilized to describe the viscoelastic behavior of flow.

2.1.2.The governing equations for flows of FENE-P fluids

The governing equations for incompressible fluids are written next in indicial notation. The conservation of mass is

$$\frac{\partial u_k}{\partial x_k} = 0, \tag{2- 1}$$

$$\rho\left(\frac{\partial u_i}{\partial t} + u_k \frac{\partial u_i}{\partial x_k}\right) = -\frac{\partial P}{\partial x_i} + \frac{\partial \tau_{ij}}{\partial x_k}, \tag{2- 2}$$

where u_i is the velocity vector, P is the pressure and ρ is the fluid density. The fluid extra stress τ_{ij} is given as the sum

$$\tau_{ij} = \tau_{ij}^s + \tau_{ij}^p. \tag{2- 3}$$

of the Newtonian solvent stress (τ_{ij}^{s}) and a polymer contribution (τ_{ij}^{p}). The solvent stress is

$$\tau_{ij}^{s} = 2\rho v_s S_{ij}, \tag{2- 4}$$

The polymer stress contribution (τ_{ij}^{p}) is given by the FENE-P model [26,35] as

$$S_{ij} = \frac{1}{2}\left(\frac{\partial u_i}{\partial x_j} + \frac{\partial u_j}{\partial x_i}\right). \tag{2- 5}$$

The zero-shear rate viscosity (v_0) is the sum of solvent and polymer kinematic viscosities

$$v_0 = v_s + v_p. \tag{2- 6}$$

The ratio of the solvent kinematic viscosity to the solution viscosity at zero shear-rate is defined as

$$\beta_s = \frac{v_s}{v_s + v_p} = \frac{v_s}{v_0}. \tag{2- 7}$$

The FENE-P model is used to describe the rheology of dilute polymer solution, in the FENE-P model ensemble of molecules are represented by dumbbells, which are pairs of beads connected by massless nonlinear springs, as it is shown in (Figure 2. 1).

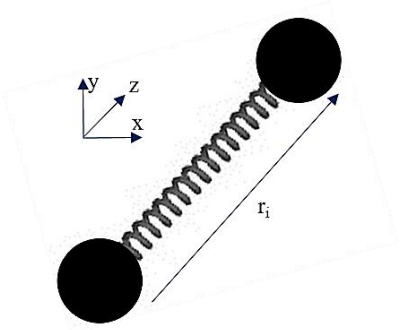

Figure 2. 1- The schematic of dumbbells in FENE-P model

The polymer stress contribution (τ_{ij}^{p}) is given by the FENE-P model [26,27] as:

$$\tau_{ij}^{p} = \frac{\rho v_p}{\lambda}\left[f(C_{kk})C_{ij} - f(L)\delta_{ij}\right], \tag{2- 8}$$

where ν_p is the zero-shear rate polymer kinematic viscosity coefficient, λ is the longest relaxation time of the polymer molecules, δ_{ij} is the identity tensor and C_{ij} is the dimensionless conformation tensor. This tensor expresses the orientation and stretch of the model polymer dumbbell at each

flow point (cf. [26]) and needs to be given by an adequate evolution equation. The conformation tensor is defined as

$$C_{ij} = \frac{\langle r_i r_j \rangle}{\langle R^2 \rangle_0} \tag{2- 9}$$

where r_i is the end-to-end vector connecting the two beads of the dumbbells, is then normalized by the square of its equilibrium radius $\langle R^2 \rangle_0$. Finally, $f(C_{kk})$ is the Peterlin function, a scalar function of the trace of the conformation tensor and $f(L)$ is usually its equilibrium value (value at rest) that depends on the square of the maximum normalized dumbbell extensibility. There are several variants of the FENE-P model, that differ in the Peterlin function used, of which we single out the following three, which give essentially identical responses provided $L^2 \gg 3$.

$$f(C_{kk}) = \frac{L^2}{L^2 - C_{kk}} \text{ and } f(L) = \frac{L^2}{L^2 - 3} \tag{2-10a}$$

$$f(C_{kk}) = \frac{L^2}{L^2 - C_{kk}} \text{ and } f(L) = 1 \tag{2-10b}$$

$$f(C_{kk}) = \frac{L^2 - 3}{L^2 - C_{kk}} \text{ and } f(L) = 1. \tag{2- 10c}$$

In Eq. (2-10) L is the maximum dumbbell extensibility and C_{kk} is the trace of the conformation tensor. The form of Eq. (2-10a) is the original, modified to Eq. (2-10b) by Bird et al. [26] as discussed in Beris and Edwards [42]. The functions in Eq. (2- 10c) have been used first by Vaithianathan and Collins (2003) [43] and since then have been used extensively in investigations of turbulent flows of polymer solutions[13,16,44, 45]. Even though the formulation to be presented is general and independent of the model, the final numerical results pertain to the last set of functions, except in Section 6.2.3, where our numerical data are compared with Olagunju's results [19], and we use the same set of functions that he relied upon, Eq. (2-10b). Regardless of the set of functions, the evolution equation for the dimensionless conformation tensor is

$$\frac{\partial C_{ij}}{\partial t} + u_k \frac{\partial C_{ij}}{\partial x_k} = C_{jk} \frac{\partial u_i}{\partial x_k} + C_{ik} \frac{\partial u_j}{\partial x_k} - \frac{1}{\lambda}\left[f(C_{kk}) C_{ij} - f(L)\delta_{ij}\right]. \tag{2- 11}$$

a differential equation of hyperbolic type. The first and second terms on the left-hand-side represent time variation and advective transport of elastic energy, whereas on the right-hand-side the first and second terms represent distortion and dissipation of elastic energy, respectively.

In the following after discussing the characteristics turbulent flows, we briefly review the main studies on both laminar and turbulent viscoelastic fluid.

2.2.Turbulent flow

Turbulent flows can be found in countless situations in nature, such as in a flowing river, rising smoke from chimney or many industrial processes. There is no unique definition for turbulent flow, however there are some common characteristics that are well described in the literature. Turbulent flow is a complex time-dependent, three-dimensional, rotational flow which its flow properties such as velocity and pressure vary in a chaotic-like manner. Turbulent flows are characterized by strong irregularity, high dissipation of energy, intense mixing and diffusivity and the existence of a broad range of scales of motion. The study of turbulent flows leads better understanding of its natural processes and turbulent flow characteristics which requires for optimum design of system in the industries [46].

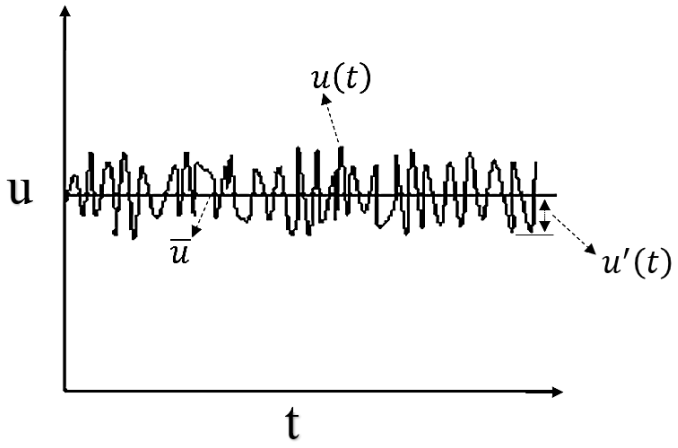

Figure 2. 2- The variation of velocity in time for turbulent steady mean flow, mean velocity is depicted by $\overline{u}$ and the velocity fluctuation by $u'(t)$, therefore $u(t) = \overline{u} + u'(t)$.

Since chaotic behavior is the nature of turbulent flow, it is easily understood by observing for instance the flow velocity variation at specific points inside the flow, as displayed in Figure 2. 2. As shown, the velocity fluctuations are chaotic and irregular, but the flow is statistically steady. For studying statistically steady turbulent flows, the ergodic hypothesis is utilized. The ergodic hypothesis explains that the time averaged of physical quantities are equal to their statistical quantities, the ensemble average, in a very long observation [47]. The idea of using ergodic

hypothesis considerably decreases the complexity and the volume of required information for studying the turbulent flow and limit the number of physical and statistical quantities [48].

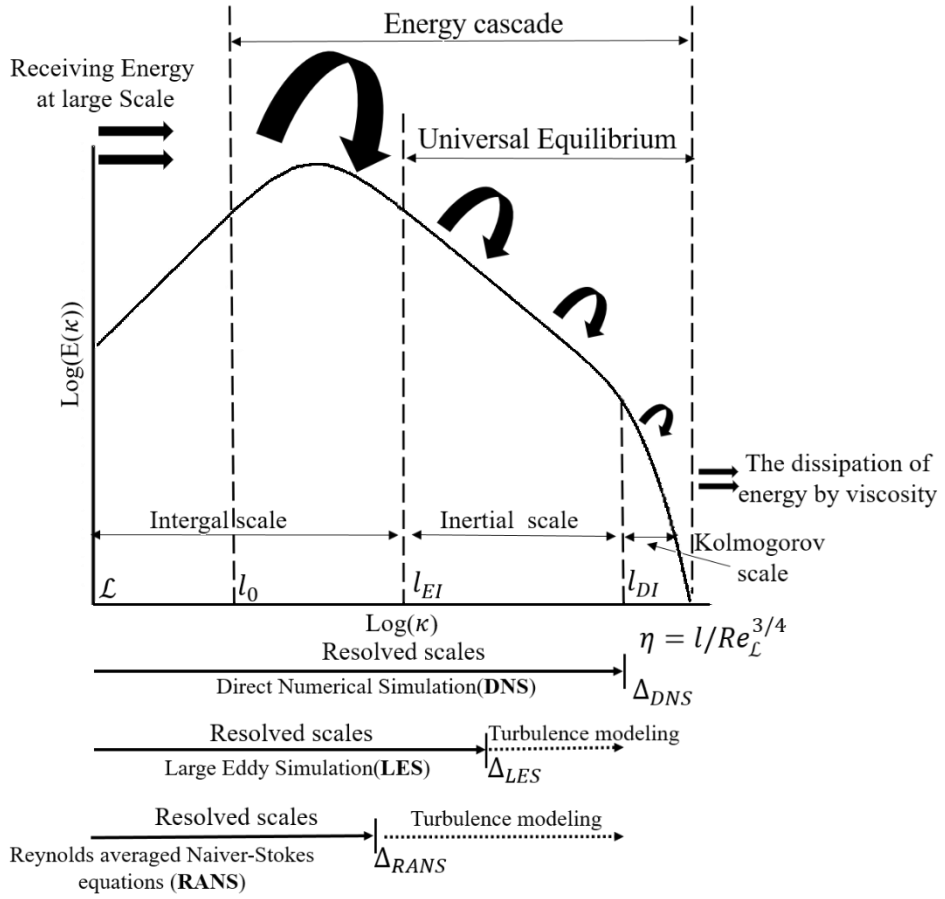

Figure 2. 3- Energy distribution at various scales of flow according to Kolmogorov hypothesis, and the comparison of DNS, LES and RANS

The existence of a broad range of scales is one of the fundamental features of turbulent flow. The large-scales size are related to the flow geometry and boundary conditions. In regard to the small scales and the whole range of scales, Richardson [49] in 1922 elaborated on how energy transfer takes place (by inviscid processes) from mean flow to the smallest scales in which viscosity plays the dominate role and dissipates the energy. He summarized his idea on a poem “Big whorls have little whorls, that feed on their velocity, And little whorls have lesser whorls, And so on to viscosity, (in the molecular sense)”. In 1949, Onsager [50] called this concept “energy cascade”. Figure 2. 3 explains the Richardson-Kolmogorov hypothesis according to the wave number space is shown here by (κ).

Earlier in 1941, Kolmogorov [51] proposed his theory about turbulent flow, which is based on three hypotheses. The first one is local isotropy of small scale, which says that the small scales are statistically isotropic in high Reynolds number flows, (in the wave number space $\kappa_{EI} < \kappa$, the subscript of *EI* stand for inertial range). The second hypothesis, also called the first similarity hypothesis, states that in high Reynolds number flows, the small-scale statistics are universal and only specified by kinematic viscosity and the rate of energy dissipation $\kappa_{DI} < \kappa$, the subscript of *DI* stand for dissipation range. The third hypothesis is called the second similarity hypothesis, states that in high Reynolds number flows, there is an intermediate range of scales between the large and small scales, which is called Taylor micro-scales. These scales are universal and are specified only by the rate of energy dissipation but are independent of kinematic viscosity. This intermediate range is called the inertial range in which the energy spectrum of the cascade of energy is a function of the wave number (κ) and characterized by a slope of -5/3 in log-log coordinates, the equation is valid in the subrange of $\kappa_{EI} < \kappa < \kappa_{DI}$ or in the other word in the inertial subrange (Figure 2. 3). This power law relation is one of the important features of turbulent flow [46].

Obukhov (1941) [46][52] presented a formula for the Kolmogorov hypothesis in the spectral space. If the wave number is expressed by $\kappa = \frac{2\pi}{l}$ in which *l* is the characteristic length scale and the turbulent kinetic energy is also obtained from the integral of *E(κ)* the whole range of wavenumber space

$$K = \int_0^\infty E(\kappa)\, d\kappa, \tag{2- 12}$$

where *E(κ)* quantifies the amount of energy at the specific eddy size *l* or its wave number *κ*

$$E(\kappa) = C_k\, \varepsilon_s^{\frac{2}{3}} \kappa^{-\frac{5}{3}}. \tag{2- 13}$$

in which dissipation rate is denoted by ε_s and C_k is the universal Kolmogorov constant. Eq. (2-13) is well known as the -5/3 power law equation and was presented by Obukhov[46],[52].

2.2.1.Numerical simulation of turbulent flows

Beside experimental studies, by increasing the computing capacity of modern computers, the study of turbulent flow by utilizing numerical simulation has gained much attention due to its

advantages, such as greatly reducing the cost and time of new designs, performing study when carrying out experimental studies are impossible or dangerous, and providing unlimited level of detail with very good accuracy.

There are three main approaches to deal with the numerical simulation of turbulent flow. Direct numerical simulation (DNS) is a straightforward numerical technique to study turbulent flow in which no turbulence modeling is utilized. The first attempt to apply DNS method was performed by Orszag and Patterson for numerical simulations of three-dimensional homogeneous isotropic turbulence in 1972 [53]. Although DNS is the most accurate method, it has some constrains. Increasing the Reynolds number (*Re*) broadens the scales of motion range. To capture all range of motion scales in turbulent flow, DNS requires very fine computational meshes and time steps, the number of grids points is of the order $ORe^{9/4}$ for adequate three-dimensional simulation [48], in addition, the large memory storage requirements, so DNS is considered as a very expensive technique which is not sufficiently fast and cheap for engineering type calculations [54].

The numerical simulation of engineering flows under turbulent flow conditions relies on the use of Reynolds-averaging the governing equations (RANS) proposed by Reynolds [55], which remains a primary approach for engineering application, due to rather simple implementation algorithm, beside low or reasonable computational cost. It is based on the Reynolds decomposition of the physical variables and subsequent. It introduces unknowns which need to be modelled for a closed problem. Dealing with the unsteady and transient flow, flow with separation, and rotation and flow faced with strong curvature are the main constraints of the many RANS models. Although RANS models may predict the mean properties of the many flows, many important characteristics of the flow, such as the dominating flow frequencies, cannot be estimated [48,12]. Due to overcome the shortcomings of RANS and DNS, there is a middle ground solution, is cost-effective comparing with DNS and more accurate comparing with RANS, is called Large eddy simulation (LES).

Large eddy simulation (LES) is an intermediate approach between DNS and RANS, introduced by Smagorinsky in the 1960s for simulation of atmospheric flows [56] and then utilized by Deardorff in 1970s [57]. Since then several sub-grid scale (SGS) models were developed to address model shortcomings [48]. In LES the large scales are estimated explicitly and the small scales, called SGS, are split by implementing low-pass filtering on the Navier–Stokes equations required to be

modeled. The computational cost of LES is considerably lower than DNS. In addition, in principle, proposing a model only for isotropic small scales may be easier and more accurate than the RANS models which should cover all range of scales of motion, as shown Figure 2. 3. comprehensive review of LES approach can be found in [58-60].

2.3.Viscoelastic turbulent flow in dilute polymer solutions

Since observation of the drag reduction phenomenon by Toms [1], various numerical and experimental studies have been performed to explain its mechanisms by proposing several theories. One of the main theories is based on the enhance of the extensional viscosity explained by Lumley [61], Procaccia et al. [62], it is explained that the high shear rate of some regions such as buffer layer causes the stretching of coiled polymer and increase the extensional viscosity effect. This procedure would weaken turbulent fluctuations and suppress the small eddies, thicken the viscous sublayer and accordingly causes the onset of drag reduction. Furthermore, Lumley states that the polymer relaxing time should be larger than the flow time scale in order to onset of the drag reduction. The schematic of coiled and stretched configuration of polymer due to shear rare are shown in Figure 2. 4.

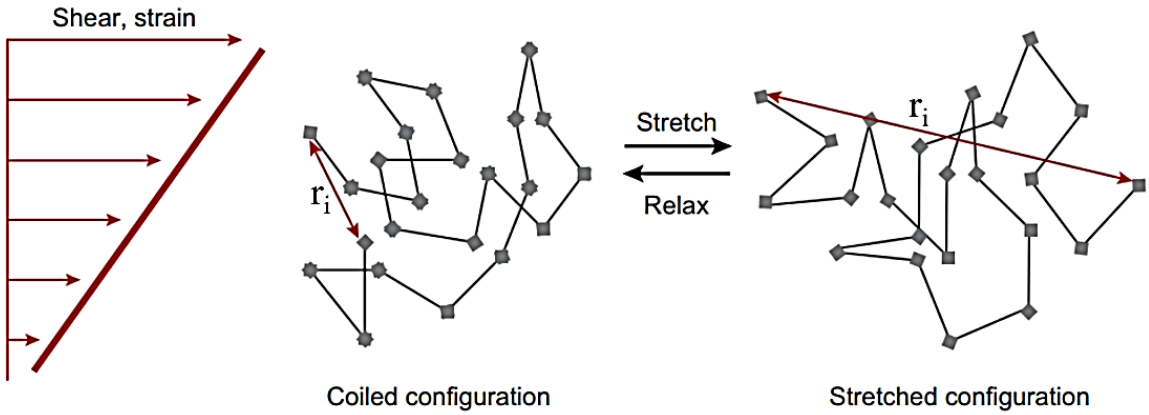

Figure 2. 4- Schematic of coiled and stretched polymer configuration in shear flow. Polymer stretch is characterized by the change in r_i, which is the end-to-end vector of the molecule. [63]

However, the Lumley theory was criticized by some observation in which the polymer was injected at the center on the pipe where is far away for being affected by wall. Those observation lead to another theory discussed by McComb and Rabie [64], Bewersdorff [65], Tabor and de Gennes [66], De Gennes [67] is called elastic theory which described that the wall effect on turbulence

structure are negligible and the small scale of turbulence only affected by elasticity. The theory states that the stretched polymer molecules stored some amount of elastic energy, when the quantity of this accumulated energy become equivalent to kinetic energy in the buffer layer region causes the onset of DR. The consequence of this procedure is suppressing the small scale of motion, thickening of buffer layer region and finally DR phenomenon [66,67]. As discussed, the major contradiction of both theories comes from the how energy transfer to polymer and then in which range of scale the phenomenon occurs. The other conflict is about energy spectrum prediction, in which Lumley explained that existence of polymer increase the energy dissipation rate, while de Gennes mentioned that there should be a truncation in the kinetic energy cascade of turbulence when the kinetic energy convert into elastic energy stored in the polymer. The former explanation is supported by experimental [68,69]and numerical studies [70-73].

Recently, Xi et al. [74] proposed new theory extended from Tabor and de Gennes study [66] called energy flux balance theory. They explained that the onset of DR occurs when elastic energy flux increase by decreasing the scale length causes gradually weaken of kinetic energy transfer to small scale of motions via energy cascade procedure and consequently dampen the small scale of motion. They clarified the influence of elasticity on turbulence in the inertial range, in where the elastic energy flux and the turbulence energy cascade are in balance which is called elastic length scale.

Li et al. [75] proposed another theory based on some observation of friction DR on DNS of turbulent channel flows of dilute polymer solutions. They noticed the time scale of vortex which are close to the wall play key role in onset of DR. They observed that the near-wall vortexes transfer their energy to the polymers and then polymers give back the energy to the high-speed streak. This procedure known as upwash and downwash phenomenon. To elucidate this procedure, they introduced the effective Deborah number as the ratio of polymer relaxation time to the time scale of fluctuations in the streamwise and near-wall vortexes. They stated that this ratio remains at $O(1)$ in all range of DR from the onset of DR until the upper limit of DR known as the maximum drag reduction (MDR) asymptote. Increasing the elastic forces cause the stabilization of streamwise vortexes close to the wall, leading to longer and slower rotation of them. This phenomenon highlights that there is a balance between elastic forces and the mean rotation speed of streamwise and close to the wall vortices which clarify the Reynolds stress production and upwash and downwash phenomenon. They also showed that by increasing DR the ratio of the

fluctuation time scale of streamwise vortices to the vorticity rotation time scale decrease. It was also stated that the maximum drag reduction phenomenon happens when these two mentioned time scales become nearly equal.

Li and Graham [76,77] proposed another theory to shed light on DR phenomenon. They declared that the time intervals, which is called the turbulence hibernation phenomenon, has an important role in the maximum drag reduction phenomenon. They observed that the turbulence hibernation is assisted by viscoelasticity effect which prevents the occurrence of active turbulence. Although at low elasticity level the mean time scale of active turbulence period is constant, this time period reduces considerably above certain level of elasticity and consequently the time duration of hibernation increase. Generally speaking, active turbulence causes polymer molecules are stretched significantly which leads to suppressing the turbulence and convert the flow to a very weakly turbulent hibernating regime. However, in the time of hibernation the polymer molecules are not under the considerable stress, so they are somehow relaxed similar to an equilibrium condition. When hibernation is terminated by the initiation of new turbulent fluctuations, the flow regime is changed to active turbulence which starts to stretch the polymer molecules again and the whole procedure is replicated.

2.3.1.Turbulent models for viscoelastic fluid

As briefly explained earlier, there are three main approaches to deal with the numerical simulation of turbulent flow, DNS, RANS, and LES. Comparing to DNS of Newtonian flows the computational cost of DNS of turbulent viscoelastic flows is higher an account of the additional of variables and governing equations and the numerical limitations they impose. In addition, there are some available RANS models for viscoelastic fluids in turbulent flows [78-82], however they were developed based on wall-turbulent flow due to the extensive industrial applications and also suffer from well-known RANS limitations which explained earlier, therefore they are not consider in the review section of the present study. On account of mentioned constrains, LES is also considered as a proper approach to utilize for turbulent flows of viscoelastic fluids. Regarding to turbulent flow of viscoelastic fluid, the advantages of numerical simulation over experimental studies can be summarized as follows: detail study of velocity field, solvent and Reynolds stress, and polymer stress components determining the mean orientation of the polymer

molecules, which can elucidate the mechanisms of drag reduction phenomena from low versus high DR. Numerical simulation is a more convenient approach to study the effect viscoelasticity considered by of the ratio between the polymer viscosity and the solution zero-shear rate viscosity, is comparable with polymer concentration quantity β_p, the maximum dumbbell extensibility L, and the longest relaxation time of the polymer molecules λ.

To develop a proper LES model, it is required to fully understand the main role of SGS model in the dynamic of the turbulent flow. The main role of SGS model is representing the kinetic energy transfer between grid-scales (GS), and sub-grid scales [46,83]. The Richardson-Kolmogorov energy cascade concept is behind many successful SGS models for turbulent Newtonian fluids since it explains the interscale interaction motion scale in Newtonian turbulent flows very well [54,46, 83], however, care should be taken in implementing it into non-Newtonian turbulent flow due to the complex SGS interactions with the fluid rheology which may cause difficult conditions.

In the HIT, It was observed that the interaction of turbulent strcuture with the fluid elasticity may change the energy distribution of motion scales. This energy variation is more apparent and significant in the inertio-elastic turbulence, which is called to a regime of viscoelastic turbulent flow in which polymer relaxation time is larger than the turbulence time scales and the shear time scales of the gradient imposed by the wall [13,14]. In some studies, it was observed that the polymer additives dissipate the main portion of the transferred energy from the large to the small scales which may lead to establishment of second energy cascade known as a polymer-induced energy cascade [12,13,14,28]. This polymer-induced energy cascade can compete with the classical energy cascade [13,14,29, 41]. These complex interaction of GS/SGS/viscoelastic fluid interactions play a vital role in the dynamics of turbulent flow of viscoelastic fluids, so it must be considered in any future SGS model. There are only a few studies about SGS model for turbulent flows of non-Newtonian fluids highlighted as follows.

Ohta et al. [84] performed several DNS and LES in turbulent channel flow for various types of purely viscous non-Newtonian fluids based on power law and Casson model. Since they wanted to study the deviation of the turbulence structures of non-Newtonian fluid from Newtonian fluid in a region near a wall, the main portion of their study focused on low-Reynolds-number wall turbulence of non-Newtonian fluids, but due to the purely viscous nature these type of flows are close to turbulent Newtonian fluids. The model was developed by considering the effect of variable

viscosity into the Smagorinsky model for Newtonian fluid. They proposed an extended Smagorinsky model, with a modification on the filter width based on the results of non-Newtonian turbulent channel flow. They stated that their LES and DNS results were consistent and can precisely estimate mean velocity profiles and SGS stress in shear-thinning and shear-thickening flows.

Thais et al. [85] proposed the first SGS model for temporal large eddy simulations (TLES) for viscoelastic fluid flows based on the FENE-P constitutive equation. Their SGS model was based on a temporal approximate deconvolution method (TADM) for both the SGS terms of the Newtonian and polymer stresses in the momentum and conformation tensor equations. The model was calibrated with wall-flow and utilized in turbulent channel flow. The TLES model was stable and it could reduce computational time considerably comparing with DNS, and the calculated percentage of DR prediction was in good agreement with DNS. However, the model has some drawbacks. First of all, the model is only active near the wall in where the level of SGS activity is known to be lower than in wall-free or high Reynolds number flows so it is hard to assess the performance of SGS model comparing with wall-free or high Reynolds number flows. In addition, the model is very complicated to implement as well as the proposed SGS model was developed only based on mathematical properties which make it hard to input physical properties of turbulent flow in it. Viscoelastic interactions in small scales play a vital role in the dynamics of turbulent non-Newtonian fluids, so the effect of GS/SGS/viscoelastic fluid interactions must be considered in any future SGS model.

Wang et al. [15] used the SGS model of Thais for forced homogeneous isotropic turbulence (FHIT) of FENE-P fluids at moderate Taylor Reynolds number. They studied the influence of polymer additives on some important flow properties such as strain, vorticity, drag reduction (DR) in the wall-free flow. They reported that the presence of polymers prevents the small-scale vortex structures and small-scale intermittency, which cause turbulence suppression comparing with turbulent Newtonian fluids. They did not recognize any significant difference in the self-similarity scaling law between so-called modified Kolmogorov scaling law of turbulent flow of viscoelastic fluid and Kolmogorov scale of turbulent flow of Newtonian fluid in their simulations.

Li et al., [86] utilized the idea of temporal SGS model of Thais [85] to filter the constitutive equation of a simplified version of the multi-mode FENE-P model based on multiple relaxation

times to study DR in viscoelastic turbulent channel flow. The main aim of their research was to reduce the computational cost of the traditional multi-mode model while keeping its good computational accuracy. They stated that the new model describes the real physical process much better than the conventional model. Because their new model considers more parameters, it is more adaptable to utilize for wider applications comparing with the single-mode FENE-P model which consider single relaxation time. Furthermore, they could calculate the viscosity of the polymer solution more accurately than the single mode FENE-P model especially in large shear rates. However, they could not capture the shear-thickening of the surfactant solution. They also reported that the SGS model had a good performance in the simulation of viscoelastic turbulent channel flow, and they could predict some turbulent properties such as DR rate, the quadrant analysis[2] of Reynolds shear stress, and the contributions of shear stresses on turbulent frictional resistance accurately.

Masoudian et al. [21] performed DNS of turbulent channel viscoelastic fluids described by FENE-P. They performed an *a-priori* test to analyse and evaluate the effect of the polymer additives on the subgrid-scale (SGS) energy in the filtered momentum and FENE-P constitutive equations. They observed a considerable reduction in the SGS stresses and energy in the viscoelastic turbulent flow comparing with the Newtonian turbulent flow. Then by analyzing the terms that are responsible for kinetic energy transfer between grid-scale (GS) and SGS energy, they observed that forward scatter events are considerably reduced due to the existence of polymers. They showed that the ratio of the shear stress component of momentum equation to its strain rate decreases in turbulent viscoelastic fluids comparing with turbulent Newtonian fluids, however its overall shape and behavior remains proportional to that for Newtonian fluids. Then by filtering the DNS fields and analysing the new terms which comes from the filtered governing equations of FENE-P fluids, they identified and ignored the negligible terms such as the subgrid-scale of conformation advection tensor and determined the terms which require SGS closures such as subgrid-scale of polymer stretching tensor.

Ferreira et al. [12] proposed a new (SGS) model for isotropic homogeneous turbulence of viscoelastic fluids described by FENE-P which is called distortion similarity model (DSIM). The

[2]- The quadrant analysis is a method of analysising and determining whether two different random variables are correlated by plotting their joint probability density function.

model was developed based on two main hypotheses: the self-similarity of the polymer stretching terms, and the global equilibrium of the trace of conformation tensor. The classical Smagorinsky model was implemented for the SGS term of the momentum equation. They assessed the performance of the DSIM closure by comparing with DNS of forced homogeneous isotropic turbulence by utilizing a priori tests. The proposed DSIM model was simple to implement with acceptable computational cost. Their analysis showed that the subgrid-scale polymer stretching term is the only term that requires an SGS closure while all the other SGS terms in the conformation tensor are negligible. They reported that their LES model could estimate the global flow properties, as the SDR, the flow structures, the kinetic energy spectra accurately.

2.3.2.Turbulent planar jet flow

As mentioned, the main objective of the present study is to develop LES models for in-homogeneous and wall-free flow of FENE-P fluids, for this reason, the planar jet flow is selected in the present study. Since planar jet flow are categorized as a shear free flow it can provide a facility to better assessment of the SGS model performance, without facing with the problem that exists in the presence of solid walls. Figure 2. 5 shows the quantity of Reynolds stress is very low near the wall and increase by increasing the distance from the wall. The planar jet flow lets us investigate the effect of inhomogeneities on the SGS model performance as well.

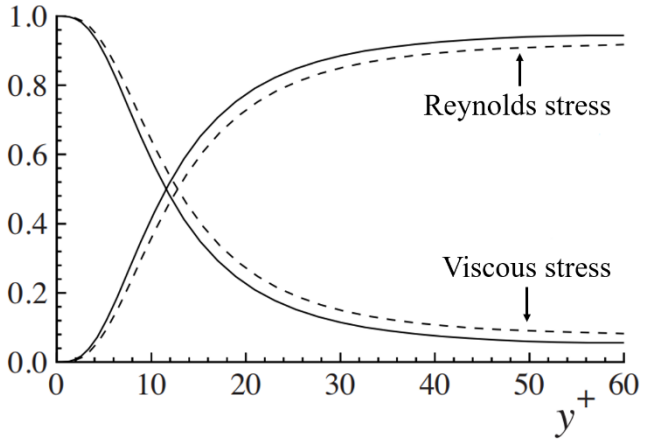

Figure 2. 5- The normal variation of viscous and Reynolds stress normalized by total stress, for two Reynolds numbers, dashed lines, Re = 5,600; solid lines, Re = 13,750 [46].

In fluid dynamics, a shear layer is a region of flow in which there are significant velocity gradients. When this layer occurs between two different flows streams and away from walls it defines what is called a free shear layer. A planar jet is a type of free shear layer flow. In a jet, a stream of high momentum fluid intrudes into another fluid of low or null momentum at the corresponding. A Cartesian coordinate of system is used in the present work, the main flow direction (streamwise direction) is x, the planar jet spreads in the normal direction (y) and the mean velocity is null in the third direction, also called neutral or spanwise direction (often the z-direction). Accordingly, on the mean, the turbulent planar jet flow can be regarded as a two-dimensional flow, in which the global structure of the flow is independent of Reynolds number for high enough Reynolds numbers [46]. The jet half-width is defined as the transverse distance between the centerline to the location where the local streamwise mean velocity equals half the local centerline velocity on the centreline and the co-flow velocity as it is shown in Figure 2. 6(a).

Turbulent planar jet can be divided into three main sub-regions, as illustrated on Figure 2. 6 (b): potential core is the first region, called to the region between the two up and down shear layers close to the jet inlet, developed by large velocity gradient of inlet flow and quiescent outside this region. The next region is transition region in which flow goes through transition process and convert to fully developed turbulent flow. The last region is self-similarity region, the main features of turbulent jet flow are observed in this region, in which if velocity and other scalar properties are being properly scaled, they can be collapsed and show self-similar behavior.

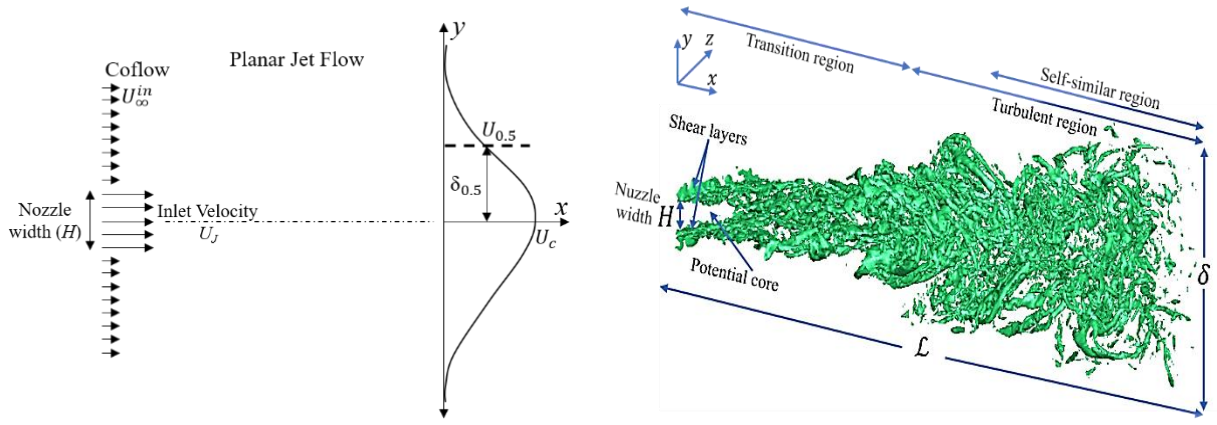

Figure 2. 6- The schematic of turbulent planar region

2.3.3.Roadmap

To develop the LES model, the starting point is to extend the distortion similarity model – DSIM which was proposed by Ferreira et al. [12] into planar jet FENE-P fluids to assess its performance and check whether its satisfying or not. The model may need some modification or calibration to be implemented properly. Furthermore, developing LES model required to extract data of corresponding DNS code which need to validate at first. This requirement can be fulfilled by comparing the DNS results with RheoFoam toolbox and semi-analytical solution. In addition, due to the wide range of industrial and academic applications of laminar flow, proposing semi-analytical solution will also provide a facility to study the effect of viscoelasticity on the corresponding laminar flow characteristics.

2.4.The laminar boundary layer type flow of viscoelastic fluid

In this section, some earlier studies of laminar non-Newtonian fluids with special attention on viscoelastic fluid studies are reviewed briefly.

2.4.1.The planar jet flow

In fluid dynamics, a shear layer is a region of flow in which there are significant velocity gradients. When this layer occurs between two different flows streams and away from walls it defines what is called a free shear layer. Planar jet flow is a type of the classical wall-free shear flows. In a jet flow, a stream of high momentum fluid intrudes into another fluid of low or null momentum at the corresponding. The earliest investigations of jet flows of viscoelastic fluids concerned turbulent flow conditions and were experimental, aimed at understanding the behavior of polymer solutions in wall-free turbulence and to contrast with the provocative effects of polymers in wall turbulence. However, the use of intrusive methods, as in the Pitot tube experiments of White [87], did not allow the proper assessment of the viscoelastic effects. It was with the advent of optical methods, such as the laser-Doppler anemometer, that the first reliable experiments detailing the flow field with viscoelastic fluids took place with Barker [88], Berman and Tan [89] and Koziol and Glowacki [90], whereas Usui and Sano [91] relied on particle tracking. All dealt with the turbulent

axisymmetric jet, easier to construct, and generally speaking reported the suppression of small eddies and the enhancement of coherent structures, leading to a delay in jet spreading relative to the corresponding turbulent Newtonian jet. This qualitatively agreed with early findings on other viscoelastic turbulent free shear flows, such as the mixing layer flows of polymer solutions by Kwade [92] and Hibberd et al. [93], amongst others.

As far as we are aware of the corresponding laminar viscoelastic jet flow has not been studied and there is a similar absence of data for the planar jet. Our interest in the planar jet flow of viscoelastic fluids is related to the extension of the previous direct numerical simulations (DNS) of forced homogeneous isotropic turbulence of polymer solutions [13],[14], to numerical studies of turbulent flow in wall-free turbulence with the same fluids. In such endeavor, the laminar viscoelastic planar jet solution is an essential tool not only to help understand some of the viscoelastic planar jet flow characteristics, but also as a set of data for validation of the DNS code under controlled conditions.

2.4.2.The boundary layer flow

Boundary layer flows are ubiquitous in industrial and natural flows in such a variety of conditions that more than 100 years after the seminal work of Prandtl [94] it continues to be the source of relevant research, as in [95-97]. The topic has been far less investigated for fluids of non-Newtonian rheology and in particular when they exhibit viscoelastic characteristics. One exception though is the particular case of the fully-developed pipe or channel flow, the study of drag reduction by Toms in 1949 [1], fostered a wealth of experimental [61,98], theoretical[99,100] and numerical [101] research that continues up to this day. This particular topic has been the subject of many reviews, and one of the latest by White and Mungal [63].

The fundamental boundary layer flow over a flat plate remains less investigated for viscoelastic fluids and is the one topic of interest in this work, which focus on laminar flow conditions. Srivastasa [102] and Rajeswari and Rathna [103] proposed approximate solutions by utilizing the Kármán-Pohlhausen method [104,105] to study the boundary layer flows of second order incompressible Rivlin–Ericksen fluids in the vicinity of a stagnation point. Later and inspired by Prandtl's boundary layer theory, Beard and Walters [106] proposed a similarity solution for boundary layer flows of viscoelastic Oldroyd-B fluids near a stagnation point and reported that

increasing the elasticity increases the velocity inside the boundary-layer and also enhances the stress on the wall. In 1982, Rajagopal et al. [107] studied Falkner-Skan flows of homogenous incompressible second order fluids and concluded that this type of solution requires not only a large Reynolds number (*Re*), a dimensionless parameter which describes the ratio of inertial to viscous force in a flow, but also that $Re/Wi \gg 1$, where *Wi* is the Weissenberg number, the ratio between elastic and viscous forces. In contrast with Newtonian fluids, which follow a single rheological constitutive equation, non-Newtonian fluids are characterized by a wide range of behaviors and this may be accompanied by a variety of rheological constitutive equations [25]. Early constitutive models, as used in the above works, were essentially derived from continuum mechanics, which described in an incomplete form some of the relevant non-Newtonian fluid properties (Rivlin-Eriksen and second order fluids may not be even valid on account of the large deformation rates encountered in boundary layer flows). The advent of structural or kinetic-theory based constitutive models has resulted in better qualitative, and in some cases quantitative, descriptions of the rheology of real fluids [108]. A well-known example of the former is the successful description of the rheology of some polymer melts by the Phan-Thien-Tanner model [109,110]. Paradoxically, the description of dilute polymer solutions has remained more elusive, but one of the simplest constitutive equations that is able to describe their main rheological features, and has been abundantly used in recent research [45,13], is the model known as FENE-P [26] (acronym for "finitely extensible nonlinear elastic" model with Peterlin's closure [35]), as discussed earlier.

In regards to the boundary layer flow of FENE-P fluids, Olagunju [19,20] proposed an approximate similarity solution in contrast to the Newtonian case for which there is a global self-similar solution [111]. Olagunju called it a local self-similar solution, because it still depends on two independent spatial variables, the streamwise coordinate and the Newtonian similarity variable, as will be discussed in Section 4. In his works, Olagunju only provided information on the profiles of velocity and on the law of variation for the friction coefficient. No information is given on other relevant quantities such as the laws of variation of the boundary layer, displacement and momentum thicknesses, on the profiles of the polymer stress contribution, and on the effects of maximum polymer extensibility (L^2) and polymer concentration (β_p) (although his solution contained L^2 and β_p, he did not explore their effects). In addition, Olagunju ignored non-negligible elastic contributions to the rheological constitutive equation, which did not affect significantly the

velocity profiles, but certainly do affect the polymer stresses as was found for the laminar planar jet flows of viscoelastic FENE-P fluids by Parvar et al. [112,113]. In particular, Parvar et al. [112] showed that an Olagunju type of solution of the planar jet is unable to properly estimate the normal streamwise component of the polymer conformation tensor (C_{xx}) at very low Wi and also the normal transverse component (C_{yy}) in the whole range of Wi. Bearing in mind that the wall in a boundary layer flow imposes significantly higher rates of deformation, and consequently higher elastic stresses, than exist in a planar jet (for similar characteristic fluid velocities), the extent of Olagunju's polymer stress simplifications [19] needs to be assessed, while also providing the missing information on boundary layer flow characteristics. This sets the stage for the present work, in which we provide a different and more complete solution to the boundary layer flow over a flat plate at zero pressure gradient for FENE-P fluids.

Since mixing layer can also be described through boundary layer-type equations [23,24], in the present study we also decided to extend the theory of boundary layer flows to observe the effect of viscoelasticity on mixing layer flows properties.

2.4.3.The mixing layer flow

The mixing layer flow is one of the three canonical wall-free shear flows (the others being the free jet and wake flows), which are relevant to our understanding of modern fluid mechanics in addition to being present in many natural and industrial flows. As described below, there is a wealth of literature on steady laminar mixing layer flows of incompressible and compressible Newtonian fluids, but our concern is the behavior of viscoelastic solutions.

As discussed, the boundary layer theory of Prandtl [94] allowed the similarity solution of the planar boundary layer flow by Blasius [111], and those ideas and methods were subsequently applied to the wall-free shear flows of Newtonian fluids. The simplified governing equations, benefitting from boundary layer approximations, are the same for both flows, each flow obeying specific boundary conditions. For the laminar steady flow between parallel streams, or laminar mixing layer flow, Lessen [114] and Chapman [115] were among the first to obtain the solution, the former for incompressible fluids, the latter for compressible fluids, but including the incompressible case as a limit case. Lessen [114] investigated the stability of the mixing layer flow, following Kuethe

and Von Kármán [116] by assuming the velocity profiles to be continuous functions in the streamwise and normal directions, but they neither presented profiles nor the corresponding numerical values, just indicated how they could be obtained. In contrast, Chapman [115] presented profiles at various Mach numbers, including the incompressible flow case (zero Mach number). Tabulated data were listed by Lock [117], who provided the full solution through an extension of Lessen's work to parallel streams of fluids with different properties. Other developments considered the case of a non-uniform velocity incompressible fluid stream meeting fluid at rest by Nash [118], while Ting [119] and Klemp and Acrivos [120] further extended the compressible Newtonian mixing layer flow analysis.

Although laminar Newtonian mixing layer flows have been investigated extensively, for the corresponding non-Newtonian flows the literature is scarcer, in particular when fluids of interest are viscoelastic fluids. However there are some studies regarding effect of viscoelasticity on stability/instability of mixing later flow [121, 122, 123]which is out of scope of the present thesis.

Part II

Laminar Viscoelastic Flows

"There is nothing that can be said by mathematical symbols and relations which cannot also be said by words. The converse, however, is false. Much that can be and is said by words cannot successfully be put into equations, because it is nonsense."

-Clifford Truesdell

(February 18, 1919 – January 14, 2000)

An American mathematician, natural philosopher.

Chapter 3: The laminar boundary layer flow of viscoelastic FENE-P fluids

3.1. Flow problem

The laminar planar flat plate flow is sketched in Figure 1. A uniform free stream velocity (U_∞) flows over a thin immobile semi-infinite flat plate of length $\mathcal{L}$ at zero incidence and a streamwise null pressure gradient is imposed outside the boundary layer, the thickness of which is denoted by δ. The origin of the coordinate system is at the plate leading edge, with x, y denoting the streamwise and transverse coordinates, respectively. At the wall the no-slip boundary condition is imposed, and the fluid velocity increases with wall distance across the boundary layer approaching asymptotically the free-stream value. To define the boundary layer thickness the criterion of local streamwise velocity equal to 99% of the free stream velocity is used [23,24].

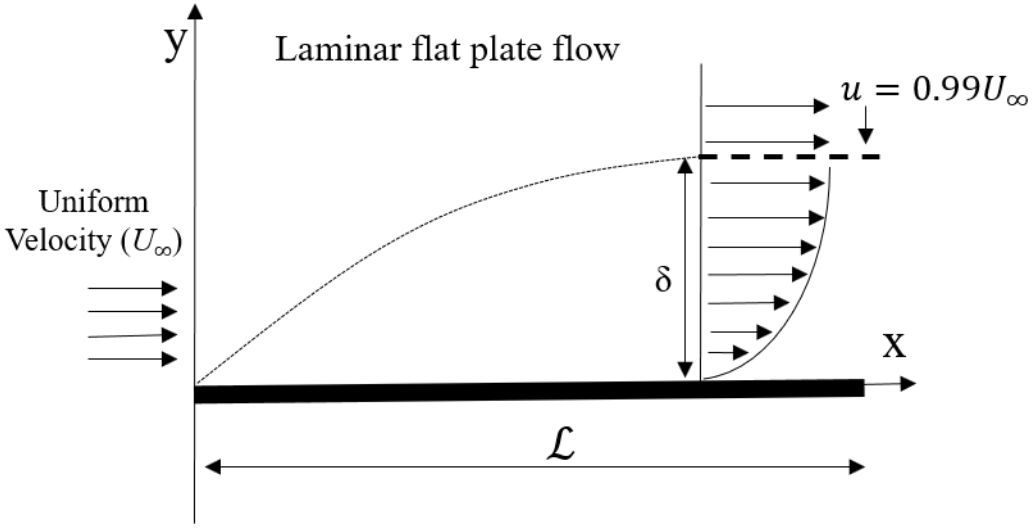

Figure 3. 1- Schematics of the flat plate flow with definition of boundary layer thickness and coordinate system.

3.2. Momentum equation

We follow the standard procedure for boundary layer analysis (cf. [23,24]): we start by making the governing equations dimensionless prior to simplifying them through an order of magnitude analysis. In this process, we follow on the steps of the analysis performed by Parvar et al.[112,113] for the planar jet flow of FENE-P fluids. To normalise the equations, the length of the domain ($\mathcal{L}$)

and free-stream velocity (U_∞) are used as characteristic length and velocity scales. The Reynolds number ($Re_{\mathcal{L}}$) is defined by

$$Re_{\mathcal{L}} = \frac{U_\infty \mathcal{L}}{\nu_0}, \tag{3- 1}$$

where υ_0 is the zero-shear rate kinematic viscosity of the solution ($\nu_0 = \nu_s + \nu_p$). We define the ratio between the polymer viscosity and the solution zero-shear rate viscosity, β_p,

$$\beta_p = \frac{\nu_p}{\nu_s + \nu_p} = \frac{\nu_p}{\nu_0}, \tag{3- 2}$$

which is proportional to the polymer concentration. The Weissenberg number ($Wi_{\mathcal{L}}$) is

$$Wi_{\mathcal{L}} = \frac{\lambda U_\infty}{\mathcal{L}}, \tag{3- 3}$$

The following normalized lengths and velocities (denoted with *) are defined to ensure that their dimensionless derivatives in the continuity equation are at most of the order of unity (in particular $\mathcal{L} >> \delta$)

$$x^* = \frac{x}{\mathcal{L}}, y^* = \frac{y}{\delta}, u^* = \frac{u}{U_\infty}, v^* = \frac{v\mathcal{L}}{U_\infty \delta}, p^* = \frac{P}{\rho {U_\infty}^2}. \tag{3-4}$$

Back-substitution into the continuity equation leads to

$$\frac{U_\infty}{\mathcal{L}}\left(\frac{\partial u^*}{\partial x^*} + \frac{\partial v^*}{\partial y^*}\right) = 0. \tag{3-5}$$

The normalized *x*-momentum equation divided by ρ becomes:

$$\begin{aligned} &\frac{{U_\infty}^2}{\mathcal{L}}\left(u^*\frac{\partial u^*}{\partial x^*} + v^*\frac{\partial u^*}{\partial y^*}\right) = -\frac{{U_\infty}^2}{\mathcal{L}}\frac{\partial P^*}{\partial x^*} + \upsilon_s U_\infty\left(\frac{1}{\mathcal{L}^2}\frac{\partial^2 u^*}{\partial x^{*2}} + \frac{1}{\delta^2}\frac{\partial^2 u^*}{\partial y^{*2}}\right) \\ &+\frac{\upsilon_p}{\lambda}\left(\frac{1}{\mathcal{L}}\frac{\partial([f(C_{kk})C_{xx} - f(L)])}{\partial x^*} + \frac{1}{\delta}\frac{\partial([f(C_{kk})C_{xy}])}{\partial y^*}\right), \end{aligned} \tag{3-6}$$

which simplifies to

$$u^*\frac{\partial u^*}{\partial x^*} + v^*\frac{\partial u^*}{\partial y^*} = -\frac{\partial P^*}{\partial x^*} + \frac{(1-\beta_p)}{Re_{\mathcal{L}}}\frac{\mathcal{L}^2}{\delta^2}\left(\frac{\delta^2}{\mathcal{L}^2}\frac{\partial^2 u^*}{\partial x^{*2}} + \frac{\partial^2 u^*}{\partial y^{*2}}\right) \tag{3-7}$$

$$+\frac{\beta_{\mathrm{p}}}{Wi_{\mathcal{L}}Re_{\mathcal{L}}}\frac{\mathcal{L}}{\delta}\left(\frac{\delta}{\mathcal{L}}\frac{\partial[f(C_{kk})C_{xx}-1]}{\partial x^*}+\frac{\partial\left[f(C_{kk})C_{xy}\right]}{\partial y^*}\right),$$

As in Parvar et al.[112,113] for the planar jet, the following relations are valid: $\frac{(1-\beta_{\mathrm{p}})}{Re_{\mathcal{L}}}\left(\frac{\mathcal{L}}{\delta}\right)^2\frac{\partial^2 u^*}{\partial y^{*2}} \gg \frac{(1-\beta_{\mathrm{p}})}{Re_{\mathcal{L}}}\frac{\partial^2 u^*}{\partial x^{*2}}$ and $\frac{\beta_{\mathrm{p}}}{Wi_{\mathcal{L}}Re_{\mathcal{L}}}\left(\frac{\mathcal{L}}{\delta}\right)\frac{\partial([f(C_{kk})C_{xy}])}{\partial y^*} \gg \frac{\beta_{\mathrm{p}}}{Wi_{\mathcal{L}}Re_{\mathcal{L}}}\frac{\partial([f(C_{kk})C_{xx}-f(L)])}{\partial x^*}$, since $\mathcal{L}/\delta \gg 1$. Also, as argued by Olagunju [19,20], the leading coefficients of $\frac{\partial^2 u^*}{\partial y^{*2}}$ and $\frac{\partial([f(C_{kk})C_{xy}])}{\partial y^*}$ must be of $O(1)$ for the polymer and solvent stresses to be of the same order of magnitude, otherwise the velocity field would be indistinguishable from that of the Newtonian solution. At high enough Reynolds numbers and since the solution is dilute ($1-\beta_{\mathrm{p}}\sim 1$), we have

$$\frac{(\mathcal{L}/\delta)^2}{Re_{\mathcal{L}}} = O(1) \rightarrow \delta = O\left(Re_{\mathcal{L}}{}^{-\frac{1}{2}}\mathcal{L}\right) \rightarrow \frac{\delta}{\mathcal{L}} \approx Re_{\mathcal{L}}{}^{-\frac{1}{2}}, \tag{3-8}$$

which indicates the classical boundary layer proportionality, and

$$\frac{\beta_{\mathrm{p}}}{Wi_{\mathcal{L}}Re_{\mathcal{L}}}\left(\frac{\mathcal{L}}{\delta}\right) = O(1) \text{ or } Wi_{\mathcal{L}} = O\left(\beta_{\mathrm{p}}Re_{\mathcal{L}}{}^{-\frac{1}{2}}\right). \tag{3-9}$$

Eq. (3-9) implies small values of $Wi_{\mathcal{L}}$, for which it can be shown from the constitutive equation that $C_{xy} \approx \lambda C_{yy}\,\partial u/\partial y$. However, the simplified momentum equation can still be used at higher values of $Wi_{\mathcal{L}}$, when C_{xy} increases significantly, provided the shear stress terms dominate over the neglected streamwise gradient of the polymer normal stress.

The order of magnitude analysis of the *y*-momentum equation leads to $\partial P^*/\partial y^* = 0$. Since the present analysis is directed to a flat plat boundary layer $\partial P^*/\partial x^* = 0$, the pressure is constant in the entire flow domain and the *y*-momentum equation is no longer needed.

We proceed with the dimensional form of the simplified *x*-momentum equation

$$u\frac{\partial u}{\partial x}+v\frac{\partial u}{\partial y} = \nu_{\mathrm{s}}\frac{\partial^2 u}{\partial y^2}+\frac{\nu_{\mathrm{p}}}{\lambda}\frac{\partial\left(f(C_{kk})C_{xy}\right)}{\partial y}. \tag{3-10}$$

Without the pressure, the *y*-momentum equation is no longer needed. Through the introduction of the stream function ψ, continuity is enforced and only the *x*-momentum equation needs to be solved. The stream function ψ is defined as

$$u = \frac{\partial \psi}{\partial y}, v = -\frac{\partial \psi}{\partial x}. \tag{3-11}$$

Back-substituting into the *x*-momentum equation leads to

$$\left(\frac{\partial \psi}{\partial y}\right)\left(\frac{\partial^2 \psi}{\partial x \partial y}\right) - \left(\frac{\partial \psi}{\partial x}\right)\left(\frac{\partial^2 \psi}{\partial y^2}\right) = \nu_s \left(\frac{\partial^3 \psi}{\partial y^3}\right) + \frac{\nu_p}{\lambda}\frac{\partial\left(f(C_{kk})C_{xy}\right)}{\partial y}. \tag{3-12}$$

To solve this equation we need the variations of C_{xy} and $f(C_{kk})$ in order to obtain a closed form solution. The stream function and all components of the conformation tensor depend simultaneously on *x* and *y*, but the use of the approximate similarity transformation discussed below will compact the solution.

3.3. Conformation tensor equation

3.3.1. The present solution

Under steady state conditions (2- 11) simplifies to

$$u_k \frac{\partial C_{ij}}{\partial x_k} = C_{jk}\frac{\partial u_i}{\partial x_k} + C_{ik}\frac{\partial u_j}{\partial x_k} - \frac{1}{\lambda}\left[f(C_{kk})C_{ij} - f(L)\delta_{ij}\right]. \tag{3-13}$$

In flows with high shear rates the distortion and dissipation contributions are usually the relevant quantities and the order of magnitude analysis of Parvar et al.[112,113] for the planar jet also showed it to be the case, with the advective term being negligible by comparison. In boundary layer flows the wall imposes a more severe shear condition than exists in a jet, so the arguments put forward by Parvar et al. [112] remain valid leading to the same simplified equations. Additionally, by substituting the velocities as defined through the stream function in Eq. (3-11), the simplified evolution equations for the non-zero components of the conformation tensor are rewritten as:

$$-2\left(C_{xx}\frac{\partial^2 \psi}{\partial x \partial y} + C_{xy}\frac{\partial^2 \psi}{\partial y^2}\right) + \frac{1}{\lambda}\left[f(C_{kk})C_{xx} - f(L)\right] = 0, \tag{3-14}$$

$$2\left(C_{yx}\frac{\partial^2 \psi}{\partial x^2} + C_{yy}\frac{\partial^2 \psi}{\partial x \partial y}\right) + \frac{1}{\lambda}\left[f(C_{kk})C_{yy} - f(L)\right] = 0, \tag{3-15}$$

$$\frac{1}{\lambda}[f(C_{kk})C_{zz} - f(L)] = 0, \tag{3-16}$$

$$-C_{yy}\frac{\partial^2\psi}{\partial y^2} + C_{xx}\frac{\partial^2\psi}{\partial x^2} + \frac{1}{\lambda}\left[f(C_{kk})C_{xy}\right] = 0, \tag{3-17}$$

These equations can be further simplified by considering $\partial\psi/\partial y >> \partial\psi/\partial x$ and that outside very low Weissenberg number flows, the normal components of C_{ij} are higher than the shear components (at rest $C_{xx} = C_{yy} = C_{zz} = 1$ and $C_{ij\ (i\neq j)}$=0). Hence, we keep cross derivative terms when multiplying normal components of C_{ij} leading to

$$-2\lambda C_{xx}\frac{\partial^2\psi}{\partial x\partial y} - 2\lambda C_{xy}\frac{\partial^2\psi}{\partial y^2} + f(C_{kk})C_{xx} = f(L), \tag{3-18}$$

$$2\lambda C_{\mathrm{yy}}\frac{\partial^2\psi}{\partial x\partial y} + f(C_{kk})C_{\mathrm{yy}} = f(L), \tag{3-19}$$

$$f(C_{kk})C_{zz} = f(L), \tag{3-20}$$

$$-\lambda C_{\mathrm{yy}}\frac{\partial^2\psi}{\partial y^2} + f(C_{kk})C_{\mathrm{xy}} = 0. \tag{3-21}$$

The underlined terms in the equations for C_{xx} and C_{yy} are new, i.e., they are not present in Olagunju's solution [19,20], but through Peterlin's function they affect the other components of C_{ij}. However, since their effect on the polymer shear stress is weaker than on normal stresses, the impact on the velocity profiles will be weak as will be shown later.

Further manipulation of Eqs. (3-18)–(3-21) provides the following final expressions for the conformation tensor components

$$C_{xx} = \frac{f(L) + 2\lambda C_{xy}\frac{\partial^2\psi}{\partial y^2}}{\left(f(C_{kk}) - 2\lambda\frac{\partial^2\psi}{\partial x\partial y}\right)} = f(L)\frac{f(C_{kk})\left(2\lambda\frac{\partial^2\psi}{\partial x\partial y} + f(C_{kk})\right) + 2\lambda^2\left(\frac{\partial^2\psi}{\partial y^2}\right)^2}{f(C_{kk})\left(f(C_{kk})^2 - \left(2\lambda\frac{\partial^2\psi}{\partial x\partial y}\right)^2\right)}, \tag{3-22}$$

$$C_{yy} = \frac{f(L)}{\left(2\lambda\frac{\partial^2\psi}{\partial x\partial y} + f(C_{kk})\right)}, \tag{3-23}$$

$$C_{zz} = \frac{f(L)}{f(C_{kk})}, \tag{3-24}$$

$$C_{xy} = \frac{\lambda C_{yy}\frac{\partial^2\psi}{\partial y^2}}{f(C_{kk})} = \frac{\lambda f(L)\frac{\partial^2\psi}{\partial y^2}}{f(C_{kk})\left(f(C_{kk}) + 2\lambda\frac{\partial^2\psi}{\partial x\partial y}\right)}. \tag{3-25}$$

In this set of coupled algebraic equations, C_{ij} depends on the flow characteristics, via the stream function, other C_{ij} components and its trace through the Peterlin function. The determination of the Peterlin function, defined in Eq. (2- 10c) is rather elaborate, as explained next. From the three normal components above, the trace C_{kk} is given by

$$C_{kk} = f(L)\frac{3f(C_{kk})^2 + 2\lambda^2\left(\frac{\partial^2\psi}{\partial y^2}\right)^2 - 4\lambda^2\left(\frac{\partial^2\psi}{\partial x\partial y}\right)^2}{f(C_{kk})\left(f(C_{kk})^2 - 4\lambda^2\left(\frac{\partial^2\psi}{\partial x\partial y}\right)^2\right)}. \tag{3-26}$$

Next we introduce variables consistent with the self-similar Newtonian thin boundary layer solution [23,24], and in dimensionless form for generality. Here, the following variables η and function $G(\eta, x)$ are utilized [23,24]:

$$\eta = \sqrt{\frac{U_\infty}{2\nu_0}}\frac{y}{x^{1/2}}, G(\eta, x) = \frac{\psi}{\sqrt{2U_\infty\nu_0}x^{1/2}}, \tag{3-27}$$

The streamwise and normal velocities are recovered from their definitions, as

$$u = U_\infty G'(\eta, x), \tag{3-28}$$

$$v = \sqrt{\frac{\nu_0 U_\infty}{2x}}\left(\eta G'(\eta, x) - G(\eta, x)\right). \tag{3-29}$$

where the prime indicates derivative in order to η. For the corresponding Newtonian flow these variables allow for a self-similar solution and function $G(\eta)$ only depends on η. This is not the case for the FENE-P fluid, even if other powers of *x* and *y* are tried, a finding that Olagunju [19,20] had previously arrived at and as investigated by Parvar et al. [112] for the planar jet. Therefore, the solution remains two-dimensional, with $G(\eta, x)$ depending on both η and x, and this variable transformation does not simplify it unless further assumptions are introduced. This we do here by considering that streamwise variations of $G(\eta, x)$ are negligible, i.e., henceforth $\partial G(\eta, x)/\partial x \approx 0$, allowing us to obtain what is here called an approximate similarity solution. As we shall see this assumption still leads to a very good description of the velocity field, while allowing for a much

simpler solution [124-129]. Without it we would end up with a far more complicated set of equations bringing little advantage over the numerical solution of the full set of original governing equations.

The Peterlin function $f(C_{kk})$ also depends on η and x, as shown below, and for mathematical clarity henceforth we use

$$K(\eta, x) = f(C_{kk}). \tag{3-30}$$

but note that it is not necessary to invoke the above simplifying assumption for this quantity. Substitution of all expressions into Eq. (2- 10c) leads to the following third order algebraic equation for $K(\eta, x)$

$$K^3 + \mathrm{C}_0 K^2 + \mathrm{C}_1(\eta G'')^2 K + \mathrm{C}_2 G''^2 + \mathrm{C}_3(\eta G'')^2 = 0 \tag{3-31}$$

with dimensionless coefficients

$$\begin{aligned} C_0 &= \left(\frac{3I - 3f(L) - L^2}{L^2}\right), \\ C_1 &= -\lambda^2 {U_\infty}^2 x^{-2} = -{Wi_x}^2, \\ \mathrm{C}_2 &= -\frac{\lambda^2 f(L) {U_\infty}^3}{\nu_0 L^2} x^{-1} = -\frac{f(L) Re_x {Wi_x}^2}{L^2}, \\ C_3 &= \frac{\lambda^2 (L^2 + f(L) - 3I) {U_\infty}^2}{L^2} x^{-2} = \frac{(L^2 + f(L) - 3I) {Wi_x}^2}{L^2}. \end{aligned} \tag{3-32}$$

Here, $I = 1$ if the Peterlin functions are given by Eq. (2- 10c) and $I = 0$ otherwise. Coefficients C_1 to C_3 in Eq. (3-32) depend on *x*, hence this shows why *K* depends on both η and *x* and it is not possible to get a full self-similar solution as for Newtonian fluids.

Regarding the *x*-momentum equation, by substituting C_{xy} (from Eq. (3-25)) into Eq. (3-10),

$$\begin{aligned} &\frac{\partial \psi}{\partial y}\left(\frac{\partial^2 \psi}{\partial x \partial y}\right) - \left(\frac{\partial \psi}{\partial x}\right)\left(\frac{\partial^2 \psi}{\partial y^2}\right) = \nu_\mathrm{s} \frac{\partial^3 \psi}{\partial y^3} \\ &+\nu_\mathrm{p} f(L) \left(\frac{2\lambda \frac{\partial^2 \psi}{\partial x \partial y}\frac{\partial^3 \psi}{\partial y^3} + f(C_{kk})\frac{\partial^3 \psi}{\partial y^3} - 2\lambda \frac{\partial^3 \psi}{\partial x \partial y^2}\frac{\partial^2 \psi}{\partial y^2} - \frac{\partial f(C_{kk})}{\partial y}\frac{\partial^2 \psi}{\partial y^2}}{\left(2\lambda \frac{\partial^2 \psi}{\partial x \partial y} + f(C_{kk})\right)^2} \right). \end{aligned} \tag{3-33}$$

together with variables η and G in Eq. (3-33) and algebraic manipulation, it becomes

$$-GG'' = (1-\beta_{\mathrm{p}})G''' + \beta_{\mathrm{p}} f(L)\left(\frac{C_4 G''^2 + KG''' - K'G''}{(K - C_4\eta G'')^2}\right), \tag{3-34}$$

with

$$C_4 = \lambda U_\infty x^{-1} = -Wi_x. \tag{3-35}$$

Again, the dependence on x in addition to the dependence on η is clear and this equation also involves the first derivative of K relative to η, which is obtained from Eq. (3-31) and is given by

$$K' = -\frac{\left(2C_5(C_1K + C_3) + 2G''G'''\left(C_2 + \eta^2(C_1K + C_3)\right)\right)}{C_6} \tag{3-36}$$

with

$$C_5 = \eta G''^2, C_6 = (3K^2 + 2C_0K + C_1(\eta G'')^2). \tag{3-37}$$

Upon back-substitution of K' of Eq. (3-36) into Eq. (3-34), further mathematical manipulation leads to the following final form of the momentum equation cast in terms of $G(\eta, x)$

$$G''' = -\frac{GG'' + \beta_{\mathrm{p}} f(L) G'' \dfrac{\left(C_4C_6G'' + 2C_5(C_1K + C_3)\right)}{(K - C_4\eta G'')^2 C_6}}{\left((1-\beta_{\mathrm{p}}) + \beta_{\mathrm{p}} f(L) \dfrac{\left(C_6K + 2G''^2\left(C_2 + \eta^2(C_1K + C_3)\right)\right)}{(K - C_4\eta G'')^2 C_6}\right)}. \tag{3-38}$$

The numerical solution of Eqs. (3-31) and (3-38) is discussed in Section 3.4 and its results presented in Section 3.5.

3.3.2. Olagunju's solution

Olagunju's solution for this same flow relied on further assumptions[19,20], in particular, terms of the conformation tensor equation were neglected that our order of magnitude analysis hinted to be relevant. However, since the effect of neglected terms on the polymer shear stress is weaker than on normal stresses, the impact of those differences on the velocity field will also be weak, as shown later. Specifically, instead of using Eqs. (3-18) to (3-21) to determine the conformation tensor, Olagunju used Eqs. (3-39) to (3-42):

$$-2\lambda C_{\mathrm{xy}} \frac{\partial^2 \psi}{\partial y^2} + [f(C_{kk})C_{\mathrm{xx}} - f(L)] = 0, \tag{3-39}$$

$$\frac{1}{\lambda}\left[f(C_{kk})C_{\mathrm{yy}} - f(L)\right] = 0, \tag{3-40}$$

$$\frac{1}{\lambda}\left[f(C_{kk})C_{\mathrm{zz}} - f(L)\right] = 0, \tag{3-41}$$

$$-\lambda C_{\mathrm{yy}}\frac{\partial^2\psi}{\partial y^2} + \left[f(C_{kk})C_{\mathrm{xy}}\right] = 0. \tag{3-42}$$

Comparing both sets of equations shows terms missing in the equations for C_{xx} and C_{yy}, which affects the other components of C_{ij} through the Peterlin function. The momentum equation is the same as ours.

3.4. Numerical solution of the governing equations

The set of simplified governing equations presented in Section 3.3 can only be solved numerically, as described below. Since we assumed $\partial G(\eta, x)/\partial x \approx 0$, each set is composed of an ordinary third-order differential equation on $G(\eta)$ and an algebraic cubic equation for $K(\eta, x)$.

To solve each set, the third-order differential equation is converted to a system of ordinary first-order differential equations with the following transformations, $G_1 = \frac{d^2G}{d\eta^2}$, $G_2 = \frac{dG}{d\eta}$ and $G_3 = G$, or alternatively written as

$$\frac{dG_1}{d\eta} = G''', \tag{3-43}$$

$$\frac{dG_2}{d\eta} = G_1, \tag{3-44}$$

$$\frac{dG_3}{d\eta} = G_2. \tag{3-45}$$

The cubic equation is solved first, with the Cardan-Tartaglia formula [130,131]. Its correct solution must be real-valued, all the normal components of C_{ij} are positive and $3 \le C_{kk} \le L^2$. Then, the system of differential equations is solved numerically by a fourth-order Runge–Kutta method coupled with a shooting technique to match the unknown boundary conditions[132,133]. The boundary conditions for the laminar flat plate boundary layer flow are [23,24]:

$$G'(\infty) \to 1, G(0) = G'(0) = 0. \tag{3-46}$$

3.5. Results and discussion

3.5.1. Validation: Newtonian fluids

The governing equations for the boundary layer flow of the viscoelastic fluid reduce to those for a Newtonian flat plate flow for $\beta_p = 0$ and this is used to verify the solution [23]. Through asymptotic analysis White [23] verified that at $\eta = 10$ the flow characteristics are very close to boundary conditions at infinity, therefore the same condition is used here. We define the local Reynolds Re_x as per Eq. (3- 1) with *x* instead of $\mathcal{L}$. We considered a maximum Re_x =1×10^5, a flow condition for which the Blasius solution remains valid [111] and below the critical condition for laminar-turbulent transition ($Re_{x,cr} = 5\times10^5$) for Newtonian fluids.

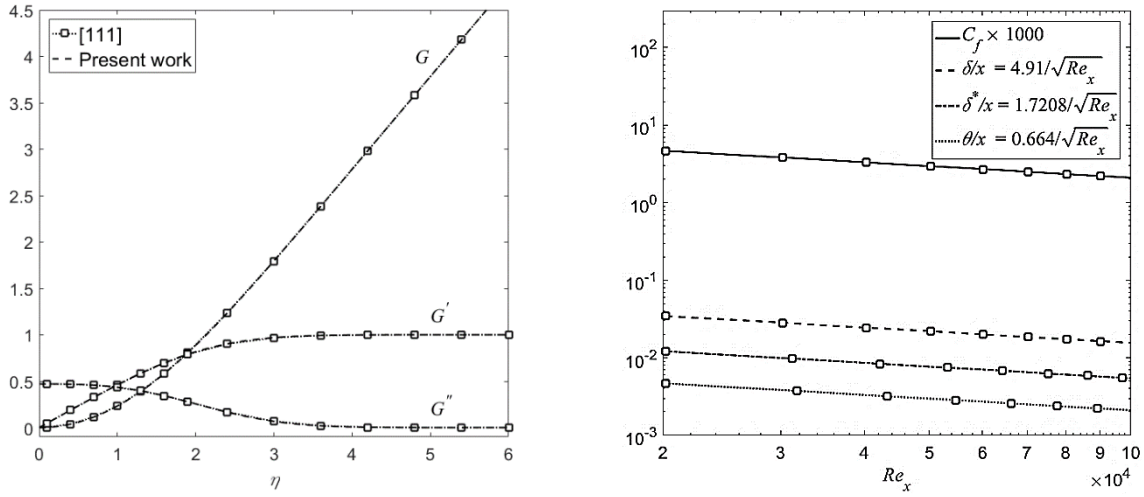

(a) (b)

Figure 3. 2- Characteristics of the Newtonian laminar boundary layer flow: a) Variation of G, G' and G" with η; b) Variation with Re_x of the normalized boundary layer thickness (δ/x), displacement thickness (δ^*/x) and momentum thickness (θ/x). Lines represent data from the present work and symbols represent data from the literature [111].

Figure 3. 2- (a) shows an excellent agreement between the numerical values of G, G' and G'' for the current solution and the literature. The plotted quantities are related to the velocity profiles *u* and *v* according to Eqs. (3-28) and (3-29).

By considering Eqs. (3-27) and (3-28), the following characteristics of the boundary layer flow were also quantified:

- the boundary layer thickness (δ) based on the 99% of free stream velocity criterion (cf. Section 3.1) is quantified by setting $G' = 0.99$ giving $\eta = 3.4723$ and consequently

$$\frac{\delta}{x} = \frac{4.9105}{\sqrt{Re_x}}, \tag{3-47}$$

- the displacement thickness (δ^*) is defined as

$$\delta^* = \int_0^\infty \left(1 - \frac{u}{U_\infty}\right) dy = \sqrt{\frac{2\nu_0 x}{U_\infty}} \int_0^\infty (1 - G') d\eta = x\sqrt{\frac{2}{Re_x}} \lim_{\eta\to\infty} [\eta - G(\eta, x)] , \tag{3-48}$$

leading to $\frac{\delta^*}{x} = \frac{1.7208}{\sqrt{Re_x}}$;

- the momentum thickness (θ) is defined as

$$\theta = \int_0^\infty \frac{u}{U_\infty}\left(1 - \frac{u}{U_\infty}\right) dy = \sqrt{\frac{2\nu_0 x}{U_\infty}} \int_0^\infty G'(1 - G') d\eta = x\sqrt{\frac{2}{Re_x}} \int_0^\infty G'(1 - G') d\eta, \tag{3-49}$$

leading to $\frac{\theta}{x} = \frac{0.664}{\sqrt{Re_x}}$, and a shape factor $H = \delta^*/\theta = 2.591$ is consistent with results from [23,46].

Furthermore, the local skin-friction coefficient C_f for the Newtonian fluid is given by

$$C_f = \left(\frac{\tau_{xy}}{\frac{1}{2}\rho {U_\infty}^2}\right)_{y=0} = \frac{\nu_s \frac{\partial^2 \psi}{\partial y^2}}{\frac{1}{2}\rho {U_\infty}^2} \tag{3-50}$$

The variations with Re_x of these four quantities are plotted in Figure 2-b) and the agreement is excellent with data from [23,24].

3.5.2. Validation: FENE-P fluids

We start with a comparison between our approximate similarity solution and the numerical solution of the full set of non-simplified governing equations using the RheoFoam toolbox of OpenFoam [17,18], and also with the approximate similarity solution of Olagunju [19,20]. Olagunju [19,20] only presented the velocity profiles and the law of variation for the friction coefficient, so we used his equations to extract other quantities.

The RheoFoam simulation relied on the use of the high-order resolution scheme CUBISTA [134] for the advective terms in the momentum and conformation equations. The computational domain

had a length $1.2\mathcal{L}$, divided into two blocks: block I upstream the plate leading edge was $0.2\mathcal{L}$ long and block II along the plate had a length of $\mathcal{L}$. The width of both blocks was set equal to $2\mathcal{L}$. Within each block the non-uniform computational grid had $N_x \times N_y \times N_z$ cells for the x, y, z directions, respectively as given in Table 3. 1 together with the expansion/contraction factors $f_x = \Delta_x^{i+1}/\Delta_x^i$ and $f_y = \Delta_y^{i+1}/\Delta_y^i$ and ratios of mesh size over boundary layer thickness at some locations. This mesh was selected after an assessment of mesh independence using four grids. Differences between the results of this grid and those obtained in a grid with twice the number of cells in each direction is below 0.05%.

Table 3. 1-Characteristics of the meshes used in the RheoFoam calculations for validation. The values of Δx and Δy are at the cells nearest the wall.

Block	N_x	N_y	N_z	f_x	f_y	$\frac{\Delta x_{x=0}}{\delta_{x=\mathcal{L}}}, \frac{\Delta y_{x=0}}{\delta_{x=\mathcal{L}}}$	$\frac{\Delta x_{x=\mathcal{L}}}{\delta_{x=\mathcal{L}}}$
I	20	600	1	0.886	1.0088	-	-
II	200	600	1	1.0116	1.0088	0.0439,0.003	0.439

On the inlet boundary a uniform velocity was imposed, on the outlet boundary a zero gradient condition was set for all quantities and no slip was imposed at the wall. At the boundary upstream the wall (block I) symmetry conditions were set. At the boundary opposite the wall, far from the boundary layer, free stream velocity conditions were imposed, both in blocks I and II.

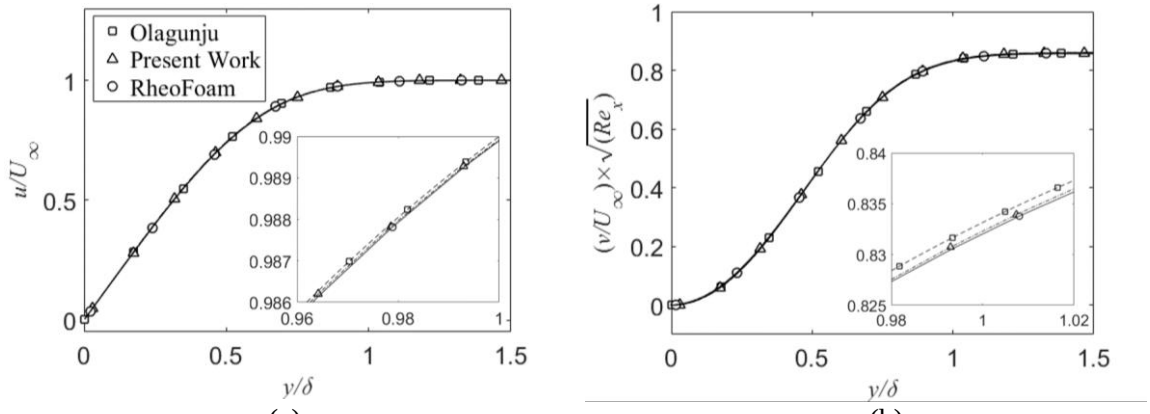

(a) (b)

Figure 3. 3- Comparison between normalized transverse velocity profiles at $\frac{x}{\mathcal{L}} = 0.4$ for $\beta_p = 0.1$, $L^2 = 900$, Re_x=2×10^4 and Wi_x= 0.1 from present and Olagunju solutions, and from RheoFoam: (a) $\frac{u}{U_\infty}$; (b) $\frac{v}{U_\infty}\sqrt{Re_x}$.

The simulation was carried out for the Peterlin function of Eq. (2- 10c) with $\beta_{\mathrm{p}} = 0.1$ and $L^2 = 900$ and the results shown pertain to $x/\mathcal{L} = 0.2$, where the local Reynolds and Weissenberg numbers are Re_x=2×10^4 and Wi_x= 0.1, respectively (the local Weissenberg number Wi_x is defined as per equation (3- 3) with x instead of $\mathcal{L}$).

Figure 3. 3 compares the normalized transverse profiles of streamwise and wall-normal velocities obtained in RheoFoam and with the present and Olagunju's semi-analytical solutions showing excellent agreement, as shown through the zooms in Figure 3. 3. Olagunju's solution very slightly over-predicts u/U_∞ and $(v/U_\infty)\sqrt{Re_x}$.

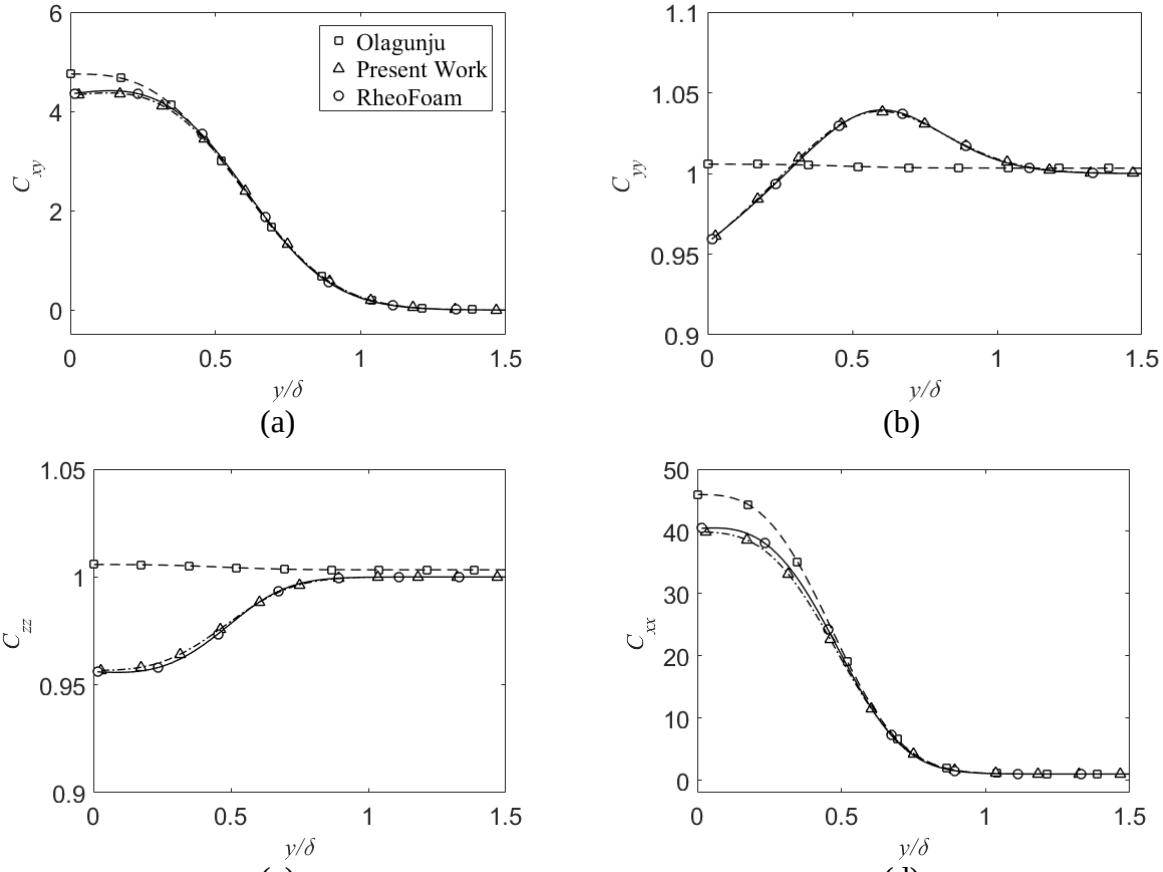

Figure 3. 4- Comparison between transverse profiles of the conformation tensor components obtained with RheoFoam and present and Olagunju solutions at $\frac{x}{\mathcal{L}} = 0.4$ for β_{p}=0.1, $L^2 = 900$, Re_x=2×10^4 and Wi_x= 0.1: (a) C_{xy}, (b)C_{yy}, (c)$C_{zz,}$(d)C_{xx}, Lines are a guide to the eye.

The corresponding transverse profiles of the conformation tensor components $(C_{xy}, C_{yy}, C_{zz}, C_{xx})$ are plotted in Figure 3. 4 and again there is a very good agreement between the results of the present work and of the RheoFoam simulation. However, Olagunju's solution shows various

differences relative to our solution and RheoFoam predictions: it over-predicts C_{xy} near the wall and, regardless of Wi_x, it always predicts the maximum C_{xy} to occur at the wall, whereas both the current solution and RheoFoam show that the maximum C_{xy} occurs at a slight distance from wall, with this offset increasing with Wi_x.

Simultaneously, Olagunju's solution over-predicts the wall peak of C_{xx} in Figure 3. 4 (d), whereas in regards to C_{yy} and C_{zz}, Figure 3. 4 (b) and (c) show that it is qualitatively incorrect even if the numerical values are not too different from 1, as they should be. As a matter of fact, the peak value of C_{yy} away from the wall, and the local minimum positive value at the wall are not captured qualitatively by Olagunju's solution, which always predicts a wall peak value, whereas for C_{zz} Figure 3. 4 (c) Olagunju's values are in excess of 1, whereas the correct value is below 1. As stated earlier, the differences between both solutions come from the simplifications in the conformation equations for C_{xx} and C_{yy} carried to the other components via the Peterlin function $f(C_{kk})$ and they increase substantially with Wi_x. In contrast, at lower *Wi*, such as Wi_x=0.005, velocity and conformation tensor profiles of both semi-analytical solutions collapse, so they are not shown for conciseness.

It is worth comparing the computational cost of the semi-analytical solutions and of the Rheofoam simulation. The latter was performed by a computer equipped with an Intel Xeon E5 processor with 12MB L3 cache and Turbo Boost up to 3.9GHz, with parallel processing using its 6 computer cores. The computational time was 4.5 hours, however for the semi-analytical solutions the same computer took about one second.

3.5.3.The boundary layer flow of FENE-P fluids

The solution presented and discussed here pertains to the Peterlin function of Eq. (2- 10c) and we vary the Reynolds and Weissenberg numbers as well as β_{p} and L^2. The local Reynolds Re_x and Weissenberg numbers Wi_x, their values at the end of the plate (Re_L and Wi_L) are also used.
It should be noted that for low and moderate *Wi* numbers only the results of the proposed semi-analytical solution are presented, however for large *Wi* numbers, we also show the results were obtained from RheoFoam simulation. The |RheoFoam simulations were performed in a rectangular

computational domain similar to that described in Section 6.2 and Table 3. 1. Two simulations were performed with Rheofoam at $Re_{\mathcal{L}} = 1 \times 10^5$, with β_p=0.1 and a very high $Wi_{\mathcal{L}} = 0.2$ and $Wi_{\mathcal{L}} = 1.0$ using $L^2 = 900$, and their results are compared with those of the derived semi-analytical solution. It is also worth to mention that for larger than presented *Wi* numbers in RheoFoam simulations we faced with numerical instabilities.

3.5.3.1. Flow field

Figure 3. 5 (a) and Figure 3. 6 (a) show transverse profiles of normalized streamwise and normal velocity as a function of the independent dimensionless numbers obtained from preset solution. By normalizing with the boundary-layer thickness, and with the local Reynolds number for the wall-normal velocity, the profiles at low elasticity levels tend to collapse on the Newtonian profiles, but by increasing elasticity the profiles progressively deviate from the Newtonian asymptote thus showing their approximate similarity nature. The deviation is small for the streamwise velocity profile, which is pinned at the wall and at the edge of the boundary layer in this normalization. For the transverse velocity, in general there is a progressive decrease with elasticity as the boundary layer edge is approached, so that the dimensionless wall-normal velocity can be 10% smaller than the Newtonian value under certain conditions of high elasticity.

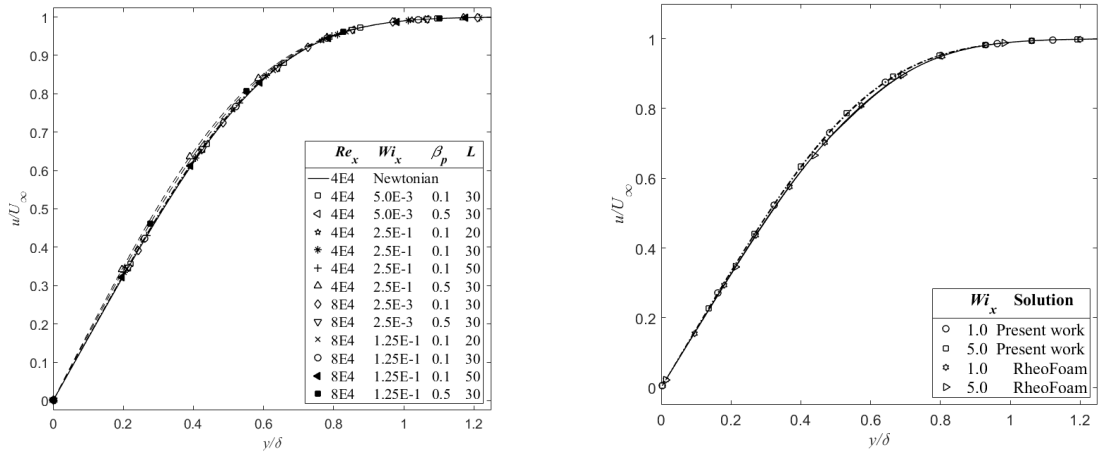

(a) (b)

Figure 3. 5- Normalized transverse ($\frac{u}{U_\infty}$) velocity profile for various rheological properties:(a) from present BL theory ,Dashed lines are a guide to the eye, (b) from present BL theory (dashdotted lines) and RheoFoam (solid lines) for β_p=0.1, $L^2 = 900$, $Re_x = 2 \times 10^4$.

Figure 3. 5 (b) and Figure 3. 6 (b) display the comparison of the normalised transverse velocity profiles (u/U_∞) and $(v/U_\infty)\sqrt{Re_x}$ at location, $x/\mathcal{L} = 0.2$. Even at large Wi numbers (note that $Wi_x = (\mathcal{L}/x)(Wi_\mathcal{L})$ the present solution can still predict well these profiles. It is also observed that the results accuracy increases as we move downstream (such profiles are not shown for conciseness), because Wi_x decreases, but this is also due to the normalisation with δ. In fact, the variation of $\delta/\mathcal{L}$ along the plate is shown in Figure 3. 8.

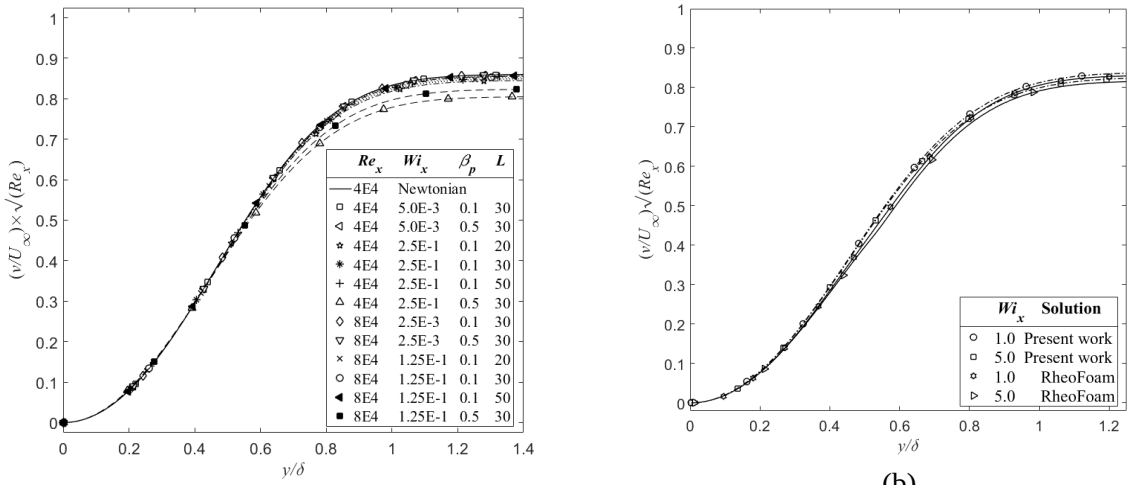

(a) (b)

Figure 3. 6- Normalized transverse $(\frac{v}{U_\infty}\sqrt{Re_x})$ velocity profile for various rheological properties:(a) from present solution, Dashed lines are a guide to the eye, (b) from present solution (dashdotted lines) and RheoFoam (solid lines) for β_p=0.1, $L^2 = 900$, $Re_x = 2 \times 10^4$.

The local skin-friction coefficient C_f for the FENE-P fluid is given by

$$C_f = \left(\frac{\tau_{xy}}{\frac{1}{2}\rho {U_\infty}^2}\right)_{y=0} = \frac{\nu_s \frac{\partial^2\psi}{\partial y^2} + \frac{\nu_p f(L)\frac{\partial^2\psi}{\partial y^2}}{\left(2\lambda\frac{\partial^2\psi}{\partial x\partial y} + f(C_{kk})\right)}}{\frac{1}{2}\rho {U_\infty}^2} \tag{3-51}$$

with $\frac{\partial^2\psi}{\partial x\partial y}(\mathrm{y}=0) = -\frac{Ux^{-1}}{2}(\eta(0)G''(0,x)) = 0$, thus leading to

$$C_f = \left(\frac{\tau_{xy}}{\frac{1}{2}\rho {U_\infty}^2}\right)_{y=0} = \sqrt{\frac{2}{Re_\mathcal{L}}}\left(1 - \beta_p + \frac{\beta_p f(L)}{K(0,x)}\right)G''(0,x). \tag{3-52}$$

The streamwise variations of the friction factor (C_f) and of the normalized boundary layer thickness (δ/x) are plotted in Figure 3. 7 and Figure 3. 8, respectively. As for the laminar planar jet previously investigated [112,113], when elasticity effects are weak (low $Wi_{\mathcal{L}}$, low β_{p}, high L) both quantities follow closely the corresponding Newtonian results, but as Wi and β_{p} increase or L decreases, the boundary layer thickness and the skin friction coefficient decrease on account of the stronger shear-thinning nature of the shear viscosity accompanying those changes of the independent dimensionless numbers. The semi-analytical solution can predict the friction factor (C_f) with very good accuracy at all range of large Wi numbers, but the deviation of predicted boundary layer thickness (δ/x) is below 2% at large Wi numbers as shown Figure 3. 7 (b) and Figure 3. 8 (b).

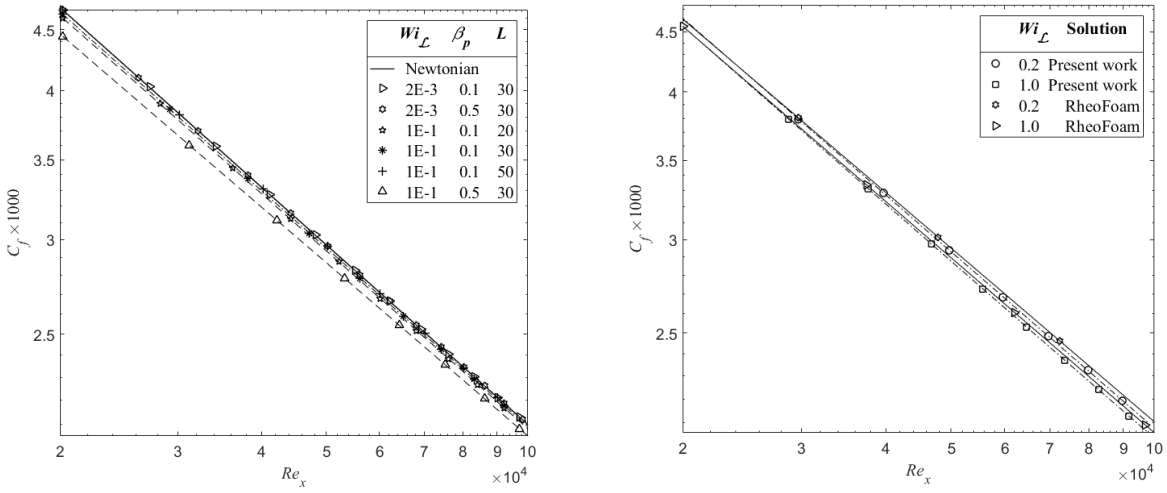

(a) (b)

Figure 3. 7- Streamwise variation of C_f as a function of flow and fluid characteristics. Dashed lines are a guide to the eye. (a) the present work result (b) from present solution (dashdotted lines) and RheoFoam (solid lines) for β_p=0.1, $L^2 = 900$.

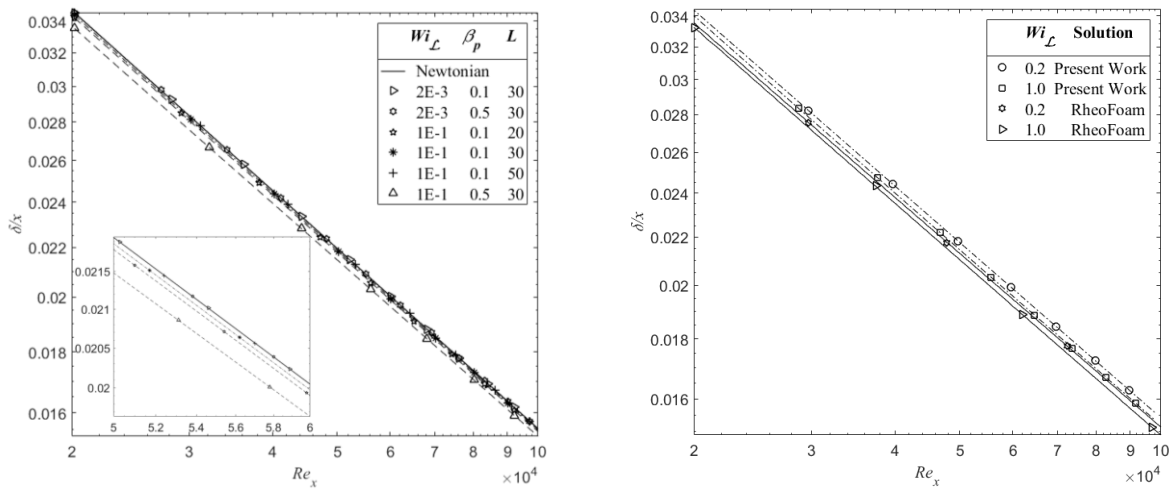

(a) (b)

Figure 3. 8- Streamwise variation of the normalized boundary layer thickness (δ/x) as a function of flow and fluid characteristics. Dashed lines are a guide to the eye. (a) the present work result (b) from present solution (dashdotted lines) and RheoFoam (solid lines) for β_p=0.1, $L^2 = 900$.

Before presenting more results, one critical point needs to be clarified. That point concerns the characteristic length used in the definition of the Weissenberg number, a problem that has similarities with the definition of the Reynolds number in classical boundary layer theory and that has implications on the interpretation of what are low or high *Wi* flows. We use a distance measured from the plate leading edge (the local distance (x) or the full length of the plate, $\mathcal{L}$) as this makes the definition of *Wi* (and of *Re*) independent of the solution. However, from a physical point of view it makes more sense to use the boundary layer thickness in the ratio of time scales, since the flow is dominated by shear (except at very large *Wi* where extensional effects may become important as explained above). The problem is that δ is part of the solution and it is always difficult to know *a priori* what the value of Wi_δ will be. For instance, in the present study we use the range $0.01 < Wi_x$<5.0, as shown in in Figure 3. 9(a), these range corresponds to 0.3< Wi_δ<150, shown in Figure 3. 9.(b). In conclusion, these values of Wi_δ are hardly low values of elasticity and the highest values of *Wi* used in the paper are large enough to study the effects of high elasticity on the boundary layer flow, even if quantified as Wi_x.

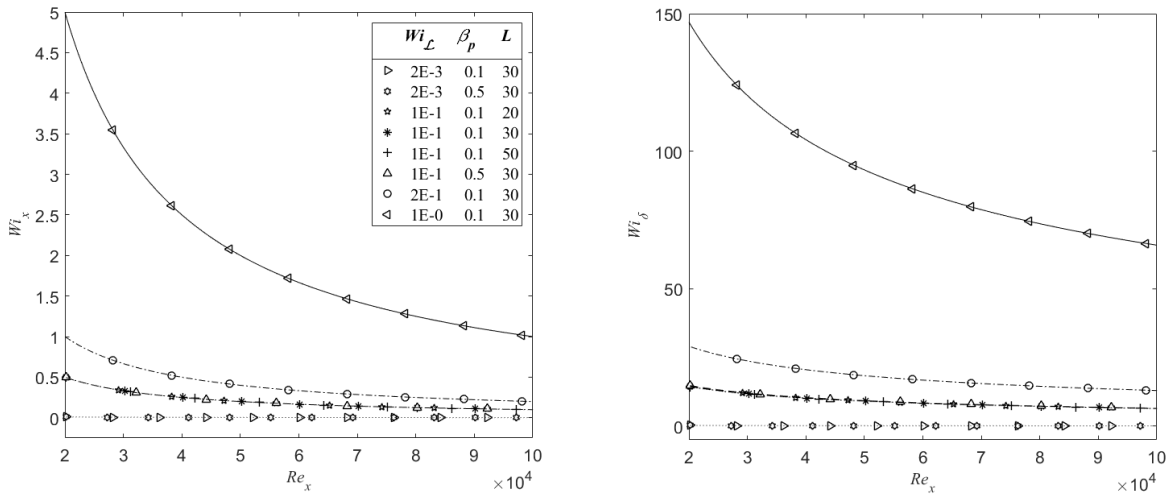

(a) (b)

Figure 3. 9- Streamwise variation of Wi as a function of flow and fluid characteristics. Dashed lines are a guide to the eye. (a) Wi_x (b) Wi_δ.

Figure 3. 10 and Figure 3. 11 show the corresponding streamwise variations of the dimensionless displacement and momentum thicknesses. Again, at low elasticity levels both quantities follow closely the corresponding Newtonian laws, however by increasing the elasticity level δ^*/x and θ/x decrease on account of the fuller velocity profiles associated with the shear-thinning of the shear viscosity. The accuracy of predicting both δ^*/x and θ/x are very good even at very large *Wi* numbers

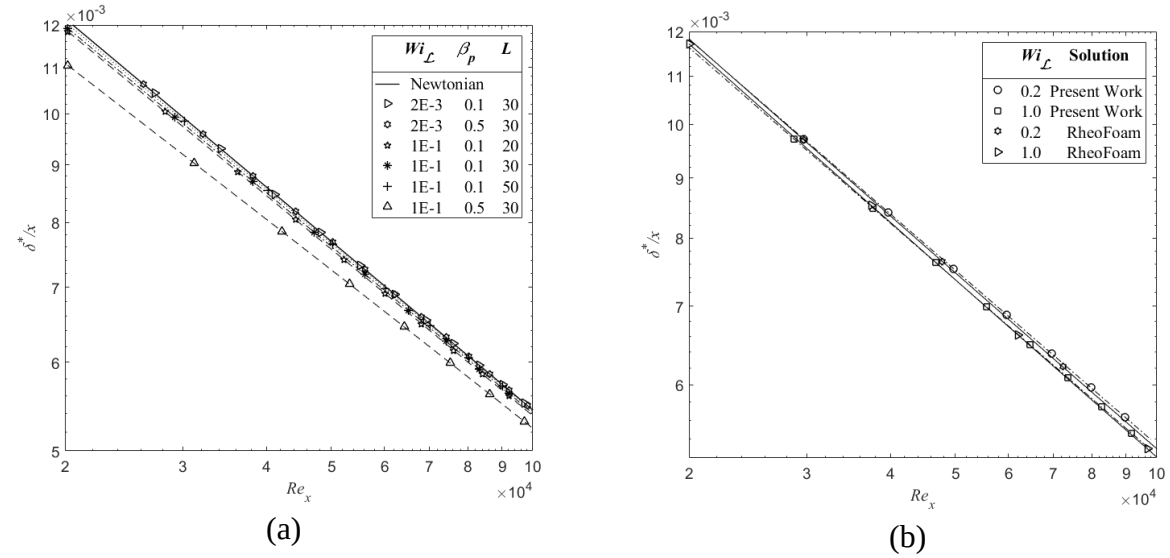

(a) (b)

Figure 3. 10- Streamwise variation of the dimensionless displacement thickness (δ^*/x) as a function of flow and fluid characteristics. Dashed lines are a guide to the eye. (a) the present work result (b) comparison with RheoFoam at large *Wi.*

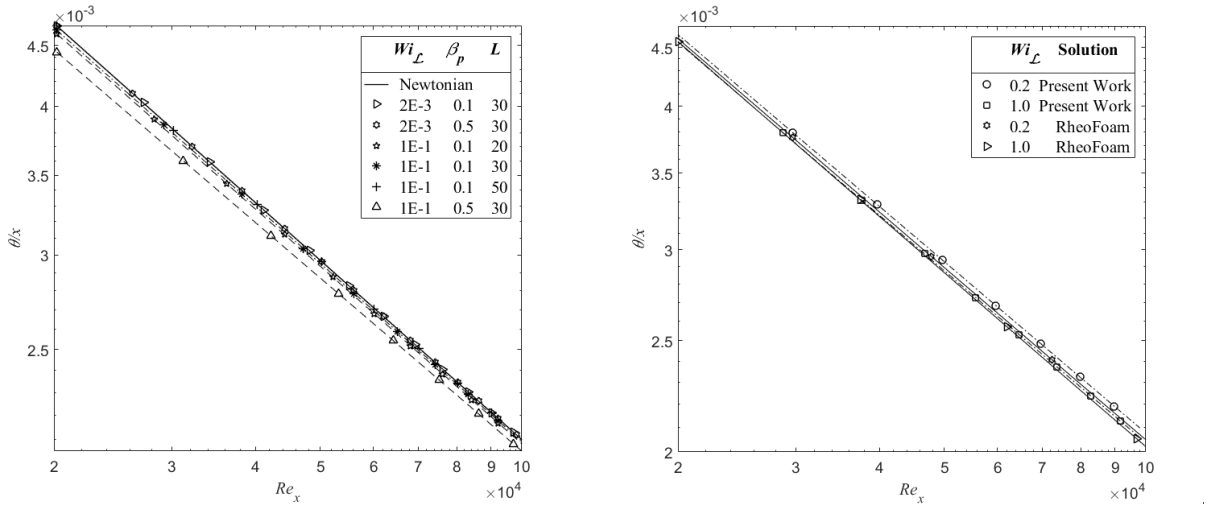

(a) (b)

Figure 3. 11- Streamwise variation of the dimensionless momentum thickness (θ/x) as a function of flow and fluid characteristics. Legend as in Fig. 9. Dashed lines are a guide to the eye. (a) the present work result (b) comparison with RheoFoam at large Wi.

Figure 3. 12 shows the variation of so-called shape or flatness factor ($H = \delta^*/\theta$) as a function of flow and fluid characteristics. As expected $H > 1$ and has a constant value for flows with vanishing elasticity, but as $Wi_{\mathcal{L}}$, β_p and L increase H decreases and varies non-linearly along the plate, but always tending to the Newtonian value as Re_x increases.

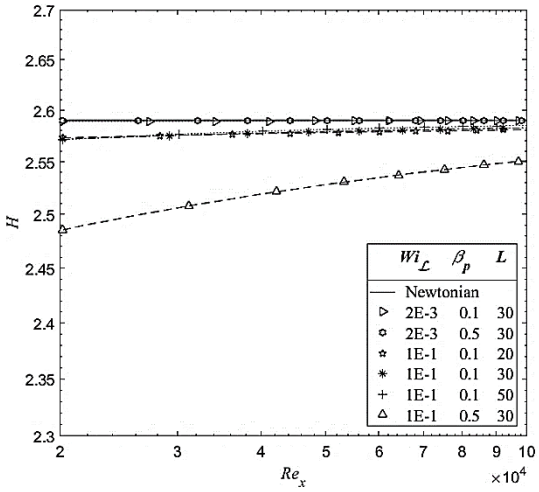

Figure 3. 12- Streamwise variation of the shape factor H as a function of flow and fluid characteristics. Dashed lines are a guide to the eye.

3.5.3.2. Conformation and stress tensors

We can plot the streamwise variation of local quantities in two different ways: (i) mimicking a specific boundary layer flow, $Re_{\mathcal{L}}$ and $Wi_{\mathcal{L}}$ are fixed for each flow condition and at each $x/\mathcal{L}$ the data pertain to different local values of Re_x and Wi_x since $Re_x \sim x$ and $Wi_x \sim x^{-1}$; (ii) alternatively, one may compare physical quantities at the same local values of Re_x and Wi_x, but then, at each $x/\mathcal{L}$, data correspond to different $Re_{\mathcal{L}}$ and $Wi_{\mathcal{L}}$.

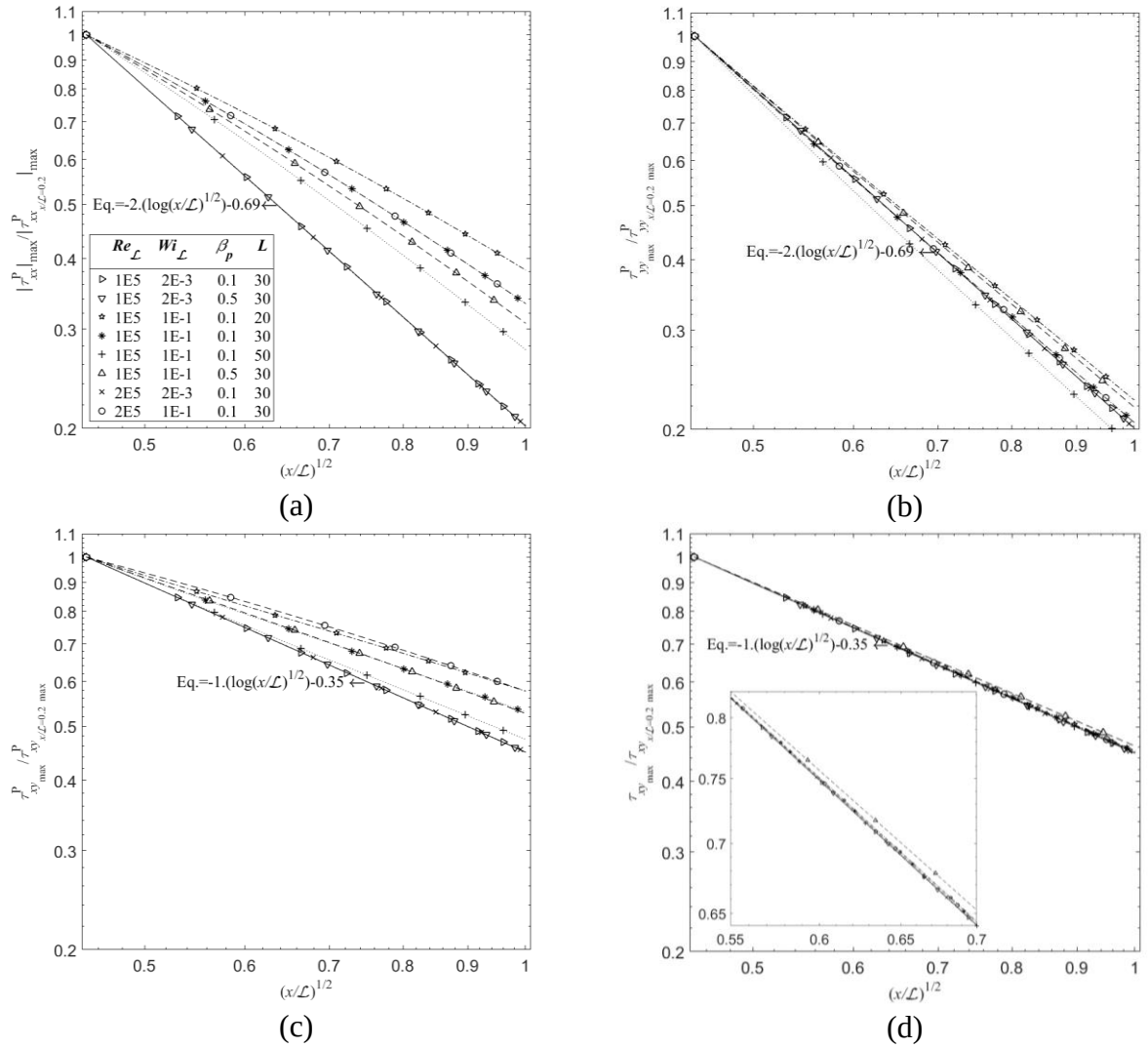

Figure 3. 13- Streamwise variation of local peak values of the polymer stress and total shear stress for various flow conditions: (a)τ_{xx}^{p}, (b)τ_{yy}^{p}, (c)τ_{xy}^{p}, (d)τ_{xy}. Data are normalised by the corresponding stress at $x/\mathcal{L} = 0.2$. Lines are a guide to the eye; the solid line is the low elasticity asymptote.

Figure 3. 13 (a)-(d) shows the streamwise decrease of the peak values of the polymer stress components and of the total shear stress, normalized by the corresponding peak values at $x/\mathcal{L}$ =0.2. For viscoelastic fluids, the local Weissenberg number increases as the leading edge is approached, therefore the boundary layer theory is not valid between the leading edge, where its assumptions do not hold even for Newtonian fluids, and some location downstream where the local Weissenberg number is still excessively high. For values of $Wi_{\mathcal{L}}$ below 0.002 the local value of Wi_x at $x/\mathcal{L}$ =0.2 is within the range of validity of the boundary layer theory assumptions hence we chose the peak stress values at this location for stress normalization.

For all components, the normalized data plotted in Figure 3. 13 follow equations of the form,

$$\log_{10}\frac{\left|\tau_{ij}^{p}\right|_{max}}{\left|\tau_{ij}^{p}\right|_{max@\frac{x}{\mathcal{L}}=0.2}} = m\log_{10}\left[\left(\frac{x}{\mathcal{L}}\right)^{1/2}\right] - b. \qquad (1)$$

which are also shown as lines. At low elasticity levels the normalized peak stress curves tend to an asymptote, which is indicated in each plot as a solid line.

The low elasticity asymptotic decay rate of τ_{xx}^{p} is twice as fast as for the shear stresses, because in this limit $\tau_{xx}^{\mathrm{p}} \propto (\partial u/\partial y)^2$, whereas the polymer shear stress varies linearly with $\partial u/\partial y$ as does the Newtonian solvent shear stress, and consequently the total shear stress τ_{xy}. The transverse normal stress τ_{yy}^{p} is much smaller than τ_{xx}^{p} and the rate of decay of its local peak depends on the streamwise variations of $\partial v/\partial y$ and C_{yy}. Further manipulation of Eqs. (3-27) to (3-29) shows that the streamwise variations of $\partial v/\partial y$ and $\partial u/\partial y$ are related, but the quantities involved are very small and simple order of magnitude arguments are unable to explain the rate of decay shown in Figure 3. 13 (b) that only accurate numerical calculations can provide.

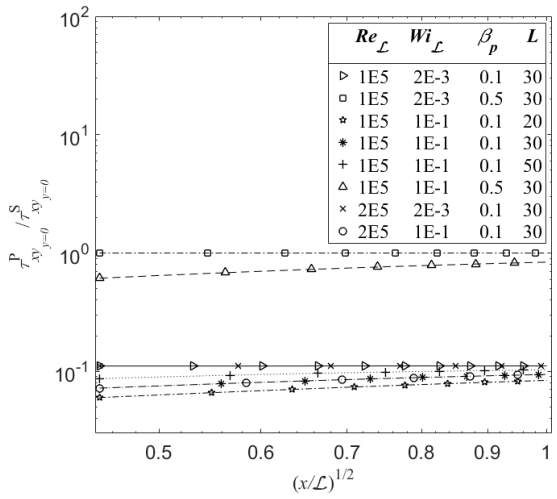

Figure 3. 14- Streamwise variation of the ratio of wall polymer shear stress (τ_{xy}^{p}) to wall solvent shear stress (τ_{xy}^{s}). Lines are a guide to the eye; the solid line is the low elasticity asymptote.

At low elasticity, the linear dependence of both shear stresses on $\partial u/\partial y$ is equivalent to having a constant ratio for $\tau_{xy}^{\mathrm{p}}/\tau_{xy}^{\mathrm{s}}$ equal to the ratio of viscosity coefficients $\nu_{\mathrm{p}}/\nu_{\mathrm{s}} = 1/9$ for $\beta_{\mathrm{p}} = 0.1$ and $\nu_{\mathrm{p}}/\nu_{\mathrm{s}} = 1$ for $\beta_{\mathrm{p}} = 0.5$, as shown in Figure 3. 14. On account of shear-thinning effects, as *Wi* increases there is a decrease in the stress ratio $\tau_{xy}^{\mathrm{p}}/\tau_{xy}^{\mathrm{s}}$ and in the decay rates for all stresses shown.

The ratios of local maximum polymer over local maximum solvent stresses ($\tau_{ij_{\max}}^{\mathrm{p}}/\tau_{ij_{\max}}^{\mathrm{s}}$) show similar behaviors for the shear and wall-normal components. At low elasticity levels the maximum shear stresses are at the wall so the behavior is that of Figure 3. 15, but as elasticity increases the peak polymer shear stress moves away from the wall to the near wall vicinity, where the corresponding conformation tensor component peaks, and the ratio $\tau_{xy_{\max}}^{\mathrm{p}}/\tau_{xy_{\max}}^{\mathrm{s}}$ decreases below $\nu_{\mathrm{p}}/\nu_{\mathrm{s}}$. In regards to τ_{yy}^{p} and τ_{yy}^{s} their maxima are offset from the wall, where under low shear rate conditions they essentially depend linearly on $\partial v/\partial y$ hence their ratio is also equal to the ratio of viscosity coefficients $\nu_{\mathrm{p}}/\nu_{\mathrm{s}}$, cf. Figure 3. 15-(a). However, τ_{xx}^{p} and τ_{xx}^{s} behave differently as depicted in Figure 3. 15-(b): whereas τ_{xx}^{s} is purely viscous and depends only on the small value of $\partial u/\partial x$, being negative, the polymer stress τ_{xx}^{p} exhibits the nearly quadratic dependence on the large values of $\partial u/\partial y$ and is positive, therefore the ratio $|\tau_{xx}^{\mathrm{p}}|_{\max}/|\tau_{xx}^{\mathrm{s}}|_{\max}$ takes on large values even in the limit of small elasticity and increases with $Wi_{\mathcal{L}}$ or β_{p} and in inverse proportion to L^2.

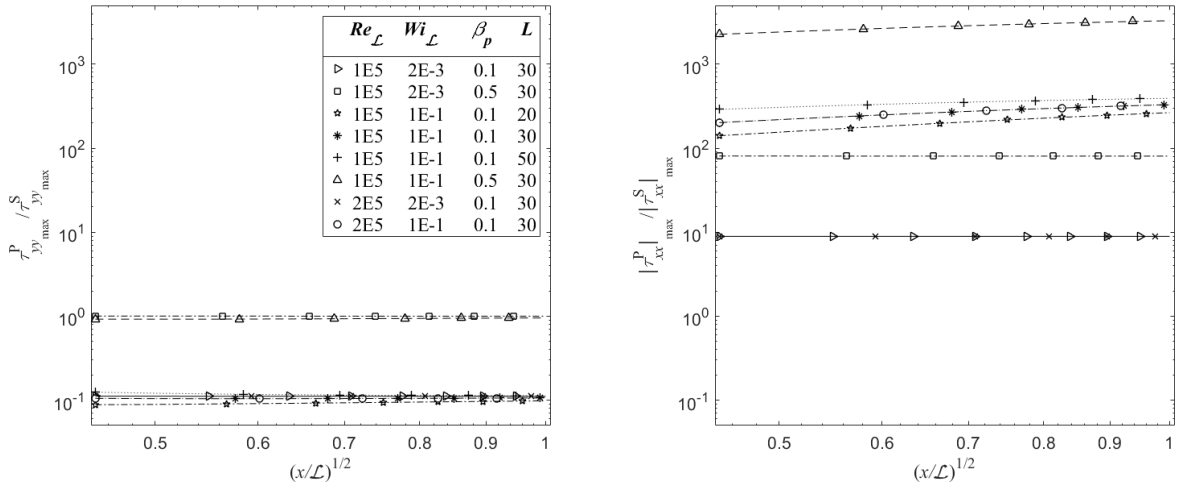

(a) (b)

Figure 3. 15- Streamwise variation of ratios between local maximum polymer (τ_{ij}^{p}) over local maximum solvent stresses (τ_{ij}^{s}) : (a) $\tau_{yy_{\max}}^{\mathrm{p}}/\tau_{yy_{\max}}^{\mathrm{s}}$, (b) $\left|\tau_{xx}^{\mathrm{p}}\right|_{\max}/|\tau_{xx}^{\mathrm{s}}|_{\max}$. Lines are a guide to the eye; the solid line is the low elasticity asymptote.

By increasing the elasticity level, the ratio of streamwise polymer stress to polymer shear stress ($\frac{\tau_{xx}^{\mathrm{p}}}{\tau_{xy}^{\mathrm{p}}}$) increases. The ratio reach to approximately $\tau_{xx}^{\mathrm{p}}/\tau_{xy}^{\mathrm{p}} = 100$ at very large $Wi_{\mathcal{L}} = 1$, therefore at large $Wi_{\mathcal{L}}$ the normal streamwise stress become dominate polymer stress meaning that ($\tau_{xx}^{\mathrm{p}} \gg \tau_{xy}^{\mathrm{p}}$) as shown in Figure 3. 16. Regarding to the influence of these polymer stresses on momentum equation, as mentioned earlier the streamwise derivation of τ_{xx}^{p} ($\frac{\partial \tau_{xx}^{\mathrm{p}}}{\partial x}$) and normal derivation τ_{xy}^{p} ($\frac{\partial \tau_{xy}^{\mathrm{p}}}{\partial y}$) affect the momentum equation. Therefore, the streamwise variation of $\left|\frac{\partial \tau_{xx}^{\mathrm{p}}}{\partial x}\right|_{\max}$ / ($\left|\frac{\partial \tau_{xy}^{\mathrm{S}}}{\partial y}\right|_{\max} + \left|\frac{\partial \tau_{xy}^{\mathrm{p}}}{\partial y}\right|_{\max}$) for different *Wi* number are shown in Figure 3. 17. Generally speaking, if $\left|\frac{\partial \tau_{xx}^{\mathrm{p}}}{\partial x}\right|_{\max}/(\left|\frac{\partial \tau_{xy}^{\mathrm{S}}}{\partial y}\right|_{\max} + \left|\frac{\partial \tau_{xy}^{\mathrm{p}}}{\partial y}\right|_{\max}) < 0.05$ our proposed semi-analytical solution can precisely predicts all flow properties, however above this criterion the accuracy of predicted polymer stresses reduce, but the solution can still predict velocity profiles and velocity relevant properties such as boundary layer, displacement, and momentum thicknesses with acceptable accuracy.

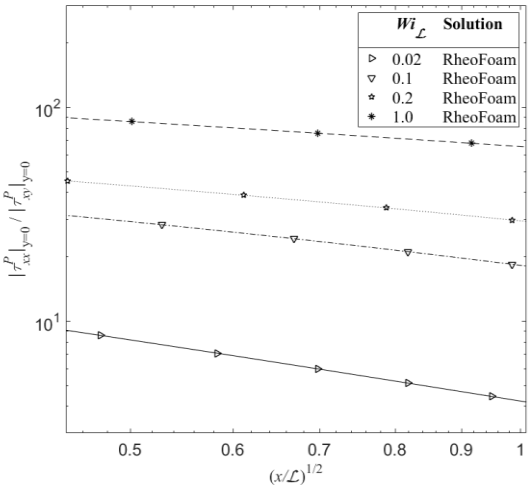

Figure 3. 16- Streamwise variation of the ratio of polymer normal stress (τ^{p}_{xx}) to solvent shear stress (τ^{p}_{xy}) on the flat plate surface. Lines are a guide to the eye; the solid line is the low elasticity asymptote.

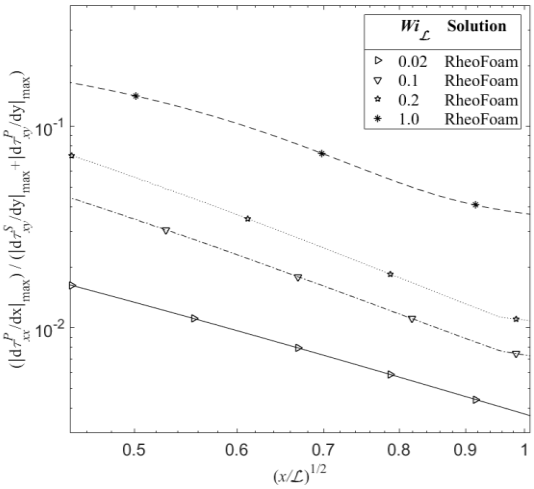

Figure 3. 17- Streamwise variation of the ratio of $\left|\frac{\partial \tau^{\mathrm{p}}_{xx}}{\partial x}\right|_{\max} / \left(\left|\frac{\partial \tau^{\mathrm{s}}_{xy}}{\partial y}\right|_{\max} + \left|\frac{\partial \tau^{\mathrm{p}}_{xy}}{\partial y}\right|_{\max}\right)$. Lines are a guide to the eye; the solid line is the low elasticity asymptote.

Figure 3. 18 plots the variation across the boundary layer of $\tau^{\mathrm{p}}_{xy}/\tau^{\mathrm{s}}_{xy}$ at some representative locations, as given through the values of Re_x and Wi_x, showing that there are shear-thinning effects, and suggesting that the peak polymer stress values may occur at some distance from the wall. As the edge of the boundary layer is approached and the shear rates decrease this stress ratio approaches the viscosity coefficient ratio $\nu^{\mathrm{p}}/\nu^{\mathrm{s}} = \beta_{\mathrm{p}}/(1-\beta_{\mathrm{p}})$. Note however, that the variation of the total shear stress across the boundary layer is monotonic, with peak values at the wall (such profiles are not shown for conciseness).

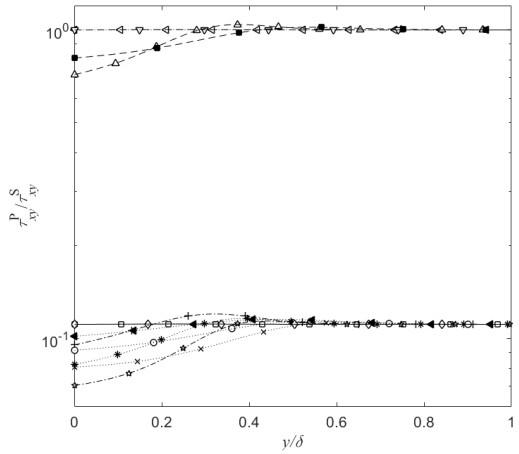

	Re_x	Wi_x	β_p	L
□	4E4	5.0E-3	0.1	30
◁	4E4	5.0E-3	0.5	30
☆	4E4	2.5E-1	0.1	20
✱	4E4	2.5E-1	0.1	30
+	4E4	2.5E-1	0.1	50
△	4E4	2.5E-1	0.5	30
◇	8E4	2.5E-3	0.1	30
▽	8E4	2.5E-3	0.5	30
×	8E4	1.25E-1	0.1	20
○	8E4	1.25E-1	0.1	30
◀	8E4	1.25E-1	0.1	50
■	8E4	1.25E-1	0.5	30

Figure 3. 18- Variation across the boundary layer of $\tau^{\mathrm{p}}_{xy}/\tau^{\mathrm{s}}_{xy}$. Lines are a guide to the eye; the solid line is the low elasticity asymptote.

At this stage it is important to remember that the approximate similarity nature of the solution is introduced by the conformation equations. Transverse profiles of conformation tensor component quantities, normalised by the corresponding local absolute peak values, are plotted in Figure 3. 19 (a)-(d) for a wide range of conditions at two different locations (expressed through the values of Re_x and Wi_x).

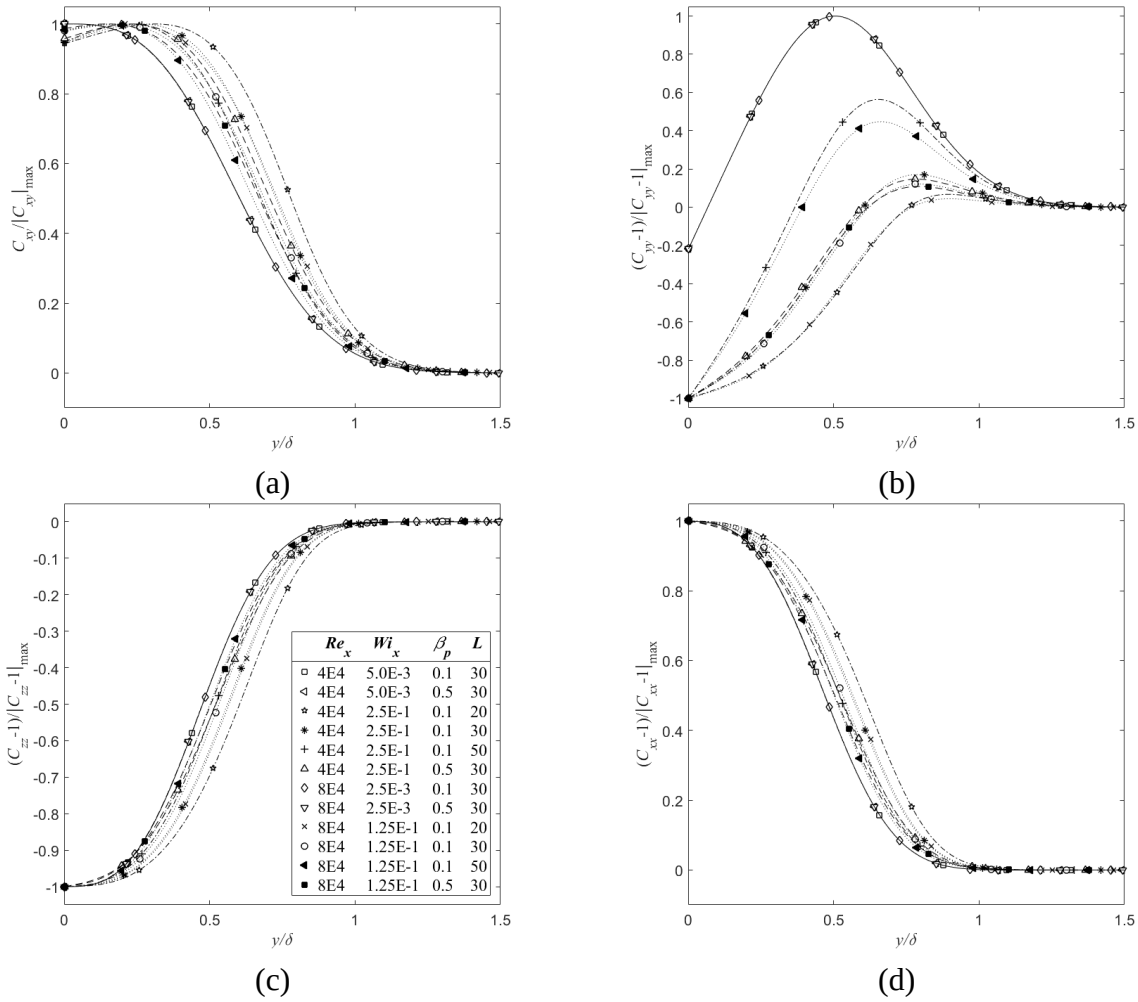

Figure 3. 19- Transverse profiles of conformation tensor component quantities normalised by their corresponding absolute local peak values for various flow conditions: (a) C_{xy}, (b) $C_{yy} - 1$, (c) $C_{zz} - 1$(d)$C_{xx} - 1$. Lines are a guide to the eye; the solid line is the low elasticity asymptote.

As expected, at low elasticity $Wi_x \leq 0.005$ the profiles collapse on asymptotic curves (solid lines); for increasing levels of viscoelasticity the profiles progressively deviate from the asymptotes and an approximate similarity behavior sets in. The normalised profiles of C_{xy}, $C_{zz} - 1$ and $C_{xx} - 1$ all exhibit their large variations taking place further away from the wall than in their asymptotic curves, and for the shear component the location of the peak value also moves away from the wall.

C_{yy} is always positive, but the large variations of the normalised profiles of $C_{yy} - 1$ are a consequence of the ratio involving very small numbers due to very small variations of C_{yy} around 1. At the wall $C_{yy} < 1$ hence the negative values plotted. In addition, whereas at low elasticity levels the maximum $C_{yy} - 1 > 0$ and occurs away from the wall, at high elasticity levels the maximum difference $C_{yy} - 1 < 0$ and occurs at the wall, therefore the normalised profiles equal +1 and -1 at those specific locations, respectively. When viscoelasticity is not weak, Figure 3. 19 shows some degree of variation in terms of the normalized conformation tensor quantities due again to the amplification of small values in the ratio and also to the approximate nature of the similarity.

To assess the accuracy of the predicted polymer stresses via semi-analytical solution at large *Wi* number, the transverse profiles of the conformation tensor components $C_{xy}, C_{yy}, C_{zz}, C_{xx}$ are plotted and compared with RheoFoam results at two different location (a) at $\frac{x}{\mathcal{L}} = 0.2$ and (b) $\frac{x}{\mathcal{L}} = 1.0$ as shown in Figure 3. 20. The deviations of the conformation tensor components of the semi-analytical solution in relation to the predicted Rheofoam simulations are now very clear especially at $\frac{x}{\mathcal{L}} = 0.2$ ($Wi_x = 1.0$ and 5.0) and the discrepancies exist off to the wall. This deviation is associated with the appearance of large peak values of C_{ij} off the wall, which are rather pronounced and associated with changes in concavity in the transverse profiles. In contrast, the "well-behaved" semi-analytical solution is unable to follow these high Weissenberg number strong variations in C_{ij} on account of the imposed boundary layer simplifications. Such large local maxima are even observed to exist for the spanwise normal stresses. Again, ongoing downstream (decreasing Wi_x) the differences are reduced and at $Wi_x = 0.2$ and 1.0 ($x/\mathcal{L} = 1.0$) the match is better for lower Wi_x.

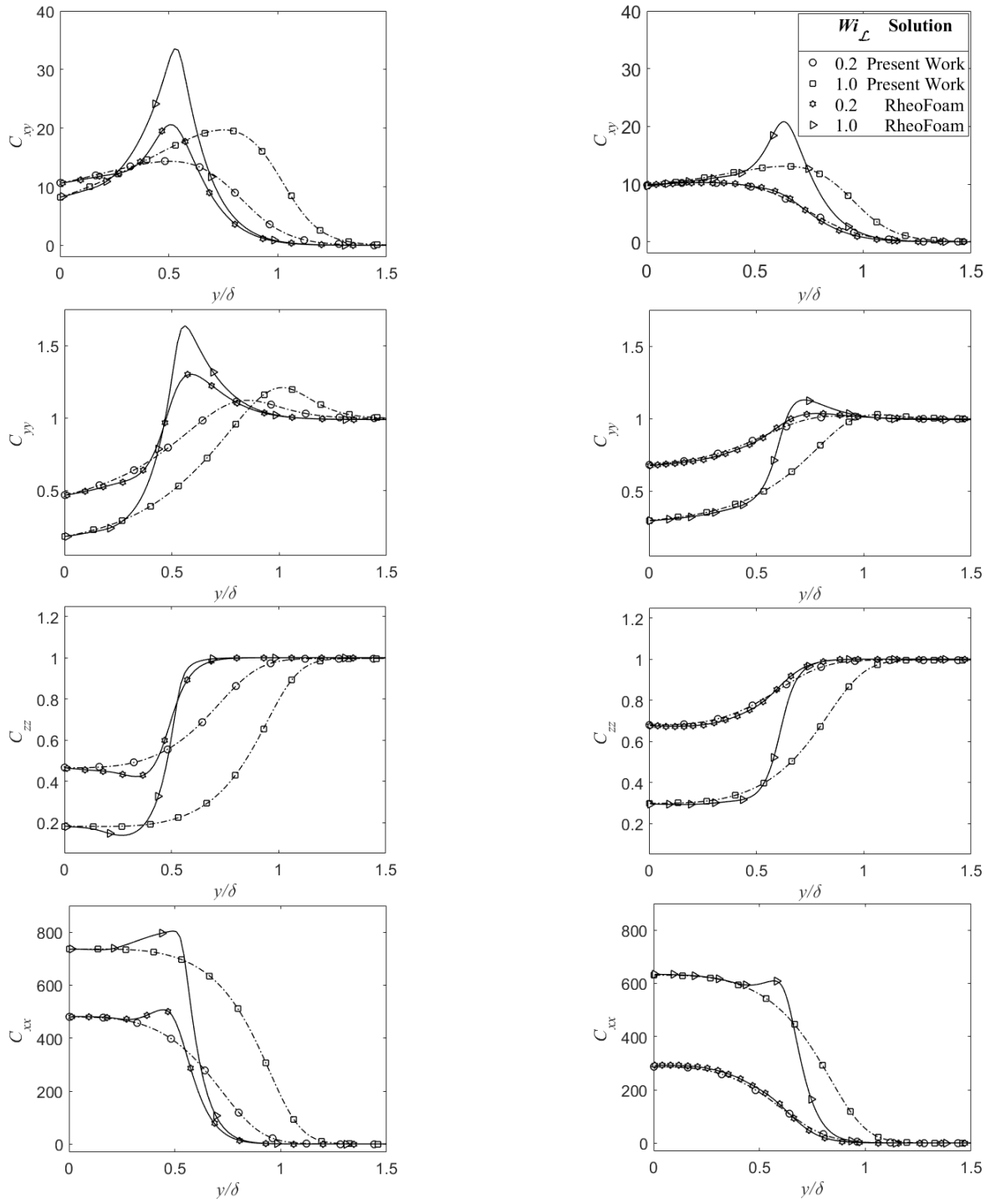

(a) (b)

Figure 3. 20- Comparison between transverse profiles of conformation tensor components $C_{xy}, C_{yy}, C_{zz,}\, C_{xx}$ from present BL theory (dashdotted lines) and RheoFoam (solid lines) for β_p=0.1, $L^2 = 900$, $Re_{\mathcal{L}} = 1 \times 10^5$ and $Wi_{\mathcal{L}} = 0.2\ and\ 1$ at: (a) $\frac{x}{\mathcal{L}} = 0.2$, (b) $\frac{x}{\mathcal{L}} = 1.0$.

Next, Figure 3. 21 plots transverse profiles of τ_{yy}^{p} and $\tau_{xy} = \tau_{xy}^{\mathrm{s}} + \tau_{xy}^{\mathrm{p}}$, normalised by the corresponding local peak values, to show better the asymptotic behavior under conditions of weak

viscoelasticity. Indeed, the plot of the total shear stress seems to be universal, but the zoom at the inset shows the existence of small differences. These differences are small because the approximate nature of the viscoelastic solution comes through the constitutive equation, i.e., through the polymer stress not through the momentum equation or the solvent stress. Both shear stresses are essentially determined by the magnitude of the shear rate $\partial u/\partial y$, and the solvent stress partially compensates for the variations of the polymer shear stress, so that the total stress profile has a near-universal shape. In Figure 3. 5 and Figure 3. 6 we also observed that the profile of normalized streamwise velocity is very weakly dependent on flow conditions showing a near-universal behavior.

Contrasting with the large variations in normalised $C_{yy}-1$ shown in Figure 3. 19-(d), the corresponding normalised $\tau_{yy}^{\mathrm{p}}/\left|\tau_{yy}^{\mathrm{p}}\right|_{\max}$ in Figure 3. 21-(a) presents a significantly better behavior because the small variations of $\left(C_{yy}-1\right)$ are partially compensated by the small variations in $f(C_{kk})$ leading to a better behaved stress (note that $\tau_{yy}^{\mathrm{p}}=f(C_{kk})\left(C_{yy}-1\right)$).

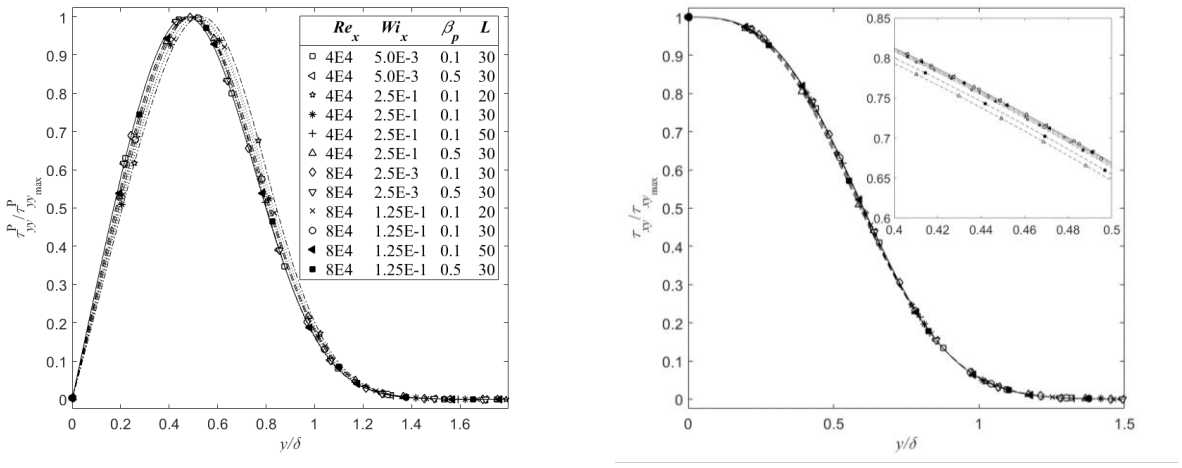

(a) (b)

Figure 3. 21- Transverse profiles of stress normalised by their local peak value for several flow conditions: (a) $\left|\tau_{yy}^{\mathrm{p}}\right|/\left|\tau_{yy}^{\mathrm{p}}\right|_{\max}$ and (b) $\tau_{xy}/\tau_{xy}{}_{\max}$. Lines are a guide to the eye; the solid line is the low elasticity asymptote.

For all flow conditions investigated, the peak values of τ_{xx}^{p} and of the total shear stress τ_{xy} are at the wall. For the polymer shear stress, under weak elasticity conditions the peak value occurs at the wall and then progressively deviates away from the wall as elasticity and shear-thinning further increases. The location of the peak values and its variation as a function of flow conditions are

plotted in Figure 3. 22 (a)-(b) for τ_{yy}^{p} and τ_{xy}^{p}, respectively, including the equations for the asymptotic locations.

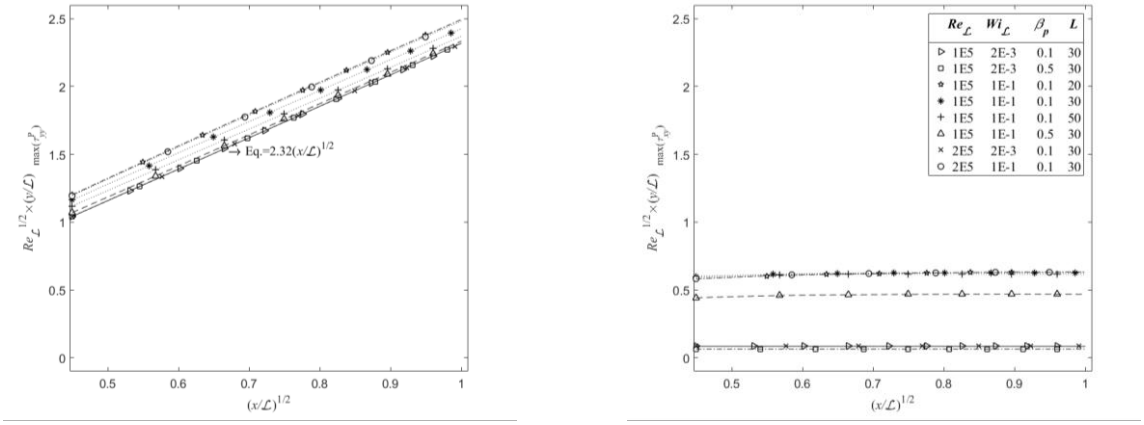

(a) (b)

Figure 3. 22- Location of peak values of some stress components: (a)τ_{yy}^{p}, (b)τ_{xy}^{p}. Lines are a guide to the eye; the solid line is the low elasticity asymptote.

The streamwise variation of the polymer wall shear stress (τ_{xy}^{p}) is plotted in Figure 3. 23, confirming the findings from the transverse profiles. The low elasticity asymptote is also plotted for polymer shear stress.

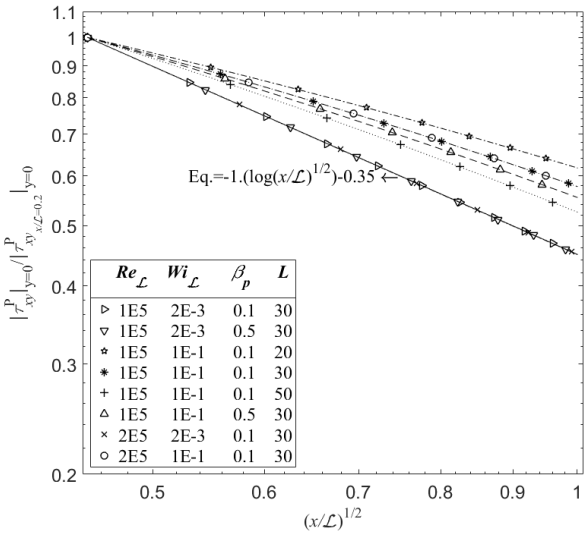

Figure 3. 23- Decay law for the polymer wall shear stress (τ_{xy}^{p}) normalized by its value at $\frac{x}{\mathcal{L}} = 0.2$. Lines are a guide to the eye; the solid line is the low elasticity asymptote.

“One good test is worth a thousand expert opinions.”

-Wernher Von Braun

(March 23, 1912 – June 16, 1977)

A German–American aerospace engineer and space architect.

“There is no such thing as an unsolvable problem.”

-Sergei Korolev

(January 12 1907 – 14 January 1966)

A lead Soviet rocket engineer and spacecraft designer.

Chapter 4: The laminar mixing layer flow of viscoelastic FENE-P fluids

4.1. Flow problem

The schematic of laminar mixing layer flow is shown in Figure 1: two parallel streams with different uniform velocities U_1 and U_2 $(U_1 > U_2)$ meet at $x = 0$, downstream a very thin frictionless plate called splitter plate (existing at $x < 0$). The interacting streams form the mixing layer, and the transverse coordinate is y. Viscous effect smoothens the velocity discontinuity and at some distance downstream the plate trailing edge the flow characteristics no longer depend on the plate characteristics (naturally, a real plate is not frictionless). For high enough Reynolds numbers, the boundary layer approximations are valid in the mixing layer flow. Since the two parallel streams remain uniform and constant far from the mixing layer, the streamwise pressure gradient is null ($\partial p/\partial x = 0$) in the free stream flows.

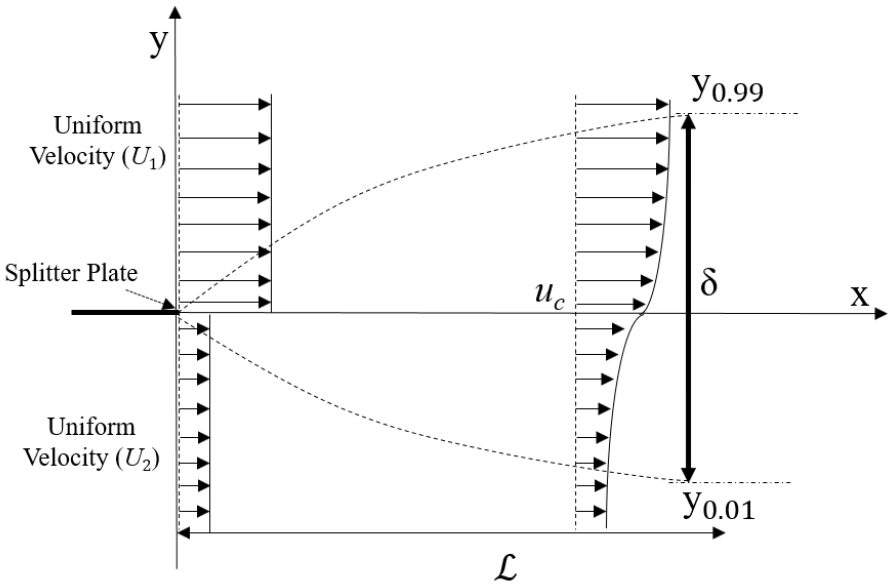

Figure 4. 1.The schematics of the mixing layer flow and mixing layer thickness definition. The *z*-coordinate is normal to the plane.

To define mixing layer thickness (δ), we get inspiration from Pope [46], in which it is required to define two local velocities shown by U_α with $\alpha = 0.01$ and 0.99 as follows

$$U_\alpha = U_2 + \alpha(U_1 - U_2) \qquad (4\text{- }1)$$

according to lower and upper free stream velocities respectively. Therefore, the developing mixing layer thickness (δ) is defined as the transverse distance between the locations of the corresponding local velocities shown by (y_α) where, i.e.

$$\delta(x) = y_{0.99} - y_{0.01} \tag{4- 2}$$

As shown in Figure 4. 1.

4.2. Governing equations & numerical solution

The governing equation of mixing layer flow are analogous to boundary layer flow Eqs. (3-31) and (3-38), even approximate similarity variables (3-28) are the same, however the difference comes from boundary condition of the problem, Defining the free-stream velocity ratio (γ) as

$$\gamma = \frac{U_2}{U_1} \tag{4- 3}$$

the boundary conditions for the laminar mixing layer flow are [23,24]:

$$G'(+\infty) \to 1, G'(-\infty) \to \gamma\,, \tag{4- 4}$$

$$G''(+\infty) = G''(-\infty) = 0. \tag{4- 5}$$

The boundary conditions at infinity are essentially verified at $\eta = \pm 10$ as discussed below, it is verified for $(\gamma = 0.5)$, however for lower value of γ, a larger domain size is required. The solution of the mixing layer flow equations is not unique ([119][120]) and shifts in the transverse direction (through η). We used an iterative procedure to find the place where $G = 0$, then the solution is shifted to the origin ($\eta = 0$). This procedure is repeated until the origin stops shifting (typically 5 to 6 iterations), so it is equivalent to forcing the following extra boundary condition

$$G(0) = 0. \tag{4- 6}$$

By considering these boundary conditions, the simplified governing equations are numerically solved as explained in Section 3.4.

4.3. Results and discussion

4.3.1. Verification: Newtonian fluids

Setting $\beta_p = 0$, the governing equations for the viscoelastic fluid reduce to those for a Newtonian mixing layer flow which is used to verify the present solution [23]. Through asymptotic analysis, we found that infinity conditions are already achieved at $\eta = \pm 10$ for $\gamma = 0.5$, so the same conditions are considered here. It is worth mentioning that to choose an adequate Reynolds number, two conditions should be satisfied: (1) the Reynolds number should be high enough for the thin layer approximations to be valid [23] and (2) it should be below the critical condition for laminar-turbulent transition. As explained by Dimotakis [135] this critical Reynolds number for a planar mixing layer is 1×10^4 if based on the mixing layer thickness (δ). Therefore, the maximum Reynolds number which is considered in the present study is $Re_\delta = \frac{U_1\delta}{\nu_0} = 1\times10^3$. Furthermore, for presenting the results, the local Reynolds number (Re_x) defined as

$$Re_x = \frac{U_1 x}{\nu_0} \tag{4- 7}$$

is used, where x is the streamwise distance from the trailing edge of the splitter plate. It is also worth mentioning that in this paper, the Reynolds number at the maximum distance from the trailing edge of the splitter plate, denoted Re_L, is also used for data normalization purposes.

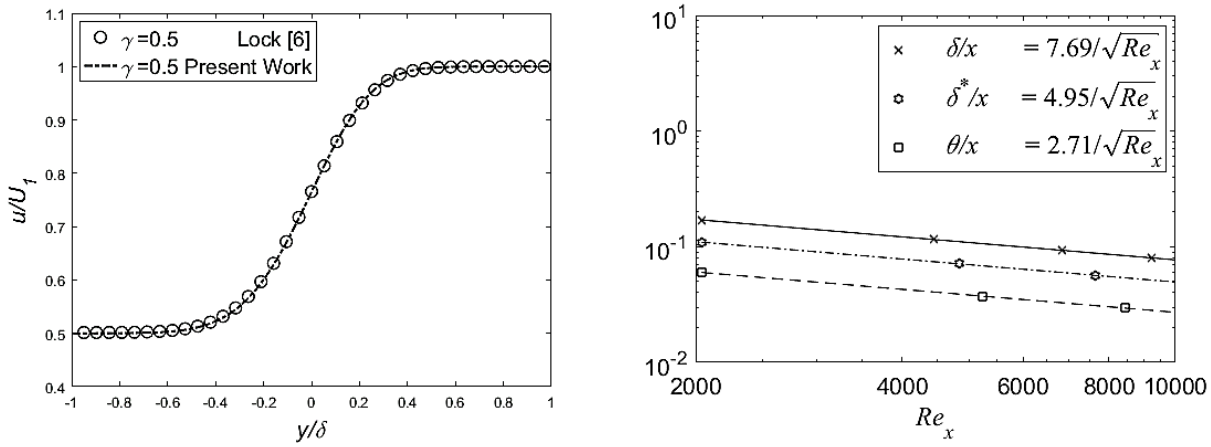

(a) (b)

Figure 4. 2. Characteristics of the steady laminar mixing layer flow of Newtonian fluids in the self-similar region for $\gamma = 0.5$: a) profiles of u/U_1 versus y/δ at Re_x=2000; b) variation of δ/x, δ^*/x and θ/x with Re_x.

Figure 4. 2 (a) shows good agreement between the computed profiles of streamwise velocity given by Eq. (3-28) and normalized by the upper free stream velocity (U_1), for $\gamma = 0.5$, and the literature[117]. The streamwise variation of other global characteristics of the laminar mixing layer flow are plotted in Figure 4. 2 (b) and compare well with the literature [23,24]. They are the mixing layer thickness (δ), defined in Eq. (4- 2), the displacement (δ^*) thickness as defined in:

$$\delta^* = \int_{-\infty}^{+\infty} \left(1 - \frac{u}{U_1}\right) dy = \left(\int_{-\infty}^{0} \left(1 - \frac{u}{U_1}\right) dy + \int_{0}^{+\infty} \left(1 - \frac{u}{U_1}\right) dy\right), \quad (4\text{- }8)$$

and the momentum (θ) thickness given by:

$$\theta = \int_{-\infty}^{+\infty} \frac{u}{U_1}\left(1 - \frac{u}{U_1}\right) dy = \left(\int_{-\infty}^{0} \frac{u}{U_1}\left(1 - \frac{u}{U_1}\right) dy + \int_{0}^{+\infty} \frac{u}{U_1}\left(1 - \frac{u}{U_1}\right) dy\right). \quad (4\text{- }9)$$

From our semi-analytical solution, and for $\gamma = 0.5$, the following relations were found for the three characteristic thicknesses: $\frac{\delta}{x} = \frac{7.69}{\sqrt{Re_x}}$, $\frac{\delta^*}{x} = \frac{4.94}{\sqrt{Re_x}}$ and $\frac{\theta}{x} = \frac{2.71}{\sqrt{Re_x}}$. From the latter two a shape factor ($H \equiv \delta^*/\theta$) of 1.8284 was obtained for $\gamma = 0.5$, again in good agreement with the literature.

4.3.2.FENE-P fluids

In this section, only the third set of Peterlin functions $f(C_{kk})$, described by Eq. (2- 10c) is used to obtain the numerical results. The keep the ratio of free stream velocities constant at $\gamma = 0.5$ and the local Weissenberg number Wi_x

$$Wi_x = \frac{\lambda U_1}{x} \quad (4\text{- }10)$$

is also used to present results.

4.3.3.Velocity field and mixing layer thickness

The dependence of the normalized transverse profiles of streamwise and normal velocities on fluid characteristics, at two different locations in the self-similar region, are shown in Figure 4. 3 (a)-(b). By normalizing the transverse coordinate with the mixing-layer thickness, and with the Reynolds number for the normal velocity, quasi-unique profiles are obtained for u and v at low

elasticity level. These low elasticity profiles coincide with the Newtonian profiles. However, by enhancing the elasticity level, small deviations from the low elasticity limit start to be observed in both velocity profiles thus showing the approximate nature of the similarity solution. These deviations are of the same magnitude as those seen for a planar laminar jet by Parvar et al. [112, 113] and less intense than seen in a boundary layer by Parvar et al.[136], where the presence of the plate wall imposes a more severe flow restriction.

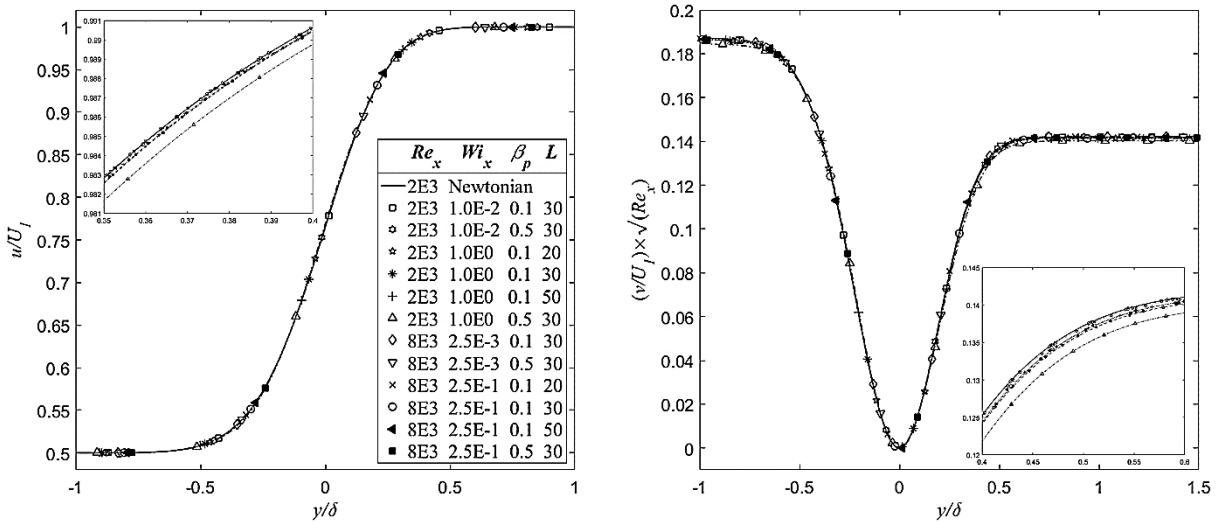

(a) (b)

Figure 4. 3. Normalized transverse velocity profiles at $Re_x = 2000$ and 8000 as a function of Reynold number, Weissenberg number, viscosity ratio and dumbbell extensibility for $\gamma = 0.5$: (a) u/U_1, (b) $v\sqrt{Re_x}/U_1$.

Figure 4. 4 shows the streamwise variation of the centerline velocity of the mixing layer (u_c/U_1) as a function of the independent dimensionless numbers, some calculated at $x = \mathcal{L}$. At low elasticity level, the velocity profiles collapse onto a single constant value identical to the velocity for a Newtonian fluid, $u_c/U_1 = 0.7652$ for $\gamma = 0.5$. Increasing the elasticity level increases the centerline velocity and makes it depend on *x*, so that the profile is no longer constant, but increases towards the splitter plate because locally flow elasticity is increasing on moving upstream on account of higher shear rates. However, these effects are small and for the tested cases the deviations are less than 1%.

The streamwise variation of the normalized mixing layer thickness (δ/x) is plotted in Figure 4. 5 as a function of $Wi_{\mathcal{L}}$, β_{p} and L. At low Weissenberg numbers δ/x collapses to the Newtonian flow variation, as previously observed in the planar jet [112,113] and flat plate flow [136], but by increasing $Wi_{\mathcal{L}}$, β_{p}, or decreasing L, the mixing layer thickness decreases.

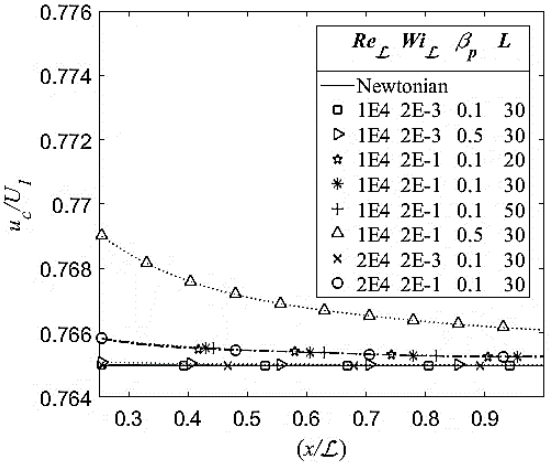

Figure 4. 4. Streamwise variation of normalised mixing layer centerline velocity (u_c/U_1) under various flow conditions for $\gamma = 0.5$. The solid line shows the Newtonian data u_c/U_1=0.7652.

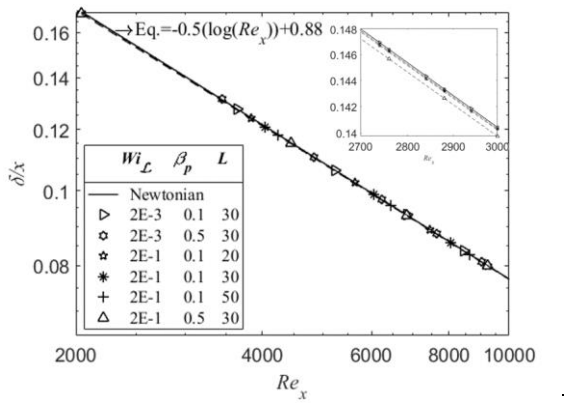

Figure 4. 5. Streamwise variation of the normalised boundary layer thickness (δ/x) under various flow conditions for $\gamma = 0.5$. The inset plots profiles for $2.7\times 10^3 \leq Re_x \leq 3\times 10^3$.

The corresponding streamwise variations of the displacement (δ^*/x) and momentum (θ/x) thicknesses are presented in Figure 4. 6 and Figure 4. 7. As expected, when the elasticity level is weak, both profiles follow closely the corresponding Newtonian laws, however by increasing the elasticity level both the dimensionless displacement thickness (δ^*/x) and the dimensionless momentum thickness (θ/x) decrease.

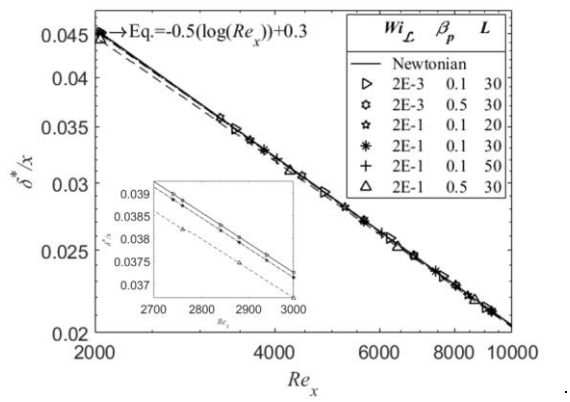

Figure 4. 6. Streamwise variation of the normalised displacement thickness (δ^*/x) under various flow conditions for $\gamma = 0.5$. The inset plots profiles for $2.7\times 10^3 \leq Re_x \leq 3\times 10^3$.

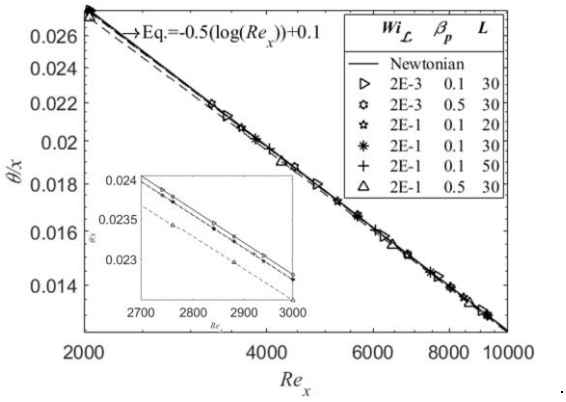

Figure 4. 7. Streamwise variation of the normalised momentum thickness (θ/x) under various flow conditions for $\gamma = 0.5$. The inset plots profiles for $2.7\times 10^3 \leq Re_x \leq 3\times 10^3$.

The ratio between these two thicknesses defines the shape factor that is plotted in Figure 4. 8. Again, at low elasticity levels the behavior collapses with the Newtonian value (H=1.8284) and increases at higher flow elasticity. Notice that for all quantities on moving downstream the local value of Weissenberg number decreases and the curves approach the low elasticity asymptote.

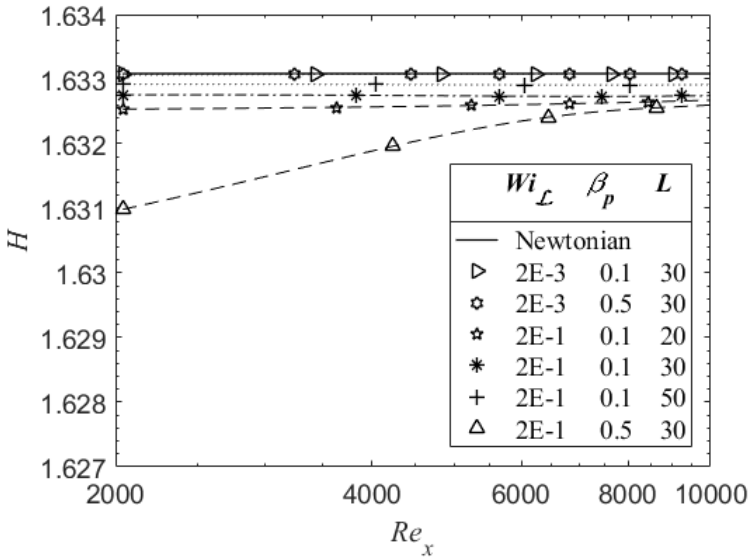

Figure 4. 8. Streamwise variation of the shape factor H for $\gamma = 0.5$ as a function of dimensionless flow and fluid characteristics.

4.3.4.Conformation and stress tensor

Next, the corresponding profiles of the conformation and stress tensor quantities are presented and discussed. Figure 4. 9 (a)-(d) plot the streamwise variations of the maximum value of the polymer stress components normalised by its corresponding value at $x/\mathcal{L}$ =0.2.

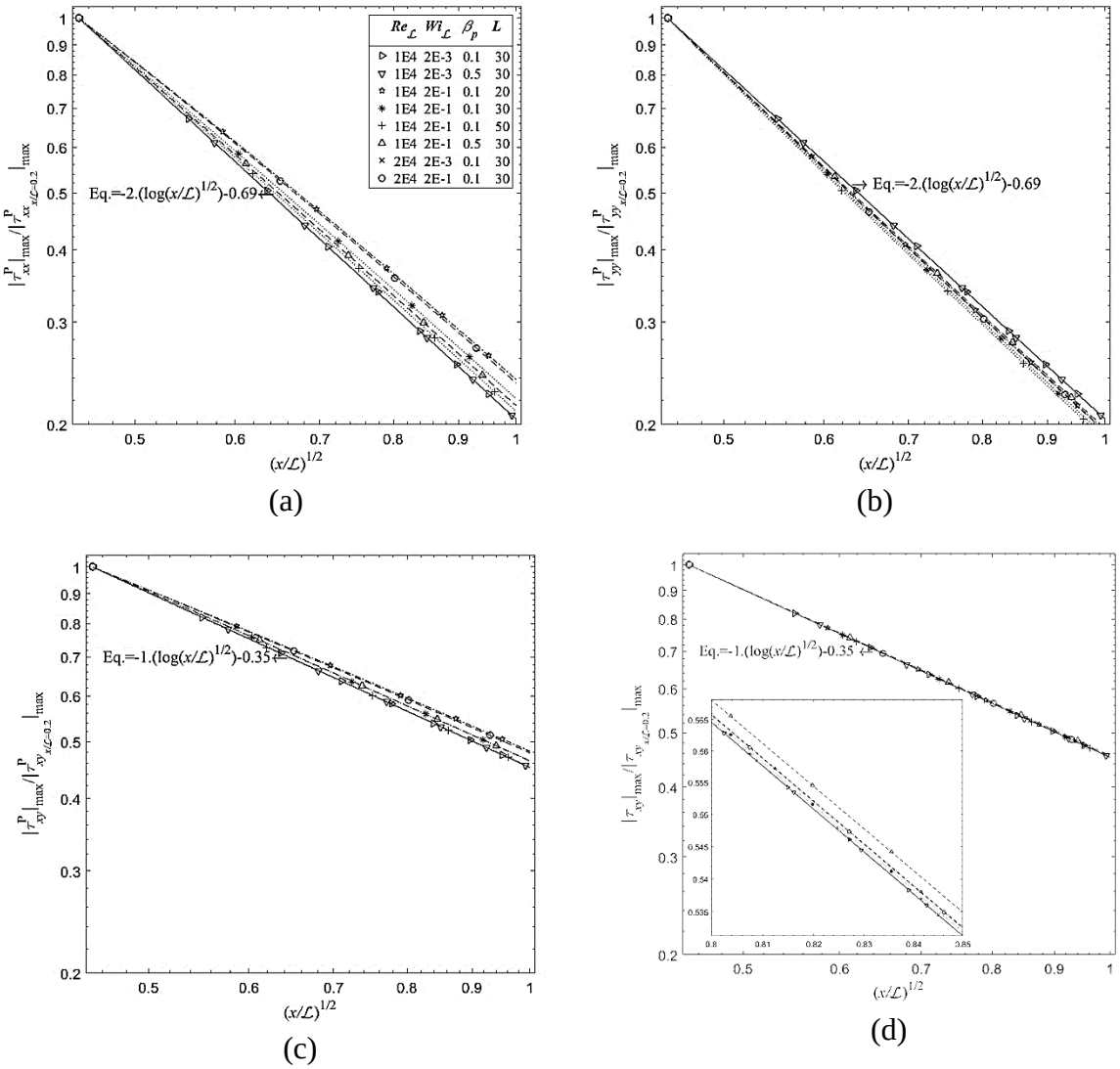

Figure 4. 9. Streamwise variation of normalized peak values of the stress tensor components for various rheological properties: (a)τ_{xx}^{p}, (b)τ_{yy}^{p}, (c)τ_{xy}^{p}, (d) τ_{xy}.

The profiles exhibit linear variations in log-log coordinates, according to Eq.(4- 11), and a low elasticity asymptote, with the rates of decay of τ_{xx}^{p} and τ_{yy}^{p} being equal to 2 and twice as fast as for the polymer (τ_{xy}^{p}) and total (τ_{xy}) shear stresses.

$$\log_{10}\frac{\left|\tau_{ij}^{\mathrm{p}}\right|_{max}}{\left|\tau_{ij}^{\mathrm{p}}\right|_{max@\frac{x}{\mathcal{L}}=0.2}} = m\log_{10}\left[\left(\frac{x}{\mathcal{L}}\right)^{1/2}\right] - b. \qquad (4\text{- }11)$$

Figure 4. 10 (a)-(b) show the location of the maximum stress tensor τ_{yy}^{p} and τ_{xy} for various flow conditions. The peak values of τ_{xy} always occur at the centerline of mixing layer in all range elasticity level. Furthermore, the maximum of τ_{yy}^{p} occur always far from the centerline and this distance from the centerline increase in the streamwise direction. It worth mentioning that the peak values of τ_{xx}^{p} and τ_{xy}^{p} occurs very close to the centerline, however such profiles are not shown for conciseness.

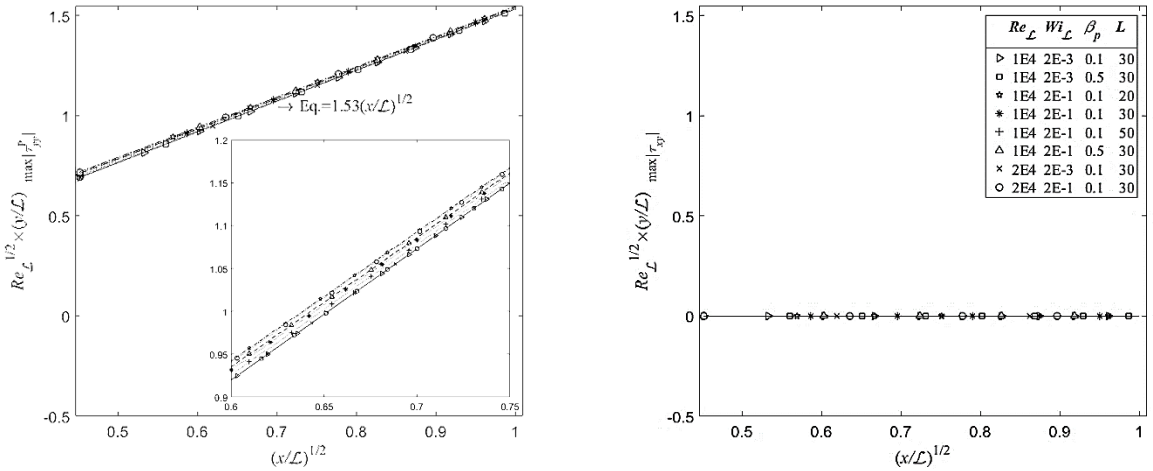

(a) (b)

Figure 4. 10. The location of peak values of the stress tensor components for various rheological properties: (b)τ_{yy}^{p}, (d) τ_{xy}.

The ratio of maximum polymer over maximum solvent stress ($\frac{\left|\tau_{ij}^{\mathrm{p}}\right|_{max}}{\left|\tau_{ij}^{\mathrm{s}}\right|_{max}}$) is shown in Figure 4. 11. At low elasticity levels, these ratios are constant and equate to the ratio of viscosities $\nu^{\mathrm{p}}/\nu^{\mathrm{s}} = \beta_{\mathrm{p}}/(1-\beta_{\mathrm{p}}) = \frac{1}{9}$ and 1 for $\beta_{\mathrm{p}} = 0.1$ and 0.5, respectively, because those stresses are essentially determined by the flow shear rate (in a rather complex way for the *yy* component). As flow elasticity increases this stress ratio decreases on account of shear-thinning behavior. However, the ratio $\frac{|\tau_{xx}^{\mathrm{p}}|_{max}}{|\tau_{xx}^{\mathrm{s}}|_{max}}$ behaves differently, being always above 1 and tending to increase significantly with elasticity since the numerator depends on the shear rate and the denominator depends on the normal strain rate.

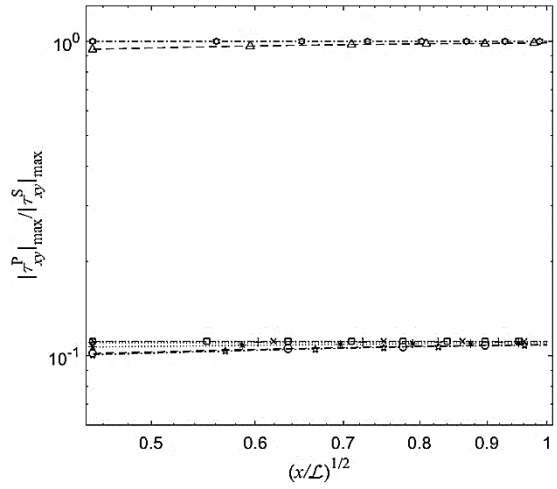

(a)

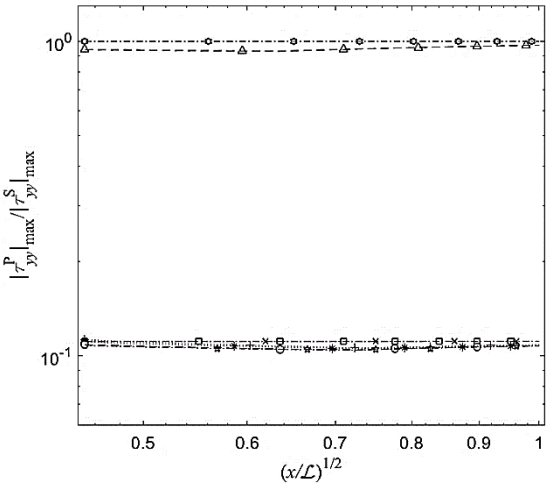

(b)

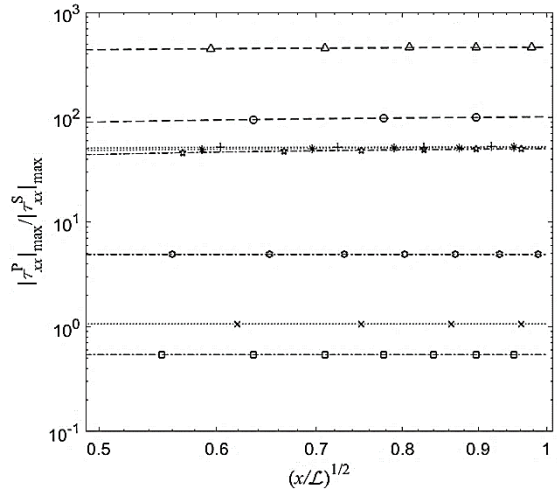

(c)

	$Re_{\mathcal{L}}$	$Wi_{\mathcal{L}}$	β_p	L
□	1E4	2E-3	0.1	30
✡	1E4	2E-3	0.5	30
✡	1E4	2E-1	0.1	20
✱	1E4	2E-1	0.1	30
+	1E4	2E-1	0.1	50
△	1E4	2E-1	0.5	30
×	2E4	2E-3	0.1	30
○	2E4	2E-1	0.1	30

(d)

Figure 4. 11. The streamwise variation of the ratio of polymer stress (τ_{ij}^{p}) to solvent stress (τ_{ij}^{s}) at the mixing layer flow (a)$\left|\tau_{xy}^{\mathrm{p}}\right|_{max}/\left|\tau_{xy}^{\mathrm{s}}\right|_{max}$ (b)$\left|\tau_{yy}^{\mathrm{p}}\right|_{max}/\left|\tau_{yy}^{\mathrm{s}}\right|_{max}$, (c) $\left|\tau_{xx}^{\mathrm{p}}\right|_{max}/|\tau_{xx}^{\mathrm{s}}|_{max}$,(d) legend.

Figure 4. 12 (a)-(d) show the approximate self-similar behavior of conformation tensor components at low elasticity, which deviates from those of low elasticity curves at higher *Wi* numbers. The data is normalised by the corresponding local maximum values and covers a wide range of flow conditions pertaining to two different locations (Re_x).

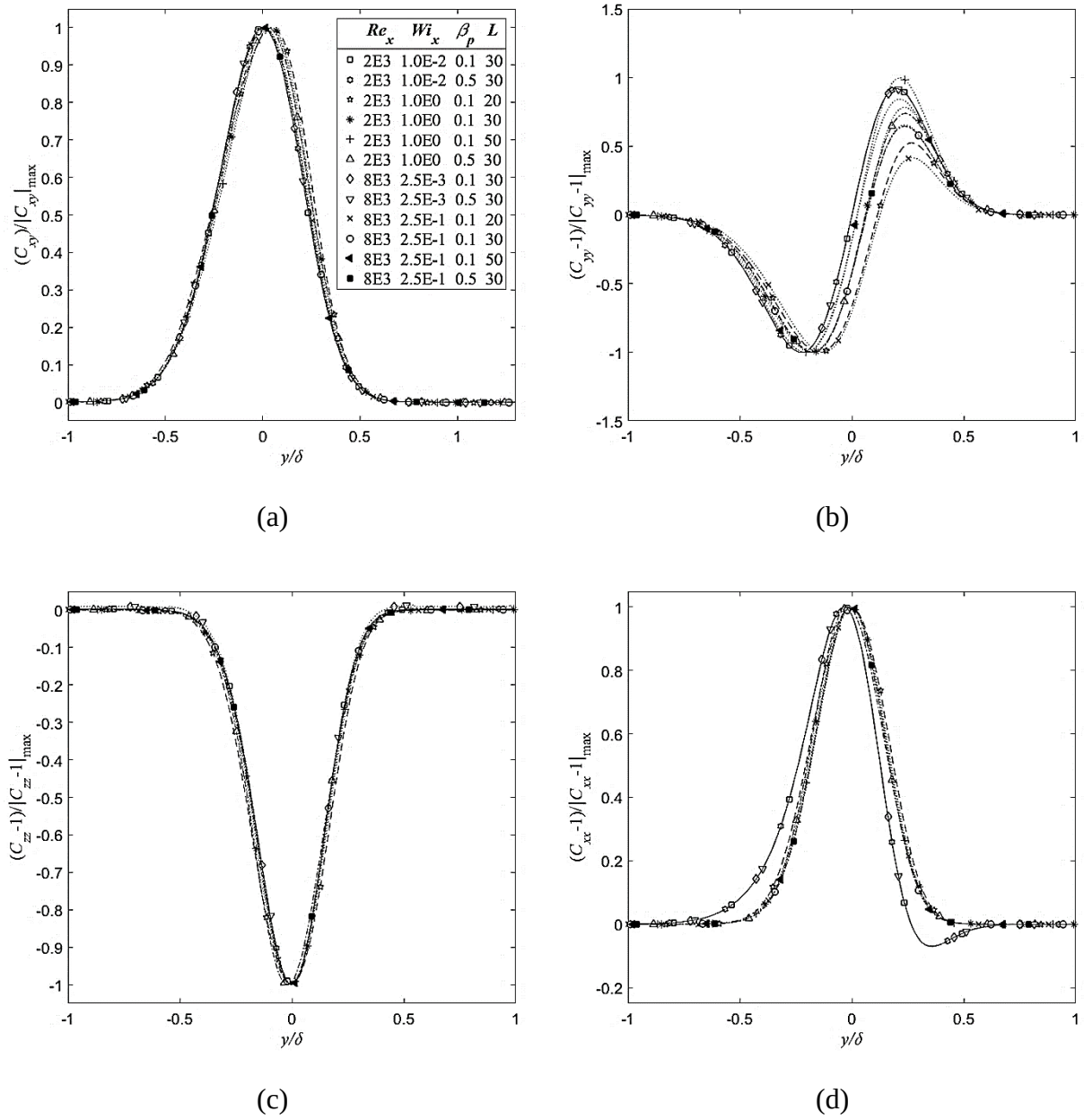

Figure 4. 12. Transverse profiles normalized components of the conformation tensor: (a) C_{xy}, (b)C_{yy}, (c) $C_{zz,}$(d) C_{xx}, for various rheological properties. Lines are a guide to the eye.

Figure 4. 13 shows the transverse variation of the total shear stress τ_{xy} normalized by corresponding peak values. Similar to conformation tensor components profiles, at low viscoelasticity levels, an approximate similarity behavior is observed, while increasing the levels of viscoelasticity lead the profiles to slightly deviate from the asymptote. The deviation is small, however, because some of the variation in the polymer stress component is taken by the

corresponding solvent stress, i.e., the total stress behaves almost as if it has approximate similarity nature of the solution.

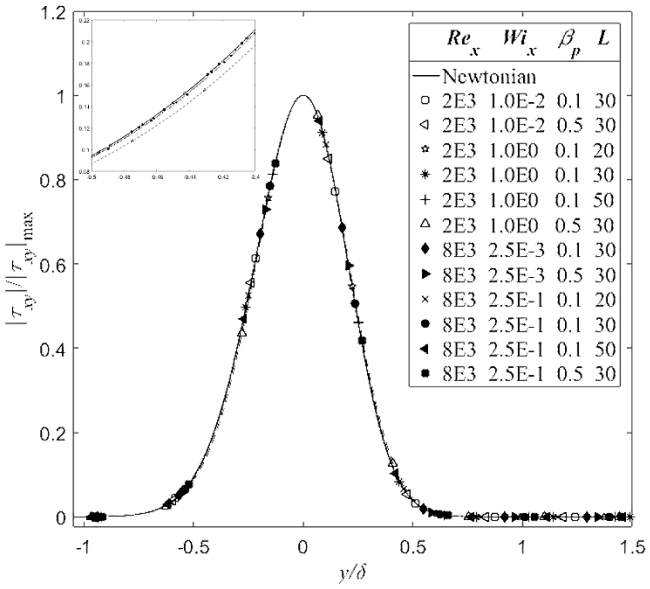

Figure 4. 13. Transverse profiles of normalized total shear stress τ_{xy} for various rheological properties.

“In the middle of difficulty lies opportunity. Imagination is everything. It is the preview of life's coming attractions.”

-Albert Einstein

(14 March 1879 – 18 April 1955)

A German theoretical physicist

Chapter 5: The laminar planar jet flow of viscoelastic FENE-P fluids

5.1. Flow problem

The laminar planar jet flow is sketched in Figure 5. 1. A uniform velocity (U) jet of width D exits a nozzle entering a sea of the same fluid, which is at rest. The edge of the central potential core becomes subject to viscous diffusion and as the jet evolves in the streamwise direction (x) it entrains fluid from the outer potential flow region, while maintaining constant the total momentum [23,24]. The jet spread in the transverse direction (y) is quantified by the streamwise increase in jet half-width (δ), which is defined as the transverse distance from the centerline to the location where the local streamwise velocity equals 1% (0.01) of the local centerline streamwise velocity (U_c), as indicated in Figure 5. 1[23].

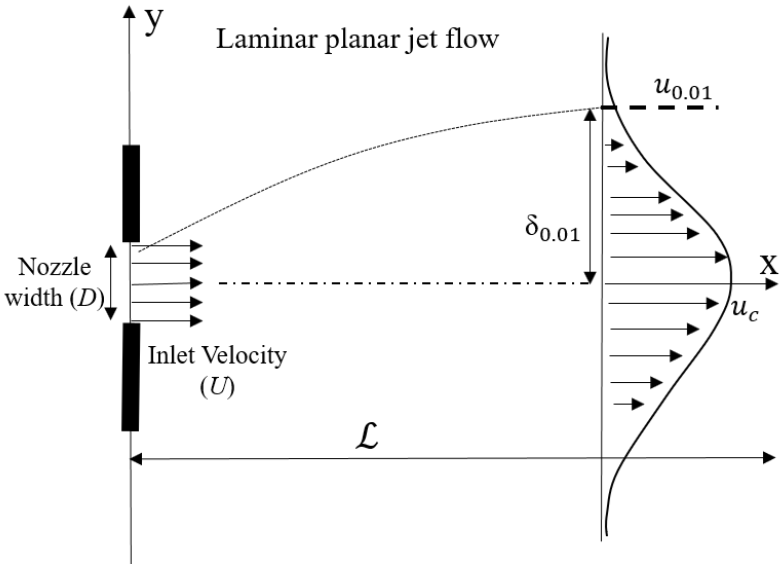

Figure 5. 1.Schematics of the planar laminar jet flow and half-width jet definition. The z-coordinate is normal to the plane.

5.2. Governing equations

The momentum equation is discussed in section (2.2), however planar jet flow required different similarity variable which is explained as follows. Before dealing with mathematical procedure of deriving governing equation it is worth to mention that since from an application point of view the nozzle width (D) is a more useful length scale than the jet length, the approximate similarity

transformations already relied on the use of *D* and henceforth *Re* and *Wi* numbers are re-defined on the basis of the nozzle width to be

$$Re = \frac{UD}{\upsilon_0}, \tag{5- 1}$$

and

$$Wi = \frac{\lambda U}{D}. \tag{5- 2}$$

5.2.1. The general solution

Next we introduce the approximate similarity transformations consistent with the underlying thin layer approximation used previously for Newtonian fluids [23,24], but for generality we work instead with dimensionless quantities. The approximate similarity variables are such that upon substitution the partial differential equations should reduce to ordinary differential equations (ODE). However, for the planar jet flow of FENE-P fluids no matter the numerical values of the exponents *n*, *m* and *p* of the similarity transformations $\eta \propto y^n x^m$ and $G(\eta, x) \propto x^p \psi$ could provide differential equations that depended exclusively on η as had also been found for the boundary layer flow of the same fluids by Olagunju [19,20] (note that each type of laminar flow has its unique type of similarity variable). Therefore, our decision to work with approximate similarity transformations adapted from those of Newtonian planar jet flow, since they provide an similarity solution in the limit of vanishing polymer additive concentration. Here, the approximate similarity variable η and function $G(\eta, x)$ are defined as

$$\eta = \frac{D^{1/6}}{3}\sqrt{\frac{U}{\nu_0}}\frac{y}{x^{2/3}} \text{ and } G(\eta, x) = \frac{\psi}{\sqrt{\nu_0 U D^{\frac{1}{3}}}x^{1/3}}, \tag{5- 3}$$

where *D* is the nozzle width shown in Figure 5. 1. The velocity profiles are computed from

$$u = \frac{UD^{\frac{1}{3}}}{3}x^{-\frac{1}{3}}G'(\eta, x), \tag{5- 4}$$

$$v = -\frac{\sqrt{\nu_0 U D^{\frac{1}{3}}}}{3}x^{-\frac{2}{3}}\big(G(\eta, x) - 2\eta G'(\eta, x)\big), \tag{5- 5}$$

where the prime indicates derivative in order to η. Similar to boundary layer flow to reduce the level of complexity, it is assumed that the streamwise derivatives of similarly functions $G(\eta, x)$, is assumed to be very small $\frac{\partial G(\eta,x)}{\partial x} \approx 0$ and it is neglected in deriving the governing equation.

Since the Peterlin function depends on the approximate similarity variables, we next assume that it can be rewritten as

$$K(\eta, x) = f(C_{kk})\,. \tag{5- 6}$$

but note that it is not necessary to invoke the above simplifying assumption for this quantity.

Using the approximate similarity variables, substitution of Eq. (5- 3) and (5- 6) into Eq. (2- 10c) leads to the following third order algebraic equation on $K(\eta, x)$

$$K^3 + C_0K^2 + C_1(G' + 2\eta G'')^2K + C_2G''^2 + C_3(G' + 2\eta G'')^2 = 0, \tag{5- 7}$$

with dimensionless coefficients

$$\begin{aligned}
C_0 &= \left(\frac{3I - 3f(L) - L^2}{L^2}\right),\\
\mathrm{C}_1 &= -\frac{4U^2D^{\frac{2}{3}}\lambda^2}{81}x^{-\frac{8}{3}} = -\frac{4{Wi_x}^2}{81}\left(\frac{D}{x}\right)^{\frac{2}{3}},\\
\mathrm{C}_2 &= -\frac{2\lambda^2 f(L)U^3D}{81\upsilon_0L^2}x^{-2} = \frac{2f(L){Wi_x}^2Re}{81L^2},\\
\mathrm{C}_3 &= \frac{4\lambda^2(L^2 + f(L) - 3I)}{L^2}\frac{U^2D^{\frac{2}{3}}}{81}x^{-\frac{8}{3}} = \frac{4(L^2 + f(L) - 3I){Wi_x}^2}{81L^2}\left(\frac{D}{x}\right)^{\frac{2}{3}}.
\end{aligned} \tag{5- 8}$$

where $I = 1$ if the Peterlin functions are given by Eq. (2- 10c) and $I = 0$ otherwise. Since coefficients C_0 to C_3 in Eq. (5- 8) depend on *x*, the solution of *K* will depend on η, and *x*, i.e., there is no full self-similarity solution for the planar jet flow of viscoelastic fluids as assumed initially. As discussed earlier in the previous sections, Olagunju [19,20] had already concluded similarly for the boundary layer flow of the FENE-P fluid, but this absence of a full similarity solution does not preclude the existence of an approximate similarity solution for the FENE-P fluid, which is presented below.

Regarding the momentum equation, by substituting C_{xy} (from Eq. (3-25)) into Eq. (3-12),

$$\frac{\partial\psi}{\partial y}\left(\frac{\partial^2\psi}{\partial x\partial y}\right)-\left(\frac{\partial\psi}{\partial x}\right)\left(\frac{\partial^2\psi}{\partial y^2}\right)=\upsilon_s\frac{\partial^3\psi}{\partial y^3}$$

$$+\upsilon_p f(L)\left(\frac{2\lambda\frac{\partial^2\psi}{\partial x\partial y}\frac{\partial^3\psi}{\partial y^3}+f(C_{kk})\frac{\partial^3\psi}{\partial y^3}-2\lambda\frac{\partial^3\psi}{\partial x\partial y^2}\frac{\partial^2\psi}{\partial y^2}-\frac{\partial f(C_{kk})}{\partial y}\frac{\partial^2\psi}{\partial y^2}}{\left(2\lambda\frac{\partial^2\psi}{\partial x\partial y}+f(C_{kk})\right)^2}\right). \quad (5\text{- }9)$$

and by utilizing the similarity variables in Eq. (5- 9), after some algebraic manipulation the momentum equation becomes

$$-\left(G'^2+GG''\right)=\left(1-\beta_p\right)G'''+\beta_p f(L)\left(\frac{C_4\left(3G''^2-G'G'''\right)+KG'''-K'G''}{(K-C_4C_5)^2}\right). \quad (5\text{- }10)$$

with

$$C_4=\frac{2\lambda UD^{\frac{1}{3}}x^{-\frac{4}{3}}}{9}=\frac{2Wi_x}{9}\left(\frac{D}{x}\right)^{\frac{1}{3}}, \quad (5\text{- }11)$$

$$C_5=(G'+2\eta G''). \quad (5\text{- }12)$$

Again, we observe a dependence on x in addition to the dependence on η. To obtain the final form of the momentum equation the derivative of K relative to η is also required, as obtained from Eq.(5-7).

$$K'=-\frac{6C_5G''(C_1K+C_3)+2\left(C_2G''+2C_5\eta(C_1K+C_3)\right)G'''}{C_6} \quad (5\text{- }13)$$

Then by substituting the derivative in Eq. (5- 13) into (5- 10), the final momentum equation (5-10) becomes the following differential equation on $G(\eta,x)$.

$$G'''=-\frac{\left(G'^2+GG''\right)+\beta_p f(L)3G''^2\left(\frac{2C_5(C_1K+C_3)+C_4C_6}{(K-C_4C_5)^2C_6}\right)}{\left(\left(1-\beta_p\right)+\beta_p f(L)\left(\frac{2G''\left(C_2G''+2C_5\eta(C_1K+C_3)\right)+C_6(K-C_4G')}{(K-C_4C_5)^2C_6}\right)\right)} \quad (5\text{- }14)$$

with coefficient

$$C_6=\left(3K^2+2C_0K+C_1{C_5}^2\right). \quad (5\text{- }15)$$

As discussed previously, this equation shows G to depend on x in addition to its dependence on η, confirming the absence of a full self-similar solution for the planar jet flow, in contrast to the situation for Newtonian flow. Nevertheless, it is still possible to obtain a numerical solution to this so-called approximate similarity solution problem, via the numerical solution of Eqs. (5- 14) and (5- 7), which is done later. The numerical method used is described in Section 3.4 and the numerical results will be presented and discussed in Section 5.4, but prior to that there are two other simpler solutions we wish to discuss below, namely the delta solution and the Olagunju-type solution, both of which rely on invoking further assumptions in regard to the conformation tensor equations.

5.2.2. Delta solutions

The general approximate similarity solution can be simplified if the flow is limited to very low Weissenberg numbers, since in this limit the deviation from 1 of the two main normal components of C_{ij} is nearly symmetric and the third normal component (C_{zz}) remains essentially unaffected, i.e., by assuming that

$$C_{\mathrm{xx}} = 1 + \Delta C, \tag{5- 16}$$

$$C_{\mathrm{yy}} = 1 - \Delta C, \tag{5- 17}$$

$$C_{zz} = 1. \tag{5- 18}$$

Then, C_{xy} is obtained from Eqs. (3-21) and (5- 17), i.e.

$$C_{\mathrm{xy}} = \lambda(1 - \Delta C)\frac{\partial u}{\partial y}. \tag{5- 19}$$

and consequently $f(C_{kk}) = 1$. So, the constitutive equation now provides the solution for ΔC, but since we now have a single unknown (ΔC) rather than the original C_{xx} and C_{yy} unknowns, the algebraic equation for ΔC can be formed either from the C_{xx} equation or from the C_{yy} equation, i.e., there are two possible delta solutions. There are two possible delta solutions depending on the equation used to determine ΔC: the original equations for C_{yy} or for C_{xx}. Below we present both, starting with C_{yy} and then C_{xx}. The conformation tensor components for steady planar jet flows of FENE-P fluids at very low Weissenberg number can be approximated as in Eqs. (5- 16) to (5- 19)

and consequently $f(C_{kk}) = 1$. The approximate similarity variable η and function $G(\eta, x)$ are the same as for the general solution, but the unknown function $K(\eta, x)$, needed to determine the conformation tensor, components is now defined as

$$K(\eta, x) = \Delta C. \tag{5- 20}$$

1) To obtain the so-called Delta$_{yy}$ solution, we substitute eq. (5- 3) into Eq. (3-19) to get

$$K = \frac{C_7 C_8 + (f(L) - 1)}{C_7 C_8 - 1}, \tag{5- 21}$$

where

$$C_7 = \frac{2\lambda U D^{\frac{1}{3}} x^{-\frac{4}{3}}}{9} = \frac{2Wi_x}{9}\left(\frac{D}{x}\right)^{\frac{1}{3}}, \tag{5- 22}$$

$$C_8 = G' + 2\eta G''.$$

Using Eq. (5- 19) into Eq. (3-12) leads to the following form of the momentum equation

$$\frac{\partial \psi}{\partial y}\left(\frac{\partial^2 \psi}{\partial x \partial y}\right) - \left(\frac{\partial \psi}{\partial x}\right)\left(\frac{\partial^2 \psi}{\partial y^2}\right) = (v_s + v_p(1 - \Delta C))\frac{\partial^3 \psi}{\partial y^3} - v_p \frac{\partial \Delta C}{\partial y}\frac{\partial^2 \psi}{\partial y^2}. \tag{5- 23}$$

which, after manipulation, becomes

$$-\left(G'^2 + GG''\right) = \left(1 - \beta_p K\right)G''' - \beta_p(K'G''). \tag{5- 24}$$

This equation needs the following derivative of *K*, determined from Eq. (5- 21)

$$K' = \frac{\left(C_7(3G'' + 2\eta G''')\right)(1 - K)}{(C_7 C_8 - 1)}. \tag{5- 25}$$

Back-substitution gives the final momentum equation that needs to be numerically solved

$$G''' = \frac{-\left(G'^2 + GG''\right) + \beta_p \frac{3C_7 G''^2 (1 - K)}{(C_7 C_8 - 1)}}{\left(\left(1 - \beta_p K\right) - \beta_p \frac{2\eta C_7 G''(1 - K)}{(C_7 C_8 - 1)}\right)}. \tag{5- 26}$$

2) To obtain the other solution, called Delta$_{xx}$, we substitute Eq. (5- 3) into Eq. (3-18) to get

$$K = \frac{(f(L) - 1) - C_9 C_{11} + C_{10} G''^2}{C_{12}}, \tag{5- 27}$$

where

$$C_9 = \frac{2\lambda U D^{\frac{1}{3}} x^{-\frac{4}{3}}}{9} = \frac{2Wi_x}{9}\left(\frac{D}{x}\right)^{\frac{1}{3}}, \tag{5- 28}$$

$$C_{10} = \frac{2\lambda^2 U^3 D}{81\upsilon_0} x^{-2} = \frac{2{Wi_x}^2 Re}{81},$$

$$C_{11} = G' + 2\eta G'',$$

$$C_{12} = \left(C_9 C_{11} + C_{10} {G''}^2 + 1\right).$$

The momentum equations (5- 23) and (5- 24) remain the same, but the derivative of *K* is now given by

$$K' = -\frac{3C_9 G''(K+1) + \left(2\eta C_9 (K+1) + 2C_{10} G''(K-1)\right) G'''}{C_{12}} \tag{5- 29}$$

so that the final momentum equation that needs to be numerically solved is

$$G''' = -\frac{\left({G'}^2 + GG''\right) + \beta_p \frac{3C_9 {G''}^2 (K+1)}{C_{12}}}{\left(\left(1-\beta_p K\right) + 2\beta_p G'' \frac{\eta C_9 (K+1) + C_{10} G''(K-1)}{C_{12}}\right)}. \tag{5- 30}$$

The general solution is more accurate than either of the Delta solutions, but on the low elasticity limit they are essentially equivalent. However, as elasticity increases there is a progressive deviation away from the general solution, which is faster for the Delta_{xx} solution than for the Delta_{yy} solution. This is so on account of the links between the various equations. The momentum equation involves the gradient of the polymer shear stress (so of C_{xy}), which Eq. (3-21) shows to depend more on C_{yy} than on C_{xx}. Since the Delta_{yy} solution uses Eq. (3-19) to describe C_{yy} and to obtain ΔC, the description of C_{xy} is more accurate in the Delta_{yy} solution than in the Delta_{xx} solution.

5.2.3. Olagunju's type solution

Olagunju's type solution for the planar jet relies on further assumptions, as invoked by Olagunju [19,20] for the boundary layer flow of FENE-P fluids. In particular, it neglects terms that our order of magnitude analysis hinted to be relevant, that will affect the conformation tensor components

and consequently the polymer stress components, but have negligible effect on the velocity field, as shown in the Results Section. Instead of using the conformation tensor Eqs. (3-18) to (3-21) of the general solution, the conformation tensor equations, simplified following Olagunju's hypothesis, are Eq. (3-39) to (3-42). The comparison between both sets shows that here some terms are missing in the equations for C_{xx}, C_{yy} and C_{xy}. The conformation tensor equations for steady planar jet flow of FENE-P fluids, invoking Olagunju [19,20] assumptions, are Eqs. (3-39) to (3-42), leading to

$$C_{\mathrm{xx}} = \frac{2\lambda C_{xy}\left(\frac{\partial^2\psi}{\partial y^2}\right) + f(L)}{f(C_{kk})} = \frac{2\lambda^2\left(\frac{\partial^2\psi}{\partial y^2}\right)^2 + f(C_{kk})^2}{f(C_{kk})^3}, \tag{5- 31}$$

$$C_{\mathrm{yy}} = C_{\mathrm{zz}} = \frac{f(L)}{f(C_{kk})}\ , \tag{5- 32}$$

$$C_{\mathrm{xy}} = \frac{\lambda C_{\mathrm{yy}}\frac{\partial u}{\partial y}}{f(C_{kk})} = \frac{\lambda f(L)\frac{\partial^2\psi}{\partial y^2}}{f(C_{kk})^2}\ . \tag{5- 33}$$

The trace of the conformation tensor takes the form

$$C_{kk} = f(L)\frac{2\lambda^2\left(\frac{\partial^2\psi}{\partial y^2}\right)^2 + 3f(C_{kk})^2}{f(C_{kk})^3}\ , \tag{5- 34}$$

and back-substituting into Eq. (2- 10c) provides $f(C_{kk})$. The approximate similarity variables are in Eq. (5- 3) and function $K(\eta, x)$ is now defined as

$$K(\eta, x) = \frac{1}{f(C_{kk})}. \tag{5- 35}$$

After back-substitution the following algebraic cubic equation is obtained for $K(\eta, x)$

$$C_{13}G''^2K^3 + C_{14}K + L^2 = 0\ . \tag{5- 36}$$

with

$$C_{13} = \frac{-2\lambda^2 f(L)U^3D}{81\upsilon_0 x^2} = \frac{-2f(L)Wi_x{}^2Re}{81}, \tag{5- 37}$$

$$C_{14} = (-3f(L) - L^2 + 3).$$

This is again an approxiamte similarity solution. The momentum equation is obtained by substituting C_{xy} (from Eq. (5- 33)) into Eq. (3-12)

$$\frac{\partial\psi}{\partial y}\left(\frac{\partial^2\psi}{\partial x\partial y}\right)-\left(\frac{\partial\psi}{\partial x}\right)\left(\frac{\partial^2\psi}{\partial y^2}\right) \tag{5- 38}$$
$$= \upsilon_s\frac{\partial^3\psi}{\partial y^3}+\upsilon_p f(L)\left(\frac{\partial^3\psi}{\partial y^3}f(C_{kk})+\frac{\partial f(C_{kk})}{\partial y}\frac{\partial^2\psi}{\partial y^2}\right).$$

Substituting the approximate similarity variables (Eq. (5- 3) and (5- 35)) into Eq. (5- 38) and manipulating algebraically, leads to

$$-\left(G'^2+GG''\right)=\left(G'''-\beta_p G'''+\beta_p f(L)G'''K+\beta_p f(L)K'G''\right). \tag{5- 39}$$

$K'=dK/d\eta$ is obtained from the derivative of (5- 36), as

$$K'=-\frac{2C_{13}G''G'''K^3}{3C_{13}K^2G''^2+C_{14}}. \tag{5- 40}$$

Upon back-substitution of K' the final form of the momentum equation that needs to be solved numerically is

$$G'''=\frac{-\left(G'^2+GG''\right)}{1-\beta_p+\beta_p f(L)K-\beta_p f(L)\dfrac{2C_{13}G''^2K^3}{C_{14}+3C_{13}K^2G''^2}}. \tag{5- 41}$$

5.3. Numerical solution of the governing equations

The three sets of simplified governing equations presented at the Section 5.2. provide three different solutions that can only be solved numerically and the method is described in section 3.4. It is worth mentioning that the boundary condition of jet flow is different from boundary layer and mixing layer flow. The boundary conditions for laminar planar jet flow needed to solve the system of differential equations are:

$$G'(\mp\infty)\to 0\ , G(0)=G''(0)=0 \quad \text{(symmetry)} \tag{5- 42}$$

5.4. Results and discussion

5.4.1. Verification: Newtonian fluids

The governing equations for the FENE-P fluid reduce to those of a Newtonian planar jet if $\beta_p = 0$ and this is used to verify the solution [23,24], where a Reynolds number *Re* =100 is considered. Figure 5. 2 compares the current Newtonian solution for G'', G' and G with the literature and shows the excellent agreement. These quantities are related to the velocity profiles *u* and *v* according to Eqs. (5- 4) and (5- 5).

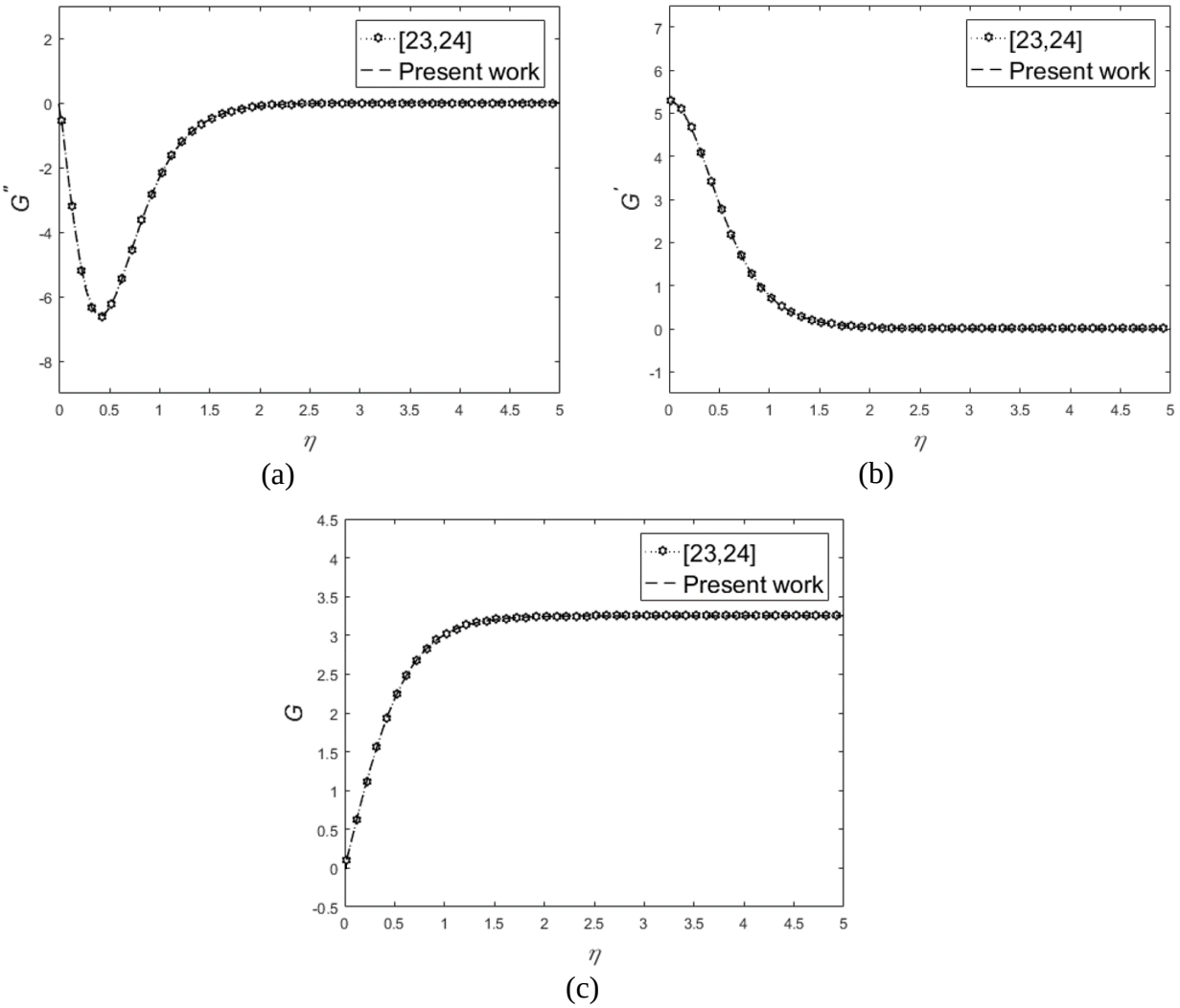

Figure 5. 2. The variation of a) G", b) G', c) G with η in the self-similar region for a Newtonian steady planar jet flow at *Re*= 100.

5.4.2.FENE-P fluids

Since the FENE-P solution is not fully self-similar, a universal set of profiles is not obtained as for the Newtonian solution, rather a mixture of variables is required for a full description of the flow characteristics, and in particular for the polymer conformation and stress. Therefore, for easier understanding, all results are presented using the natural coordinates/variables and here we chose *D* as the reference length scale to normalize coordinates, even though this solution is sufficiently far from the inlet for the flow characteristics to be independent of *D*.

5.4.2.1.Comparison of solutions

We start by comparing the results of the three proposed self-similar solutions for the FENE-P jet; note that the delta approximation allows for two possible slightly different solutions presented in Section 5.2.2. Profiles of the velocity and conformation tensor components are compared in Figure 5. 3 to Figure 5. 5 for *Wi*=0.1 and 1, *L*=30, *Re*=100 and $\beta_p = 0.1$. The various methods give essentially the same result as far as the dimensionless velocity profiles are concerned, as shown in Figure 5. 3, with a very slight under-prediction of u/u_c at $y/D \geq 4$ for the Delta_{xx} solution that is also compensated by the corresponding v/u_c profile through mass conservation (u_c is the centerline velocity of the jet). A similar behavior is observed for the shear component of the conformation tensor (C_{xy}) in Figure 5. 4 (a) and Figure 5. 5 (a) for flows with $Wi \leq 1$, where the Delta_{xx} profile deviates very slightly again from the others (note the scaling used). Small differences appear as *Wi* becomes larger, but we do not show further data for conciseness.

However, differences are more obvious for the normal components of the conformation tensor, even if they are small and observed only through zooming-in, as in Figure 5. 4 and Figure 5. 5 (b)-(d). These plots show that Olagunju's method is unable to capture the transverse variations of C_{yy}, but it does capture the shape of the profile of C_{xx}, except at low Weissenberg numbers (for *Wi*=0.01, not shown, the difference in C_{xx} between Olagunju's method and the general method is larger than for *Wi*=0.1). In any case, the values of the normal components of the conformation tensor are close enough to 1 to make little difference on $f(C_{kk})$, hence the correct prediction of C_{xy}, and of corresponding shear stress (not shown here) and finally of the streamwise velocity profile.

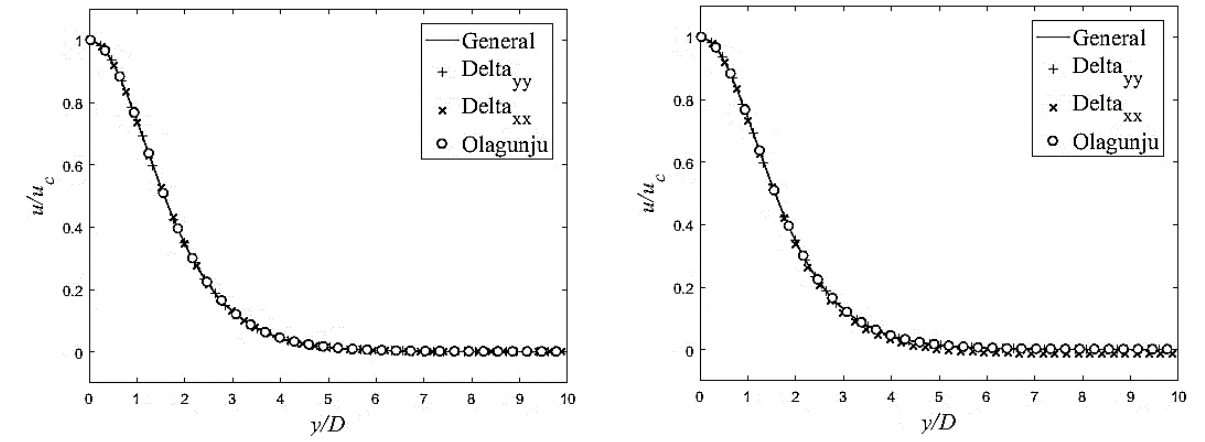

(a)

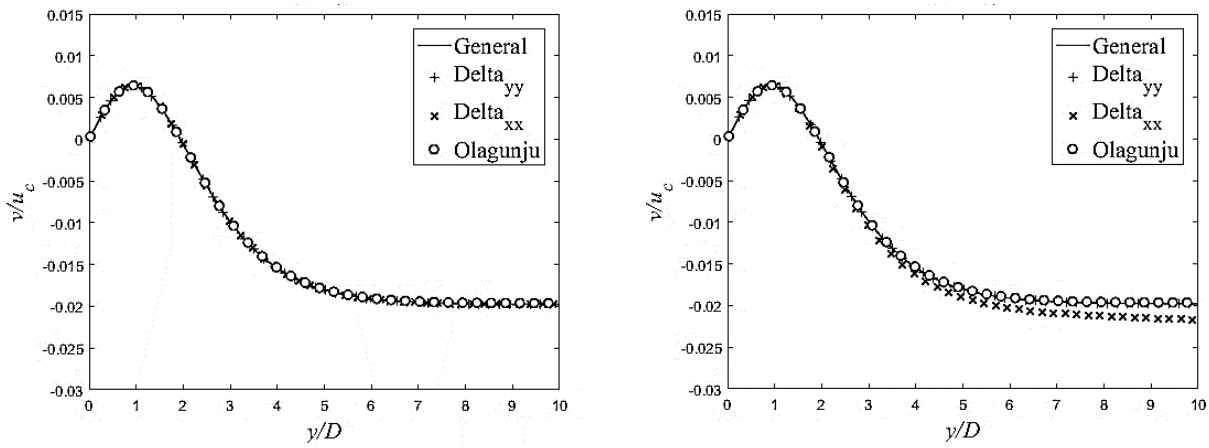

(b)

Figure 5. 3. Comparison between different solutions for the transverse profiles of normalized streamwise (u/u_c) velocity (a) and transverse (v/u_c) velocity (b) at $\frac{x}{D} = 30$. Left column is for Wi=0.1, right column for Wi=1.0.

In contrast, both delta solutions capture well all components of the conformation tensor provided the Weissenberg number remains very low and, as expected, their predictions deteriorate as Wi increases as was already observed at Wi=0.1. The two alternatives are not equivalent though, with the Delta$_{yy}$ variant performing better than the Delta$_{xx}$ variant. The prediction of the shear component (C_{xy}) remains reasonable even for the higher values of Wi, hence the good prediction of the velocity profiles at these Wi.

In conclusion, the general solution is the most appropriate for predicting accurately the velocity and stress profiles since it does not introduce excessive simplifications and in particular it is

capable to compute well all components of the conformation tensor over a wide range of *Wi* number. Therefore, it is used below to investigate in more detail the effects of rheology on flow characteristics and to obtain variation laws for the decay of the centerline velocity and for the jet spreading rate measured by its half-width, as well as to assess possible variation laws for the conformation tensor components.

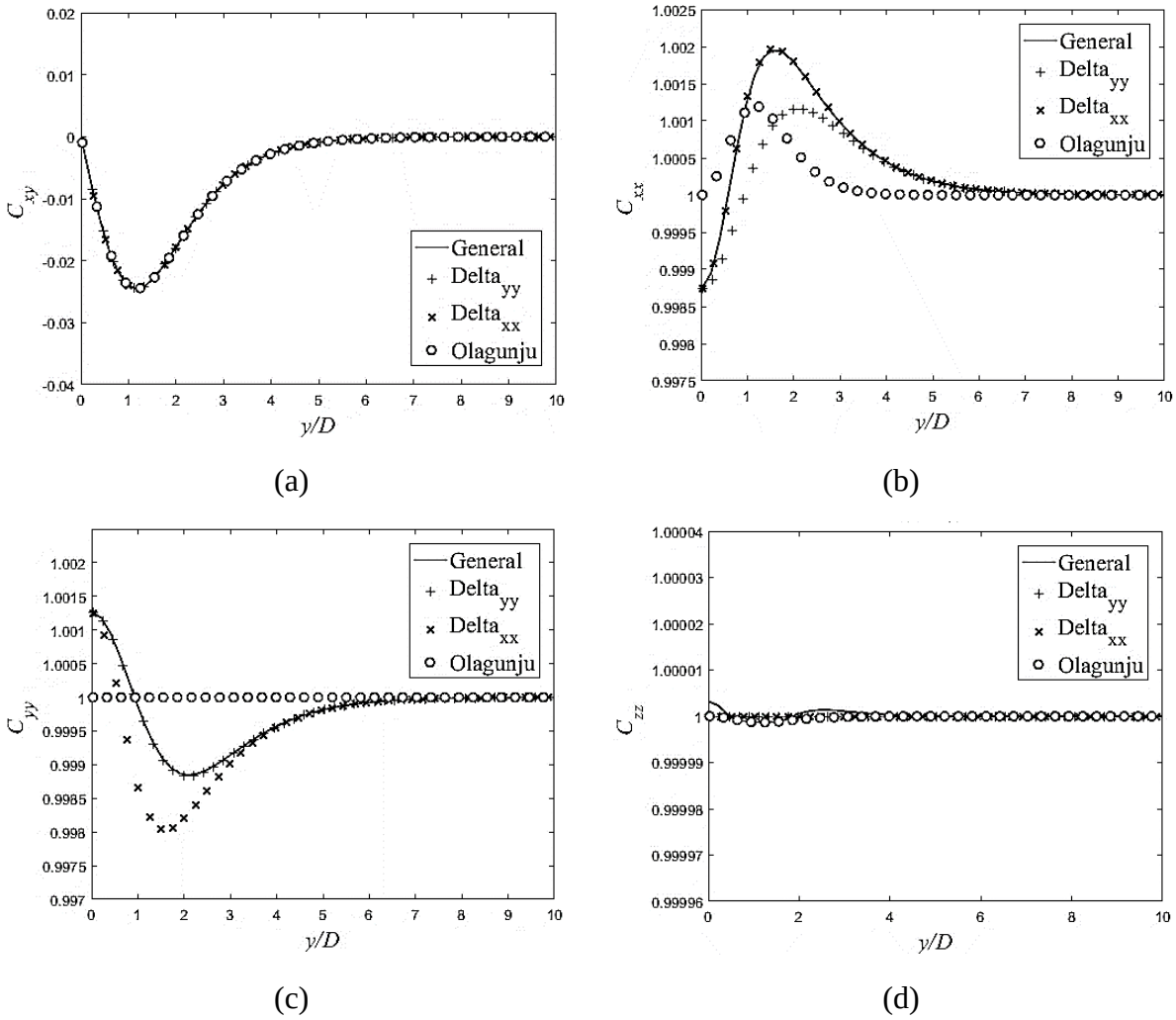

Figure 5. 4. Comparison between different solutions of the transverse profiles C_{xy} (a), C_{xx} (b), C_{yy} (c) and C_{zz} (d) at $\frac{x}{D} = 30$ (*Wi*=0.1)

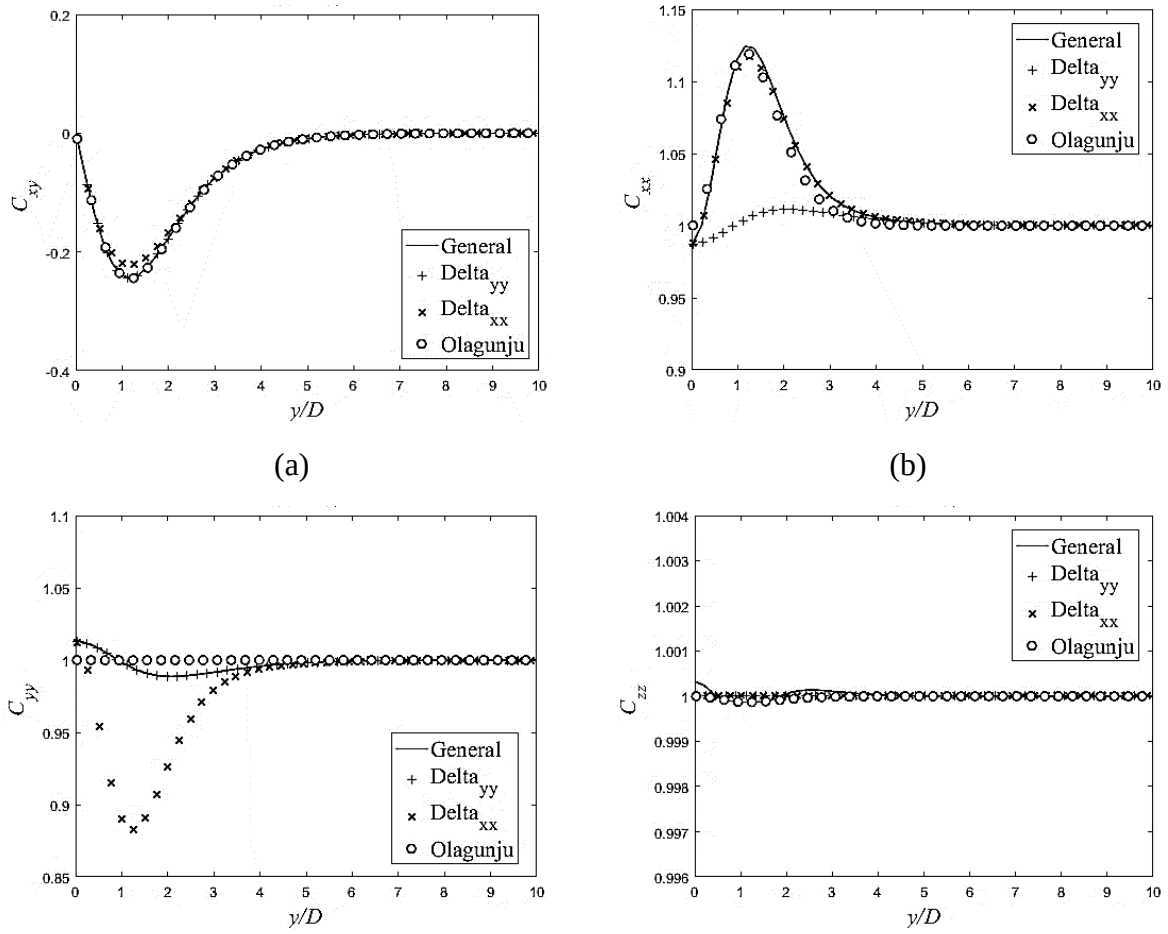

Figure 5. 5. Comparison between different solutions of the transverse profiles of C_{xy} (a), C_{xx} (b), C_{yy} (c) and C_{zz} (d) in the self-similar region at $\frac{x}{D} = 30$ for *Wi*=1.0.

5.4.2.2.Decay law for the centerline velocity and jet spreading rate

Important laws for the planar jet are the relationships expressing the decay of the centerline velocity and the growth of the jet half-width. From the analytical solution, the normalized centerline velocity (u_c/U) is given by

$$\frac{u_c}{U} = \frac{1}{3}\left(\frac{x}{D}\right)^{-\frac{1}{3}} G'(0,x). \qquad (5\text{- }43)$$

The decay of the centerline velocity is plotted in Figure 5. 6 (a) for a wide range of conditions (different values of L^2, β_p, *Re* and *Wi*) and an excellent collapse of data is observed, suggesting

that there is only dependence on *Re*, which is captured through an adequate normalization. However, this is not exactly true and there is a very weak dependence on fluid rheology that cannot be observed in Figure 5. 6. The velocity profiles, which are proportional to $G'(\eta, x)$, exhibit a local maximum at the centreline ($\eta = 0$) implying $G''(0, x) = 0$, in addition $f(L) = 1$ and $K(0, x) \simeq 1$, therefore on the centreline Eq. (5- 14) simplifies to

$$G''' = \frac{G'^2 + GG''}{1 - \beta + \frac{\beta f(L)}{K - C_4 G'}} \tag{5- 44}$$

Inspection of the numerical data for the cases reported in Figure 6 shows that on the centreline the denominator of Eq. (5- 44) differs from 1 by less than 0.01% and for practical purposes Eq. (5- 14) becomes identical to that for the centerline velocity of a Newtonian planar jet flow. Disregarding this very weak dependence, in Figure 5. 6 (b) the data is plotted differently to show the power law dependence on (x/D) with a power law exponent of $-1/3$ and slope of 0.3797. For practical purposes, this decay law can be considered to be universal and independent of flow and rheological properties.

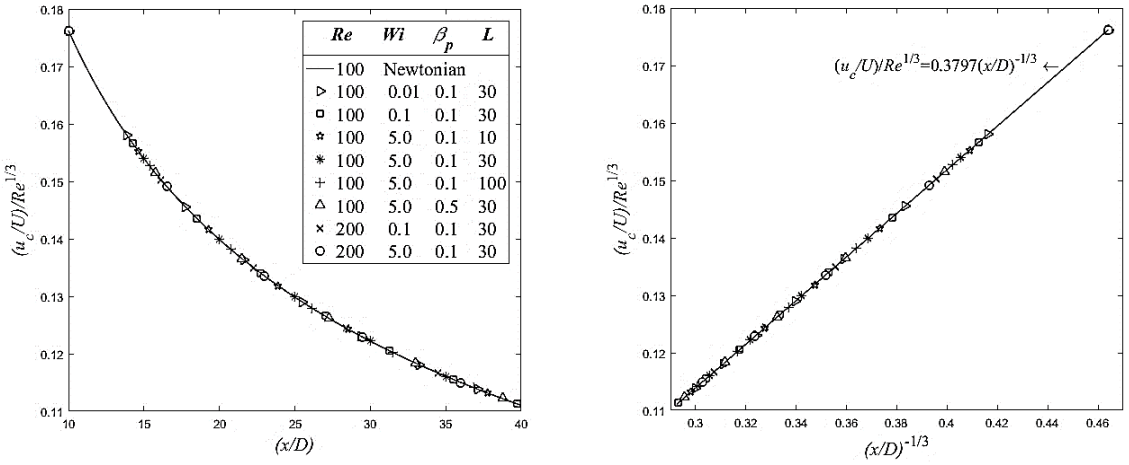

(a) (b)

Figure 5. 6. Evolution of the jet centerline velocity for planar laminar jet flow: (a) decay with *x/D*; (b) variation with $(x/D)^{(-1/3)}$ for the same cases in (a). The solid line simultaneously pertains to the Newtonian data and the fitted linear equation with slope of 0.3797.

In Figure 5. 6 (b) the data is plotted differently to show the power law dependence on (x/D) with a power law exponent of $-1/3$ and slope of 0.3797. This decay law is universal and independent of flow and rheological properties.

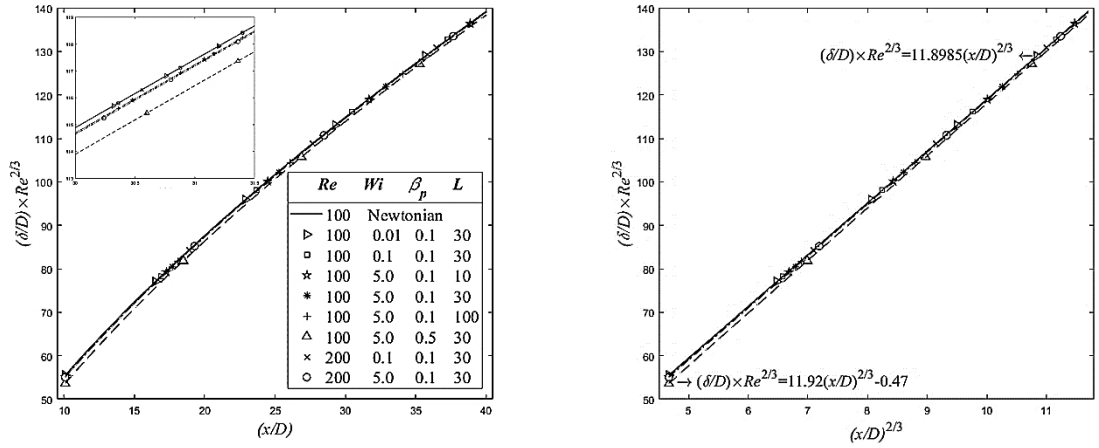

(a) (b)

Figure 5. 7. Evolution of the jet half-width (δ) for planar laminar jet flow: (a) variation with *x/D*; (b) variation with $(x/D)^{2/3}$ for the same cases in (a). In (b) the solid line simultaneously pertains to the Newtonian data and the corresponding fitted linear equation. Dashed lines are also fitted linear equations to some cases and a guide to the eye.

The jet spreading rate, measured by the jet half-width (δ), as defined in Figure 5. 1, increases with the streamwise coordinate (x), as the jet entrains surrounding fluid. According to Eqs. (5- 4) and (5- 5) this leads to

$$\frac{\delta}{D} = \frac{y_{0.01}}{D} \equiv 3\sqrt{\frac{\nu_0}{DU}}\left(\frac{x}{D}\right)^{2/3}\eta_{0.01} \quad \text{where} \quad G'(\eta_{0.01}, x) = 0.01G'(0, x). \tag{5- 45}$$

As shown in Figure 5. 7 (a) and (b), for flows with low elasticity, i.e. flows at low *Wi*, low β_p and high *L*, the spreading rates of Newtonian and FENE-P jets are essentially the same, exhibiting a similar dependence on *Re* (proportional to $Re^{-2/3}$) and on x/D (proportional to $(x/D)^{2/3}$) as is clear from Figure 5. 7 (b), where the linear fit shows a slope of 11.9. Further inspection of Figure 5. 7 (b) shows that on increasing elasticity effects, i.e., increasing *Wi* or β_p or decreasing *L*, there is a reduction in the spreading rate together with an enhancement of the rate of variation of the spreading rate (the slope of the fitted linear law for the flow at *Wi*=5, *Re*=100, *L*= 10 is now 12.74). These are most likely associated with a reduction of the viscosity in the jet shear layers, where

entrainment occurs, on account of the prevailing shear rates there pertaining to the shear-thinning region of the FENE-P fluid, when increasing *Wi*. However, on going downstream the effects of *Wi* reduce because the local flow shear rates decrease as the jet spreads, therefore the local viscosity increases towards the low shear rate Newtonian plateau value while simultaneously the viscoelastic normal stresses decrease, i.e., in the far field the FENE-P flow tends to a Newtonian fluid behavior.

To better understand these arguments it is useful to define the local Reynolds number ($Re_\delta \equiv u_c\delta/\upsilon_0$) and the local Weissenberg number ($Wi_\delta \equiv \lambda u_c/\delta$), given by Eqs. (5- 46) and (5- 47), respectively. These expressions clearly show that Reynolds number effects increase downstream, whereas Weissenberg number effects decrease. The latter predominate and this is well shown through the so-called viscoelastic Mach numbers.

$$Re_\delta \equiv \frac{u_c\delta}{\upsilon_0} = \sqrt{Re}\eta_{0.01}G'(0,x)\left(\frac{x}{D}\right)^{1/3} \tag{5- 46}$$

$$Wi_\delta \equiv \frac{\lambda u_c}{\delta} = \frac{1}{9}Wi\sqrt{Re}\frac{G'(0,x)}{\eta_{0.01}}\left(\frac{x}{D}\right)^{-1} \tag{5- 47}$$

The mean flow viscoelastic Mach number (M) is defined as ($M \equiv \sqrt{ReWi}$), but we are interested in the local viscoelastic Mach number ($M_\delta \equiv \sqrt{Re_\delta Wi_\delta}$) given by

$$M_\delta = \frac{1}{3}\sqrt{ReWi}G'(0,x)\left(\frac{x}{D}\right)^{-1/3} \longrightarrow \frac{M_\delta}{MRe^{1/3}} = 0.3797\left(\frac{x}{D}\right)^{-1/3}, \tag{5- 48}$$

where use was made of the universal fitted decay law of the centerline velocity. It is clear that viscoelastic effects are stronger at low *x/D*, and decay on going downstream. In this regard it is also important to note that Figure 5. 6 and Figure 5. 7 contain results for flows with $M_\delta > 1$ and $M_\delta < 1$ and that $M_\delta \to 0$ data approach the low elasticity limit, in which the jet tends to behave as Newtonian.

5.4.2.3.Velocity field

In contrast to the Newtonian jet flow, which accepts a full similarity solution expressed through the single relationship between the similarity variables η and $G(\eta)$, the FENE-P solution admits approximate similarity solution due to the rheological constitutive equation, i.e., no single profile

is obtained for different fluid and flow characteristics. Figure 5. 8 (a)-(b) show transverse profiles of streamwise and normal dimensionless velocities at various locations and rheological properties, for *Re*=100. The velocities are normalized by the centerline velocity and the transverse coordinate is normalized by the jet half-width.

Both parts of Figure 5. 8 show near collapse of all profiles for flows of "low" elasticity, with deviations from the Newtonian curve progressively increasing with elasticity. Elasticity effects are enhanced on going upstream (decreasing x/D), and more so when *Wi* or β_p are increased or *L* decreased with all other quantities kept constant. Hence, it comes as no surprise that the profiles most distant from the Newtonian curves simultaneously have the highest *Wi* combined with the highest β_p, and the lowest *L* and are the closest to the inlet of those plotted, i.e. *Wi*=5.0, $\beta_p = 0.5, L = 10$ and $x/D = 10$. The normal velocity component, plotted in Figure 5. 8 (b), is a more sensitive quantity, so these effects stand out more clearly. There is also a coupling effect of elasticity involving the Reynolds number as is clear from the expression for the local viscoelastic Mach number that depends on *Re*, i.e., elastic effects are enhanced if *Re* increases with all other quantities fixed. This will be more clearly shown when discussing the conformation tensor, in the next section.

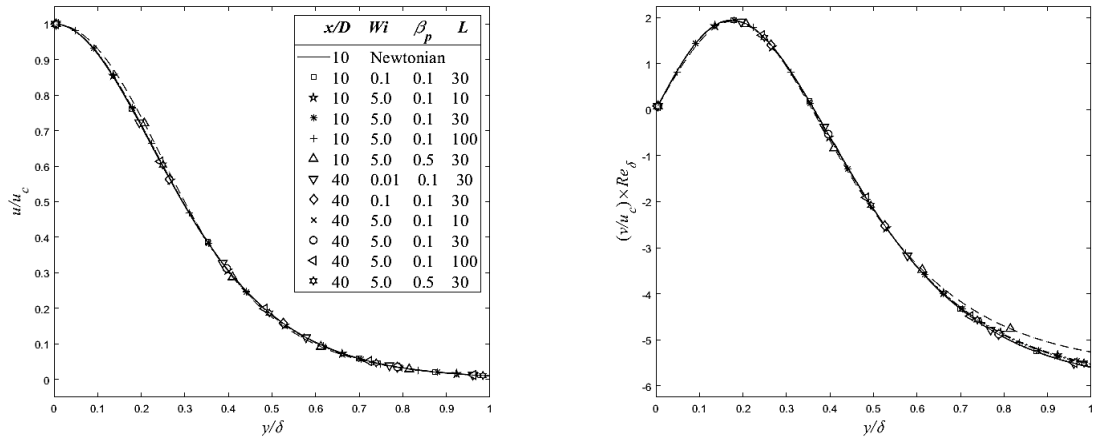

(a) (b)

Figure 5. 8. Transverse profiles of normalized velocity at *Re* =100 as a function of x/D, Wi, β_p and *L*: (a) u/u_c and (b) v/u_c. Dashed lines are a guide to the eye.

The streamwise velocity profile becomes fuller with elasticity, i.e., the region of higher u/u_c around the center plane is wider than for a lower elasticity jet and correspondingly the values of

v/u_c are lower in magnitude, meaning weaker entrainment, in agreement with the slower spreading rate and slower rates of decay already discussed.

It is also interesting to compare profiles at $x/D = 10$ and 40 for the most elastic cases, to see how quickly the impact of a decreasing local elasticity shifts the different fuller upstream profiles to a profile closer to the Newtonian profile, which coincides with the low elasticity limit behavior. Stronger viscoelastic effects could be shown by plotting profiles closer to the inlet, but we chose not to do so because lower values of x/D would be unrealistic from a practical point of view. After all, in a real jet the nearly uniform inlet profile will take some distance for the potential flow core to vanish through molecular diffusion.

In summary, even though the Newtonian profiles coincide with the low elasticity limit profile, the variation of the shape of the velocity profiles with any of Wi, β_p, L and x/D is not identical, since each of them impacts differently on fluid viscoelasticity.

5.4.2.4.Conformation and stress tensors

As the jet spreads on going downstream, the local flow deformation rates decrease and the polymer stresses decrease (as well as the Newtonian solvent stresses). Hence, prior to analyzing profiles of the conformation tensor, normalized by their peak values, we need to look at the decay laws for those peak values, which take place at jet shear layer.

Of course, as elasticity effects decrease, polymer stresses decrease to purely viscous, and the corresponding profiles of C_{ij} asymptote to uniform profiles equal to their limit values at rest, i.e., $C_{ij} \to 0$ when $i \neq j$ and $C_{ij} \to 1$ for $i=j$ (on going downstream the rates of deformation are also decreasing). Nevertheless, there is a general decay law for the streamwise variation of the ratio between the peak values and the corresponding reference peak value at a fixed x/D; we chose as reference $x/D = 10$. This is well shown in Figure 5. 9 and the decay laws are approximately of the form

$$\log_{10} \frac{|C_{ij}-\delta_{ij}|_{max}}{|C_{ij}-\delta_{ij}|_{max@x/D=10}} = m \log_{10} \left[\left(\frac{x}{D} \right)^{2/3} \right] + b. \qquad (5\text{- }49)$$

In Figure 5. 9 this low elasticity asymptotic behavior was obtained for jets having values of $M < 0.1$, in particular for M=0.0194 (Wi=3.76 × 10^{-6}), corresponding to values of $M_\delta = 0.01$ and 0.0156 at x/D of 40 and 10, respectively (the case plotted has values of M and M_δ one order of magnitude higher ($Wi \sim O(10^{-4})$)). For the C_{xy}, C_{yy} and C_{zz} components the low elasticity asymptote is reached even for flows of $M \approx 1$, but for C_{xx}, the most sensitive component, it is necessary to have M≈0.01.

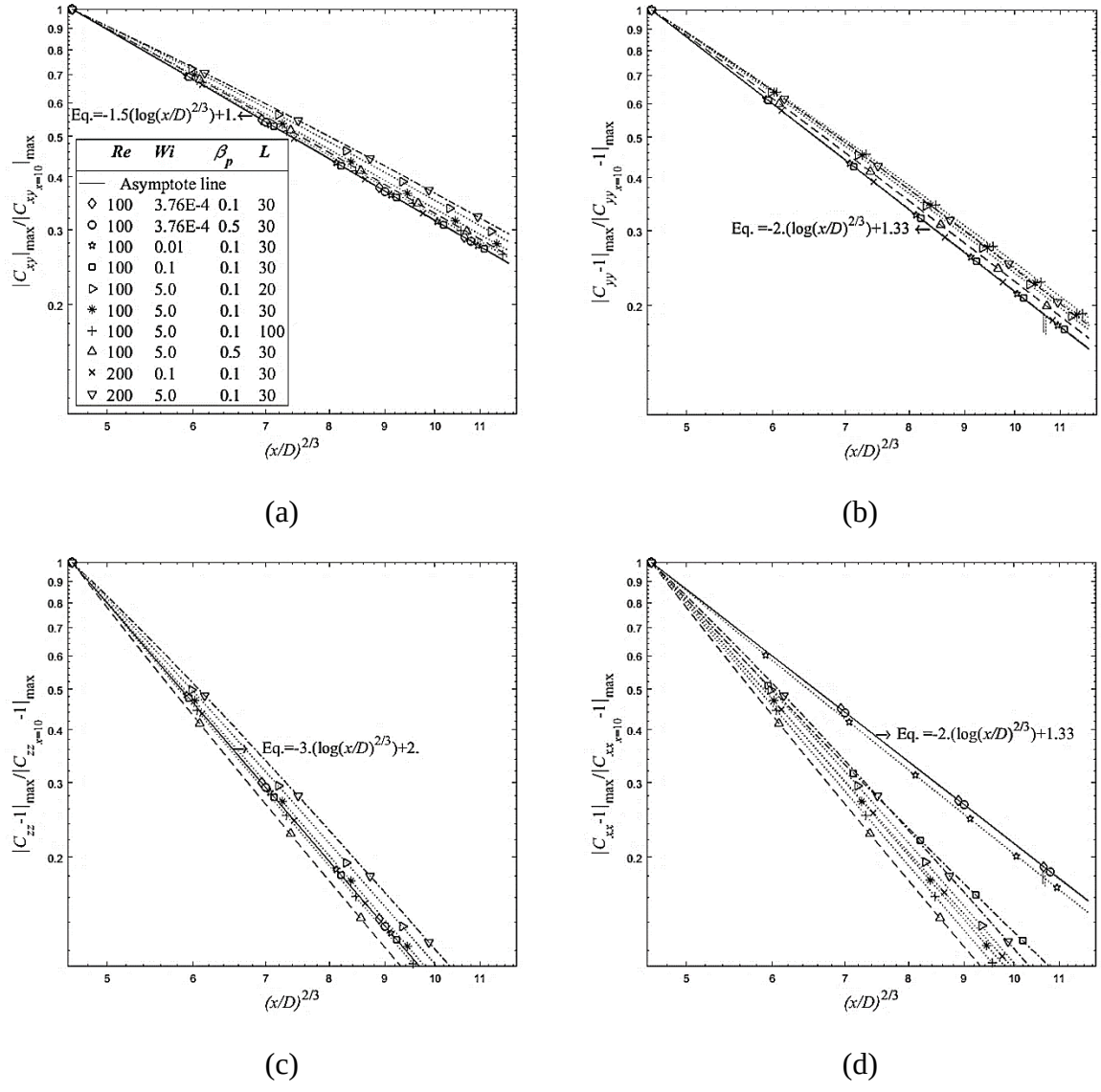

Figure 5. 9. Decay laws for the jet shear layer peak values of conformation tensor components (normalized by the corresponding peak values at $x/D = 10$): (a) $\frac{|C_{xy}|_{max}}{|C_{xy}|_{max@x/D=10}}$, (b) $\frac{|C_{yy}-1|_{max}}{|C_{yy}-1|_{max@x/D=10}}$, (c) $\frac{|C_{zz}-1|_{max}}{|C_{zz}-1|_{max@x/D=10}}$, (d) $\frac{|C_{xx}-1|_{max}}{|C_{xx}-1|_{max@x/D=10}}$.

C_{zz} is the component that approaches 1 the fastest, therefore its slope is the highest, as shown in Figure 5. 9 (c) (d). C_{zz} approached machine precision very quickly, hence we could not obtain reliable data for $Wi < 10^{-4}$. Note the identical asymptotes for C_{xx} and C_{yy}.

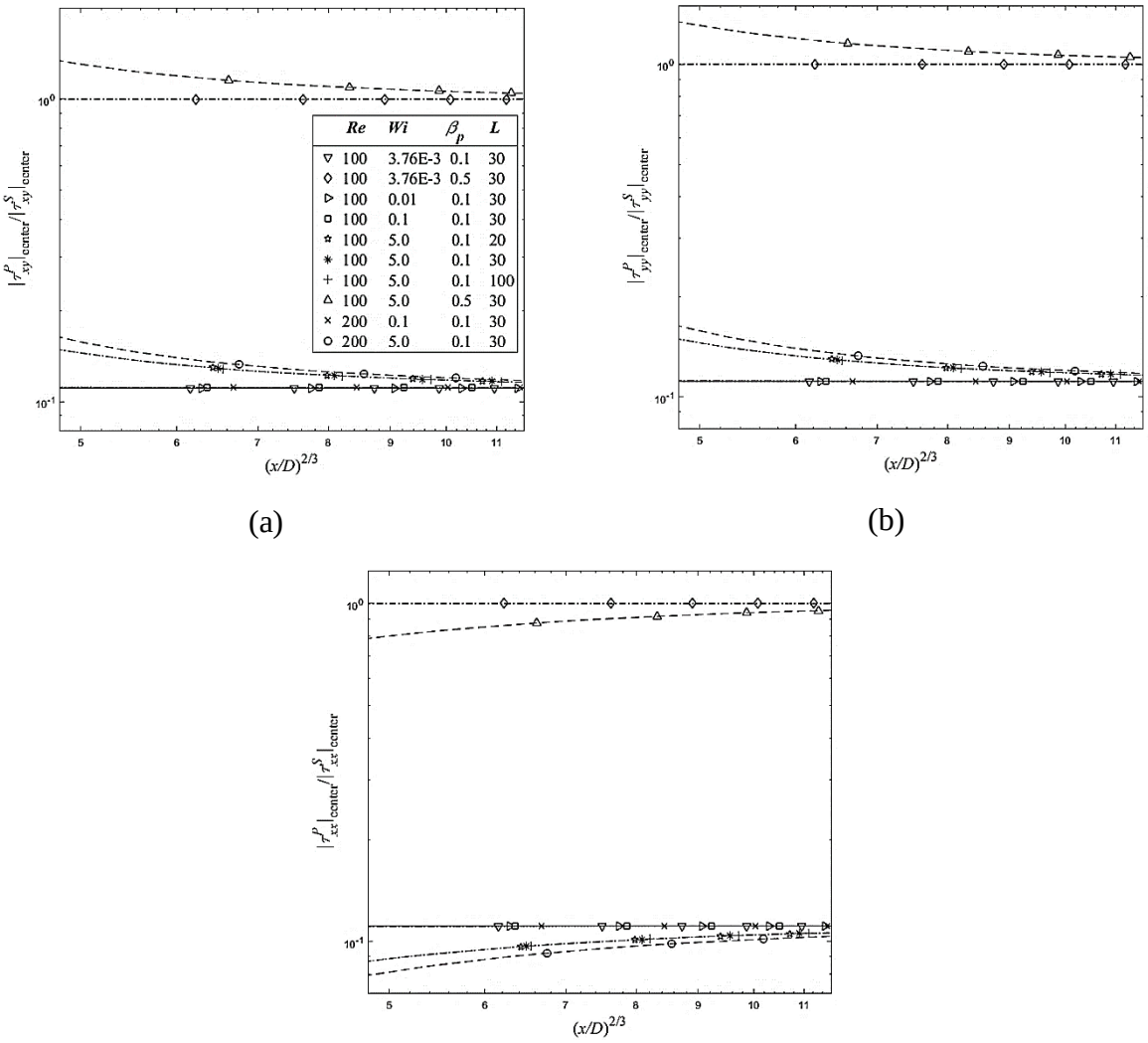

Figure 5. 10. Streamwise variation of the ratio of polymer stress (τ_{ij}^p) to solvent stress (τ_{ij}^s) at the centerline of jet: (a) *xy*; (b) *yy*; (c) xx.

The variation along the jet centerline of the ratio of polymer over solvent stresses $|\tau_{ij}^p|/|\tau_{ij}^s|$ is plotted in Figure 5. 10. At low elasticity and/or on going downstream, all components of this ratio asymptote to $\nu_p/\nu_s = \beta_p/(1-\beta_p)$, which is equal to 1/9 and 1 for β_p of 0.1 and 0.5, respectively.

This clearly confirms that the elastic part of the polymer stress decreases faster than its viscous stress, therefore far from the inlet the jet tends to a Newtonian behavior. This is also observed to happen with the ratio of maximum stresses plotted in Figure 5. 11, with the ratio $|\tau_{xx}^{p}|/|\tau_{xx}^{s}|$ taking longer than the other component ratio to approach the asymptote ν_p/ν_s when $Wi \geq 0.01$, because τ_{xx}^{p} is the stress component with the highest elastic contribution.

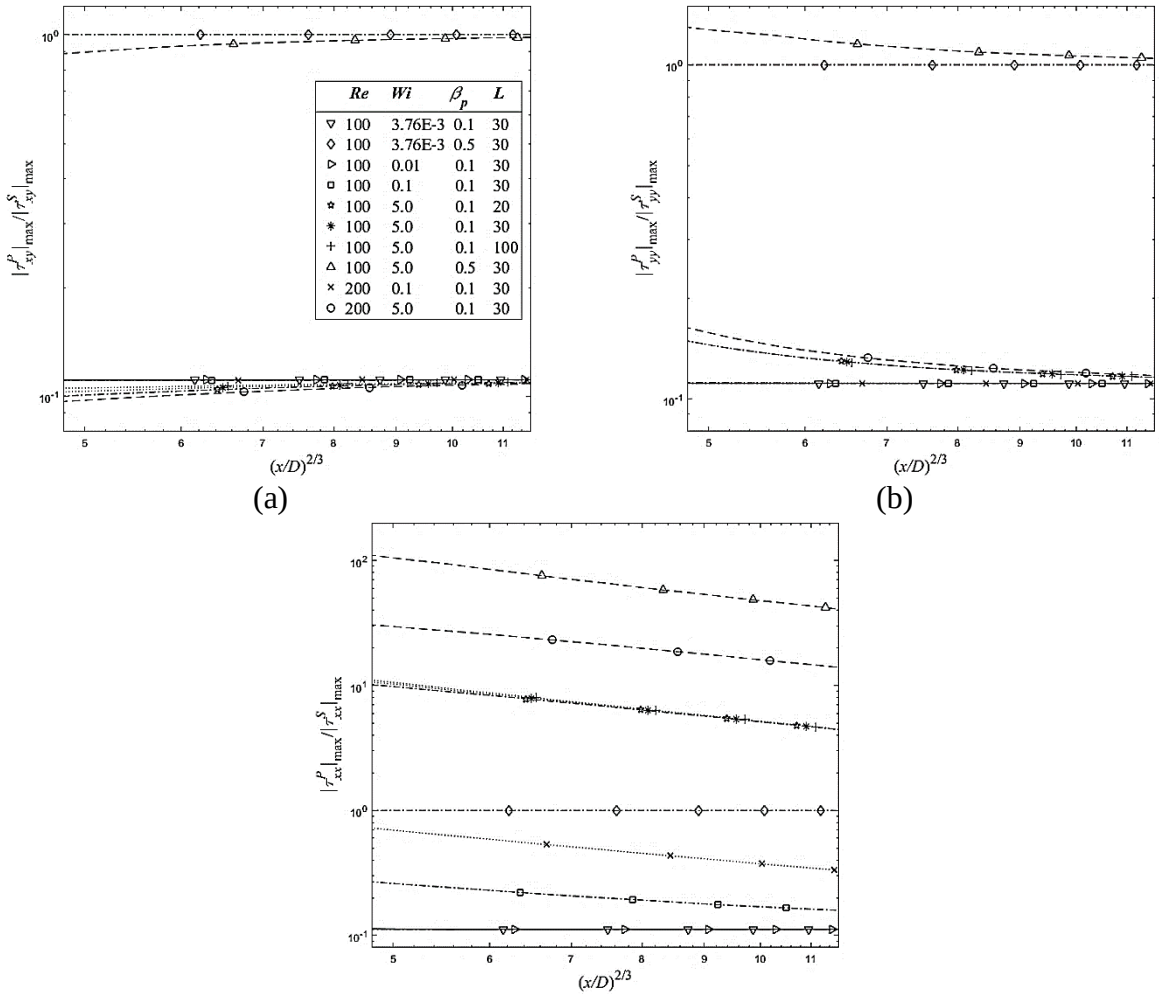

Figure 5. 11. Streamwise variation of the ratio of maximum polymer stress $\left|\tau_{ij}^{p}\right|_{max}$ to the maximum solvent stress $\left|\tau_{ij}^{s}\right|_{max}$: (a)$xy$; (b)$yy$; (c)$xx$.

Using the peak values of C_{ij} for normalization, the transverse profiles of the conformation tensor are plotted in Figure 5. 12, which show again a collapse of profiles in the limit of low elasticity (for C_{zz} in Figure 5. 12(c) the two curves at $Wi \sim \mathcal{O}(10^{-6})$ were not plotted because data approached machine precision), which is independent of position and of flow and fluid parameters, i.e., in the low elasticity limit there is an approximate universal similarity behavior. Indeed, this

collapse is independent of L, since the dumbbells are weakly extended ($C_{kk} << L^2$ as elasticity $\rightarrow$ 0), and also of β_p since in the low elasticity limit the polymer stress contribution is essentially viscous rather than elastic and *Re* was kept constant. For local values of $M_\delta \leq 0.1$, we cannot visually distinguish the curves even if their values of M_δ are not identical. In any case, the plots include two collapsed curves at $M_\delta = 0.01$, representative of low elasticity jets (cases with $Wi \sim \mathcal{O}(10^{-6})$).

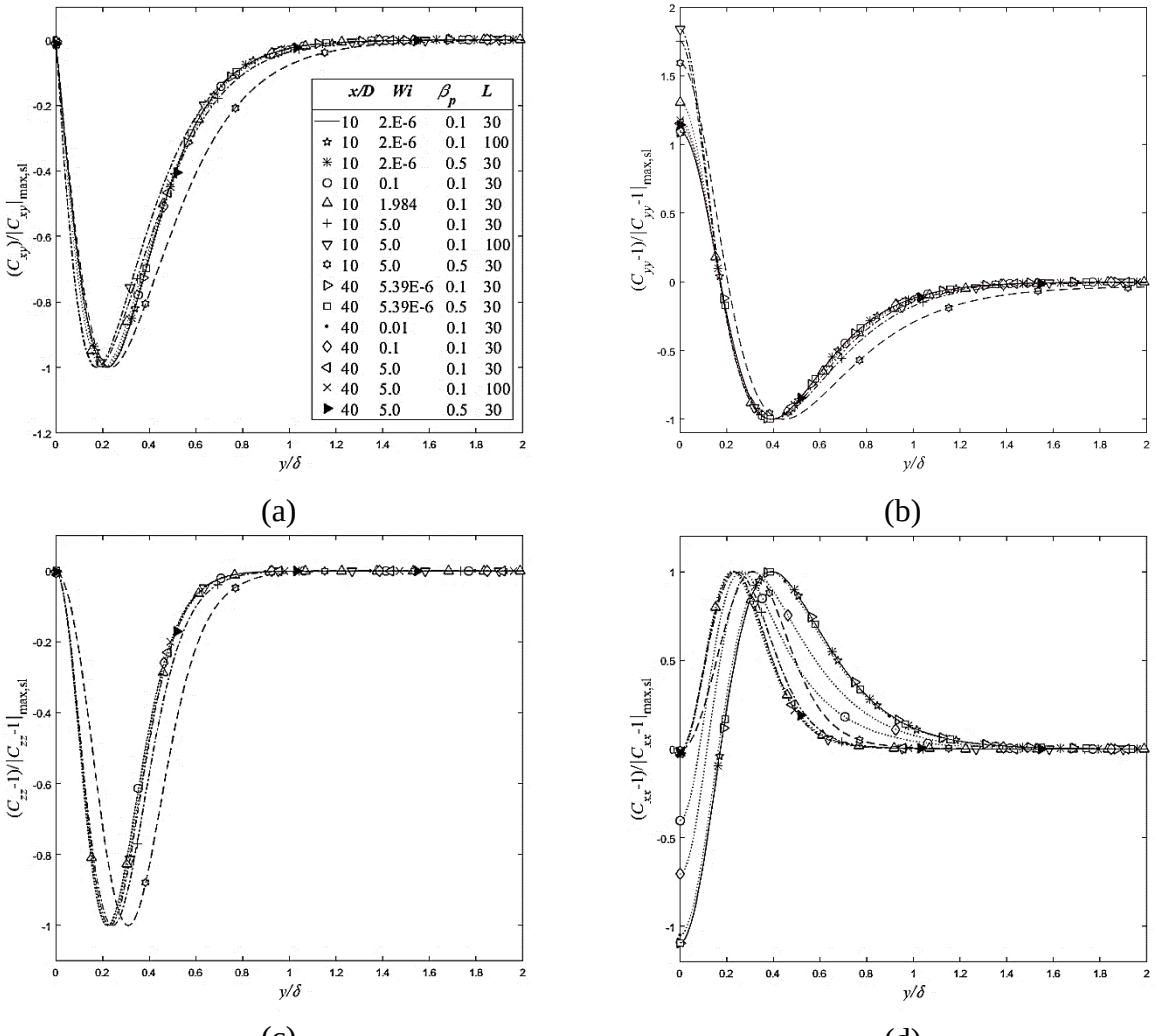

Figure 5. 12. Transverse profiles of the normalized conformation tensor components at *Re*=100: (a) $C_{xy}/|C_{xy}|_{max}$, (b) $(C_{yy}-1)/\left(|C_{yy}-1|_{max,sl}\right)$, (c) $(C_{zz}-1)/\left(|C_{zz}-1|_{max,sl}\right)$ and (d) $(C_{xx}-1)/\left(|C_{xx}-1|_{max,sl}\right)$. Subscript "*max,sl*" refers to local maximum value at the jet shear layer.

As elasticity increases beyond the low elasticity limit, through any of the conditions identified previously, there is a progressive deviation of the transverse profiles away from the low elasticity asymptote, with C_{yy} and C_{zz} peaks shifting away from the centreline, C_{xx} peak moving towards the centreline and C_{xy} peak exhibiting a mixed behavior, but with very little variation. The sense of variation and its magnitude depend on the quantity that is varied. In all cases, as elasticity increases the approximate nature of similarity becomes clear, as expected. However, it is not essential to have profiles at the same location to see approximate similarity, what really matters is the value of the local viscoelastic Mach number, M_δ, provided the values of L and of β_p are identical. Indeed, the plots include two collapsed curves at $M_\delta = 11.52$ representative of strongly elastic jets, one at x/D=10 (Wi=1.984) and the other at x/D=40 (Wi=5, other quantities equal). This is seen for all components, but C_{xx} is particularly sensitive as the most elastic component. The profiles of C_{xx} in Figure 5. 12(d) show another interesting feature: when elasticity effects increase, there seems to be a high elasticity asymptote.

The location of the peak values of all components of the conformation tensor, plotted in Figure 5. 9, are plotted in Figure 5. 13. As for the peak values of C_{ij} at low elasticity, for which there were asymptotes, the position of these peaks follow straight lines in the coordinates used and there is a single line in the limit of low elasticity, which is of type

$$\frac{y}{D}Re^{2/3} = m\left(\frac{x}{D}\right)^{2/3}. \qquad (5\text{- }50)$$

Figure 5. 13 confirms what was said above in regards to the variation of the curves of C_{ij} (and its peak values) with elasticity, and regarding inertia, the dependence is identical to that of the jet half-width. In addition, the fitted low elasticity asymptotes are identical for C_{xx} and C_{yy}, which is consistent with the asymptotic behavior of the corresponding peak values discussed in Figure 5. 12, and confirms the righteousness of one of the assumptions inherent to the so-called Delta solutions. More surprising, since unexpected, is the identical low elasticity asymptote for C_{xy} and C_{zz} .

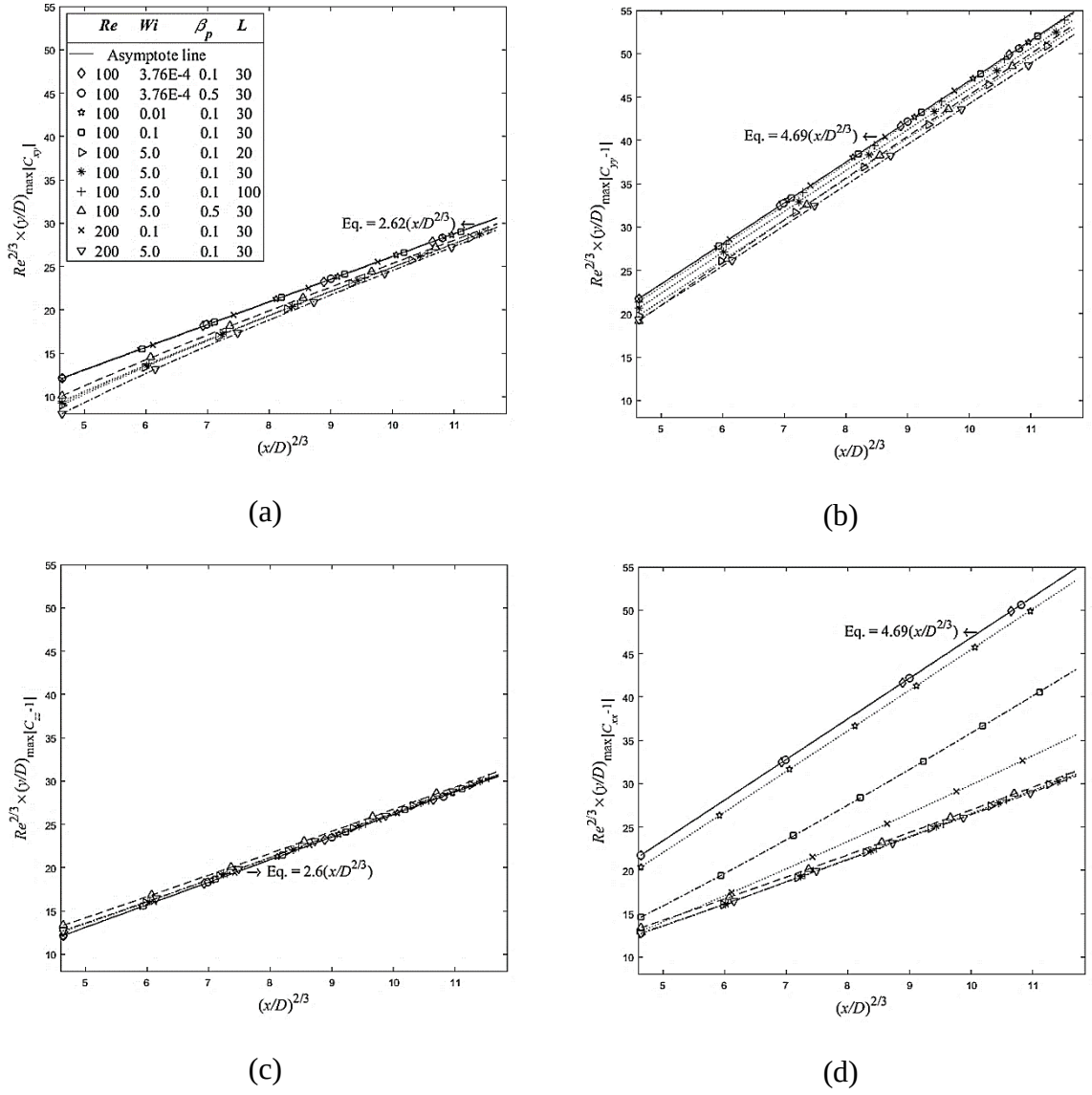

Figure 5. 13. Location of peak values of the conformation tensor components in the jet shear layer as a function of fluid and flow dimensionless numbers: (a)C_{xy}, (b) C_{yy}, (c) C_{zz} , (d) C_{xx}.

The observation made in Figure 5. 12 (d) of what seemed to be a high elasticity asymptotic profile for normalized C_{xx} is mirrored here in an asymptote for the location of its peak values at high levels of elasticity as shown in Figure 5. 13 (d). This effect is not seen for the other components of C_{ij}, therefore we did not fit an equation to this limit.

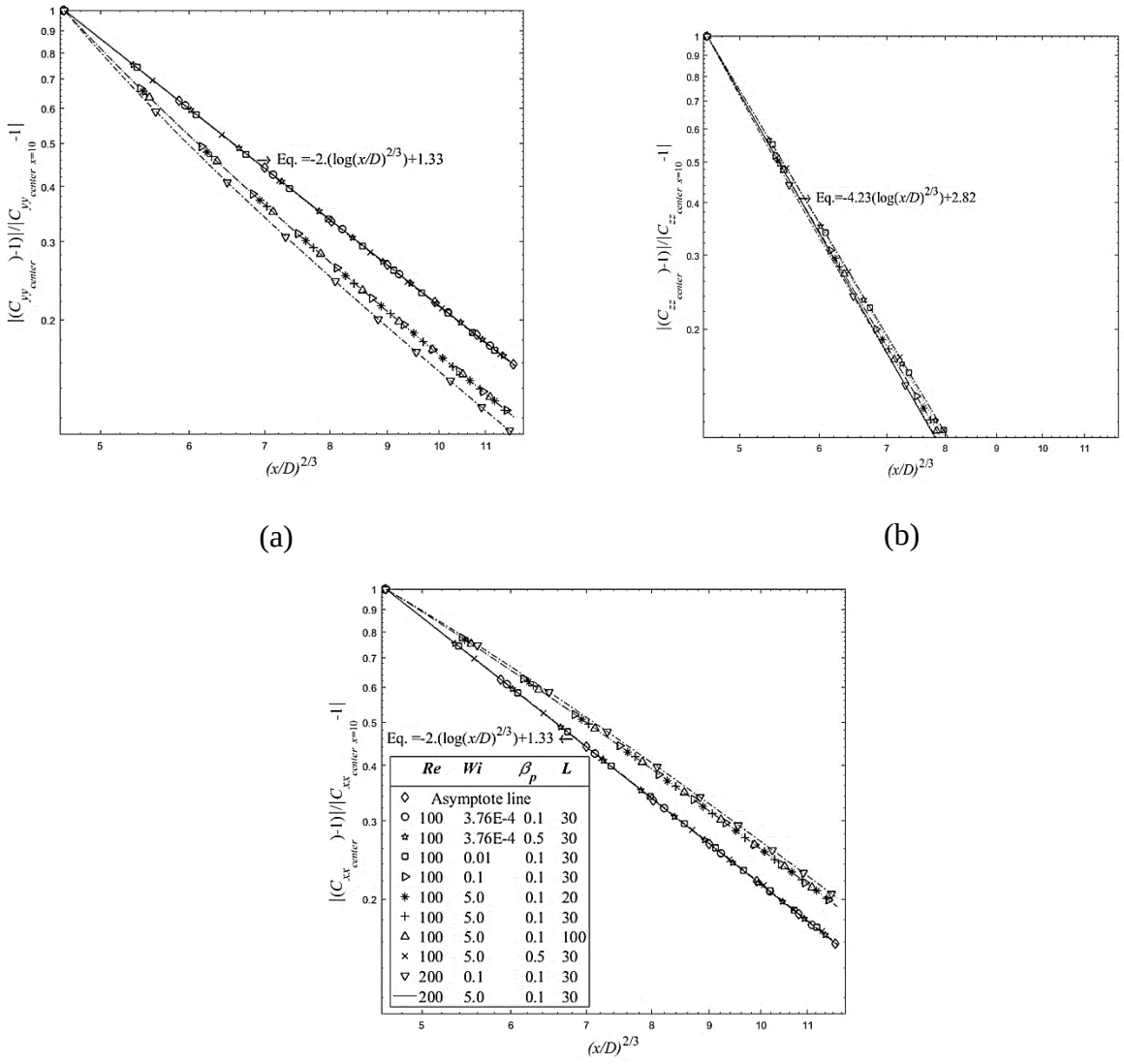

Figure 5. 14. Decay laws for the center plane values of the normal components of the conformation tensor (normalized by the corresponding values at $x/D = 10$): (a)C_{yy}, (b)C_{zz}, (c) C_{xx}.

The conformation tensor profiles in Figure 5. 12 have shown the existence of a second local peak value on the center plane, for the normal components of C_{ij}. These also decrease on going downstream, and exhibit also a low elasticity asymptote like Eq. (5- 50), which is identical to the asymptotes of the first peak value except for C_{zz}, as shown in the plots of Figure 5. 14. This different asymptote of C_{zz} could be a numerical artifact since the numerical values of this component decrease very quickly towards machine precision. The normalization in Figure 5. 14 is done with the corresponding center plane values at $x/D = 10$.

In practical terms it is useful to define a criterion separating the flow conditions above which flow elasticity cannot be ignored from those that correspond to essentially a Newtonian behavior. For this purpose, the most sensitive quantities to the effects of elasticity are the shear (C_{xy}) and normal (C_{xx}) components of the conformation tensor. If we fix a criterion of 1% difference relative to the low elasticity asymptote, to accommodate the simultaneous variations of Re and Wi, the 1% difference criterion corresponds to $M_\delta \leq 0.01$.

Part III

Turbulent Flow of Viscoelastic Fluid

[To] mechanical progress there is apparently no end: for as in the past so in the future, each step in any direction will remove limits and bring in past barriers which have till then blocked the way in other directions; and so what for the time may appear to be a visible or practical limit will turn out to be but a bend in the road.

-Osborne Reynolds

(23 August 1842 – 21 February 1912)

An English fluid dynamicist

Chapter 6: The numerical methods of DNS/LES and validation

6.1.Intorduction

Two final comparisons of the planar jet flow solution are worth doing as they represent independent checks of the solution presented here as well as a validation of a code to be used in the investigation of turbulent planar jet flow: (1) the comparison with the results of numerical simulations carried out with the RheoFoam toolbox of OpenFoam [17,18], which implements the full governing equations for the FENE-P fluid, can be thought of as a validation of the semi-analytical solution, even though care has to be exercised considering the different boundary conditions; (2) the comparison with the in-house DNS code to be used in our future investigations of turbulent planar jet flows acts as a second independent check of this semi-analytical solution, as well as a validation of the DNS code. This DNS code was modified from an existing code for Newtonian fluids in order to incorporate the viscoelastic FENE-P constitutive equation.

6.2.Numerical methods of DNS/LES code

The in-house three-dimensional direct numerical simulation (DNS) of Newtonian fluid been developed by Reis [137] and then Lopes [138] added some LES models for simulating turbulent Newtonian flow as well as some statistics modules and post-processing tools into the code. The code has been tested and verified by [137,138,139]. It uses a sixth-order compact differencing scheme [140] in the streamwise (x) direction and a pseudo-spectral method [141] in the normal (y) and spanwise (z) directions[138,137]. An explicit three-step third-order low-storage Runge-Kutta time-stepping scheme is utilized as temporal discretization.

Recently, the code has been developed by Guimarães et al [16] for simulation of turbulent flow of FENE-P fluids. Discontinuities in the polymer stress are the main difficulty of the numerical issue in implementing FENE-P model for direct numerical simulation polymer flow. That causes conformation tensor loses its symmetric positive definite or SPD features by calculating negative eigenvalues and finally lead the growth of Hadamard instabilities[142]. Several methods have been proposed to handle this problem. Sureshkumar and his colleague added artificial stress diffusivity to the right-hand side of the conformation tensor equation to avoid that problem [101,143]. However, utilizing artificial diffusivity in the numerical schemes may affect the fluctuation of

polymer stress. Some independent research has been analyzed the conformation tensor equations in 2001 until 2004 [43,144,145], they deduced that utilizing inappropriate numerical scheme to solve convective terms leads to producing negative eigenvalues and Hadamard instabilities. To prevent this issue, Vaithianathan and his coworkers used a different strategy[146]. They applied a specific mathematic technique to decompose conformation tensor. Although they reported that the computation is unconditionally stable, their numerical scheme does not calculate only positive eigenvalues. The negative eigenvalue set to zero in their numerical scheme to stabilize the computation, leading to dissatisfying the conservation law [146].

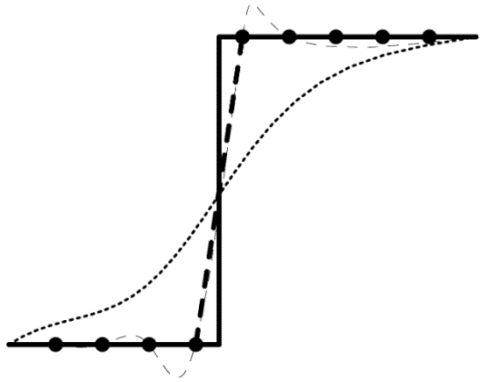

Figure 6. 1.The schematic of discontinuity (a shock) shown by a thick solid line. The computational grids are depicted by dots, and the ideal representitve of the discontinuty on the grid points are shown by thick dash line. Furthermore, The thin dashed line displays a spectral representation while no artificial stress diffusivity are utilized, with overshoots and undershoots (Gibbs phenomenon).The dotted line indicates the effect of adding the stress diffusivity to the spectral representation (plotted by Vaithianathan et al [146]).

The other obstacle that causes by the discontinuity of polymer stress happens when the spectral method utilized to solve conformation tensor. That leads to generate Gibbs phenomenon [147] in the vicinity of discontinuity and produce negative eigenvalue [146]. The schematic both discontinuity and Gibbs problem are plot by Vaithianathan et al [146] and shown Figure 6. 1. As a result of these constraints, spectral method and conventional high-order compact scheme are not the proper treatment for solving conformation tensor in adjacent to discontinuity. Yu and his colleague implemented the slope limiter to each component of the conformation tensor, but the method does not guarantee SPD condition of conformation tensor [145]. In 2006, Vaithianathan and Collins [43] utilized Kurganov and Tadmor or KT [148] numerical scheme to handle all mentioned issues. The KT scheme is a central difference, second-order accurate in physical space, and independent of the time step. The KT scheme calculates only positive eigenvalue and satisfies

the conservation law of conformation tensor. The KT scheme for the cartesian grid and physical domain is described in the following. Since the advection term $\left(u_k \frac{\partial C_{ij}}{\partial x_k}\right)$ of conformation tensor (Eq.(7- 9)) causes the formation of a sharp gradient in predicting C_{ij} and then the growth of Hadamard instabilities, the KT scheme is treated this term as follows:

$$u_k \frac{\partial C_{ij}}{\partial x_k} = -\frac{1}{\Delta x}\left(H^x_{i+\frac{1}{2},j,k} - H^x_{i-\frac{1}{2},j,k}\right) - \frac{1}{\Delta y}\left(H^y_{i,j+\frac{1}{2},k} - H^y_{i,j-\frac{1}{2},k}\right) - \frac{1}{\Delta z}\left(H^z_{i,j,k+\frac{1}{2}} - H^z_{i,j,k-\frac{1}{2}}\right) \quad (6\text{- }1)$$

where the convective flux term in each direction calculated by

$$H^x_{i+\frac{1}{2},j,k} = \frac{1}{2}u_{i+\frac{1}{2},j,k}\left(C^+_{i+\frac{1}{2},j,k} + C^-_{i+\frac{1}{2},j,k}\right) - \frac{1}{2}\alpha^x_{i+\frac{1}{2},j,k}\left(C^+_{i+\frac{1}{2},j,k} - C^-_{i+\frac{1}{2},j,k}\right) \quad (6\text{- }2)$$

$$H^y_{i,j+\frac{1}{2},k} = \frac{1}{2}u_{i,j+\frac{1}{2},k}\left(C^+_{i,j+\frac{1}{2},k} + C^-_{i,j+\frac{1}{2},k}\right) - \frac{1}{2}\alpha^y_{i,j+\frac{1}{2},k}\left(C^+_{i,j+\frac{1}{2},k} - C^-_{i,j+\frac{1}{2},k}\right) \quad (6\text{- }3)$$

$$H^x_{i,j,k+\frac{1}{2}} = \frac{1}{2}u_{i,j,k+\frac{1}{2}}\left(C^+_{i,j,k+\frac{1}{2}} + C^-_{i,j,k+\frac{1}{2}}\right) - \frac{1}{2}\alpha^z_{i,j,k+\frac{1}{2}}\left(C^+_{i,j,k+\frac{1}{2}} - C^-_{i,j,k+\frac{1}{2}}\right) \quad (6\text{- }4)$$

which α is the local velocity of information propagation from discontinuities at interfaces, it is calculated by

$$\alpha^x_{i+\frac{1}{2},j,k} = \left|u_{i+\frac{1}{2},j,k}\right| \quad (6\text{- }5)$$

$$\alpha^y_{i,j+\frac{1}{2},k} = \left|v_{i,j+\frac{1}{2},k}\right| \quad (6\text{- }6)$$

$$\alpha^z_{i,j+\frac{1}{2},k} = \left|w_{i,j,k+\frac{1}{2}}\right| \quad (6\text{- }7)$$

The superscripts '$\pm$' on the right-hand side in Eq. (6- 8)-(6- 10)determine values of the conformation tensor at the interface which obtained in the limit approaching the point of interest from the right (+) or left (−) side, respectively. As a result, second-order, piecewise, linear approximations are implemented to calculate the conformation tensor C.

$$C^{\pm}_{i+\frac{1}{2},j,k} = C^+_{i+\frac{1}{2}\pm1,j,k} \mp \left(\frac{\Delta x}{2}\right)\left(\frac{\partial C}{\partial x}\right)_{i+\frac{1}{2}\pm1,j,k} \quad (6\text{- }8)$$

$$C^{\pm}_{i,j+\frac{1}{2},k} = C^{+}_{i,j+\frac{1}{2}\pm 1,k} \mp \left(\frac{\Delta y}{2}\right)\left(\frac{\partial C}{\partial y}\right)_{i,j+\frac{1}{2}\pm 1,k} \tag{6- 9}$$

$$C^{\pm}_{i,j,k+\frac{1}{2}} = C^{+}_{i,j,k+\frac{1}{2}\pm 1} \mp \left(\frac{\Delta z}{2}\right)\left(\frac{\partial C}{\partial z}\right)_{i,j,k+\frac{1}{2}\pm 1} \tag{6- 10}$$

To estimate the value of gradient following equations are used.

$$\left(\frac{\partial C}{\partial x}\right)_{i,j,k} = \begin{cases} \dfrac{1}{\Delta x}\left(C_{i+1,j,k} - C_{i,j,k}\right) \\ \dfrac{1}{\Delta x}\left(C_{i,j,k} - C_{i-1,j,k}\right) \\ \dfrac{1}{2\Delta x}\left(C_{i+1,j,k} - C_{i-1,j,k}\right) \end{cases} \tag{6- 11}$$

In this case, when two or more derivative approximations satisfy the condition, the derivative approximation is chosen which maximizes the minimum eigenvalue for two tensors. It should be mentioned that when none the derivative approximation satisfies the condition, the derivative approximation set to zero and the accuracy of scheme reduces to first order in space. Utilizing equation guarantee the positive value of eigenvalue and maintains SPD tensor while computing C^{+} and C^{-}.

Area-averaged velocities are required to finite volume update for C at the border of volume surrounding each grid point. Therefore, the following procedure was proposed by the authors:

$$u_{i\pm\frac{1}{2},j,k} = F^{-1}\left\{\hat{u}e^{\pm ik_x\frac{\Delta x}{2}}\frac{\sin\left(k_y\frac{\Delta y}{2}\right)}{k_y\frac{\Delta y}{2}}\frac{\sin\left(k_z\frac{\Delta z}{2}\right)}{k_y\frac{\Delta z}{2}}\right\} \tag{6- 12}$$

$$v_{i,j\pm\frac{1}{2},k} = F^{-1}\left\{\hat{v}e^{\pm ik_y\frac{\Delta y}{2}}\frac{\sin\left(k_z\frac{\Delta z}{2}\right)}{k_y\frac{\Delta z}{2}}\frac{\sin\left(k_x\frac{\Delta x}{2}\right)}{k_x\frac{\Delta x}{2}}\right\} \tag{6- 13}$$

$$w_{i,j,k\pm\frac{1}{2}} = F^{-1}\left\{\hat{w}e^{\pm ik_z\frac{\Delta z}{2}}\frac{\sin\left(k_x\frac{\Delta x}{2}\right)}{k_x\frac{\Delta x}{2}}\frac{\sin\left(k_y\frac{\Delta y}{2}\right)}{k_y\frac{\Delta y}{2}}\right\} \tag{6- 14}$$

where $u_{i\pm\frac{1}{2},j,k}$, $v_{i,j\pm\frac{1}{2},k}$and $w_{i,j,k\pm\frac{1}{2}}$ are calculated the averaged velocities at the border of the volume surrounding at each grid point. In addition,$\hat{u}(k_x,k_y,k_z)$, $\hat{v}(k_x,k_y,k_z)$ and $\hat{w}(k_x,k_y,k_z)$ are calculated the Fourier coefficients of velocities at each grid point.

It is very important to mention that the stability of this scheme does not influence by how polymer stress is computed, it means that the stress can be computed even with a high-order compact finite difference scheme [148]. Furthermore, the described procedure is utilized to solve the advection term of conformation tensor, and the other terms of conformation tensor are solved by central difference, second-order accurate in physical space scheme. For the inlet boundary condition, the analytical solution of laminar Couette flow of FENE-P fluid has been proposed by Pinho et al [78] is implemented and periodic boundary conditions has been utilized for lateral boundaries. For the verification, the DNS planar jet turbulent flow of FENE-P fluid has been tested and verified by Guimarães et al [16] and Parvar et al [112,113] which proposed semi-analytical solution for laminar planar jet flow of FENE-P fluid, as explained in section 5, and later extend to Boundary layer [136] and mixing layer flow [150] of FENE-P Fluid.

It is worth to mention that, regarding the RheoFoam/OpenFoam simulation, a third order QUICK scheme with total variation diminishing (TVD) for time-stepping scheme is utilized. The scheme is called CUBISTA, which stands for Convergent and Universally Bounded Interpolation Scheme for the Treatment of Advection [134].

6.3.The validation of DNS/LES code

Identical computational domains of size 30 D × 30 D × 0.46875 D were used for the calculations with both codes, in the streamwise, transverse and spanwise directions, respectively. The grids used were also identical, with 512×512×8 control volumes in the corresponding directions. The Reynolds number was set at $Re = 100$ and $\beta_p = 0.1$. The maximum molecule extensibility and Weissenberg number were fixed at L=30 and Wi= 0.5, respectively. A second DNS simulation (DNS2) was also carried out using a domain size of 60 D × 60 D × 0.9375 D in a mesh of 1024×1024×16 control volumes to confirm the causes of differences observed in the transverse velocity profile.

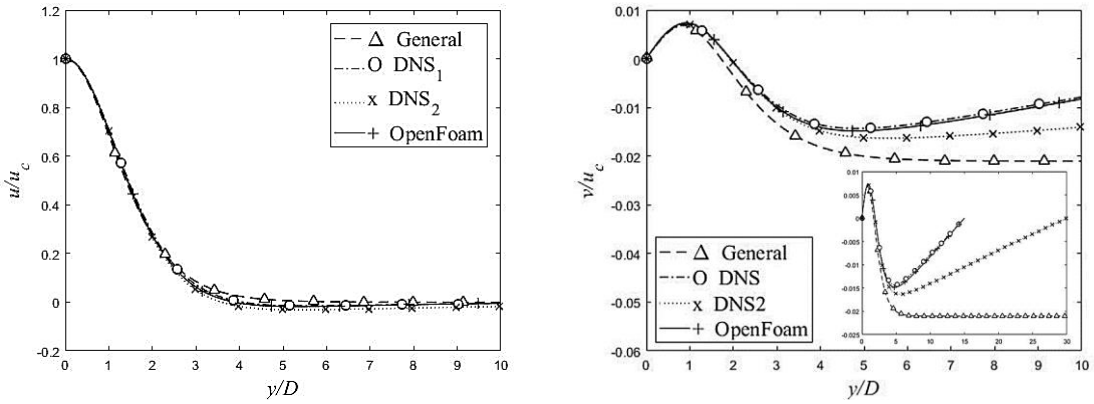

(a) (b)

Figure 6. 2.Normalized transverse velocity profiles at $x/D = 25$, *Wi*=0.5, *L*=30, *Re*=100 and $\beta_p = 0.1$: (a) u/u_c and (b) v/u_c (the inset plots v/u_c for $0 \leq y/D \leq 30$).

Figure 6. 2 (a)-(b) compare the normalized transverse profiles of streamwise and normal velocities at $x/D = 25$, where the computed profiles are already in the self-similar region. The streamwise velocity profiles of DNS, DNS2 and OpenFoam simulations are very close to the general solution profile, but there are differences in the profiles of the normal velocity away from the shear layers of the jet, because of the different boundary conditions. Whereas the general solution is entraining fluid from far away above (top) and below (bottom) the jet, therefore leading to a non-zero constant v far from the jet centerline, the DNS and OpenFoam codes rely on co-flow through the side wall, where the jet inlet is located, and entrain no fluid from the top (above) and bottom boundaries, therefore v tends to zero far from the jet centerline (at those boundaries). Since the boundary conditions are identical for the two codes, the profiles of v/u_c of the OpenFoam and DNS codes match well and do not show non-zero values far from the jet.

The corresponding profiles of C_{xy} and C_{xx} in the self-similar region at $x/D = 25$, are compared in Figure 6. 3 (a)-(b). The results of DNS are consistent with the general solution, and the RheoFoam results are only slightly underpredicted in comparison with those of the general solution, but agree better with the DNS data (notice the zoomed-in ordinate scaling). The corresponding profiles of C_{yy} and C_{zz} are plotted in Figure 6. 3 (c)-(d) showing again a very good agreement, with the small differences associated with the zoomed-in ordinate scaling used. The good comparison between the results of the RheoFoam and DNS codes also validate the implementation of the FENE-P equations onto the latter code.

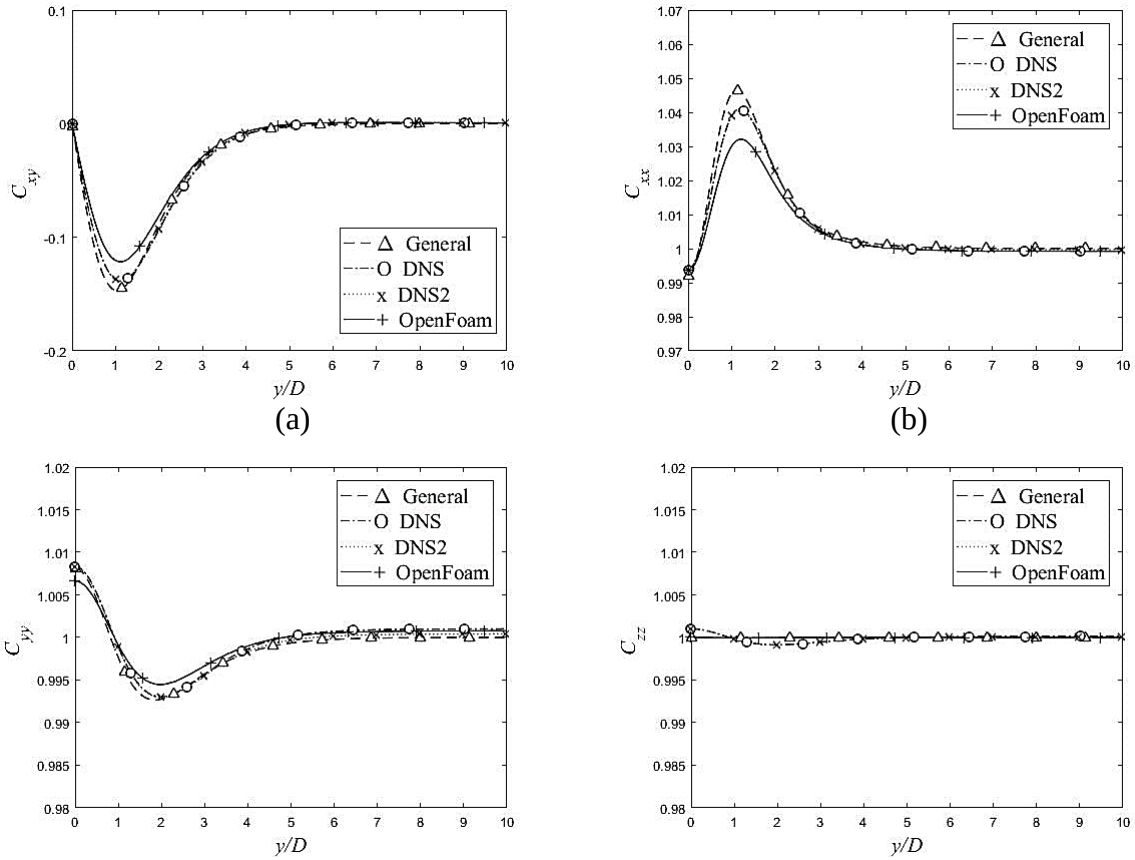

Figure 6. 3.Normalized transverse profiles of C_{ij} at $x/D = 25$ for *Wi*=0.5, *L*=30, *Re*=100 and $\beta_p = 0.1$: (a) C_{xy}, (b) C_{xx}, (c) C_{yy}, (d) C_{zz}(d).

There must be no barriers to freedom of inquiry. There is no place for dogma in science. The scientist is free, and must be free to ask any question, to doubt any assertion, to seek for any evidence, to correct any errors.

-J. Robert Oppenheimer

(April 22, 1904 – February 18, 1967)

An American theoretical physicist

Chapter 7: LES of planar jet flow of viscoelastic FENE-P fluids

7.1.Governing equation of turbulent viscoelastic fluid

The governing equation of turbulent viscoelastic flow is discussed in the following. We started with explaining the filtering procedure which follows by filtered governing equations. Two LES models called classical Smagorisnky and Dynamic Smagorinsky, for modeling the solvent SGS stress term has been presented, afterwards, the procedure of deal with SGS in conformation tensor equations is explained.

7.1.1.Filtered governing equations

To obtain the governing equation for LES of viscoelastic fluids described by the FENE-P model one needs to filter the equations listed in the previous section, as described in detail in Masoudian et al. [21] and in Ferreira et al. [12], so that any flow variable $\varphi(\vec{x},t)$, is split into the sum of a resolved (grid-scale - GS) $\overline{\varphi}(\vec{x},t)$, and an unresolved (subgrid-scale - SGS), contribution,

$$\varphi(\vec{x},t) = \overline{\varphi}(\vec{x},t) + \varphi'(\vec{x},t) \tag{7- 1}$$

Where the GS contribution is defined by a spatial low pass filtering operation,

$$\overline{\varphi}(\vec{x},t) = \int_{\Omega} \overline{\varphi}(\vec{x}',t)\, G_{\Delta}(\vec{x}-\vec{x}')d\vec{x}', \tag{7- 2}$$

in which G_{Δ} is the convolution kernel that determines the filter type, and Δ is the filter width. In the present study, a classical top-hat (box) convolution filter is utilized to separate the resolved and unresolved scales of motion, which for a one-dimensional case reads,

$$G_{\Delta}(x) = \begin{cases} \dfrac{1}{\Delta} & \text{if } |x| \leq \dfrac{\Delta}{2} \\ 0 & \text{otherwise} \end{cases} \tag{7- 3}$$

The box filter is local in the physical space and non-local in the spectral space but the filtering operation is equivalent to a finite difference or finite volume discretization which are commonly used in LES of engineering applications [48]. By applying a low pass filter to the governing equations, the filtered continuity and momentum equations are obtained (Masoudian et al. [21] and in Ferreira et al. [12]),

$$\frac{\partial \overline{u}_k}{\partial x_k}, \tag{7- 4}$$

$$\frac{\partial \overline{u}_i}{\partial t} + \overline{u}_k \frac{\partial \overline{u}_i}{\partial x_k} = -\frac{1}{\rho}\frac{\partial \overline{P}}{\partial x_i} + \upsilon_s \frac{\partial}{\partial x_k}\left[2\overline{s}_{ij}\right] + \frac{\partial \overline{\tau_{ij}^{sgs}}}{\partial x_k} + \frac{\partial \overline{\tau_{ij}^{p}}}{\partial x_k}, \tag{7- 5}$$

where $\overline{\tau_{ij}^{\mathrm{sgs}}} = [\overline{u_i u_j} - \overline{u}_i \overline{u}_j]$ is the SGS tensor and the last term on the RHS of Eq. (7- 5) is the filtered polymer stress contribution given by

$$\overline{\tau_{ij}^{\mathrm{p}}} = \frac{\rho \upsilon_{\mathrm{p}}}{\lambda}\left[\overline{f(C_{kk})C_{ij}} - f(L)\delta_{ij}\right]. \tag{7- 6}$$

The Eq. (7- 6) can be re-written as a

$$\overline{\tau_{ij}^{\mathrm{p}}} = \frac{\rho \upsilon_{\mathrm{p}}}{\lambda}\left[f(\bar{C}_{kk})\bar{C}_{ij} + \chi_{ij} - f(L)\delta_{ij}\right]. \tag{7- 7}$$

in which the SGS of the filtered $\overline{f(C_{kk})C_{ij}}$, is defined as

$$\chi_{ij} = \overline{f(C_{kk})C_{ij}} - f(\bar{C}_{kk})\bar{C}_{ij}. \tag{7- 8}$$

The filtered evolution equation for the conformation tensor is,

$$\frac{\partial \overline{C}_{ij}}{\partial t} + \overline{u_k \frac{\partial C_{ij}}{\partial x_k}} = \overline{\frac{\partial u_i}{\partial x_k} C_{jk}} + \overline{\frac{\partial u_j}{\partial x_k} C_{ik}} - \frac{1}{\lambda}\left[\overline{f(C_{kk})C_{ij}} - \delta_{ij}\right], \tag{7- 9}$$

where the last term on the LHS is the filtered advection of the conformation tensor, and the first two terms on the RHS are the filtered polymer stretching, whereas the last term on the RHS is the filtered polymer dissipation. Eq. (7- 9) can be re-written in a way that singles out the resolved and subgrid-scale quantities in the conformation tensor equation as discussed in Masoudian et al. [21] and Ferreira et al. [12],

$$\frac{\partial \overline{C}_{ij}}{\partial t} + \overline{u}_k \frac{\partial \overline{C}_{ij}}{\partial x_k} = \frac{\partial \overline{u}_i}{\partial x_k}\overline{C}_{jk} + \frac{\partial \overline{u}_j}{\partial x_k}\overline{C}_{ik} - \frac{1}{\lambda}\left[f(\bar{C}_{kk})\bar{C}_{ij} + \chi_{ij} - \delta_{ij}\right] - \psi_{ij} + \gamma_{ij}, \tag{7- 10}$$

with χ_{ij} defined in Eq. (7- 8), and the unresolved (SGS) conformation advection tensor defined as

$$\psi_{ij} = \overline{u_k \frac{\partial C_{ij}}{\partial x_k}} - \overline{u}_k \frac{\partial \overline{C}_{ij}}{\partial x_k}, \tag{7- 11}$$

and,

$$\gamma_{ij} = \left[\overline{\frac{\partial u_i}{\partial x_k} C_{jk}} - \frac{\partial \overline{u}_i}{\partial x_k}\overline{C}_{jk}\right] + \left[\overline{\frac{\partial u_j}{\partial x_k} C_{ik}} - \frac{\partial \overline{u}_j}{\partial x_k}\overline{C}_{ik}\right], \tag{7- 12}$$

Now, closures need to be developed for all SGS terms in all governing equations. In principle the SGS stress tensor in the momentum equation may be affected by fluid rheology. However, since this is the very first work developing models for LES of viscoelastic fluids in jets and $\overline{\tau_{ij}^{\mathrm{sgs}}}$ quantifies inertial effects, as a first approximation we will consider that the closures developed for $\overline{\tau_{ij}^{\mathrm{sgs}}}$ with Newtonian fluids remain valid and the effect of polymers on it is carried over through the filtered velocity and rate of deformation fields. The closures used for $\overline{\tau_{ij}^{\mathrm{sgs}}}$ are presented next.

7.1.2.Smagorinsky model (Sm):

In the present work the SGS stress tensor $\overline{\tau_{ij}^{sgs}}$ is modelled using two different models: the classical and the dynamic Smagorinsky models. Both models were previously implemented in the present code in the turbulent planar jet flow (for a Newtonian fluid) by Silva and al. [138,139].

The Smagorinsky model was originally developed by Smagorinsky [56] and is based on an eddy viscosity given by,

$$\nu_t(x,t) = (C_{sm}\bar{\Delta})^2(|\bar{S}(x,t)|^2)^{\frac{1}{2}}, \tag{7- 13}$$

where $|\bar{S}| = \left(2\overline{S}_{ij}\overline{S}_{ij}\right)^{1/2}$ is the filtered strain magnitude, and $\overline{S_{ij}}$ is the filtered rate-of-strain which is obtained by filtering Eq. (2- 5), C_{sm} is the Smagorinsky constant, and $\bar{\Delta}$ is the filter size calculated by $\bar{\Delta}= (\Delta x \times \Delta y \times \Delta z)^{\frac{1}{3}}$ [48]. The main drawback of the classical Smagorinsky model is that it cannot consider backward energy transfer since it is only a dissipative model, the local equilibrium assumption is not valid and the model it is too dissipative. However, the Smagorinsky model is simple and very popular in the study of turbulent flow and has a very the low computational cost. In the present work, we take $C_{sm} = 0.16$ for the Smagorinsky constant [138,139]. This model, with the same value of C_{Sm}, was used previously by Ferreira et al. [12] for FENE-P fluids in forced homogeneous isotropic turbulence, with very good results.

7.1.3.Dynamic Smagorinsky model (Dyn):

To deal with the limitations of the classical Smagorinsky closure, the dynamic Smagorinsky model was proposed by Germano et al [149]. Here, the eddy viscosity is still given by Equation (7- 13),

but with C_{Dyn} instead of C_{Sm}, where C_{Dyn} is assumed to depend on time and space and computed by utilizing the Germano identity. As a result, the coefficient is now computed in the entire domain as $C_{\mathrm{Dyn}}(x,y,t)=\frac{\langle M_{ij}L_{ij}\rangle}{\langle M_{ij}M_{ij}\rangle}$, where $\langle\quad\rangle$ represents an averaging in the homogenous flow direction, which in the present planar jet flow is the *z*-direction. The coefficient depends on the Leonard stress tensor,

$$L_{ij}=\widetilde{\bar{u}_i\bar{u}_j}-\tilde{\bar{u}}_i\tilde{\bar{u}}_j \tag{7- 14}$$

obtained by applying a spatial test filter, of size equal to 2Δ and identified by the tilde,

and on $M_{ij}=\left(k\Delta\right)^2\left|\tilde{\bar{S}}\right|\tilde{\bar{S}}_{ij}-\Delta^2\widetilde{\left|\bar{S}\right|\bar{S}_{ij}}$. (7- 15)

For a test filter size equal to 2Δ, the coefficient *k* is assumed to be $k=\sqrt{5}$, $|\bar{S}|$ is defined in the previous section and $\left|\tilde{\bar{S}}\right|=\sqrt{2\tilde{\bar{S}}_{ij}\tilde{\bar{S}}_{ij}}$ is the magnitude of the double filter sized of the large-scale strain rate tensor. To prevent the existence of numerical instabilities during the simulations due to excessively large negative values of coefficient C_{Dyn}, a clipping procedure was implemented and $C_{\mathrm{Dyn}}\geq 0$ was imposed everywhere.

7.2.*A-priori* tests: DNS of turbulent planar jet FENE-P fluid

As in Ferreira et al. [12] we begin the present investigation by performing a-*priori* tests, by using here the DNS of turbulent viscoelastic planar jets carried out by Guimarães et al. [16]. The physical and computational parameters of these simulations are now described (more details are described in Guimarães et al. [16]).

An hyperbolic tangent profile is used as an inlet condition for the mean inlet velocity profile [83],

$$\bar{u}(x=0,y)=\frac{U_J+U_\infty^{in}}{2}+\frac{U_J-U_\infty^{in}}{2}\tanh\left[\frac{H}{4\theta}\left(1-\frac{2|y|}{H}\right)\right], \tag{7- 16}$$

where again U_J is the maximum mean streamwise velocity and U_∞^{in} is the jet co-flow velocity, and for inlet condition for the FENE-P fluid we use the analytical solution of laminar couette flow of a FENE-P fluid proposed by Pinho et al. [78]. Periodic boundary conditions are used for the lateral boundaries (y and z directions). In addition, the amplitude of noise for all inlet velocity fluctuations of DNS is set at 10% and the ratio between the inlet slot-width and momentum thickness is H/θ = 30 [139,16]. The Reynolds number (*Re*) is defined by,

$$Re_H = \frac{(U_J - U_\infty^{in})H}{\upsilon_s}, \quad (7\text{- }17)$$

where H is the inlet slot-width of the jet and υ_s is kinematic solvent viscosity. The global Weissenberg number is the ratio between the elastic and integral time scales, which for the turbulent jet is defined as,

$$Wi = \frac{\lambda\left(U_J - U_\infty^{in}\right)}{H}, \quad (7\text{- }18)$$

where λ is the maximum relaxation time of the polymer molecules. In all simulations the Reynolds number was set equal to *Re*=3500, and the ratio of between the solvent and the total viscosity (β_s) is defined as $\beta_s = \frac{\upsilon_s}{\upsilon_s+\upsilon_p} = \frac{\upsilon_s}{\upsilon_0}$ where the zero shear rate viscosity of the fluid (υ_0) is the sum of solvent and polymer kinematic viscosities $\upsilon_0 = \upsilon_s + \upsilon_p$, which was set to $\beta_s = 0.8$. In all cases the computational domain length was equal to 18*H* and the size of the grid size was 512×512×128, in the streamwise, normal, and spanwise direction respectively The maximum extensibility of the dumbbell was imposed be equal to $L^2 = 10^4$, while the relaxation time for FENE-P fluid flows were $\lambda = 0.4$, 0.8, and 1.2, leading to the global Weissenberg numbers equal to *Wi* = 1.1, 2.2, and 3.3, respectively. A reference Newtonian DNS was also carried out for comparison and is denoted by an in the following discussion. The main physical and computational details of the DNS are summarized in Table 7. 1 (Guimarães et al. [16]).

Table 7. 1. Summary of physical and computational parameters of the DNS used to perform a-priori tests, extracted from Guimarães et al. [16]. A_δ, A_{U_c} and A_{σ_c} are slopes of the laws of variation of jet width (δ), centerline velocity (U_c) and centerline stress (σ_c) discussed later, Domain size $\frac{L_x \times L_y \times L_z}{H^3} = 18 \times 18 \times 4.5$.

	Wi	λ	β_s	*L*	Grid points	A_δ	A_{U_c}	A_{σ_c}
DNS_N	0	0	1.0	NA	512×512×128	0.110	0.21	NA
$DNS_{1.1}$	1.1	0.4	0.8	100	512×512×128	0.111	0.208	1.40
$DNS_{2.2}$	2.2	0.8	0.8	100	512×512×128	0.095	0.176	0.56
$DNS_{3.3}$	3.3	1.2	0.8	100	512×512×128	0.080	0.141	0.37

The statistical data extracted from the DNS by Guimarães et al. [16] we initially used to analyze the order of magnitude of each terms from Eqs. (7- 10)-(7- 12), and to simplify the corresponding equations by proposing relevant hypothesis, named (H1)-(H6) and finally to introduce an LES closure. It is very important to mention that *a-priori* tests were performed on the available

instantaneous DNS data, provided by Guimarães et al. [16], which was very limited if we only consider one specific location , at specific (x, y), therefore we decided to perform the tests inside self-similarity region ($10 \leq x/H \leq 18$) at the centerline of jet ($y/H = 0$) to extract more data for assessment of all hypothesis.

We are looking for closures for tensor-based quantities appearing in Eqs. (7- 10)-(7- 12) and these will necessarily involve coefficients which can be independent of the component (isotropic) or not (anisotropic). Both types of coefficient will be investigated here through the *a-priori* testing, but when analysing the isotropic coefficients we will rely on a governing equation for the filtered trace of the conformation tensor, as was done previously by Ferreira et al. [12] for forced HIT. Additionally, for conciseness, when analysing some SGS terms we will also show plots involving the corresponding quantities from the filtered trace equation. The filtered evolution equation for the trace of the conformation tensor can be written as,

$$\underbrace{\frac{\partial \bar{C}_{ii}}{\partial t}}_{C_t} + \underbrace{\bar{u}_k \frac{\partial \bar{C}_{ii}}{\partial x_k}}_{C_a} = 2\underbrace{\frac{\partial \bar{u}_i}{\partial x_k}\bar{C}_{ik}}_{C_p} - \frac{1}{\lambda}\left[\underbrace{\overline{f(C_{kk})}\bar{C}_{ii} + \chi_{ii}}_{C_d} - \delta_{ii}\right] - \psi_{ii} + \gamma_{ii} \tag{7- 19}$$

where C_t and C_a are the temporal and advection terms while C_p and C_d are the production and dissipation of the trace of the filtered conformation tensor components ($\bar{C}_{ii}$), respectively. The two remaining terms on the RHS of Eq. (7- 19), χ_{ii}, ψ_{ii} and γ_{ii}, are the unknown subgrid-scale contributions from the sink, the advection and polymer stretching respectively.

Next, a series of six hypothesis will be tested in order to develop the closures needed by the filtered governing constitutive equation.

7.2.1.Sink of the filtered conformation tensor transport equation: hypothesis H1

The first hypothesis (**H1**) deals with the filtered nonlinear conformation tensor term (χ_{ij}) in the filtered conformation tensor evolution equation and in Eqs. (7- 6)-(7- 8) for the filtered polymer stress, which needs to be assessed in order to develop a LES closure [12,21]. The term can be decomposed as on the left side of the arrow in Eq. (7- 20), where the difference inside the parenthesis is the SGS contribution. The hypothesis is that the SGS term is very small and can be

neglected, therefore the filtered term equals the GS contribution as on the right-hand-side of the arrow in Eq. (7- 20).

$$\overline{f(C_{kk})C_{ij}} = f(\bar{C}_{kk})\bar{C}_{ij} + \left(\underbrace{\overline{f(C_{kk})C_{ij}} - f(\bar{C}_{kk})\bar{C}_{ij}}_{\chi_{ij}} \right) \quad \text{(7- 20)}$$

$$\rightarrow \overline{f(C_{kk})C_{ij}} \approx f(\bar{C}_{kk})\bar{C}_{ij} \quad or\ \chi_{ij} \cong 0$$

Note that in homogeneous flows and considering the filtering properties for a box filter one concludes that $\overline{f(C_{kk})} = f(\bar{C}_{kk})$. Even though the jet flow is not homogeneous, this equality will still be assumed.

Figure 7. 1 (a)-(c) show the joint probability density function (JPDF) of the $c_d = \overline{f(C_{kk})C_{ii}}$ and $C_D = \overline{f(C_{kk})}\bar{C}_{ii}$ in the viscoelastic turbulent planar jet flow for Wi = 1.1, 2.2, 3.3, and for a filter size equal to $\Delta/\Delta x = 4$ (for filter sizes $\Delta/\Delta x = 2$ and 8 similar results are observed). The two quantities are strongly correlated and the correlation coefficient is very close to 1, which means that the two quantities are closely matched. Note that the JPDF plotted involves the trace of the conformation tensor (C_{ii}), but hypothesis (**H1**) remains valid if the sink terms are assessed individually. These are not shown for conciseness. Masoudian et al. [21] and Ferreira et al. [12] reached similar results for turbulent channel flow and forced isotropic turbulence of FENE-P fluids, respectively. The results in Figure 7. 1 confirm the validity of assumption **H1** for a free flow in the presence of mean shear. Therefore, this assumption is used henceforth in the present study.

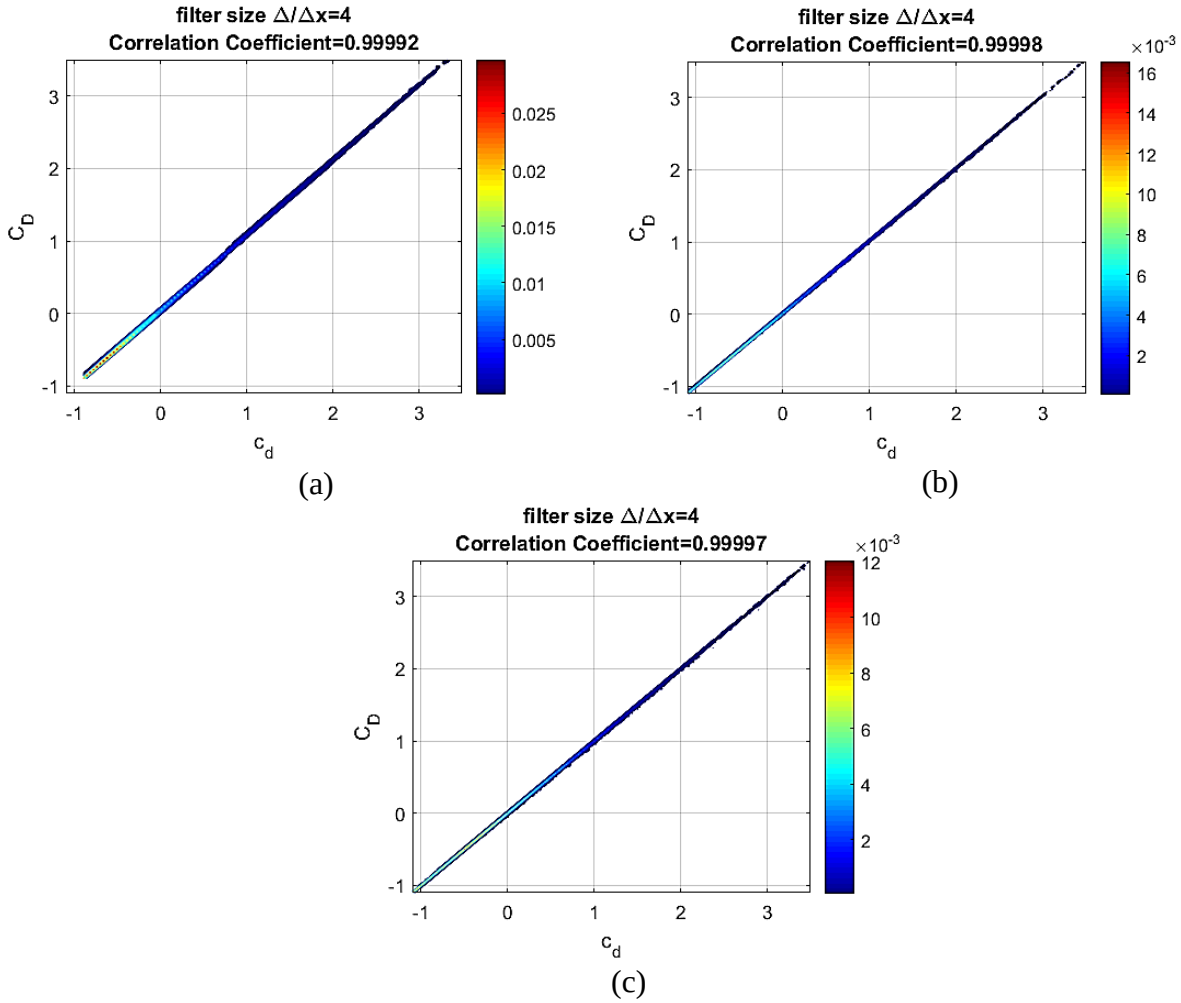

Figure 7. 1.Joint Probability density function (JPDF) of $c_d = \overline{f(C_{kk})C_{ii}}$ and $C_D = \overline{f(C_{kk})}\bar{C}_{ii}$ normalised by their root-mean-square, for the DNS with *Wi*=1.1(a), 2.2(b), 3.3(c) *and filter size* $\Delta/\Delta x$ = 4, at the jet centerline (*y/H*=0) for $10 \leq x/H \leq 18$, lines are a guide to the eye.

7.2.2.Subgrid-scale conformation tensor advection term: hypothesis H2

The second hypothesis **(H2)** deals with the subgrid-scale advection and we analyse next the corresponding term for the trace of the filtered conformation tensor, denoted by ψ_{ii} using Eq. (7-11).

Hypothesis **H2** assumes that the SGS contribution of the advection from the filtered conformation tensor equation is negligible when compared with the resolved advection term. Figure 7. 2 (a)-(c) plots the variations of all terms of Eq. (7- 19) averaged in the homogeneous direction; as shown $\langle\psi_{ii}\rangle$ is much smaller than the other quantities, and in particular smaller than $\langle C_a\rangle$. In Figure 7. 2,

we consider data at an instant of time at specific (x, y) points on the jet centerline, but within the self-similarity region. Each data point marked in the abscissa actually corresponds to the average of the 128 points in the homogeneous z- direction of the domain (at that value of (x, y)), i.e., in contrast to the figures showing the joint PDFs we are not mixing data at all points. For clarity only data from 30 (x, y) points are shown, but we observe a similar behavior when considering all points in that region. It is not shown here for conciseness, but hypothesis **H2** remains valid when comparing individually $\langle \psi_{ij} \rangle$ with $\langle C_{a_{ij}} \rangle$.

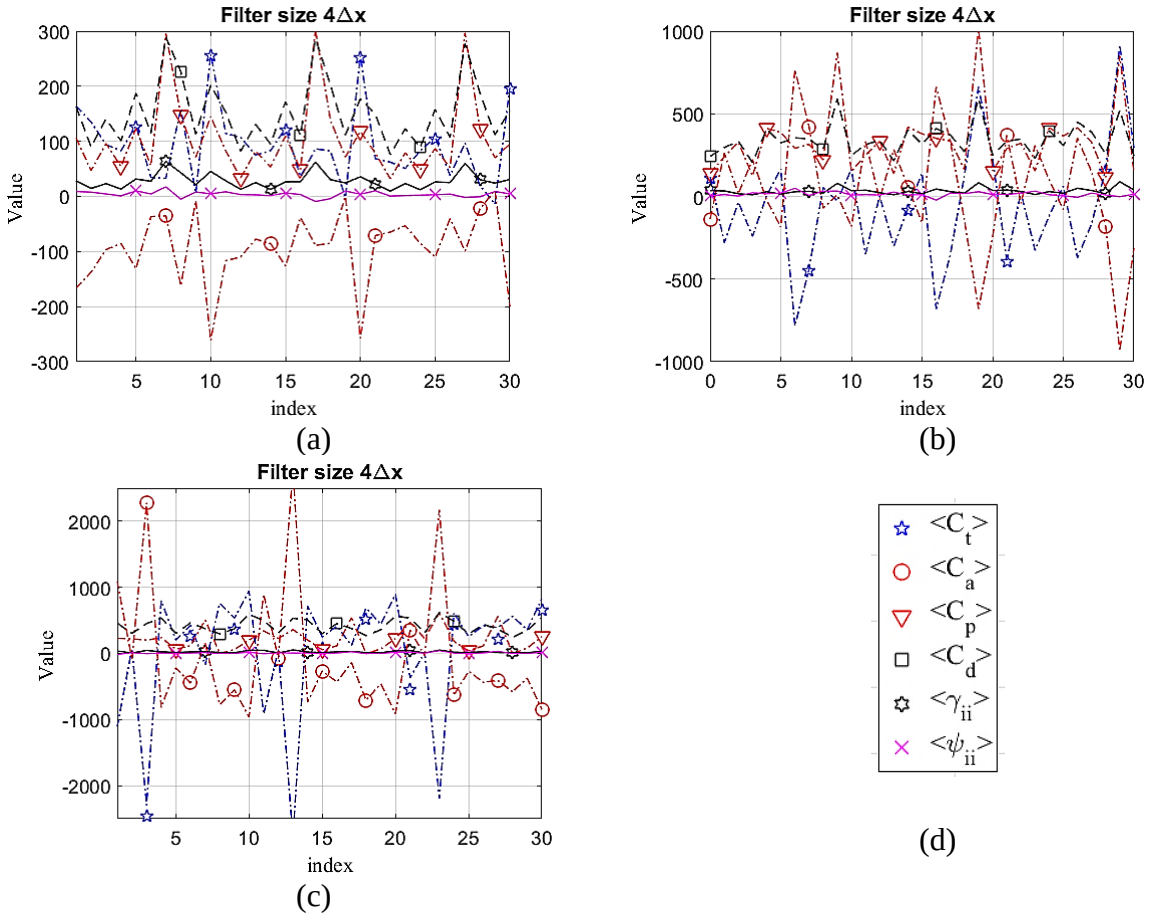

Figure 7. 2. The variation of the averaged in the homogeneous direction of Eq. (7- 10) terms for the DNS with *Wi*=1.1(a), 2.2(b), 3.3(c) and legend (d) with filter size Δ/Δx = 4, at the jet centerline (*y/H*=0) of jet for $10 \leq x/H \leq 18$ (see the top of (a) for the key of plotted quantities), lines are a guide to the eye. In the present figure, x-axis label "index" means the number of samples cases which obtained from DNS.

Figure 7. 3(a)-(c) shows the probability density function (PDF) of ψ_{ii} and γ_{ii} at the self-similar region of the turbulent viscoelastic jet for W_i = 1.1, 2.2, 3.3, respectively, for a filter size equal to

$\Delta/\Delta x = 8$. These confirm that locally, the quantities of $\psi_{ii} \ll \gamma_{ii}$. As shown, the skewness of γ_{ii} is also significantly more intense than that of ψ_{ii}, so $\langle \gamma_{ii} \rangle_{z-direction} \neq 0$, whereas $\langle \psi_{ii} \rangle_{z-direction} \approx 0$. Masoudian et al. [21] and Ferreira et al. [12] also reported that ψ_{ii} is negligible in DNS of turbulent channel flows and forced isotropic turbulence of FENE-P fluids, respectively. Therefore, the comparison shows that the SGS of polymer stretching γ_{ii}, or γ_{ij}, cannot be ignored.

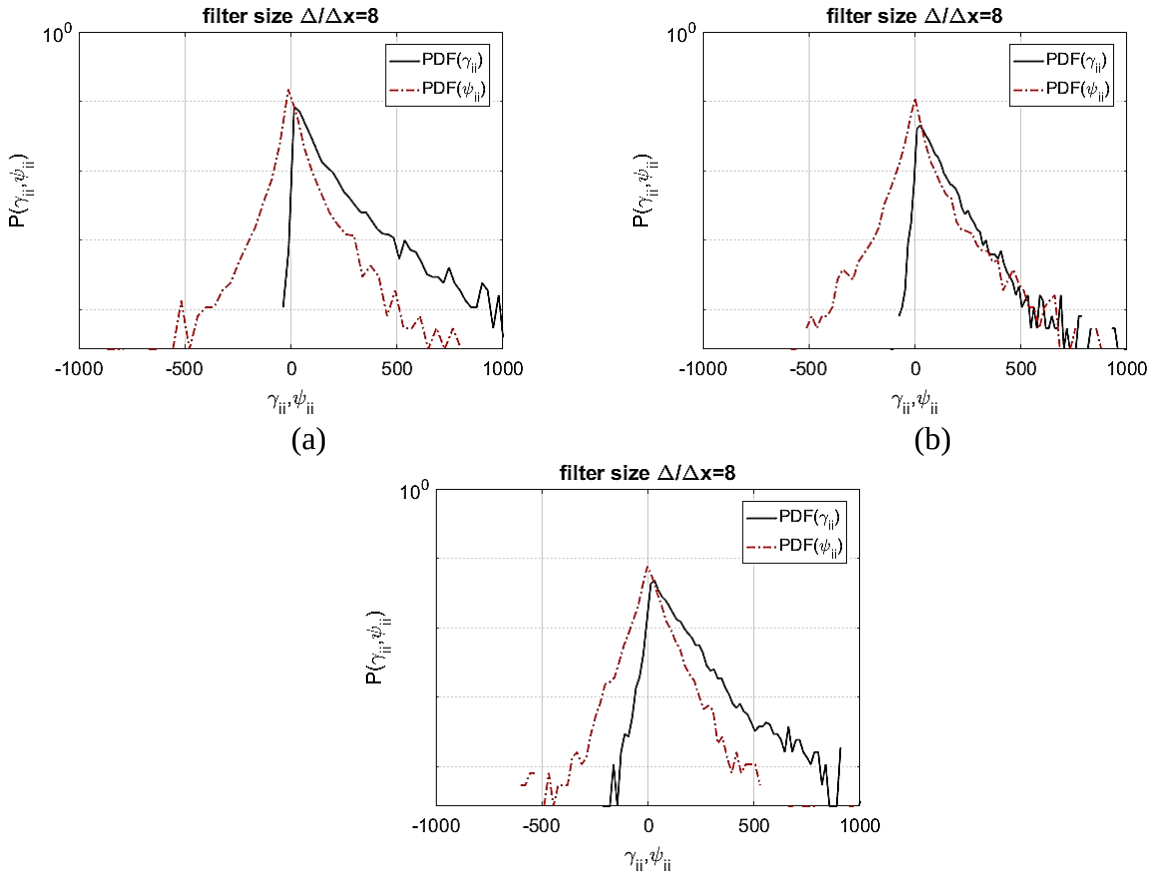

Figure 7. 3. PDF of the SGS of both advection of the trace of the conformation tensor and polymer stretching terms, for the DNS with *Wi*=1.1(a), 2.2(b), 3.3(c) and filter size $\Delta/\Delta x = 8$, at the jet centerline (*y/H*=0) for $10 \leq x/H \leq 18$, lines are a guide to the eye.

It is also observed in Figure 7. 3 that by increasing *Wi*, not only the skewness of the polymer stretching SGS, but also the tendency of having negative quantities of it, both increase. The same behavior was observed and reported by Ferreira et al. [12] and interpreted there as a sign of the formation of the polymer induced energy cascade at larger *Wi* number, which was explained in detail by [14].

7.2.3.Scale-similarity of the subgrid-scale polymer stretching: hypothesis H3

One of the main characteristics of turbulent flows is the existence of self-similarity in the inertial range of scales, which allows the computation of a given subgrid-scale quantity by assessing the same quantity defined at a nearby scale [151]. This assumption has been previously used in the development of many SGS models for Newtonian turbulent flows [60] and prompted Ferreira et al. [12] to develop the DSIM model for γ_{ij} in Eq. (7- 12) in isotropic turbulence by applying this concept to the computation of the SGS polymer stretching term. It is important to assess this assumption in the present inhomogeneous flow configuration. Specifically, the self-similarity of subgrid-scales was originally proposed by Bardina [152], for the SGS stress tensor of the momentum equation. The model assumes that the SGS stress (for a Newtonian fluid) can be approximated by,

$$\tau_{ij}^{\mathrm{sgs}} = c\left(\widetilde{\overline{u}_i\overline{u}_j} - \widetilde{\overline{u}}_i\widetilde{\overline{u}}_j\right), \tag{7- 21}$$

where C is a constant of order $O(1)$, and $\tilde{\Delta}$ is the width of the test filter, often taken as having of twice the width of the original filter. By applying this concept to the subgrid-scale polymer stretching term (γ_{ij} in Eq. (7- 12)) the subgrid-scale polymer stretching at the test filter width is,

$$G_{ij} = \left[\widetilde{\overline{\frac{\partial u_i}{\partial x_k}C_{jk}} - \frac{\partial\tilde{\overline{u}}_i}{\partial x_k}\tilde{\overline{C}}_{jk}}\right] + \left[\widetilde{\overline{\frac{\partial u_j}{\partial x_k}C_{ik}} - \frac{\partial\tilde{\overline{u}}_j}{\partial x_k}\tilde{\overline{C}}_{ik}}\right]. \tag{7- 22}$$

By considering the self-similarity of the subgrid-scales computed at filter widths Δ and $\tilde{\Delta}$, (here we take $\tilde{\Delta}= 2\Delta$) the SGS of polymer stretching tensor is calculated by,

$$\gamma_{ij} = C_\gamma G_{ij}, \tag{7- 23}$$

where C_γ is a numerical coefficient that needs to be computed. This constitutes the assumption **H3** used by Ferreira et al. [12] in homogeneous turbulence.

To assess this assumption in the turbulent jet flow configuration, Figure 7. 4 (a)-(c)) show the joint probability density functions (JPDFs) of the trace of the SGS polymer stretching terms γ_{ii} and G_{ii} with Wi = 1.1, 2.2 and 3.3 and for filter size $\Delta/\Delta x$ = 4 and 8.

The two quantities are clearly correlated, and the correlation coefficient between γ_{ii} and G_{ii} varies between 0.83 to 0.599, so of order 1, depending on the filter size and Wi number. Specifically, the correlation coefficient decreases when increasing Wi and the filter size, which are similar to the

behavior and values described in Ferreira et al. [12]. The correlation coefficients and shape of the PDFs attest that the scale-similarity assumption (**H3**) is also valid for inhomogeneous free shear flows and can be used in the development of SGS closures.

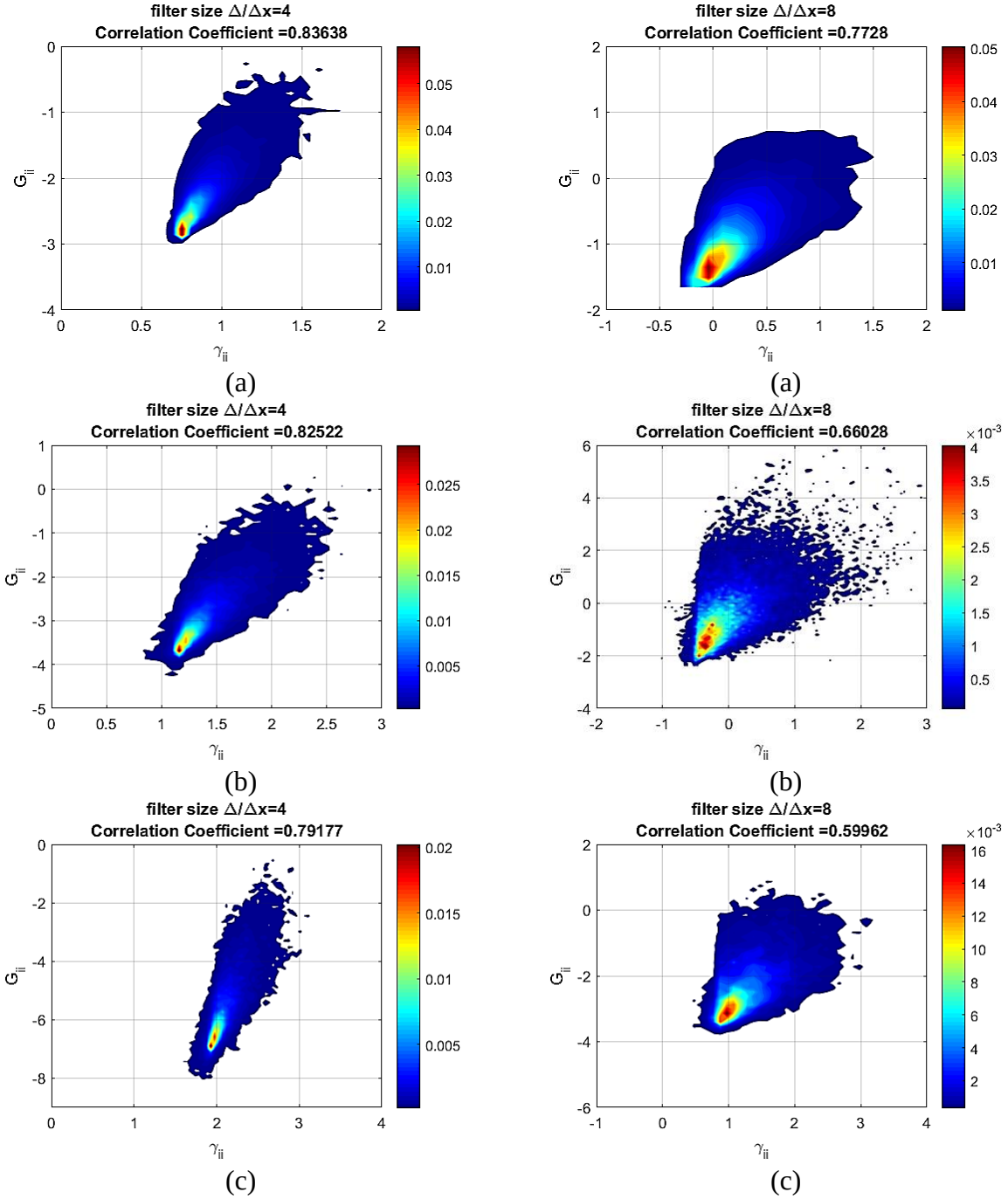

Figure 7. 4. JPDF between the trace of SGS polymer stretching terms γ_{ii} and G_{ii} normalized by their root-mean-square, for the DNS with *Wi*=1.1(a), 2.2(b), 3.3(c) and filter size Δ/Δx = 4 (left column) and Δ/Δx = 8 (right column), at the jet centerline (*y/H*=0) for $10 \leq x/H \leq 18$, lines are a guide to the eye.

The closure in Eq. (7- 21) has the same coefficient for all tensor components, i.e., it is an isotropic model, still to be determined. As in Ferreira et al. [12] we now investigate the possibility of using anisotropic model coefficients $C_{\gamma_{ij}}$, defined by a rewriting of assumption **H3** as,

$$\gamma_{ij} = C_{\gamma \mathrm{ij}} G_{ij} (\text{no summation on } i \text{ and } j) \qquad (7\text{- }24)$$

To investigate this need Figure 7. 5 and Figure 7. 6 show the JPDF between $C_{\gamma 11} = \frac{\gamma_{11}}{\mathcal{G}_{11}}$ and $C_{\gamma 22} = \frac{\gamma_{22}}{G_{22}}$, and between $C_{\gamma 11} = \frac{\gamma_{11}}{G_{11}}$ and $C_{\gamma 12} = \frac{\gamma_{12}}{G_{12}}$, respectively, for filter size $\Delta/\Delta x = 4$.

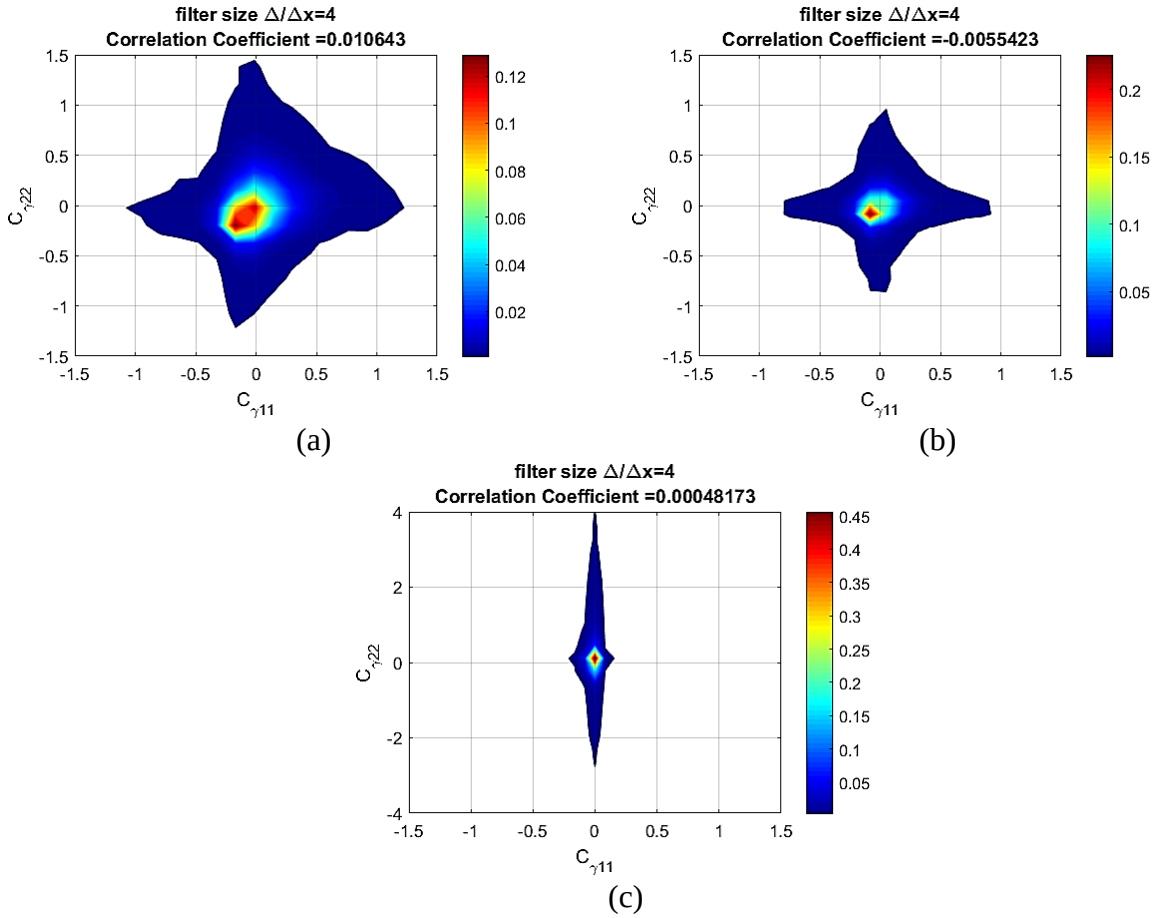

Figure 7. 5. JPDF between the $C_{\gamma 11}$ and $C_{\gamma 22}$ (calculated from Eq. (7- 24)), for the DNS with *Wi*=1.1(a), 2.2(b), 3.3(c) and filter size $\Delta/\Delta x = 4$, at the jet centerline (*y/H*=0) for $10 \leq x/H \leq 18$, lines are a guide to the eye.

As in Ferreira et al. [12] for homogeneous turbulence, the figures clearly show that the correlation coefficients between $C_{\gamma 11}$ and $C_{\gamma 22}$ and between $C_{\gamma 11}$ and $C_{\gamma 12}$ are approximately zero, meaning that these quantities are statistically independent, which validates the assumption of using an isotropic C_{γ} in the DSIM SGS model, also for the inhomogeneous flow configuration used in the

present work. For other combinations of coefficients not shown, the correlation coefficient was equally very small.

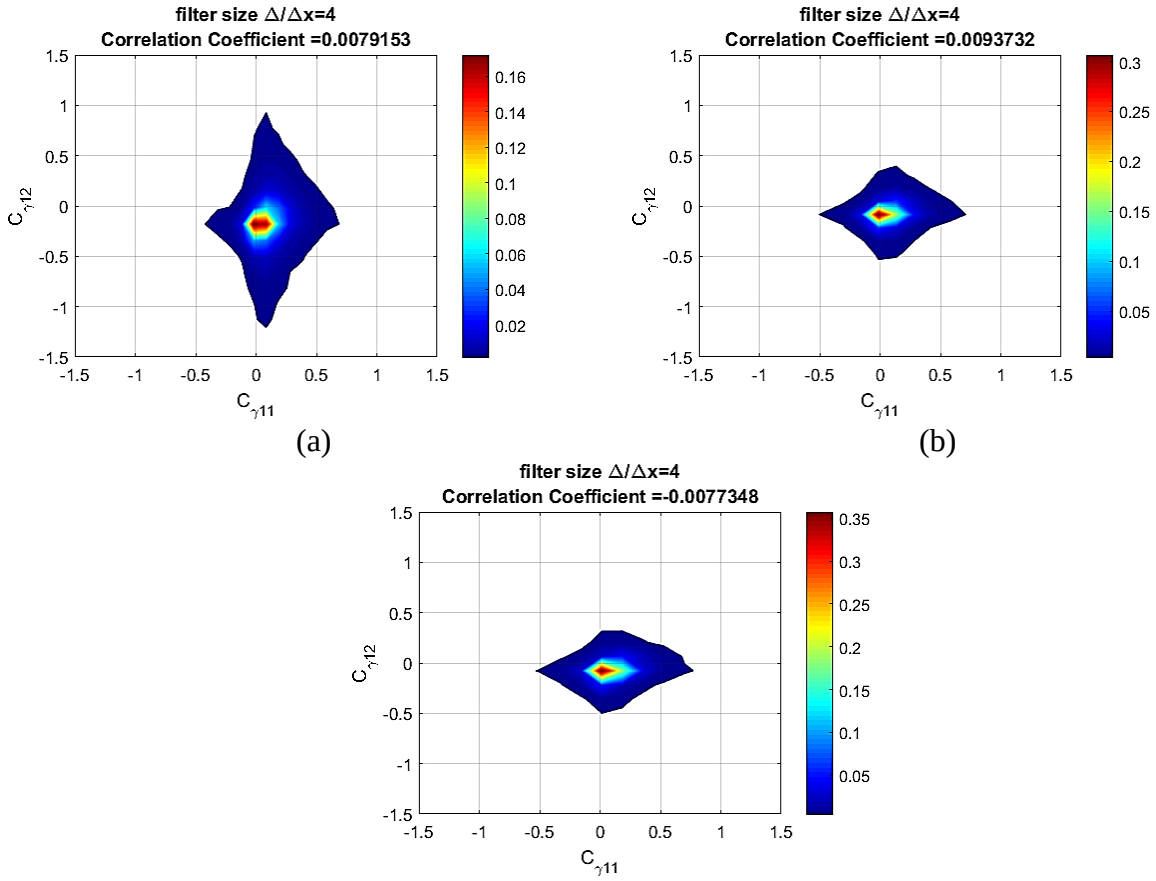

(a) (b) (c)

Figure 7. 6. JPDF between the $C_{\gamma 11}$ and $C_{\gamma 12}$(calculated from Eq. (7- 24)), for the DNS with *Wi*=1.1(a), 2.2(b), 3.3(c) and filter size Δ/Δx = 4, at the jet centerline (*y/H*=0) for $10 \leq x/H \leq 18$, lines are a guide to the eye.

7.2.4.Local equilibrium of the polymeric elastic energy and statistically stationary flow: hypothesis H4, H5 & H6

We now investigate the hypothesis used by Ferreira et al. [12] to compute the model constant C_{γ}, defined in Eq. (7- 24). By using Eq. (7- 19) and by employing the condition of statistical stationarity and homogeneity Ferreira et al. [12] arrived at the following expression,

$$\langle 2\overline{\frac{\partial u_i}{\partial x_k} C_{ik}} \rangle = \langle \frac{1}{\lambda} \left[\overline{f(C_{kk}) C_{ii}} - \delta_{ij} \right] \rangle, \qquad (7\text{- }25)$$

where the brackets <> denote an ensemble averaging operation which was performed in all three homogeneous directions in the homogeneous isotropic turbulence configuration of Ferreira et al. [12]. In such context, this expression represents the 'global' equilibrium of the resolved elastic energy i.e., in statistically stationary isotropic turbulence the elastic energy produced by the interaction between the polymer molecules and the turbulent velocity fluctuations is balanced by its transfer into the polymer molecules where it is stored as elastic energy, so that the total (resolved) elastic energy - which is proportional to $\bar{C}_{kk} = \bar{C}_{xx} + \bar{C}_{yy} + \bar{C}_{zz}$ - remains constant. We denote this assumption as **H4**.

It is important to clarify how this assumption can be used in the context of the present flow configuration, since it is clear that in turbulent jet flows, as well as in other inhomogeneous flow configurations, Eq. (7- 26) will not be exactly verified, and one needs to assess how this expression, or some sort of variant of it, can be used in order to extend the DSIM model into free shear flows.

We start by noting that statistically stationarity in the far field (fully developed) region of the jet allows one to write also,

$$\langle \frac{\partial \overline{C}_{ii}}{\partial t} \rangle = 0. \tag{7- 26}$$

(we denote this assumption by **H5**). The brackets still refer to averaging in the homogeneous direction, which in the present context is the *z*-direction. By averaging Eq. (7- 19) and considering a negligible $\langle \psi_{ii} \rangle$ (**H2**), together with the self-similarity assumption for the SGS polymer stretching term (**H3**), this equation can be written as,

$$\langle \bar{u}_k \frac{\partial \bar{C}_{ii}}{\partial x_k} \rangle = \langle 2 \frac{\partial \bar{u}_i}{\partial x_k} \bar{C}_{ik} \rangle - \langle \frac{1}{\lambda} \left[f(\overline{C_{kk}}) \bar{C}_{ii} - \delta_{ii} \right] \rangle - \langle C_\gamma G_{ii} \rangle \tag{7- 27}$$

Notice that the term on the LHS of Eq. (7- 27) is the mean advection of the trace of the conformation tensor, which is rigorously zero in isotropic turbulence due to the homogeneity of the flow, but has to be retained in inhomogeneous turbulent flows, such as in turbulent viscoelastic jets. However, it is likely that this term is negligible compared to the other terms. Indeed, whereas the advection of $\bar{C}_{ii}$ is clearly associated with the largest scales of motion in the jet, the terms representing the production and dissipation of $\bar{C}_{ii}$ – the first and second terms on the RHS of Eq. (7- 27) - are governed by the smallest scales of the flow. We denote this assumption (neglecting the advection of $\bar{C}_{ii}$) by **H6**. We can therefore use an expression similar to the one used by Ferreira

et al. [12] for the determination of the model constant C_γ, with only minor corrections related to the averaging procedure.

By inserting all the aforementioned hypotheses into Eq. (7- 27) the model constant C_γ can be obtained from the following expression,

$$C_\gamma = \frac{\left\langle \frac{1}{2\lambda}\left[\overline{f\left(C_{kk}\right)C_{ii}} - \delta_{ii}\right]\right\rangle_z - \left\langle \frac{\partial \overline{u}_i}{\partial x_k}\overline{C}_{ik}\right\rangle_z}{\left\langle \widetilde{\frac{\partial u_i}{\partial x_k}C_{ik}} - \frac{\partial \tilde{\overline{u}}_i}{\partial x_k}\tilde{\overline{C}}_{ik}\right\rangle_z} \tag{7- 28}$$

where the averaging procedure now consists on a spatial average carried out along the only flow direction where the flow is homogeneous (z - direction).

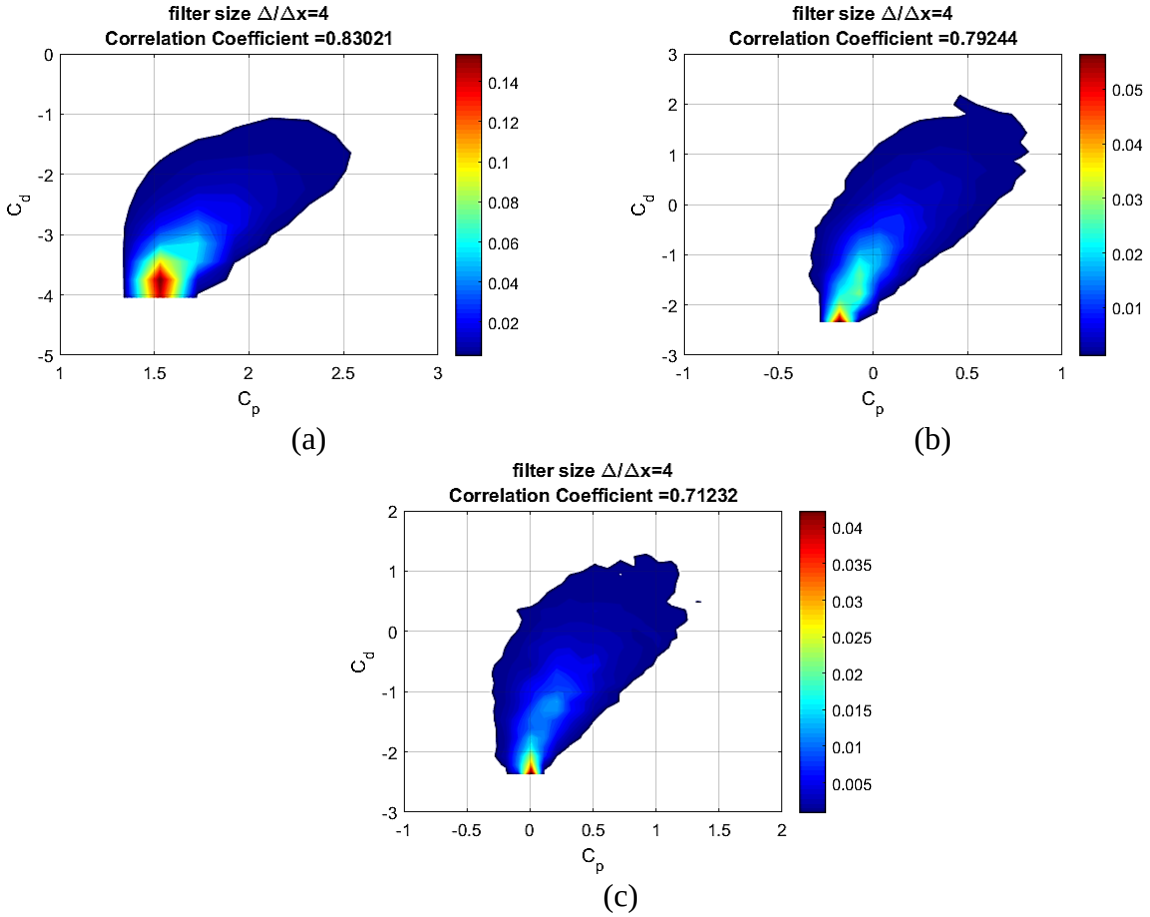

Figure 7. 7. JPDF functions between polymer stretching C_p and dissipation C_d terms of the trace of the filtered conformation tensor evolution equation, for the DNS with *Wi*=1.1(a), 2.2(b), 3.3(c) and filter size Δ/Δx = 4, at the jet centerline (*y/H*=0) for $10 \leq x/H \leq 18$, lines are a guide to the eye.

Hypothesis **H5** does not need to be assessed as it stems directly from the concept of statistical stationarity, whereas hypothesis **H4** and **H6** are somehow related and need to be assessed simultaneously.

In order to assess the hypothesis **H4-H6** dealing with local equilibrium assumption, Figure 7. 7 shows the joint probability density functions (JPDFs) of the polymer stretching (C_p) and dissipation (C_d) of the trace of the conformation tensor defined in Eq.(7- 19), for Wi = 1.1 , 2.2, and 3.3 and filter size $\Delta/\Delta x = 4$. The correlation coefficients between C_p and C_d are very high, with 0.84, 0.79, and 0.71 for Wi = 1.1, 2.2, and 3.3, respectively, with $\Delta/\Delta x = 4$. This confirms that, as in isotropic turbulence, C_p and C_d are in approximately local equilibrium, even though the correlation coefficient slightly decreases with increasing Wi numbers.

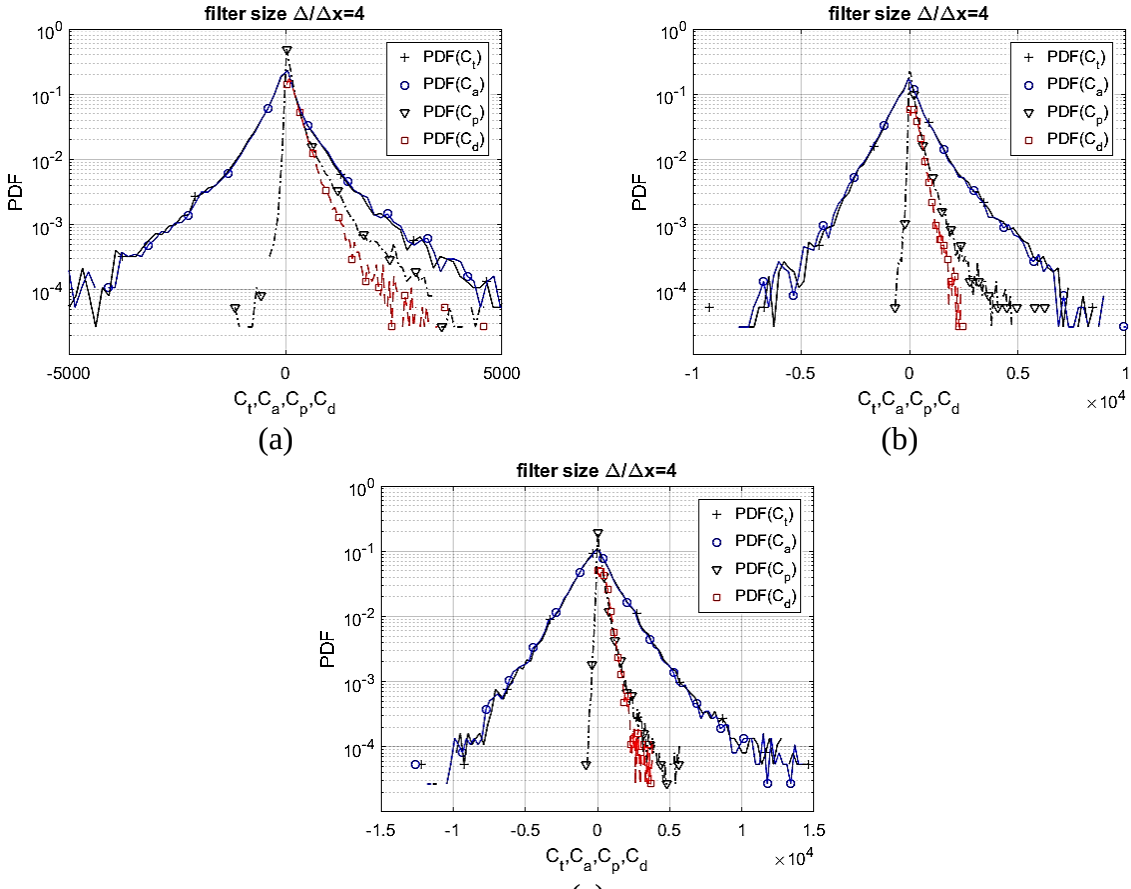

Figure 7. 8. PDF of the traces of subgrid-scale polymer strechting terms γ_{ij} and $\mathcal{G}_{ij}$ normalised by their root-mean-square, for the DNS with Wi=1.1(a), 2.2(b), 3.3(c) and filter size $\Delta/\Delta x$ = 4, at center line of jet for $10 \leq x/H \leq 18$.

To complete the assessment of the **H4-H6** assumptions, it is important to shown that the other terms of Eq. (7- 19) terms (C_t and C_a) are negligible in comparison with C_p and C_d terms.

Figure 7. 8 shows the probability density function of all terms of Eq. (7- 19) (C_t, C_a, C_p and C_d) for $\Delta/\Delta x = 4$ and Wi = 1.1, 2.2, and 3.3. The PDF of C_t and C_a are symmetric which explains why the local value of the sum of these quantities is approximately 0. Finally, Figure 7. 9 shows the joint probability density functions between temporal variation C_t and advection terms C_a of the trace of the conformation tensor, for Wi = 1.1, 2.2, and 3.3 and filter size $\Delta/\Delta x = 4$. The correlation coefficient between C_t and C_a is equal to -0.95, -0.94, and -0.92 which finally confirms that all hypotheses **H4, H5** and **H6** are verified.

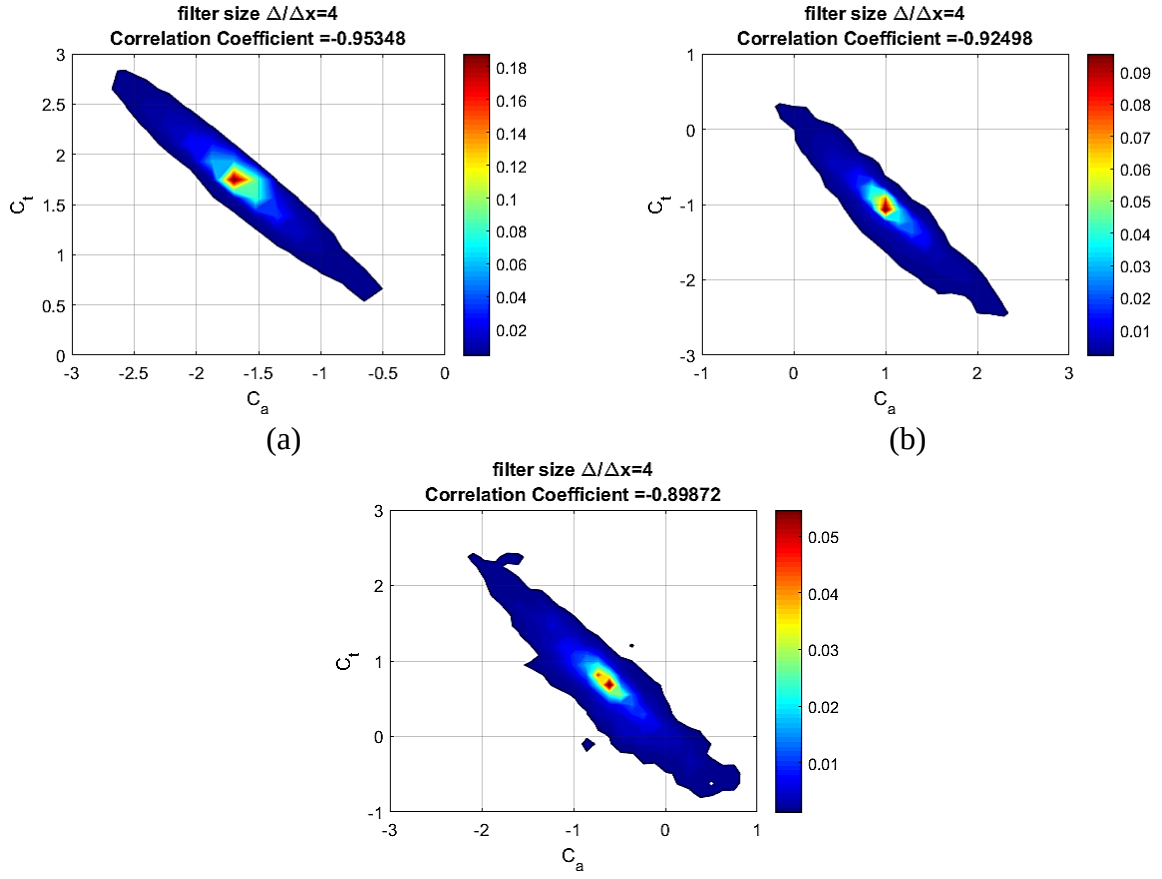

Figure 7. 9. JPDF functions between temporal C_t and advection C_a terms from the trace of the conformation tensor transport, for the DNS with Wi=1.1(a), 2.2(b), 3.3(c) and filter size $\Delta/\Delta x$ = 4, at center line of jet for $10 \leq x/H \leq 18$.

To summarize, all the *a-priori* testes conducted in the reference DNS of turbulent viscoelastic jets clearly show that all the assumptions used by Ferreira et al. [12] in the development of the DSIM

model in isotropic turbulence are also valid in the present inhomogeneous free turbulent flow configuration, and are likely valid in other free shear flows of viscoelastic fluids such as wakes and mixing layers. In the next section we assess the combination of all closures through *a-posteriori* (LES) tests.

7.3.*A-posteriori* tests: LES of turbulent planar jet FENE-P fluid

Several LES of turbulent planar jet flow of FENE-P fluid were performed with the various closures presented, including Smagorinsky and dynamic Smagorinsky for SGS term of momentum equation and the DSIM model for the SGS polymer stretching term in the conformation equation, and their results were assessed against the reference DNS of Guimarães et al. [16]. The results are discussed in this section, in what are typically called *a-posteriori* tests, confirming that the DSIM model, in its original formulation and in particular in combination with the dynamic Smagorinsky closure for the SGS stress, performs well in planar turbulent jets, and arguably the same should be true for other free shear flows. Incidentally, we did also some tests using the Vreman [157] and the shear improved Smagorinsky [158] closures for the SGS stress, but no advantages were observed relative to the dynamic Smagorinsky model, therefore for the sake of conciseness such results are neither presented nor those closures introduced.

Table 7. 2. Summary of physical and computational features of LES used in the *a-posteriori* tests with Domain size $\frac{L_x \times L_y \times L_z}{H^3} = 19.2 \times 24 \times 6$.

	Wi	λ	β_s	L	Grid points	A_δ	A_{U_c}	A_{σ_c}
LES_N	0	0	1.0	NA	192×192×48	0.124	0.165	NA
$LES_{1.1}$	1.1	0.3	0.8	100	192×192×48	0.108	0.169	1.8
$LES_{2.2}$	2.2	0.6	0.8	100	192×192×48	0.090	0.156	0.63
$LES_{3.3}$	3.3	0.9	0.8	100	192×192×48	0.084	0.155	0.34
LES_{Nf}	0	0	1.0	NA	256×256×64	0.124	0.180	NA
$LES_{1.1f}$	1.1	0.3	0.8	100	256×256×64	0.122	0.187	1.65
$LES_{2.2f}$	2.2	0.6	0.8	100	256×256×64	0.094	0.167	0.57
$LES_{3.3f}$	3.3	0.9	0.8	100	256×256×64	0.085	0.154	0.38

The LES were carried out with the same numerical code used in Guimarães et al. [16] and the physical and computational parameters are chosen as close as possible to those of the reference DNS, naturally using coarser grids than in the DNS.

The amplitude of noise for all inlet velocity fluctuations was set at 10%, as in Guimarães et al. [16], however the ratio between the inlet slot-width and momentum thickness was set to $H/\theta = 15$ [16,139], to avoid the Gibbs phenomena that could arise with the coarser grids used in LES. In the following we use subscripts "N" (Newtonian fluid), "Sm" (Smagorinsky) and "Dyn" (dynamic Smagorinsky) to denote the various subgrid-scale stress closures used in the computation. Subscript "f" represents a second LES carried out using a finer grid. The main details of the simulations are summarized in Table 7. 2, where the reported values of $A_\delta, A_{U_c}, A_{\sigma_c}$ were obtained using the dynamic Smagorinsky model.

In all simulations and similarly to the DNS of Guimarães et al. [16], the Reynolds number was equal to Re=3500, and the ratio of the solvent to total viscosity, and the maximum dumbbell extensibility were equal to $\beta = 0.8$ and $L^2 = 10^4$, respectively. The domain size was $L_x = 19.2H$, $L_y = 24H$ in the streamwise and normal directions, and $L_z = 6H$ in the spanwise direction, for a 'normal' grid size with 192×192×48 grid points, and a 'finer' grid size with 256×256×64 points. By considering $\lambda = 0.3, 0.6, 0.9$ s, the global Weissenberg number became equal to Wi = 1.1, 2.2, 3.3.

7.3.1.Instantaneous vorticity and trace of conformation tensor field

Figure 7. 10 (a)-(d) show contours of instantaneous vorticity magnitude normalized by $\left(U_J - U_\infty^{in}\right)/H$ in the (x,y) plane of the turbulent planar jet obtained by LES for Newtonian and viscoelastic flows at Weissenberg numbers, Wi=1.1, 2.2, 3.3. These results were obtained in the finer grid (LES_f) and used the dynamic Smagorinsky model.

The Newtonian contours in Figure 7. 10 (a) are very similar to those shown in Guimarães et al. [16], for the same physical conditions. Kelvin-Helmholtz vortices emerge at about at $x/H \approx 4$ for all simulations, and tend to break up into smaller-scale eddies after about $x/H \approx 6$. By about x/H≈10-12 the flow seems to have attained the typical features of fully developed turbulence, with a clear display of many small-scale eddies without any preferential direction.

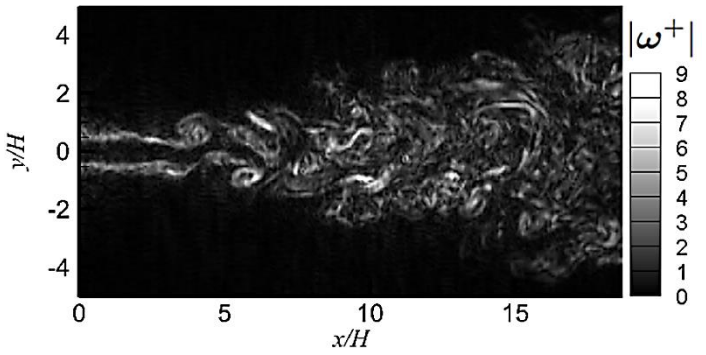

(a) *Wi*=0.0, $|\omega^+|_{max} = 9.15$

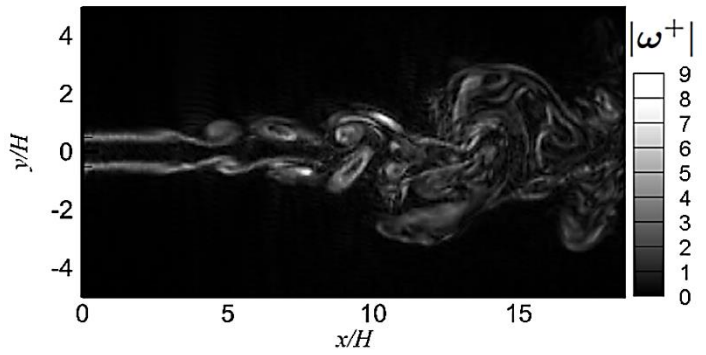

(b) *Wi*=1.1, $|\omega^+|_{max} = 7.65$

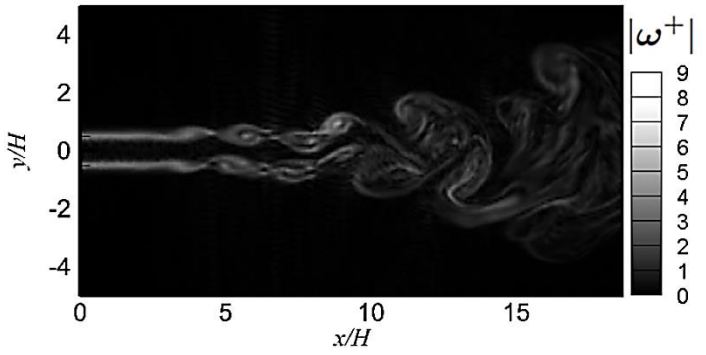

(c) *Wi*=2.2, $|\omega^+|_{max} = 4.98$

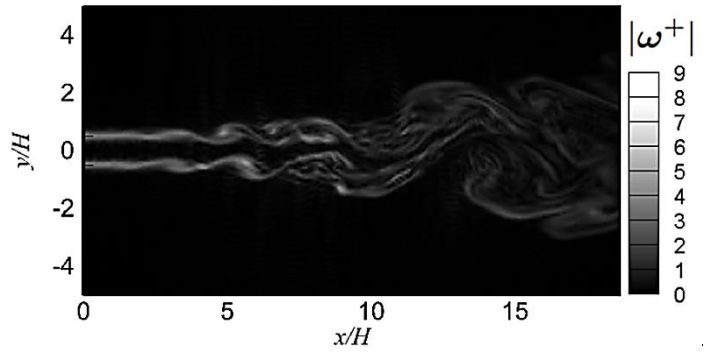

(d) *Wi*=3.3, $|\omega^+|_{max} = 4.55$

Figure 7. 10. Contours of instantaneous vorticity normalized by $\left(U_J - U_\infty^{\text{in}}\right)/H$ at the middle plane of the domain (z=0) for (a) Newtonian and viscoelastic flows at *Wi* of (b) 1.1, (c) 2.2 and (d) 3.3. The results were obtained in the finer grid (LES_f) using the dynamic Smagorinsky model.

As reported by Guimarães et al. [16] and the other extensive studies on turbulent viscoelastic fluids [153-156] the main effect of increasing the *Wi* number in the turbulent planar jet structure is *i)* a significant suppression of small-scale motions (compared to the Newtonian reference case), with a concomitant considerable reduction of the vorticity magnitude as observed by the range of values of $|\omega^+|$ obtained, *ii)* the elongation of the eddy structures, and *iii)* a reduction of the jet spreading rate. All of these features are clearly shown in Figure 7. 10.

The effect of polymers on the dampening of the vorticity magnitude can be well appreciated in these figures, Figure 7. 10, since by increasing the *Wi* number from *Wi* =0 (Newtonian) to 3.3 causes the maximum vorticity magnitude to move from $|\omega^+|_{\max} = 9.15$ for the LES of the Newtonian fluid, into $|\omega^+|_{max} = 4.55$ for the LES of FENE-P fluid, the coherent structures become more elongated and spread at a lower rate. Similar observation were reported in Guimarães et al. [16].

Figure 7. 11 shows contours of the trace of conformation tensor tr(C) which is proportional to the elastic energy stored by the stretched polymer molecules, for *Wi*= 1.1, 2.2, and 3.3, at the mid-plane of the computational domain (z=0), and at the same instant of time of Figure 7. 10. To help the visualizations, the range of the color maps was taken to be much lower than maximum tr(C) for all cases. Maxima of tr(C) occurs in the transitional region, and when approaching the far field tr(C) decreases. Similarly to other studies e.g. Valente at al. [13], Guimarães et al [16], it was observed that even for the most extreme scenario (*Wi*= 3.3), $\mathrm{tr}(C)_{\max}\approx 4500$ in the fully developed turbulence region (at $x/H\approx 14$) corresponding to $\mathrm{tr}(C)_{\max}/L^2=0.45$. However, inspection of the instantaneous fields show that the probability of having local values of $\mathrm{tr}(C)_{\max}/L^2$ is very low, and generally those values remain $\mathrm{tr}(C)_{\max}/L^2 \ll 1$.

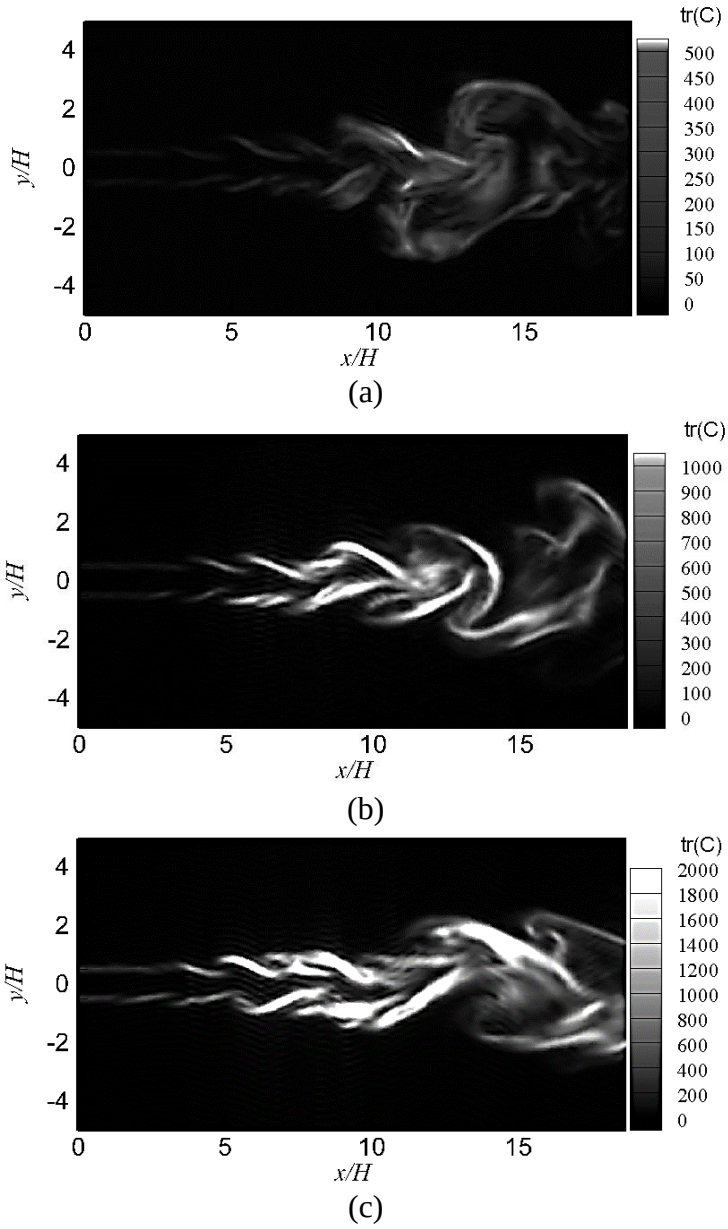

Figure 7. 11. The contour of the trace of conformation tensor tr(*C*) for (a) *Wi*= 1.1, (b) 2.2, and (c) 3.3 at the middle of the computational domain (*z*=0), and correspond to the same time of Figure 7. 10 (b)-(d). The results were obtained in the finer grid (LES_f) using the dynamic Smagorinsky model.

7.3.2.Classical statistics

In this section we analyze the statistical quantities obtained from the several LES carried out with the combined dynamic Smagorinsky and DSIM models, by comparing them with the statistics obtained in the reference DNS [16]. In some simulations the classical Smagorinsky model was also used. It is worth to mention that in this section whenever "mean" with the symbol of overbar

on the corresponding terms is used, it shows statistical quantities meaning that to obtain that quantity we perform both time average and spatial average in the homogenous direction.

Guimarães et al. [16] showed that in turbulent viscoelastic jets the shear layer thickness $\delta(x)$ and the mean centerline velocity decay $\overline{U}_c(x)$, evolve as simple functions of the streamwise distance x,

$$\frac{\delta(x)}{H} = A_\delta \left(\frac{x - x_0}{H}\right) \tag{7- 29}$$

and

$$\left(\frac{U_c(x)}{U_J}\right)^{-2} = A_{U_c} \left(\frac{x - x_0}{H}\right) \tag{7- 30}$$

where A_δ and A_{U_c} are constants and x_0 is the virtual jet origin, and that increasing the *Wi* number decreases both the shear layer thickness and the centerline velocity decay rates. Notice that because fluid viscoelasticity and the subgrid-scale models tend to delay the transition to turbulence, the comparison between the different models has to be focused on the analysis of the spreading and decay rates, as measured by A_δ and A_{U_c}, and not in the evolution of $\delta(x)$ and $\overline{U}_c(x)$ from the jet inlet.

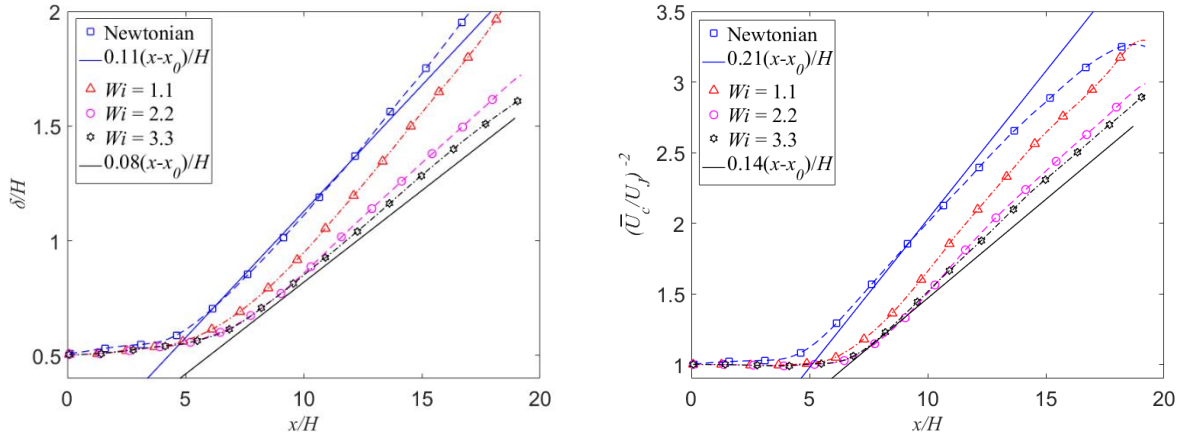

(a) (b)

Figure 7. 12. Evolution of the shear layer thickness (a) and jet centerline velocity decay (b) in LES of turbulent planar jets of Newtonian and FENE-P fluids at *Wi*=1.1, 2.2, 3.3 and the spread rate lines for low and large Wi number obtained by DNS. Closures used were the dynamic Smagorinsky and DSIM models in the finer grid ($LES_{1.1f}$, $LES_{2.2f}$, and $LES_{3.3f}$) and compared with the reference Newtonian case (LESNf). Dashed lines connecting symbols are a guide to the eye and the solid straight lines show the rate laws obtained by DNS.

Figure 7. 12 (a)-(b) show the streamwise variation of the jet half-width and centerline velocity decay, respectively, for the simulations carried out with the finer grid. The corresponding values of A_δ and A_{U_c}, in the region $9 \leq x/H \leq 18$, are listed in Table 7. 1. The decay rates A_δ and A_{U_c} for the Newtonian LES (LES_{Nf}) are within the ranges of $0.092 \leq A_\delta \leq 0.118$ and $0.093 \leq A_{U_c} \leq 0.220$, that have been reported in previous experimental [159-163] and numerical (DNS) [164] studies, for Newtonian turbulent jets. Regarding the viscoelastic LES and in agreement with the DNS of Guimarães et al. [16] the present LES show that increasing the Weissenberg number postpones the transition to fully developed turbulence and reduces the values of values A_δ and A_{U_c} at high Wi. Indeed, up to Wi=1.1, the values of A_δ and A_{U_c}remain close to the Newtonian values, however, for Wi=2.2 and 3.3 both A_δ and A_{U_c} are considerably reduced, while still obeying a linear scaling law with $A_\delta = 0.101$, and 0.082, and $A_{U_c} = 0.171$, and 0.160, respectively. Moreover, the results are qualitatively consistent with several experimental studies e.g. references [165-166].

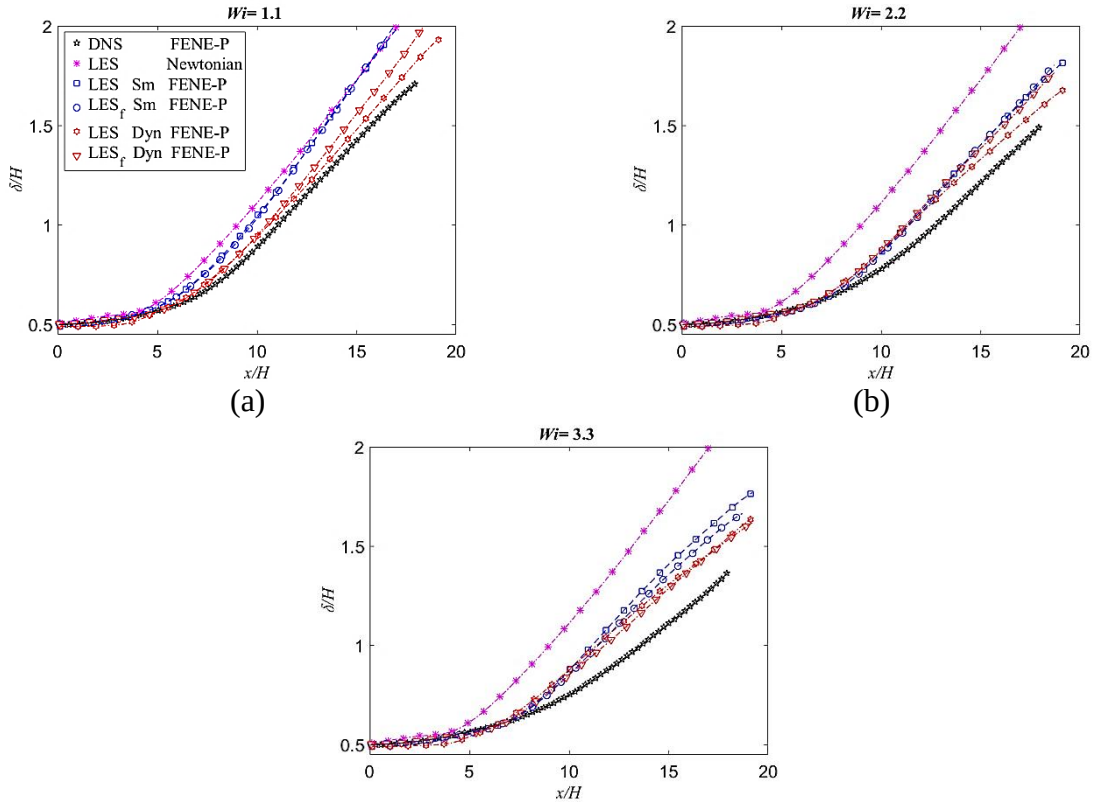

Figure 7. 13. Effect of the SGS stress model on the evolution of shear layer thickness in the streamwise direction for the turbulent planar jet flows of FENE-P fluid for different SGS stress closures at *Wi* of (a) 1.1, (b) 2.2 and (c) 3.3. The DSIM closure is used in the conformation tensor equation, and Smagorinsky and dynamic Smagorinsky for SGS tensor of momentum equation.

To study the differences from the SGS model used to compute the SGS stresses, Figure 7. 13 and Figure 7. 14 show the spreading and velocity decay rates, respectively, obtained in the LES of the turbulent jet, using the classical Smagorinsky and the dynamic Smagorinsky models. It is clear that the dynamic Smagorinsky model performs better than the Smagorinsky closure, in particular for the finer grids.

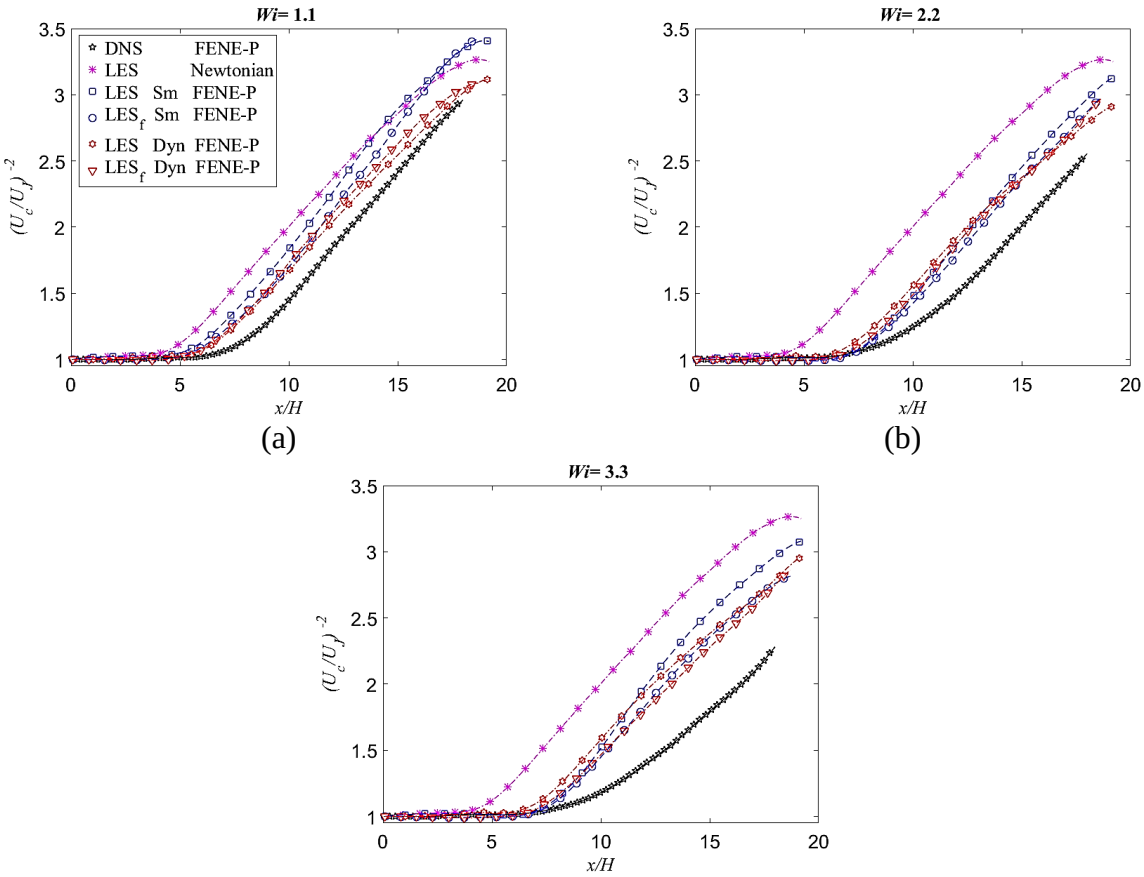

Figure 7. 14. The evolution of jet centerline velocity decay in streamwise direction-planar jet flow of FENE-P fluid for various combination of SGS and *Wi*=1.1(a), 2.2(b), 3.3(c).

Figure 7. 15 (a-c) also analyzes the effect of the SGS stress closures on the transverse profiles of the normalized mean streamwise velocity by comparing these profiles at $x/H = 12$ with the results from the reference DNS. As expected the mean streamwise profiles collapse, which is consistent in the self-similar region of the flow, but with the dynamic Smagorinsky closure performing better than the classical Smagorinsky model (results closer to the DNS data of [16]). Moreover, in agreement with the DNS of Guimarães et al. [16] the effect of increasing *Wi* number on $\overline{u}/\overline{U}_c(x)$ is negligible.

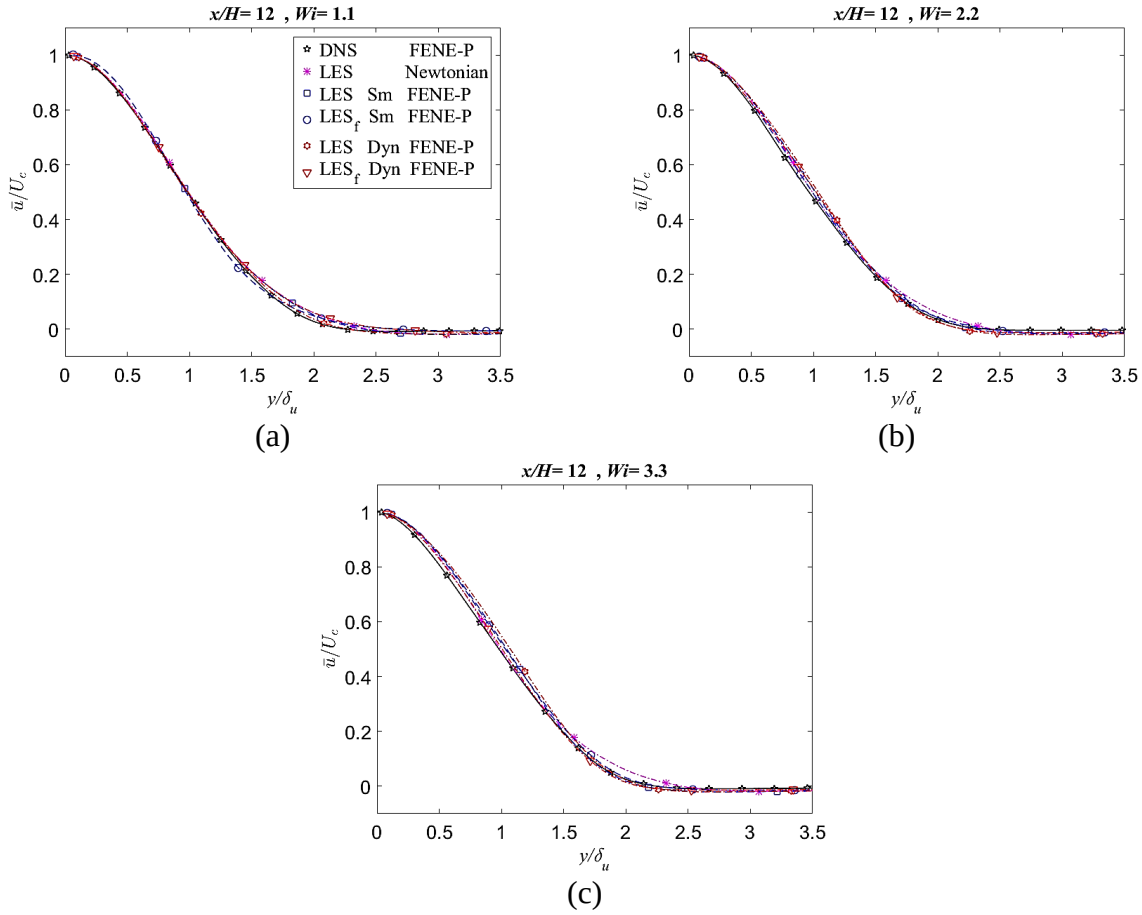

Figure 7. 15. Effect of SGS stress model on the transverse profiles of streamwise mean velocity normalized by the centerline velocity at *x/H*=12 for *Wi* of (a) 1.1, (b) 2.2 and (c) 3.3. The DSIM closure is used in the conformation tensor equation, and Smagorinsky and dynamic Smagorinsky for SGS tensor of momentum equation.

Figure 7. 16 until Figure 7. 18 (a)-(c) show the corresponding streamwise evolutions of the normal components of the Reynolds stress tensor on the centerline, here represented as root-mean-square (rms) of the velocity fluctuations $\sqrt{\overline{u'^2}}$, $\sqrt{\overline{v'^2}}$, and $\sqrt{\overline{w'^2}}$ predicted by LES, and normalized by mean centerline velocity $\overline{U}_c(x)$. The figures include data from the reference DNS (Guimarães et al. [16]). The rms of the velocity fluctuations of LES follow closely the corresponding DNS results, particularly when the combination of dynamic Smagorinsky and DSIM closures are used. For $Wi \leq 1.1$, the normal Reynolds stresses gradually increase along the transition region until a peak at the beginning of the self-similar region ($x/H \approx 11$), and further downstream their values slightly decrease as the flow attains the fully developed turbulent flow region. However, for $Wi \geq 2.2$ the magnitude of the Reynolds stresses decreases considerably, compared with the turbulent Newtonian jet. Generally speaking, as reported by Guimarães et al. [16] the role of the polymers

on the velocity fluctuations can be summarized as postponing the transition to turbulence and by reducing the Reynolds stresses in the self-similar region, due to a depletion of the small scales of motion caused by a preferential transfer of kinetic energy into the polymer molecules, instead of the classical multi-scale transfer into the solvent via the Richardson-Kolmogorov energy cascade. This tendency to the attenuation of the Reynolds stresses is also reproduced by the present LES, particularly for the combination of the dynamic Smagorinsky and the DSIM model.

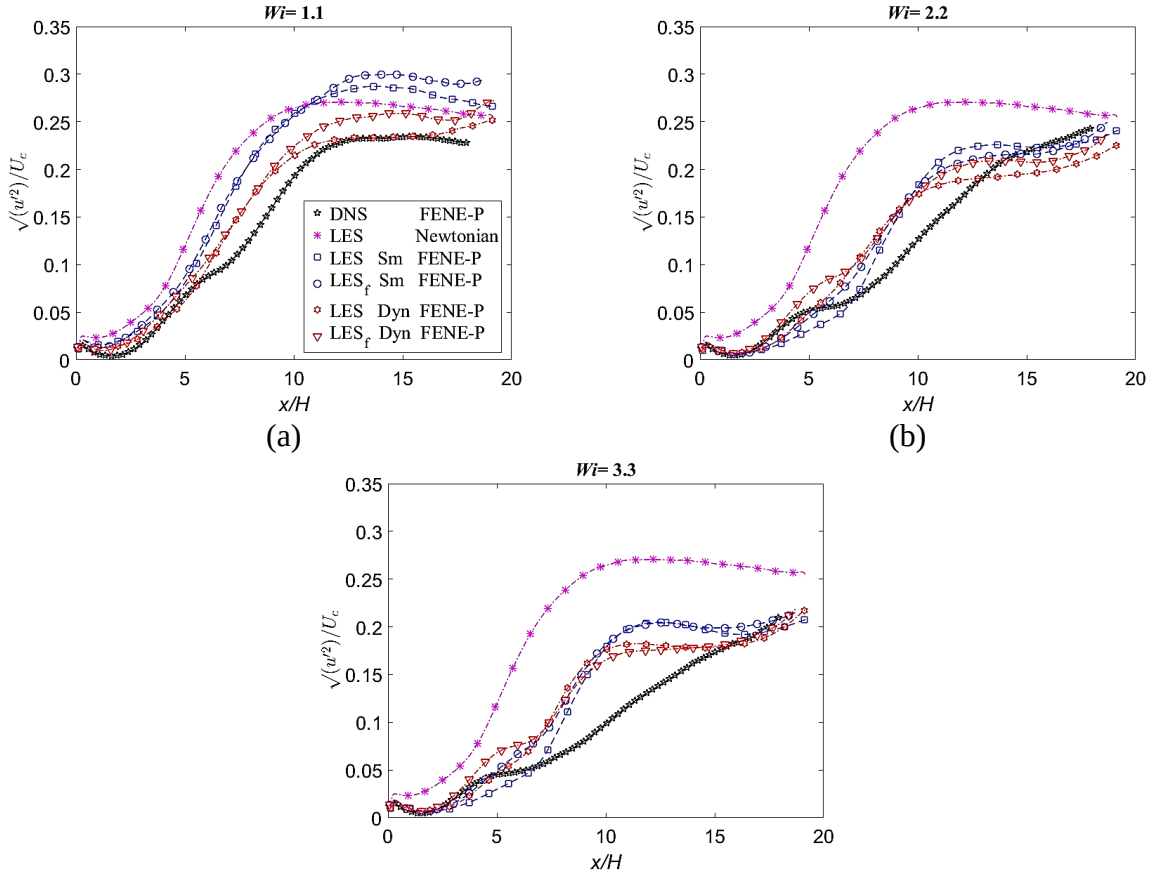

Figure 7. 16. Effect of SGS stress model on the evolution of the root-mean square of the streamwise velocity fluctuations $\sqrt{\overline{u'^2}}$ along the centerline, normalized by the centerline mean velocity ($\overline{U}_c(x)$), for *Wi* of (a) 1.1, (b) 2.2 and (c) 3.3. The DSIM closure is used in the conformation tensor equation and Smagorinsky and dynamic Smagorinsky for SGS tensor of momentum equation.

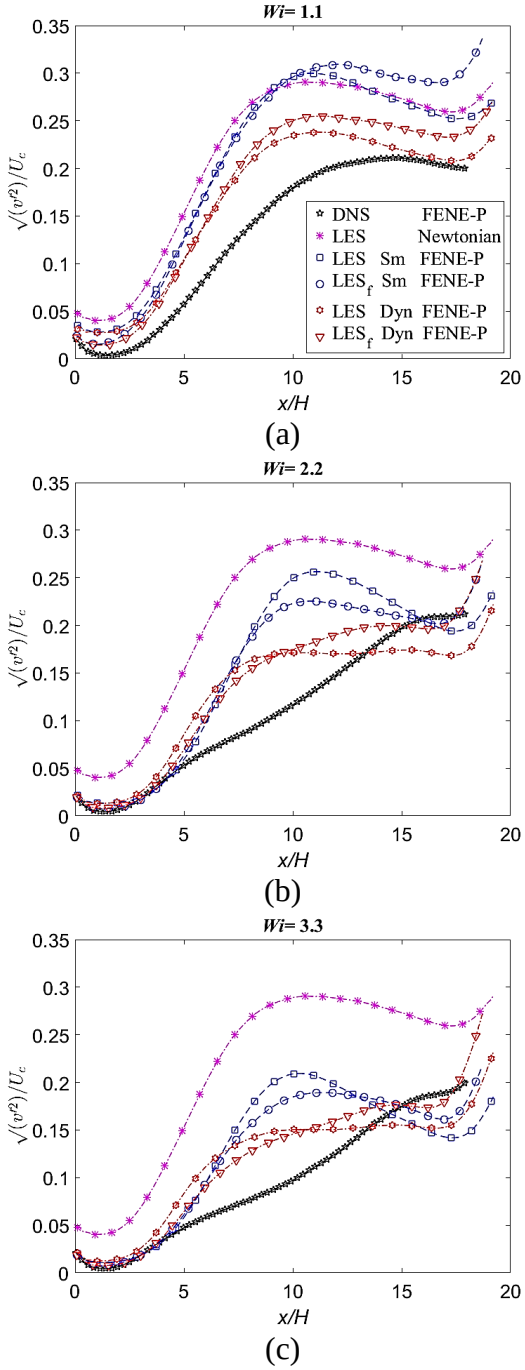

Figure 7. 17. Effect of SGS stress model on the evolution of the root-mean square of the streamwise velocity fluctuations $\sqrt{\overline{v'^2}}$ along the centerline, normalized by the centerline mean velocity ($\overline{U}_c(x)$), for *Wi* of (a) 1.1, (b) 2.2 and (c) 3.3. The DSIM closure is used in the conformation tensor equation and Smagorinsky and dynamic Smagorinsky for SGS tensor of momentum equation.

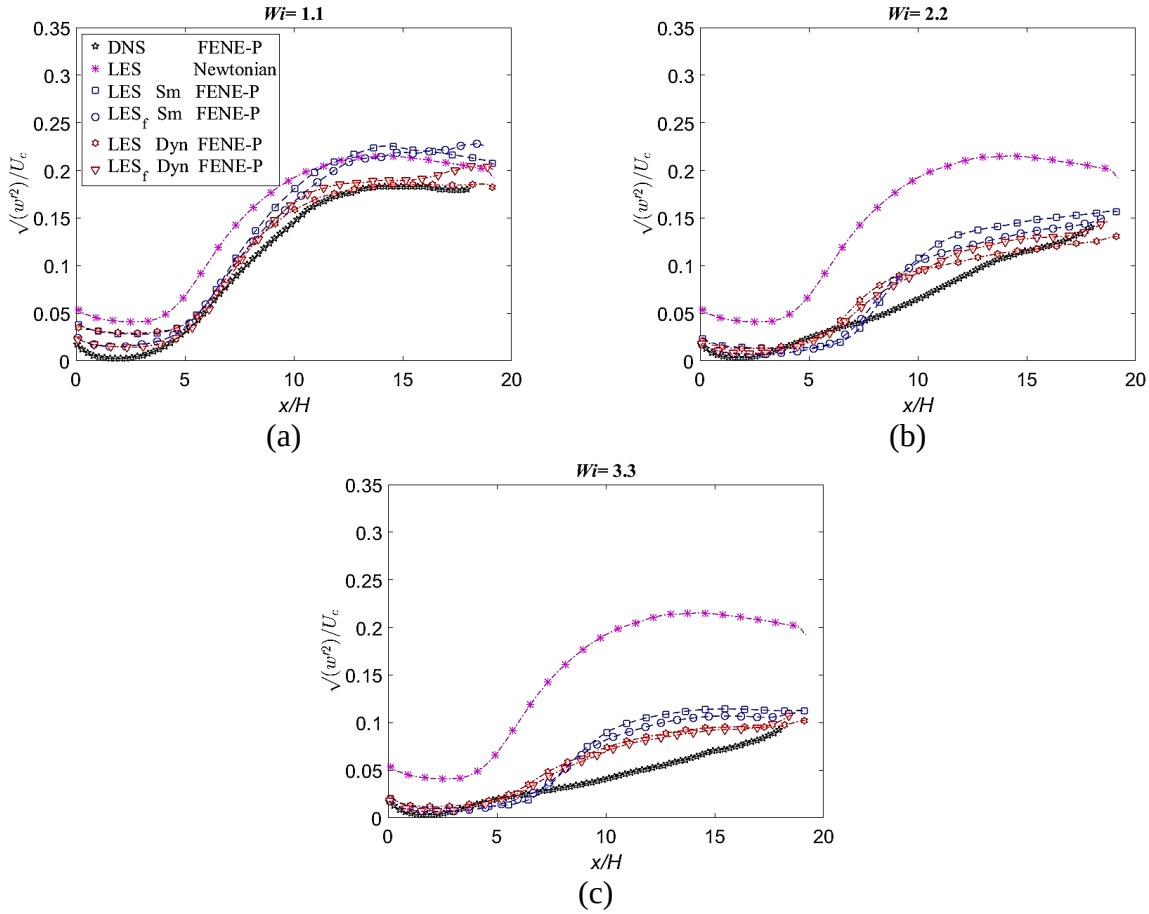

Figure 7. 18. Effect of SGS stress model on the evolution of the root-mean square of the streamwise velocity fluctuations $\sqrt{\overline{w'^2}}$ along the centerline, normalized by the centerline mean velocity ($\overline{U}_c(x)$), for *Wi* of (a) 1.1, (b) 2.2 and (c) 3.3. The DSIM closure is used in the conformation tensor equation and Smagorinsky and dynamic Smagorinsky for SGS tensor of momentum equation.

Figure 7. 19 until Figure 7. 21(a)-(c) show the corresponding effects, now on the transverse profiles of the rms of the velocity fluctuations $\sqrt{\overline{u'^2}}$, $\sqrt{\overline{v'^2}}$, and $\sqrt{\overline{w'^2}}$ predicted by LES. These are normalized by the centerline mean velocity $\overline{U}_c(x)$ and the reference DNS profiles are also shown. In the self-similar region ($x/H = 12$) the rms profiles do not collapse as seen previously with the mean velocity profiles, but are close to the DNS profiles, in particular when relying on the dynamic Smagorinsky for the SGS stress. In all cases the DSIM closure was used for the SGS distortion in the constitutive equation.

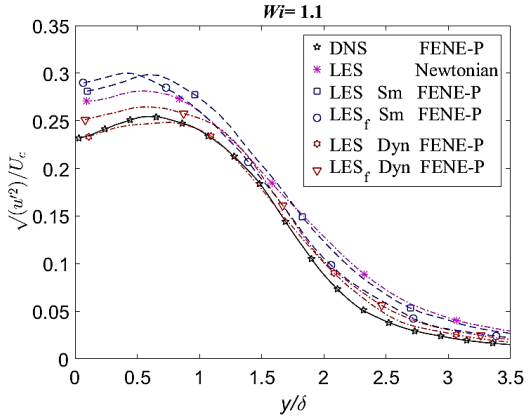

(a)

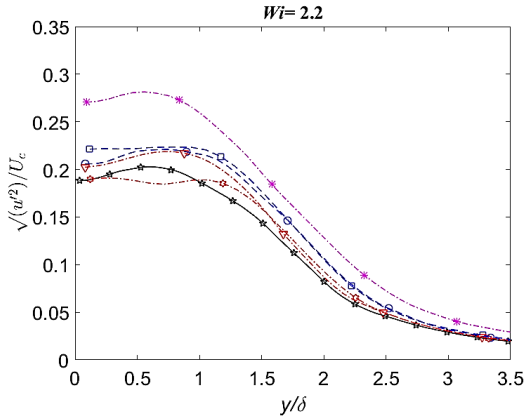

(b)

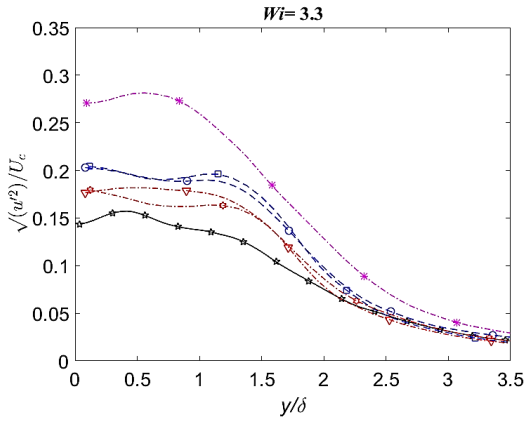

(c)

Figure 7. 19. Effect of SGS stress model on the mean profiles of the rms of the streamwise velocity fluctuations $\sqrt{\overline{u'^2}}$, normalized by the centerline mean velocity $\overline{U}_c(x)$ at $x/H = 12$ for Wi of (a) 1.1, (b) 2.2 and (c) 3.3. The DSIM closure is used in the conformation tensor equation and Smagorinsky and dynamic Smagorinsky for SGS tensor of momentum equation.

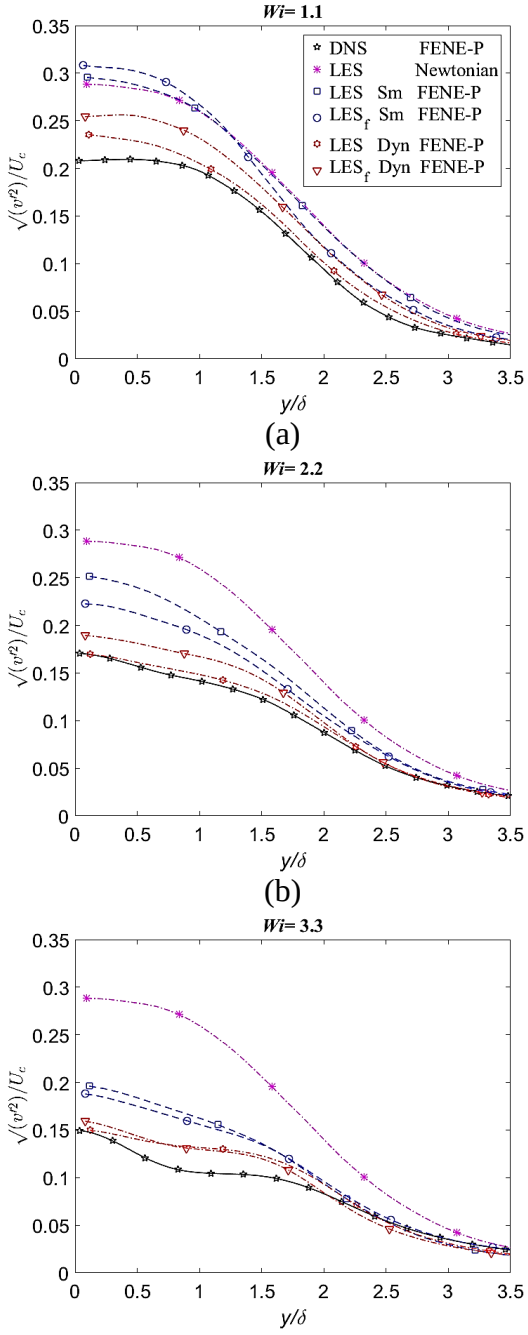

Figure 7. 20. Effect of SGS stress model on the mean profiles of the rms of the streamwise velocity fluctuations $\sqrt{\overline{v'^2}}$, normalized by the centerline mean velocity $\overline{U}_c(x)$ at $x/H = 12$ for Wi of (a) 1.1, (b) 2.2 and (c) 3.3. The DSIM closure is used in the conformation tensor equation and Smagorinsky and dynamic Smagorinsky for SGS tensor of momentum equation.

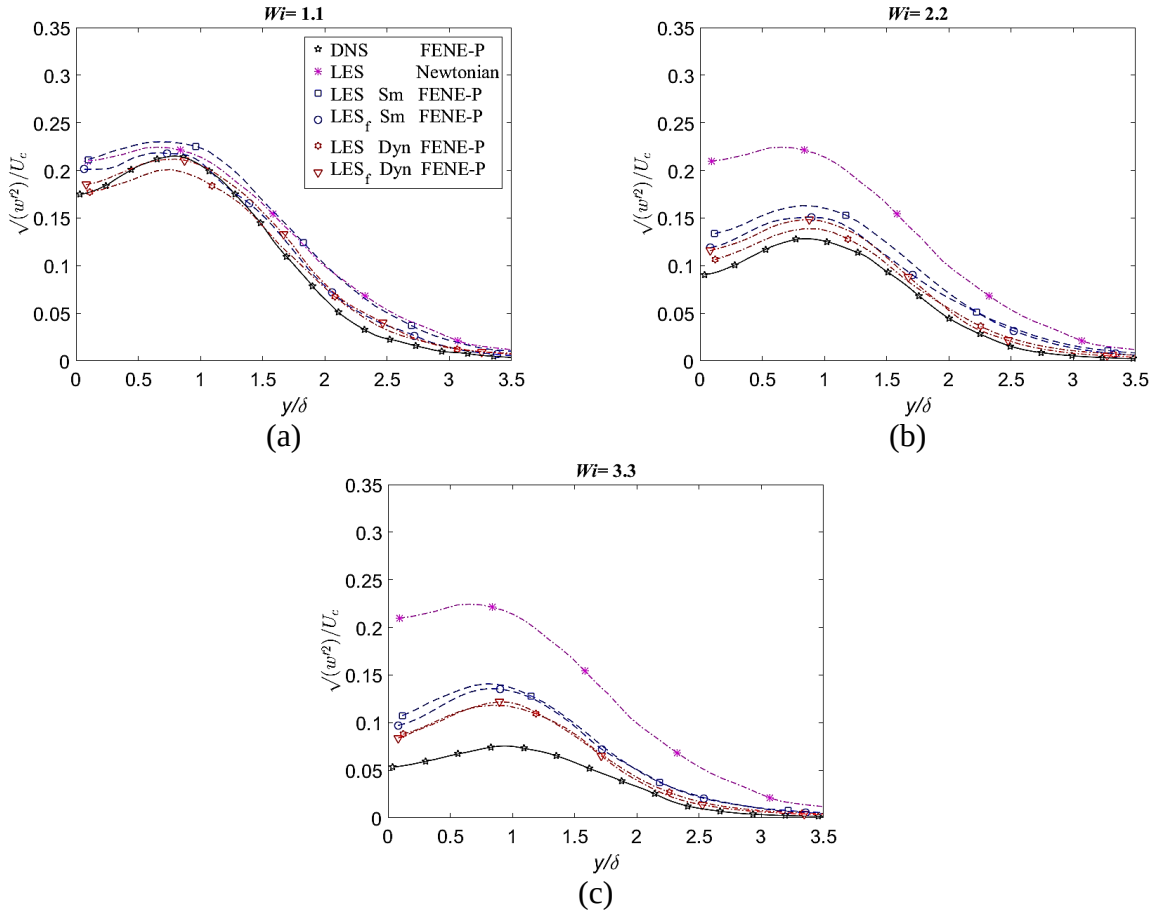

Figure 7. 21. Effect of SGS stress model on the mean profiles of the rms of the streamwise velocity fluctuations $\sqrt{\overline{w'^2}}$, normalized by the centerline mean velocity $\overline{U}_c(x)$ at $x/H = 12$ for Wi of (a) 1.1, (b) 2.2 and (c) 3.3. The DSIM closure is used in the conformation tensor equation and Smagorinsky and dynamic Smagorinsky for SGS tensor of momentum equation.

7.4.Assessment of the self-similar theory of viscoelastic turbulent planar jets

In this section we assess the performance of LES in the reproduction of the main theoretical results derived by Guimarães et al. [16] for the far field region of viscoelastic turbulent planar jets. In this theory Guimarães et al. [16] considered Townsend's hypothesis of self-preservation [167] together with the ideas put forward by Lumley [61] to describe the flow features of turbulent flows of viscoelastic fluids. In short, Lumley [61] defines characteristic velocity (u^*) and length (r^*) scales, defined as follows,

$$u^* = \sqrt{\lambda \varepsilon^s} \tag{7- 31}$$

$$r^* = \sqrt{\lambda^3 \varepsilon^s} \tag{7- 32}$$

where ε^s is the mean viscous dissipation rate of the solvent calculated by

$$\varepsilon^s = 2\upsilon_s \overline{S'_{ij} S'_{ij}} \tag{7- 33}$$

and $\overline{S'_{ij}}$ is the fluctuating rate-of-strain tensor, obtained from,

$$\overline{S'_{ij}} = \frac{1}{2}\left(\frac{\partial \overline{u'_i}}{\partial x_j} + \frac{\partial \overline{u'_j}}{\partial x_i}\right). \tag{7- 34}$$

as mentioned, in this section, the symbol of overbar means both time average and spatial average in the homogenous direction.

One of the results obtained by Guimarães et al [16] in the development of the theory of viscoelastic planar jets is the identification of the reference velocity and time scales that characterize the all the flow statistics in the self-similar far field region. In particular they found that the profiles of polymer stress all collapse into the same curve when normalized by $\rho U_c^3(x) r^* (d\delta(x)/dx)/(u^*(x)\delta(x))$. They also showed that for sufficiently high *Wi* numbers these normalized profiles are Universal.

Figure 7. 22 (a) shows the mean profiles of polymer stresses normalized as in Guimarães et al. [16], at *x/H*=12, for several Weissenberg numbers *Wi*. It is clear that the polymer stresses obtained from the present LES, using Dynamic Smagorinsky and the DSIM model, collapse into the same profile for the higher Weissenberg numbers, in agreement with the DNS and the theoretical results presented in Guimarães et al. [16].

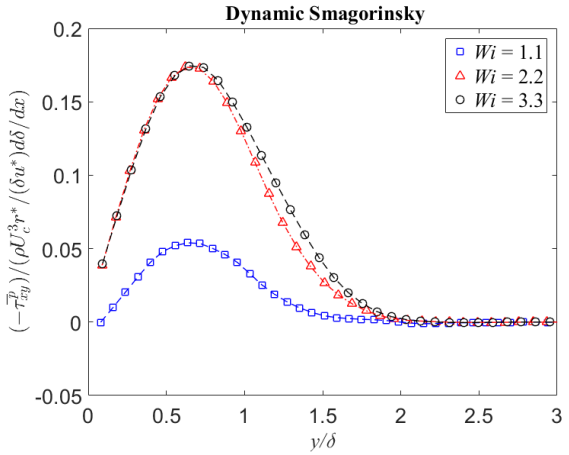

Figure 7. 22. Mean profiles of polymer shear stresses, normalized as in Guimarães et al. [16], for several Weissenberg numbers *Wi* at *x/H*=12, SGS stress closed by the dynamic Smagorinsky model.

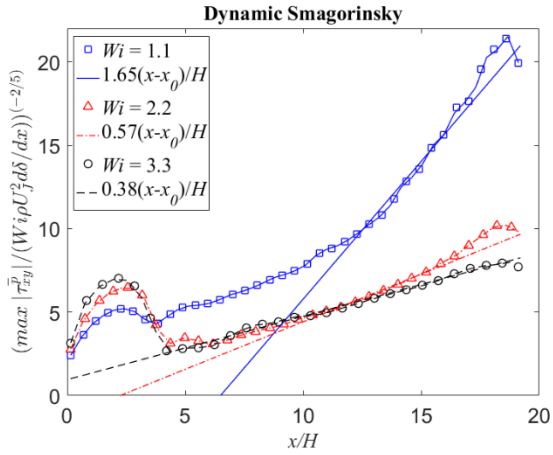

Figure 7. 23. Streamwise evolution of the maximum value of the mean polymer shear stresses, normalized as in Guimarães et al. [16], for several Weissenberg numbers, SGS stress closed by the dynamic Smagorinsky model.

Guimarães et al. [16] also derived the scaling of the decay of the maximum polymer stresses, which is described by the following relation,

$$\left(\frac{\sigma_c^p(x)}{Wi\rho U_J^2 d\delta(x)/dx}\right)^{-2/5} = A_{\sigma_c}\left(\frac{x-x_0}{H}\right), \quad (7\text{- }35)$$

where A_{σ_c} is a scaling factor. Figure 7. 23 shows the streamwise evolution of the normalized maximum polymer shear stresses obtained by LES, with the SGS stresses given by the dynamic Smagorinsky model. It is clear the present results also display the theoretical -5/2 scaling law in the self-similar far-field region, and thus agree with the turbulent viscoelastic jet theory [16]. Moreover, the constant A_{σ_c} decreases with increasing *Wi* numbers displaying values that are consistent with the DNS data of Guimarães et al. [16], particularly for the higher *Wi* numbers e.g. $Wi \geq 2$ (compare the values of this factor in Table 7. 1 and Table 7. 2).

Finally, we assess also the proposed scaling relations for the Reynolds shear stress in viscoelastic turbulent planar jets. Guimarães et al. [16] ascertained that the Reynolds shear stress should be normalized as $\overline{u'v'}\ /(\overline{U}_c^2 d\delta(x)/dx)$ for similar values of the Deborah number,

$$De = \frac{\lambda}{t_c} \quad (7\text{- }36)$$

in order to obtain the corresponding self-similar profiles. In Eq. (7- 36) $t_c = \delta(x)/U_c(x)$ is a convective time scale characteristic of the large energy-carrying eddies.

Figure 7. 24 shows profiles of normalized Reynolds shear stresses for the present LES at a single location (*x/H*=12) and *Wi*=1.1, 2.2, and 3.3, (Figure 7. 24 (a)), and at different locations *x/H*=10,11,12, for *Wi* =2.2, 3.3 (Figure 7. 24 (b)), but which correspond to approximately the same Deborah numbers ($De \approx 1.0-1.3$). Again, the profiles of the Reynolds stresses normalized as in Guimarães et al. [16] collapse into the same profile (Figure 7. 24-b), clearly indicating that the present LES recover the expected theoretical profiles observed in the reference DNS.

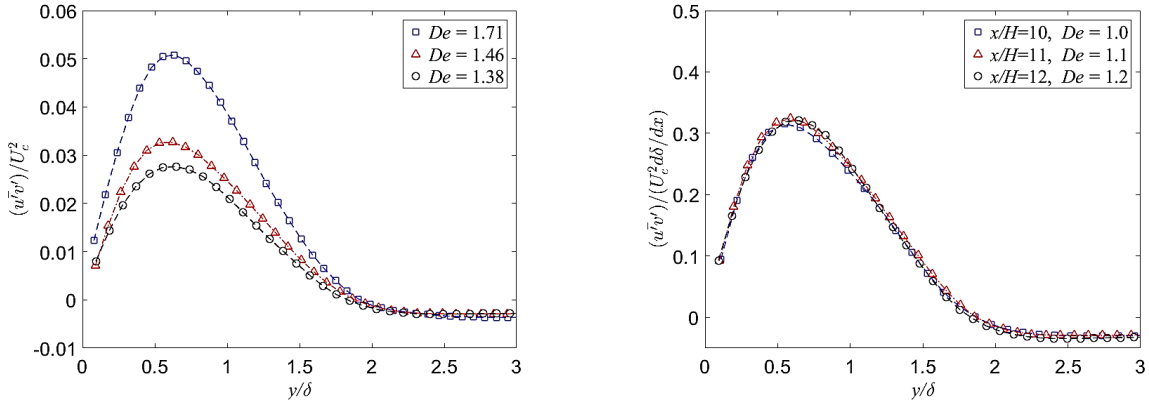

(a) (b)

Figure 7. 24. Mean profiles of Reynolds shear stresses $\overline{u'v'}$ at *x/H*=12 for several *De* numbers normalized by (a) U_c^2 and by (b) $U_c^2 d\delta(x)/dx$.

7.5.Energy spectrum

The existence of polymer would introduce another subrange between inertial range (I) and viscous dissipation range (*V*) which is called elastic subrange (*E*). As shown in (Figure 7. 25) the polymer interaction with the flow scales of motion change the slope of energy spectrum for the wave larger than a wavenumber $l_p \sim \sqrt{\varepsilon_s \lambda^3}$ is called the Lumley length scale, λ is polymer relaxation time. Fouxon and Lebedev [168] proposed the spectrum model for dilute polymer solution and Vonlanthen [169] verified it by experimental study. Vonlanthen [169] stated that the Lumley scale (l_p) separates Elastic subrange from inertial cascade region, and the features of the Elastic subrange are determined by elastic properties of fluid and turbulent dissipation rate. The partial transferred kinetic energy from Inertial subrange converted into elastic energy and stored in the stretched polymer. Although some portion of the elastic energy is dissipated because of interaction of polymer with motion scale of flow explained by viscous drag effect on polymer configuration, the remained portion of elastic energy converted and transferred back to the turbulence kinetic energy. This feature called back reaction and is the main properties of Elastic subrange [169],[170]. As a result, the energy flux continuously decrease from higher toward lower wavenumbers. Fouxon and Lebedev [168] proposed that energy spectrum as a function of the wave number (κ) in elastic subrange follow a power-law with a slope of -3 in log-log coordinates, which is valid when elastic and kinetic forces are in equilibrium. They introduced following equation for energy spectrum variation inside the elastic subrange

$$E(\kappa) = C_k \, \varepsilon_s^{\frac{2}{3}} l_p^{\frac{5}{3}} (l_p \kappa)^{-3}. \tag{7- 37}$$

n which where ε^s is dissipation rate of Newtonian solvent defined by Eq. (7- 33). For final verification, energy spectra profiles in a specific locations of different simulations are plotted in Figure 7. 26 (a)-(c).

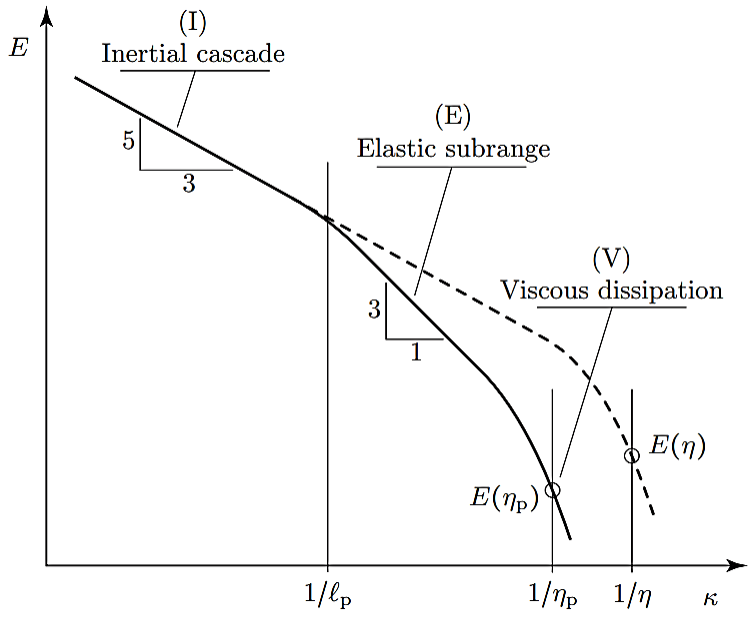

Figure 7. 25. Energy spectrum of dilute polymer solution with three main subregions: (*I*)$\kappa < 1/l_p$, Kolmogorov's inertial cascade; (E)$1/l_p < \kappa < 1/\eta_p$, Elastic subrange; (*V*) $\kappa > 1/\eta_p$, dissipation subrange is analogous to the Newtonian turbulent flow spectrum (broken line) [169].

In order to assess the performance of present LES closure, the detailed spectral energy behavior of the models is analyzed. Figure 7. 26 shows the kinetic energy spectra *E(k)* at *Wi* =1.1, 2.2, and 3.3, with combination of dynamic LES simulations and DSIM model while considering fine grids. As it is shown, the obtained energy spectra follow the -3 power law in all range of *Wi* numbers.

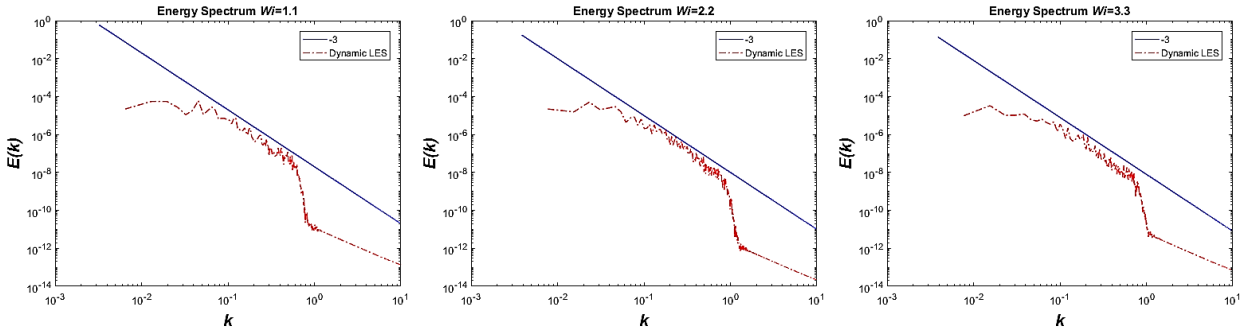

(a) (b) (c)

Figure 7. 26. The comparison Kinetic energy spectrum for LES simulation with *Wi*=1.1(a), 2.2(b), 3.3(c) at $\frac{x}{H} = 16.8$.

Part IV

Every story comes to an end

Chapter 8: Closure

8.1.Summary of main conclusions

The main objective of this thesis was the development of an LES model for viscoelastic turbulent wall-free flows, therefore the DSIM model developed by Ferreira et al. [12] for LES of homogenous isotropic turbulent flow of viscoelastic fluid was extended and assessed for the first time in an inhomogeneous turbulent flow configuration. The flow analyzed was a turbulent planar jet, for which a reference DNS exists and a new theory has been recently developed to explain the flow statistics at the far field fully developed turbulent regime (Guimarães et al. [16]). The procedure consisted in classical *a-priori* tests, which are based on applying a box filter, with filter sizes $\Delta/\Delta x = 2$, 4 and 8 to separate the resolved and unresolved/subgrid-scale components of the flow, using the reference DNS of viscoelastic turbulent planar jets carried out by Guimarães et al. [16].

The analysis revisited all the assumptions previously used by Ferreira et al. [12] in isotropic turbulence, and considered their validity in turbulent viscoelastic free flows. It turned out that all those assumptions, and most notably the assumptions of *i)* scale similarity of the subgrid-scale polymer stretching terms, and of *ii)* the local equilibrium of the elastic energy production and dissipation, hold remarkably well in the present configuration.

The DSIM model for the SGS polymer stretching term in the constitutive equation, together with the Smagorinsky and dynamic Smagorinsky models for the SGS stress in the momentum equation, were used to carry out LES of the same jets simulated in Guimarães et al. [16], although using much coarser grids. The model combining the dynamic Smagorinsky and DSIM closures gave the best results and demonstrated the ability to predict the flow structures and the classical one point statistics in the flow with reasonable accuracy.

In studying the laminar planar jet flow of viscoelastic fluids, by using arguments of boundary layer type flow and an order of magnitude analysis of the governing equations, three sets of semi-analytical solutions were obtained for steady laminar planar jet flow of FENE-P fluids, two of which are more restrictive. The more general solution was used to investigate in detail the dynamics of this laminar jet flow and was used for the purpose of validating the in-house DNS/LES code, as explained below.

The three sets of semi-analytical solutions predict essentially the same velocity fields but differ in their predictions of the viscoelastic stresses, with the general solution being able to compute all four components of the conformation tensor accurately provided the flow Weissenberg number is not too high. The accuracy of the delta method was found to deteriorate quickly with Weissenberg number, and Olagunju's type solution was unable to predict C_{xx} at very low Wi, but to properly calculate C_{yy} in the whole range of Wi. Using the general semi-analytical solution, the detailed study of the planar jet flow characteristics revealed that even though the far-field flow is approximately self-similar, at low levels of viscoelasticity all flow properties show approximately full self-similar behavior. However, as viscoelasticity becomes locally significant, the solution exhibits deviations from such low elasticity asymptotic behavior. This is the case at large values of Wi and β_p and low levels of L, while simultaneously looking at regions close to the inlet, because as the jet evolves downstream, the magnitude of the rates of deformation decrease, the effect of fluid elasticity is weakened and the flow approaches a low Wi asymptote in which both stresses are proportional.

In this condition, the ratio of polymer and solvent stress $|\tau_{ij}^{p}|/|\tau_{ij}^{s}|$ at the centerline of the jet approaches ν_P/ν_s. For low viscoelastic Mach numbers $M_\delta \leq 0.01$) the flow is essentially viscous for practical purposes, with the most sensitive quantities (C_{xx} and C_{xy}) differing from the low elasticity limit by less than 1%. In addition, outside the low elasticity flow regime the approximate similarity nature of the flow has to be understood in a broad sense, i.e., adequately normalized profiles of viscoelastic flow at different locations remain self-similar if their local viscoelastic Mach numbers are identical, for the same values of L and β_b. The variations of the peak values of the non-zero components of the conformation tensor and their locations are also reported. Rather surprisingly, the decay law for the centerline velocity was found to be very weakly dependent on fluid rheology so that for practical purposes it is essentially identical to that for Newtonian fluids. Finally, the semi-analytical general solution compared well with results of numerical simulations of jet flow undertaken with OpenFoam, based on the RheoFoam toolbox. In addition, both compared well with the numerical simulations carried out with the in-house code used to perform the direct numerical simulation (DNS) and large eddy simulations (LES) of the planar jet flows of FENE-P fluids, thus validating the code used in the turbulent flow investigation.

The boundary layer flow of FENE-P fluids over a flat plate at zero pressure gradient, initially investigated by Olagunju [20], was revisited leading to a more accurate simplified set of conformation tensor equations that still allowed a semi-analytical solution to be obtained even if limited to low values of the Weissenberg number. Due to the fluid viscoelasticity this solution showed an approximate self-similar behavior, contrasting with the full similar behavior of the corresponding Newtonian problem. The current semi-analytical solution is more accurate than Olagunju's solution for the reasons exposed above for the planar jet flow, namely because the simplifications of the conformation equation were restrictive allowing for a better description of the polymer stress tensor.

In addition, we provide a more extensive set of results of the flow characteristics than Olagunju did that include profiles of polymer stress and conformation tensor components, asymptotic laws of decay of peak stresses and conformation tensor components in the limit of low elasticity as well as laws for the location of such peak values. We also present results quantifying the boundary layer thickness as well as the displacement and momentum thicknesses. Even though the peak polymer shear stresses take place away from the wall, except in the low elasticity limit where the polymer and solvent shear stresses are proportional to each other, the peak of the total fluid shear stress is always at the wall. For large values of Wi_x and β_{p},combined with low values of L^2, one of the assumptions of the boundary layer theory starts to break down.

As is well known the boundary layer theory is not valid in the vicinity of the plate leading edge, even for a Newtonian flow, but since $Wi_x \propto x^{-1}$ this region extends further downstream of the leading edge for viscoelastic fluids. In order to assess the shortcomings of the semi-analytical solution under these conditions, and in particular at large and very large Weissenberg numbers, we provide results from the numerical solution of the full set of complete (non-simplified) governing equations using the RheoFoam toolbox of OpenFoam in order to understand the boundary layer flow and to better define the range of validity of the semi-analytical solution. For large Weissenberg numbers the semi-analytical solution still approximates reasonably well the flow characteristics, but as the Weissenberg number further increases the transverse variation of the conformation tensor components become increasing complex, exhibiting changes in the concavity of the profiles that go together with the development of large peak values within the boundary

layer when shear rates are very large, that the accuracy of semi-analytical solution for predicting polymer stress decreases.

The idea of presenting approximate similarity solutions for steady laminar viscoelastic flows was further extended to the mixing layer flow case in which boundary layer flow arguments are still valid. Hence, the same procedure was followed for the mixing layer flow of FENE-P fluids leading to a semi-analytical solution that is mathematically approximately self-similar. Again, under conditions of low elasticity, the normalised flow characteristics showed an approximately full self-similar behavior with kinematic quantities collapsing on the corresponding Newtonian self-similar data and polymer-based quantities collapsing also onto single self-similar curves. Consequently, under these low elasticity flow conditions it was also observed that the ratio of polymer over solvent stresses ($|\tau_{xy}^{\mathrm{p}}|/|\tau_{xy}^{\mathrm{s}}|$ and $|\tau_{yy}^{\mathrm{p}}|/|\tau_{yy}^{\mathrm{s}}|$) were equal to the ratio of polymer to solvent kinematic viscosities. As elasticity levels increase, by taking on larger values of Wi_x and β_p and/or low values of L, there is a progressive deviation from the low Wi asymptote curves. This thesis also reports the variations of dimensionless mixing layer thickness (δ/x), displacement thickness (δ^*/x) and momentum thickness (θ/x). At low elasticity they follow the corresponding Newtonian data, but on increasing elasticity levels a decrease of these quantities is observed. The variations of the peak values of the non-zero components of the conformation tensor and their spatial locations are also reported.

It is important to realize that the more extensive work carried out for the approximate similar boundary layer flow solution, that allowed the definition of the range of flow conditions for its validity, will necessarily have an equivalent in both the approximate laminar planar jet and planar mixing layer flows. This means that the current approximate solutions for laminar flow are accurate provided the polymer normal stress term in the streamwise momentum equation remains negligible relative to the sum of the solvent and polymer shear stress terms in the same equation. However, as elasticity effects increase to high values, there will be a severe increase in the polymer normal stress and its streamwise gradient in the momentum equation and the correct flow behavior will need the full solution of the full set of governing equations.

8.2.Suggestion for future works

The investigation in this thesis and the review of the literature has identified the need for further research in a number of topics that is discussed below.

For turbulent viscoelastic fluid flows there is still the need to develop an LES model for wall flows, whether an extension of the DSIM model or a different one. This requires performing several DNS of, say, channel or pipe flow, over a range of Reynolds and Weissenberg numbers, maximum polymer extensibility and concentration to create a bank of data which will be utilized to perform *a-priori* and *a-posteriority* tests. Afterward the DSIM closure as well as several other perspective closure of the SGS stresses should be tested to assess their performance on simulating the FENE-P turbulent wall-flow. The DSIM model may require some modification.

Regarding the SGS stress in the momentum equation, all possible LES models such as Smagorinsky, dynamic Smagorinsky, Vreman, and shear improved Smagorinsky models, to name a few, should be considered to assess their performance in turbulent wall-flow simulation in conjunction with the closures for the SGS terms of the conformation equation. In the present jet flow investigation, for the SGS term of the polymer stretching of the conformation tensor equation, the isotropic DSIM closure was found to be an adequate option to utilize in LES, however, using anisotropic DSIM model for wall-flow may provide more accurate results, consequently both options should be studied. Furthermore, it was here observed that the SGS term of advection term of conformation tensor is much lower than SGS term of polymer stretching. This hypothesis must be carefully investigated for wall-flow and, if the hypothesis fails, the advection SGS term will need to be assessed and a closure proposed for the LES model. By getting inspiration from available LES closures, one can propose new SGS models for that term.

As mentioned earlier, although the FENE-P constitutive equation has the minimum ingredients needed to describe the rheology of dilute polymer solutions, the model has its own constrains. Although FENE-P is the cheapest of FENE type models from the computational point of view and it is a proper model to study statistically steady state turbulent flows, which were the flows of interest in the present thesis, its accuracy decreases considerably if it is utilized for transient elongational flows. Therefore, another good approach is to use more accurate constitutive equations to better describe rheological properties of viscoelastic fluids. Considering the idea of Li et al., [86], utilizing the multi-mode FENE-P model would be a good start, since they stated that

the new model describes the real physical process much better than single mode FENE-P model. FENE-LS [48], FENE-PM [49], and FENE-ALS-C [50] are also appropriate models if a more elaborate model than FENE-P is required. It should be noted that implementing these two suggestions would increase the computational cost but may provide more accurate results.

In regards to the laminar flow investigations of boundary layer type flows carried out in this thesis, we observed that the proposed approximate similarity solution deviate from RheoFoam results for very large Weissenberg numbers therefore the semi-analytical solution were unable to accurately describe those flows. Furthermore, by performing an order of magnitude analysis of conformation tensor and momentum equations for highly elastic flows, a set of very complex equations were obtained. Therefore, as a suggestion of future research the present contributions could be completed if Rheofoam toolbox is utilized to study the effect of larger elasticity on flow characteristics. In addition, one may try to see whether it is possible to obtain also a semi-analytical solution under flow conditions of predominance of the normal gradient of the normal polymer stress, bearing in mind that such effort may require considerable mathematical skills.

The study of the transport phenomena, such as heat and mass, in these laminar and turbulent flows of viscoelastic fluids is another topic of interest. Of main interest in terms of industrial applications are conditions in which we have passive scalar transport to start with. For turbulent flow it will need the development of new closures for the corresponding terms in the governing equations and additional DNS simulations, for laminar flow, such endeavour can be carried out also with the use of a semi-analytical method, pursuing approximate similarity solutions limited to low *Wi* number and utilizing the Rheofoam toolbox of OpenFoam for large *Wi* number flows. Furthermore, the viscoelasticity effect on passive scalar transport in turbulent flow can be studied by the present developed DNS code.

Further investigation can be carried out for both laminar and turbulent flows by considering pressure gradient effects on turbulence models and laminar flow solutions. In the case of turbulent wall flows of viscoelastic fluids the territory is uncharted also in terms of the effects of wall roughness.

List of references

1- B. A. Toms, Some observations on the flow of linear polymer solutions through straight tubes at large Reynolds numbers, *Proceedings of the 1st International Congress on Rheologys North-Holland*, Amsterdam, Vol. 2, p. 135, 1949.

2- F. C. Li, Y. Kawaguchi, Investigation on the characteristics of turbulence transport for momentum and heat in a drag-reducing surfactant solution flow, *Phys. Fluids*, 16:3281–95, 2004.

3- A. R. Mansour, O. Swaiti, T. Aldoss, M. Issa, Drag reduction in turbulent crude oil pipelines using a new chemical solvent, *Int J Heat Fluid Fl*, 9, 316-320, 1988.

4- A. G. Fabula, Fire-fighting benefits of polymeric drag reduction, *J. Basic Eng. Trans. ASME*, 93(4), 453–455, 1971.

5- J. W. Yang, H. Park, H. H. Chun, S. L. Ceccio. M. Perlin, I. Lee, Development and performance at high Reynolds number of a skin-friction reducing marine paint using polymer additives, *Ocean Eng*, Volume 84, Pages 183-193, July 2014.

6- T. J. Ober, D. Foresti, J. A. Lewis, Active mixing of complex fluids at the microscale, Proc *Natl Acad Sci USA*.112(40): 12293–12298, 2015 Oct 6. Published online 2015 Sep 22, *Applied Physical Sciences*.

7-J. N. Marhefka, M. V. Kameneva, Natural Drag-Reducing Polymers: Discovery, Characterization and Potential Clinical Applications, *Fluids*, 1, 6, 2016.

8-A. Pribush, L. Hatzkelzon, D. Meyerstein,N. Meyerstein,The mechanism of the polymer-induced drag reduction in blood, Colloids and Surfaces B: *Bio interfaces*, Volume 103, Pages 354-359, March 2013.

9- W. J. Orts, R. E. Sojka, G. M. Glenn, Polymer additives in irrigation water to reduce erosion and better manage water infiltration, *Agro-Food-industry Hi-Tech* - July/August 2002.

10-H. Lee, K. Neville, The Challenge for High Polymers in Medicine, Surgery, and Artificial Internal Organs, *J. Macromol. Sci.*: Part A – Chemistry, Volume 4, Issue 3, 1970.

11-P. C. Sousa, F. T. Pinho, M. S. N. Oliveira, M. A. Alves, Extensional flow of blood analog solutions in microfluidic devices, *Biomicrofluidics*. 5(1): 014108, March, 2011.

12-P. O. Ferreira, F. T. Pinho, C. B. Silva, Large-eddy simulations of forced isotropic turbulence with viscoelastic fluids described by the FENE-P model. *Phys. Fluids*, 28 125104, 2016.

13-P. C. Valente, C. B. Silva, F. T. Pinho, The effect of viscoelasticity on the turbulent kinetic energy cascade. *J. Fluid Mech.*, 760, 39-62, 2014.

14- P. C. Valente, C. B. da Silva, F. T. Pinho, Energy spectra in elasto-inertial turbulence, *Phys. Fluids*, 28, 075108, 2016.

15-L. Wang, W. H. Cai, F. C. Li, Large-eddy simulations of a forced homogenous isotropic turbulence with polymer additives. *China Phys. B*, 23, 34701, 2014.

16- M. C. Guimarães, N. Pimentel, F. T. Pinho, C. B. da Silva, Direct numerical simulations of turbulent viscoelastic jets described by the FENE-P model. *J. Fluid Mech.*, vol. 899, A11, 2020. doi:10.1017/jfm.2020.402.

17-F. Pimenta, M. Alves, Stabilization of an open-source finite-volume solver for viscoelastic fluid flows, *J. Non-Newt. Fluid Mech.*, 239, 85 – 104, 2017.

18-F. Pimenta, M. A. Alves, rheoTool, https://github.com/fppimenta/rheoTool, (2016).

19-D. O. Olagunju, Local similarity solutions for boundary layer flow of a FENE-P fluid, *Appl. Math. Comput.*, 173, 593–602, 2006a.

20-D. O. Olagunju, A self-similar solution for forced convection boundary layer flow of a FENE-P fluid, *Appl Math Lett.*, 19, 432–436, 2006b.

21-M. Masoudian, C. B. Silva, F. T. Pinho, Grid and sub-grid scale interactions in viscoelastic turbulent flow and implications for modelling, *J. Turbul.*, 17:6, 543-571, 2016.

22- https://dictionary.cambridge.org/dictionary/english/fluid

23- F. M. White, *Viscous Fluid Flow*, 3rd edition, published by McGraw Hill 2006.

24-H. Schlichting, K. Gersten, *Boundary-Layer Theory*, 8th Revised and Enlarged Edition, published by McGraw Hill, 1999.

25- R. B. Bird, R. C. Armstrong, O. Hassager, *Dynamics of Polymeric Liquids*, Vol. 1: *Fluid Mechanics*, 2nd Edition, ISBN: 978-0-471-80245-7, May (1987), 672 Pages.

26-R. B. Bird, C. F. Curtiss, R. C. Armstrong, O. Hassager, *Dynamics of polymeric fluids.* Vol. 2: *Kinetic Theory*, 2nd edition, Wiley, New York, 1987.

27-R. B. Bird, P. J. Dotson, N. L. Johnson, Polymer solution rheology based on a finitely extensible bead-spring chain model. *J. Non-Newt. Fluid Mech.*, 7, 213-235, 1980.

28-Y. Dubief, V. Terrapon, J. Soria, On the mechanism of elasto-inertial turbulence, *Phys. Fluids* 25, 110817, 2013.

29-H. D. Xi, E. Bodenschatz, H. Xu, Elastic energy flux by flexible polymers in fluid turbulence, *Phys. Rev. Lett.*, 111, 24501, 2013.

30-J. G. Oldroyd, On the formulation of rheological equations of state, Proceedings Of the Royal Society A, Mathematical, *Phys. Eng. Sci.*, 1950.

31-https://en.wikipedia.org/wiki/James_G._Oldroyd.

32-H. R. Warner, Kinetic theory and rheology of dilute suspensions of finitely extendible dumbbells, *Ind. Eng. Chem. Fundam.*, 11, 379-387, 1972.

33-Q. Zhou, R. Akhavan, A comparison of FENE and FENE-P dumbbell and chain models in turbulent flow, *J. Non-Newt. Fluid Mech.*, 109, 115–155, 2003.

34-M. Chilcott, J. Rallison, Creeping flow of dilute polymer solutions past cylinders and spheres, *J. Non-Newt. Fluid Mech.*, 29, 381, 1988.

35-A. Peterlin, Streaming birefringence of soft linear macromolecules with finite chain length, *Polymer 2*, 257, 1961.

36-M. Herrchen, H. C. Ottinger, A detailed comparison of various FENE dumbbell models, *J. Non-Newt. Fluid Mech.*, 68, 17-42, 1997.

37-G. Lielens, R. Keunings, V. Legat, The FENE-L and FENE-LS closure approximations to the kinetic theory of finitely extensible dumbbells, *J. Non-Newt. Fluid Mech.*, 87, 179–196, 1999.

38-L. E. Wedgewood, D. N. Ostrov, R. B. Bird, A finitely extensible bead-spring chain model for dilute polymer solutions, *J. Non-Newt. Fluid Mech.*, 40, 119–139, 1991.

39-I. Ghosh, Y. L. Joo, G. H. McKinley, R.A. Brown, R.C. Armstrong, A new model for dilute polymer solutions in flows with strong extensional components, *J. Rheol*. 46 (5), 1057–1089, 2002.

40-R. Sizaire, G. Lielens, I. Jaumain, R. Keunings, V. Legat, On the hysteretic behaviour of dilute polymer solutions in relaxation following extensional flow, *J. Non-Newt. Fluid Mech.*, 82, 233-253, 1999.

41-T. Watanabe, T. Gotoh, Hybrid Eulerian-Lagrangian simulations for polymer-turbulence interactions. *J. Fluid Mech.*, 717, 53-575, 2013.

42-A. N. Beris, B. J. Edwards, *Thermodynamics of flowing systems with internal microstructure,* Oxford Science Publication, New York, 1994.

43-T. Vaithianathan, L. R. Collins, Numerical approach to simulating turbulent flow of a viscoelastic polymer solution. *J. Comput. Phys.* 187: 1-21, 2003.

44-C. F. Li, V. K. Gupta, R. Sureshkumar, B. Khomami, Turbulent channel flow of dilute polymeric solutions: drag reduction scaling and an eddy viscosity model, *J. Non-Newt. Fluid Mech.*,139, 177-189, 2006.

45-K. Kim, R. J. Adrian, S. Balachandar, R. Sureshkumar, "Dynamics of hairpin vortices and polymer-induced turbulent drag reduction". *Phys. Rev. Lett*., 100(13), 134504, 2008.

46-S. B. Pope, *Turbulent flows*. Cambridge University Press, Cambridge, 2000.

47-https://encyclopedia2.thefreedictionary.com/Ergodic+principle

48-P. Sagaut, *Large eddy simulation for incompressible flows*, 3rd edition, Springer, Berlin, 2005.

49-L. F. Richardson, Weather Prediction by Numerical Process. Cambridge: Cambridge University Press, 1922.

50- L. Onsager, 1949d, Nuovo Cimento, Suppl. 6, 279.

51- A. N. Kolmogorov, The local structure of turbulence in incompressible viscous fluid for very large Reynolds numbers. *Dokl. Akad. Nauk SSSR* 30, 299–303 [in Russian], 1941b.

52- A. M. Obukhov, The spectral energy distribution in a turbulent flow. *Dokl. Akad. Nauk SSSR* 32, 22–24 [in Russian], 1941.

53-A. S. Orszag, G. S. Patterson, Numerical Simulation of Three-Dimensional Homogeneous Isotropic Turbulence, *Phys. Rev. Lett.* 28, 76 – Published 10 January 1972.

54-J. Jiménez, Computing high-Reynolds-number turbulence: will simulations ever replace experiments, *J. Turbulence*, 4, N22, 2003.

55-O. Reynolds, On the Dynamical Theory of Incompressible Viscous Fluids and the Determination of the Criterion. *Philosophical Transactions of the Royal Society of London*. A, v. 186, pp. 123-164. 1895. Available online from JSTOR.

56-J. Smagorinsky, General Circulation Experiments with the Primitive Equations. *Monthly Weather Review*. 91 (3): 99–164, March 1963.

57-J. Deardorff, A numerical study of three-dimensional turbulent channel flow at large Reynolds numbers, *J. Fluid Mech.*, 41 (2): 453–480, 1970.

58-M. Lesieur, O. Metais, New trends in large eddy simulations of turbulence, *Annu. Rev. Fluid. Mech.* 1996.28:45-82.

59-U. Piomelli, Large-eddy simulation: achievements and challenges, *Progress in Aerospace Sciences*,35 (1999) 335-362,

60-C. Meneveau, J. Katz, Scale-invariance and turbulence models for large eddy simulation, *Annu. Rev. Fluid Mech*, 32:1–32, 2000.

61- J. L. Lumley, Drag reduction by additives. *Annu. Rev. Fluid Mech*. 1:367–384, 1969.

62- I. Procaccia, V. L'vov, R. Benzi, Colloquium: Theory of drag reduction by polymers in wall-bounded turbulence. *RMP*,80(1), 225, 2008.

63- C. M. White, M. G. Mungal, Mechanics and prediction of turbulent drag reduction with polymer additives, *Annu. Rev. Fluid Mech.*, 40, 235-256, 2008.

64- W. D. McComb, L. H. Rabie, Development of local turbulent drag reduction due to nonuniform polymer concentration. *Phys. Fluids* (1958-1988), 22(1), 183-185, 1979.

65- D. I. H. Bewersdorff, Effect of a centrally injected polymer thread on drag in pipe flow. *In Progress and Trends in Rheology* (pp. 233-235). Steinkopff, 1982.

66- M. Tabor, P. G. De Gennes, A cascade theory of drag reduction. *EPL (Europhysics Letters)*, 2(7), 519, 1986.

67- P. G. De Gennes, *Introduction to polymer dynamics*. CUP Archive, 1990.

68- T. Wei, W. W. Willmarth, Modifying turbulent structure with drag reducing polymer additives in turbulent channel flows, *J. Fluid Mech.*, 245, 619-641, 1992.

69- M. D. Warholic, H. Massah, T. J. Hanratty, Influence of drag reducing polymers on turbulence: effects of Reynolds number, concentration and mixing. *Exp Fluids*, 27(5), 461-472, 1999.

70- E. De Angelis, C. M. Casciola, V. S. L'vov, R. Piva, I. Procaccia, Drag reduction by polymers in turbulent channel flows: Energy redistribution between invariant empirical modes. *Phys. Rev. E*, 67(5), 056312, 2003.

71-E. De Angelis, C. M. Casciola, R. Benzi, R. Piva, Homogeneous isotropic turbulence in dilute polymers, *J. Fluid Mech.*, 531, 1-10, 2005.

72-K. D. Housiadas, A. N. Beris, Polymer-induced drag reduction: Effects of the variations in elasticity and inertia in turbulent viscoelastic channel flow, *Phys. Fluids* (1994-present), 15(8), 2369-2384, (2003).

73-Y. Dubief, C. M. White, V. E. Terrapon, E. S. Shaqfeh, P. Moin, S. K. Lele, On the coherent drag-reducing and turbulence-enhancing behaviour of polymers in wall flows, *J. Fluid Mech.*, 514, 271-280, 2004.

74-H.-D. Xi, E. Bodenschatz, H. Xu, Elastic Energy Flux by Flexible Polymers in Fluid Turbulence. *Phys. Rev. Lett.*, 111(2), 2013.

75-C.-F. Li, R. Sureshkumar, B. Khomami, Simple framework for understanding the universality of the maximum drag reduction asymptote in turbulent flow of polymer solutions, *Phys. Rev. E* 92, 043014 (2015).

76-L. Xi, M. D. Graham, Intermittent dynamics of turbulence hibernation in Newtonian and viscoelastic minimal channel flows, *J. Fluid Mech*. (2012), vol. 693, pp. 433–472.

77-L. Xi, M. D. Graham, Active and Hibernating Turbulence in Minimal Channel Flow of Newtonian and Polymeric Fluids, *Phys. Rev. Lett.*, May 2010, 1004.5159v1, physics.flu-dyn, 28 Apr 2010.

78-F. T. Pinho, C. F. Li, B. A. Younis, R. Sureshkumar, A low Reynolds number k–e turbulence model for FENE-P viscoelastic fluids, *J. Non-Newt. Fluid Mech*., 154, 89–108, 2008.

79-F. T. Pinho, C. F. Li, B. A. Younis, R. Sureshkumar, Corrigendum to ‘‘A low Reynolds number turbulence closure for viscoelastic fluids’’, *J. Non-Newt. Fluid Mech.*, 51, 181–182, 2012.

80-P. R. Resende, K. Kim, B. A. Younis, R. Sureshkumar, F.T. Pinho, A FENE-P k–e turbulence model for low and intermediate regimes of polymer-induced drag reduction, *J. Non-Newt. Fluid Mech.*, 166, 639–660, 2011.

81-G. Iaccarino, E. S. G. Shaqfeh, Y. Dubief, Reynolds-averaged modeling of polymer drag reduction in turbulent flows, *J. Non-Newt. Fluid Mech.*, 165, 376–384, 2010.

82-M. Masoudian, K. Kim, F. T. Pinho, R. Sureshkumar, A viscoelastic k-ε-v^2-f turbulent flow model valid up to the maximum drag reduction limit. *J. Non-Newt. Fluid Mech*, 202, 99-111, 2013.

83-C. B. Silva, O. Metais, On the influence of coherent structures upon interscale interactions in turbulent plane jets. *J. Fluid Mech.*, 473, 103-145, 2002.

84-T. Ohta, M. Miyashita, DNS and LES with an extended Smagorinsky model for wall turbulence in non-Newtonian viscous fluids. *J. Non-Newt. Fluid Mech*., 206, 29-39, 2014.

85-L. Thais, A. E. Tejada-Martinez, T. B. Gatski, G. Mompean, Temporal large eddy simulations of turbulent viscoelastic drag reduction flow. *Phys. Fluids*, 22, 13103, 2010.

86-J. Li, B. Yu, S. Sun, D. Sun, Y. Kawaguchi, An N-parallel FENE-P constitutive model and its application in large-eddy simulation of viscoelastic turbulent drag-reducing flow, *J. Comput. Sci.*, 29, 70–80, 2018.

87- D. A. White, Velocity measurements in axisymmetric jets of dilute polymer solutions. *J. Fluid Mech.*, 28 195, 1967.

88- S. J. Barker, Laser-Doppler measurements on a round turbulent jet in dilute polymer solutions, *J. Fluid Mech.*, 60, 721, 1973.

89- N. S. Berman, H. Tan, Two-component laser-Doppler velocimeter studies of submerged jets of dilute polymer solutions, *AIChEJ*, 31, 208, 1985.

90-K. Koziol, P. Glowacki, Turbulent jets of dilute polymer solutions, *J. Non-Newt. Fluid Mech.*, 32, 311, 1989.

91-H. Usui, Y. Sano, Turbulence structure of submerged jets of dilute polymer solutions, *J. Chem. Eng. Japan*, 13, 401, 1980.

92-M. Kwade, Beeinflussung der Turbulenzstruktur in der Ebener Mischungsschicht Zweier Ströme Durch Polymerzusätze, *Rheol. Acta* 21, 120, 1982.

93-M. Hibberd, M. Kwade, R. Scharf, Influence of drag reducing additives on the structure of turbulence in a mixing layer. *Rheol. Acta*, 21, 582, 1982.

94-L. Prandtl, in Verhandlungen des dritten internationalen Mathematiker-Kongresses in Heidelberg 1904, A. Krazer, ed., Teubner, Leipzig, Germany (1905), p. 485-491, in German. English translation: in Early Developments of Modern Aerodynamics, J. A. K. Ackroyd, B. P. Axcell, A. I. Ruban, eds., Butterworth-Heinemann, Oxford, UK (2001), p. 77.

95-D. Tempelmann, A. Hanifi, D. Henningson, Spatial optimal growth in three-dimensional boundary layers. *J. Fluid Mech.*, 646, 5-37, 2010.

96- W. S. Saric, A. L. Carpenter, H. L. Reed, Passive control of transition in three-dimensional boundary layers, with emphasis on discrete roughness elements. *Phil. Trans. Roy. Soc. Lond.* A, 369, 1352-1364, 2011.

97-G. Meneghello, P. J. Schmid, P. Huerre, Receptivity and sensitivity of the leading-edge boundary layer of a swept wing. *J. Fluid Mech.*, 775, R1, 2015.

98- P. S. Virk, Drag reduction fundamentals. *AIChE Journal*, 21(4), 625-656,1975.

99- J. L. Lumley, Drag reduction in turbulent flow by polymer additives, *J. Polym. Sci.*: Macromolecular Reviews, Vol. 7, 263-290, 1973,

100- M. Tabor, P. G. de Gennes, A cascade theory of drag reduction. *Europhys. Lett.* 2:519–22, 1986.

101- R. Sureshkumar, A. N. Beris, Effect of artificial stress diffusivity on the stability of numerical calculations and the flow dynamics of time-dependent viscoelastic flows, *J. Non-Newt. Fluid Mech.*, 60, 53–80, 1995.

102- A. C. Srivastava, The flow of a non-Newtonian liquid near a stagnation point, *Z. Angew Math. Phys.*, 9, 80–84, 1958.

103-G. Rajeswari, S. L. Rathna, Flow of a particular class of non-Newtonian visco-elastic and visco-inelastic fluids near a stagnation point, *Z. Angew Math. Phys.* 13, 43–57, 1962.

104-T. Von Kármán, "Über laminare und turbulente Reibung" (PDF). *Zeitschrift für Angewandte Mathematik und Mechanik.* 1 (4): 233–252, 1921.

105-K. Pohlhausen, Zur nähenmgsweisen Integration der Differential-gleichung der laminaren Reibungsschicht, Z. agnew, *Math, Mech*, Vol. 1, pp. 252-268, 1921.

106- D. W. Beard, K. Walters, Elastico-viscous boundary layer flow, *Proc. Camb. Philos. Soc.* 60, 667–674, 1964.

107- K. R. Rajagopal, A. S. Gupta, T. Y. Na, A note on the Falkner–Skan flows of a Non-Newtonian fluid, *J. Non-Linear Mech.* 18 (4), 313–320, 1983.

108- R. G. Larson, *The Structure and Rheology of Complex Fluids*, Oxford University Press Inc, ISBN10: 019512197X, 688 Pages, Jan 1999.

109-N. Phan-Thien, R. I. Tanner., New constitutive equation derived from network theory, *J. Non-Newton. Fluid Mech*., 2, pp. 353-365, 1977.

110- L. L. Ferrás, M. L. Morgado, M. Rebelo, G. H. McKinley, A. M. Afonso, A generalised Phan–Thien—Tanner model, *J. Non-Newton. Fluid Mech.*, Volume 269, Pages 88-99, July 2019.

111-H. Blasius, Grenzschichten in Flussikeinten mit Kleiner Reibung, *Z. Angew. Math. Phys.* Vol. 56, pp.1-37,http://naca.central.cranfield.ac.uk/reports/1950/naca-tm-1256.pdf

112-S. Parvar, C. B. da Silva, F. T. Pinho, Local similarity solution for steady laminar planar jet flow of viscoelastic FENE-P fluids, *J. Non-Newton. Fluid Mech.*, 279, 104265, 2019.

113-S. Parvar, C. B. da Silva, F. T. Pinho, Corrigendum to "Local similarity solution for steady laminar planar jet flow of viscoelastic FENE-P fluids" [*J. Non-Newt. Fluid Mech.* 279 (2020) 104265], *J. Non-Newton. Fluid Mech.*, 281, 104309, 2020.

114-M. Lessen, *On Stability of free Laminar boundary layer between parallel streams*, Report NACA-TR-979, NACA, (1950), https://ntrs.nasa.gov/search.jsp?R=19930092040, as assessed on DATE (30/06/2020).

115- D. R. Chapman, *Laminar mixing of a compressible fluid*, Report NACA-TR-958, (1950), https://ntrs.nasa.gov/search.jsp?R=19930092022, as assessed on DATE (30/06/2020).

116- A. M. Kuethe, *Investigations of turbulent mixing regions*, Thesis of Doctor of Philosophy, California Institute of Technology, Pasadena, California, (1933). https://thesis.library.caltech.edu/1459/, as assessed on DATE (30/06/2020).

117- R. C. Lock, The velocity distribution in the laminar boundary layer between parallel streams, The Quarterly *J. Mech. Appl. Math.*, Volume 4, Issue 1, (1951), 42–63.

118- J. F. Nash, *Laminar Mixing of a Non-Uniform Stream with a Fluid at Rest*, Ministry of Aviation Aeronautical research Council, C. P. No. 613, (1962), downloaded from: http://naca.central.cranfield.ac.uk/reports/arc/cp/0613.pdf, as assessed on DATE (30/06/2020).

119-L. Ting, On the Mixing of Two Parallel Streams, *J Math Phys.*, Volume38, Issue1-4, 153-165, 1959.

120- J. B. Klemp, A. Acrivos, A note on the laminar mixing of two uniform parallel semi-infinite streams, *J. Fluid Mech., vol.* 55, *part* 1, 25-30, 1972.

121-J. Azaiez,G. M. Homsy, "Linear stability of free shear flow of viscoelastic liquids," *J. Fluid Mech.* 268, 37–69, 1994.

122-P. K. Ray, T. A. Zaki, Absolute instability in viscoelastic mixing layers, *Phys. Fluids*, 26, 014103, 2014.

123-A. Varshney, V. Steinberg, Mixing layer instability and vorticity amplification in a creeping viscoelastic flow, arXiv:1809.09383v1: *Fluid Dynamics* 3 (2018).

124- T. Cebeci, P. Bradshaw, *Physical and Computational Aspects of Convective Heat Transfer*, Springer-Verlag Berlin Heidelberg.

125- E. M. Sparrow, H. Quack, C. J. Boerner, Local non-similarity boundary-layer solutions, *AIAA Journal*, Vol8, No. 11 Published Online:17 May 2012.

126- E. M. Sparrow, H. S. Yu, Local Non-Similarity Thermal Boundary-Layer Solutions. *ASME. J. Heat Transf.* November 1971; 93(4): 328–334.

127- M. Massoudi, Local non-similarity solutions for the flow of a non-Newtonian fluid over a wedge, *International J. Non-Linear Mechanics*, Volume 36, Issue 6, 2001, Pages 961-976, ISSN 0020-7462,

128- T.Y. Na, *Computational Methods in Engineering Boundary Value Problems*, Academic Press, New York (1979).

129- R. Seshadri, T.Y. Na, *Group Invariance in Engineering Boundary Value Problems*, Springer, New York (1985).

130-L. Edberg, *Introduction to computation and modeling for differential equations*, Second Edition, Published by John Wiley & Sons, Inc., Hoboken, New Jersey, Published simultaneously in Canada, 2016.

131-W. H. Press, S. A. Teukolsky, W. T. Vetterling, B. P. Flannery, *Numerical Recipes*, The Art of Scientific Computing, Third Edition, Cambridge Press, 2007.

132-G. Birkhoff, S. MacLane, A Survey of Modern Algebra (Akp Classics), *A K Peters/CRC Press*; 5th edition, 1998.

133-Https://math.vanderbilt.edu/schectex/courses/cubic/ as assessed on (6/16/2020).

134-M. A. Alves, P. J. Oliveira, F. T. Pinho, A convergent and universally bounded interpolation scheme for the treatment of advection. *Int J Numer Methods Fluids*, 41, 47–75, 2003.

135-P. E. Dimotakis, The mixing transition in turbulent flows, *J. Fluid Mech.*, vol. 409, 69-98, 2000.

136-S. Parvar, C. B. da Silva, F. T. Pinho, Revisiting the laminar boundary layer flow of viscoelastic FENE-P fluids, submitted to *Phys. Fluids*, (2020).

137-R. Reis, the dynamics of coherent vortices near the turbulent/non-turbulent interface analysed by direct numerical simulations, *PhD thesis, Instituto Superior Técnico*, 2011.

138-D. Lopes, Direct and Large-Eddy Simulations of the Turbulent Entrainment of Passive Scalars in Planar Jets, *PhD thesis, Instituto Superior Técnico*, 2014.

139-C. B. Silva, D. C. Lopes, V. Raman, The effect of subgrid-scale models on the entrainment of a passive scalar in a turbulent planar jet, *J. Turbul.*, Vol. 16, No. 4, 342–366, 2015.

140-S. K. Lele, Compact finite difference schemes with spectral-like resolution, *J. Comp. Phys.*, 103, 15–42, 1992.

141-S. A. Oszag, Numerical Methods for the Simulation of Turbulence, *Phys. Fluids*, 12 II–250, 1969.

142-F. Dupret, J.M. Marchal, Loss of evolution in the flow of viscoelastic fluids, *J. Non-Newt. Fluid Mech.*, 20, 143–171, 1986.

143-T. Min, J.Y. Yoo, H. Choi, Effect of spatial discretization schemes on numerical solutions of viscoelastic fluid flows, *J. Non-Newt. Fluid Mech.*, 100, 27–47, 2001.

144-Y. Dubief, S. K. Lele, Direct Numerical Simulation of Polymer Flow, Center for Turbulence Research, *Annual Research Briefs, NASA*, Ames/Stanford University, pp. 197–208, 2001.

145-B. Yu, Y. Kawaguchi, Direct numerical simulation of viscoelastic drag-reducing flow: a faithful finite difference method, *J. Non-Newt. Fluid Mech.* ,116, 431–466, 2004.

146-T. Vaithianathan, Ashish Robert, James G. Brasseur, Lance R. Collins, An improved algorithm for simulating three-dimensional, viscoelastic turbulence, *J. Non-Newt. Fluid Mech.* 140, 3–22, 2006.

147-H. S. Carslaw. "Chapter IX". *Introduction to the theory of Fourier's series and integrals* (Third ed.). New York: Dover Publications Inc, 1930.

148-A. Kurganov, E. Tadmor, New high-resolution central schemes for nonlinear conservation laws and convection–diffusion equations, *J. Comput. Phys.*, 160, 241–282, 2000.

149-M. Germano, U. Piomelli, P. Moin, W. H. Cabot, dynamic subgrid-scale eddy viscosity model, *Phys. Fluids* A: Fluid Dynamics 3, 1760, 1991.

150-S. Parvar, C. B. da Silva, F T. Pinho, Mixing layer flow of viscoelastic FENE-P fluids, submitted to ..., (December 2020).

151-S. Liu, C. Meneveau, J. Katz, On the properties of similarity subgrid-scale models as deduced from measurements in a turbulent jet, *J. Fluid Mech.*, 275, 83–119 1994.

152-J. Bardina, J. H. Ferziger, W. C. Reynolds, Improved subgrid model for large-eddy simulation, *AIAA*, Paper No.80-1357, 1980.

153-R. Sureshkumar, A. N. Beris, R. A. Handler, Direct numerical simulation of the turbulent channel flow of a polymer solution. *Phys. Fluids*, 9, 743-755, 1997.

154-K. Kim, C. Li, R. Sureshkumar, S. Balachandar, R. J. Adrian, Effects of polymer stresses on eddy structures in drag-reduced turbulent channel flow. *J. Fluid Mech.*, 584, 281-299, 2007.

155-K. Horiuti, K. Matsumoto, K. Fujiwara, Remarkable drag reduction in non-affine viscoelastic turbulent flows. *Phys. Fluids*, 25, 015106, 2013.

156-M. D. Graham, Drag reduction and the dynamics of turbulence in simple and complex fluids. *Phys. Fluids*, 26 (10), 101301. 2014.

157- A. W. Vreman, An eddy-viscosity subgrid-scale model for the turbulent shear flow: Algebraic theory and applications, *Phys. Fluids*, 16(10):3670, 2004.

158- E. L´eveque, F. Toschi, L. Shao, J.-P. Bertoglio, Shear-improved Smagorinsky model for large-eddy simulation of wall bounded turbulent flows. *J. Fluid Mech.*, 570:491, 502, 2007.

159-E. Gutmark, I. Wygnansky, The planar turbulent jet, *J. Fluid Mech.*,73:465–495, 1976.

160-L. J. S. Browne, R. A. Antonia, S. Rajagopalan, A. J. Chambers, Interaction region of a two-dimensional turbulent plane jet in still air, In: Dumas R, Fulachier L, editors. Structure of complex turbulent shear flow, *IUTAM Symp*. Marseille: Springer; 1982.

161-F. O. Thomas, H. C. Chu. An experimental investigation of the transition of the planar jet: subharmonic suppression and upstream feedback. *Phys. Fluids*.;1 (9):1566–1587, 1989.

162-R. C. Deo, J. Mi, G. J. Nathan, The influence of Reynolds number on a plane jet. *Phys. Fluids*, 20(7), 2008.

163-R. C. Deo, G. J. Nathan, J. Mi, Similarity analysis of the momentum field of a subsonic, plane air jet with varying jet-exit and local Reynolds numbers. *Phys Fluids*,25:015115, 2013.

164-S. Stanley, A. Sarkar, J. P. Mellado, A study of the flow field evolution and mixing in a planar turbulent jet using direct numerical simulation, *J. Fluid Mech*.,450:377–401, 2002.

165-N. S. Berman, H. Tan, Two-component laser doppler velocimeter studies of submerged jets of dilute polymer solutions. *AIChE Journal,* 31 (2), 208-215, 1985.

166-K. Koziol, P. Glowacki, Turbulent jets of dilute polymer solutions. *J. Non-Newt. Fluid Mech.* 32 (3), 311-328, 1989.

167-A. A. Townsend, *The Structure of Turbulent Shear Flow*. Cambridge: Cambridge University Press, 1976.

168-A. Fouxon and V. Lebedev. Spectra of turbulence in dilute polymer solutions, *Phys. Fluids*, 15(7):2060–2072, 2003]

169-R. Vonlanthen, *The Effects of Fluid Elasticity on Grid Turbulence*. PhD thesis, École Polytechnique Fédérale de Lausanne (EPFL), Switzerland, 2010.

170-E. Balkovsky, A. Fouxon, and V. Lebedev. Turbulence of polymer solutions, *Phys. Rev. E,* 64:056301, 2001. 2, 78, 89, 93.

Appendix

A-Local non-similarity solution for boundary layer FENE-P Flow

In the present study, an approximate similarity solution is proposed for laminar boundary layer FENE-P fluid. Although we saw the proposed solution depends on both η and x, to reduce the level of complexity, it is assumed that the streamwise derivatives of similarly functions $G(\eta, x)$, is assumed to be very small $\frac{\partial G(\eta,x)}{\partial x} = Q(\eta, x) \approx 0$ and it is neglected in deriving the governing equation in approximate similarity approach. However, the general approach to deal with such this problem is non-similarity solution [124-129] in which the streamwise derivatives of similarly functions shown by $Q(\eta, x) \neq 0$ should consider in deriving the governing equation. Again we introduce approximate similarity variables consistent with the thin boundary layer approximation for Newtonian fluids [23,24], and in dimensionless form for generality. Here, the following similarity variables η and function $G(\eta)$ are utilized [23,24]:

$$\eta = \sqrt{\frac{U_\infty}{2\nu_0}} \frac{y}{x^{1/2}}, G(\eta, x) = \frac{\psi}{\sqrt{2U_\infty \nu_0} x^{1/2}}, \tag{A- 1}$$

The streamwise and normal velocities are recovered from their definitions, as

$$u = U_\infty G'(\eta, x), \tag{A- 2}$$

$$v = \sqrt{\frac{\nu_0 U_\infty}{2x}} \left(\eta G'(\eta, x) - G(\eta, x)\right). \tag{A- 3}$$

where the prime indicates derivative in order to η. We also consider that the Peterlin function takes the form

$$K(\eta, x) = f(C_{kk}). \tag{A- 4}$$

Substitution of all expressions into Eq. (2- 10c) leads to the following third order algebraic equation for $K(\eta, x)$

$$K^3 + C_0 K^2 + C_1 C_4 K + C_2 G''^2 + C_3 C_4 = 0 \tag{A- 5}$$

with dimensionless coefficients

$$C_0 = \left(\frac{3I - 3f(L) - L^2}{L^2}\right), \tag{A- 6}$$

$$C_1 = -4\lambda^2 U^2,$$

$$C_2 = -\frac{\lambda^2 f(L) {U_\infty}^3}{\nu_0 L^2} x^{-1} = -\frac{f(L) Re_x {Wi_x}^2}{L^2},$$

$$C_3 = \frac{4\lambda^2 (L^2 + f(L) - 3I) U^2}{L^2},$$

$$C_4 = Q'^2 - x^{-1}\eta Q' G'' + \frac{x^{-2}\eta^2 G''^2}{4}.$$

Here, $I = 1$ if the Peterlin functions are given by Eq. (2- 10c) and $I = 0$ otherwise. Coefficients C_1 to C_4 in Eq. (A- 6) depend on x,η and Q', therefore the solution of K will depend on η and x and also Q'.

Regarding the x-momentum equation, by substituting C_{xy} (from Eq. (3-25)) into Eq. (3-10),

$$\frac{\partial\psi}{\partial y}\left(\frac{\partial^2\psi}{\partial x\partial y}\right) - \left(\frac{\partial\psi}{\partial x}\right)\left(\frac{\partial^2\psi}{\partial y^2}\right) = \nu_s \frac{\partial^3\psi}{\partial y^3}$$
$$+\nu_p f(L)\left(\frac{2\lambda\frac{\partial^2\psi}{\partial x\partial y}\frac{\partial^3\psi}{\partial y^3} + f(C_{kk})\frac{\partial^3\psi}{\partial y^3} - 2\lambda\frac{\partial^3\psi}{\partial x\partial y^2}\frac{\partial^2\psi}{\partial y^2} - \frac{\partial f(C_{kk})}{\partial y}\frac{\partial^2\psi}{\partial y^2}}{\left(2\lambda\frac{\partial^2\psi}{\partial x\partial y} + f(C_{kk})\right)^2}\right). \quad \text{(A- 7)}$$

together with the similarity variables in Eq. (A- 7) and algebraic manipulation, it becomes

$$G'Q' - QG'' - \frac{x^{-1}}{2}G''G = (1-\beta)\frac{x^{-1}}{2}G'''$$
$$+\beta f(L)\frac{x^{-1}}{2}\left(\frac{-2\lambda UQ''G'' + WixG''^2 - K'G''}{(2\lambda UQ' - \eta WixG'' + k)^2} + \frac{2\lambda UQ'G''' + kG'''}{(2\lambda UQ' - \eta WixG'' + k)^2}\right) \quad \text{(A- 8)}$$

again, the dependence on x in addition to the dependence on η,Q, Q', and Q'' is clear and this equation also involves the first derivative of K relative to η, which is obtained from Eq. (A- 5) and is given by

$$K' = -\frac{(C_1K + C_3)\left(2Q''Q' - x^{-1}(Q'G'' + \eta Q''G'' + \eta Q'G''') + \frac{x^{-2}}{2}\left(\eta G''^2 + \eta^2 G'''G''\right)\right)}{C_5} - \frac{2C_2 G'''G''}{C_5} \quad \text{(A- 9)}$$

in which

$$\mathrm{C}_5 = 3K^2 + 2\mathrm{C}_0K + \mathrm{C}_1C_4. \tag{A- 10}$$

Upon back-substitution of K' of Eq. (A- 9) into Eq. (A- 8), further mathematical manipulation leads to the following final form of the momentum equation cast in terms of $G(\eta, x)$

$$\begin{aligned} &G''' \\ &= \frac{2x(G'Q' - QG'') - GG''}{(1-\beta) + \beta f(L)\left(\frac{(2\lambda UQ' + k)C_5 + (C_1K + C_3)\eta C_6 + 2C_2G''^2}{C_5(2\lambda UQ' - \eta WixG'' + k)^2}\right)} \\ &+ \frac{\beta f(L)\left(\frac{\left(2\lambda UQ''G'' - WixG''^2\right)C_5 - (C_1K + C_3)G''(2Q''Q' - x^{-1}\eta Q''G'' + C_6)}{(3K^2 + 2C_0K + C_1C_4)(2\lambda UQ' - \eta WixG'' + k)^2}\right)}{(1-\beta) + \beta f(L)\left(\frac{(2\lambda UQ' + k)C_5 + (C_1K + C_3)\eta C_6 + 2C_2G''^2}{C_5(2\lambda UQ' - \eta WixG'' + k)^2}\right)} \end{aligned} \tag{A- 11}$$

where

$$C_6 = \frac{x^{-2}}{2}\eta G''^2 - x^{-1}Q'G''. \tag{A- 12}$$

To solve the final governing Eq. (A- 11) which depends on Q, Q', and Q'', it is required to derivate of the Eq. (A- 11) on streamwise direction (x) three times to have individual differential equations for Q, Q', and Q'', now these four coupled differential equations must be solved. As you can see the complexity of the problem increase considerably. However, it is very interesting to mention that when we consider $Q(\eta, x) \approx 0$, we will reach the same equation that we proposed in Eq. (3-38).

Beyond the Seas

پشت دریاها

I'll build a boat, I'll set it afloat. I'll get far away from this weird land, where there's nobody in the woods of love, to wake up the heroes and the heroines.

قایقی خواهم ساخت، خواهم انداخت به آب. دور خواهم شد از این خاک غریب، که در آن هیچ کسی نیست که در بیشه‌ی عشق، قهرمانان را بیدار کند.

The boat is devoid of fishing nets and my heart does not covet any pearls. I will sail on. I will fall in love neither with the blue of the seas, nor with the mermaids that emerge, and cast their spell on the lonesome fishermen.

قایق از تور تهی و دل از آرزوی مروارید، هم چنان خواهم راند. نه به آبی‌ها دل خواهم بست، نه به دریا پریانی که سراز خاک به در می‌آرند، و در آن تابش تنهایی ماهی‌گیران، می‌فشانند فسون از سر گیسوهاشان.

I will sail on. I will sing, "Far away one must get. Far away one must go." The men of that city did not possess any myths. The women of that city were not as plentiful as grapes. No mirror reflected happiness over there. Even the puddles did not reflect the faintest light.

هم چنان خواهم راند. هم چنان خواهم خواند: «دور باید شد، دور. مرد آن شهر اساطیر نداشت. زن آن شهر به سرشاری یک خوشه‌ی انگور نبود. هیچ آینه‌ی تالاری، سرخوشی‌ها را تکرار نکرد. چاله آبی حتی، مشعلی را ننمود.

Far away one must get. Far away one must go, sang softly the night. And now it's high time the windows sang their songs. I will sail on, I will sing on. Beyond the seas, there's a city where the windows look out on revelation.

دور باید شد، دور. شب سرودش را خواند، نوبت پنجره‌هاست. هم چنان خواهم خواند. هم چنان خواهم راند. پشت دریاها شهری است که در آن پنجره‌ها رو به تجلی باز است.

The roofs there house the doves that contemplate the fountain of human intelligence. There's a bough of knowledge in every child's hand in the city.

بام‌ها جای کبوترهایی است که به فواره‌ی هوش بشری می‌نگرند. دست هر کودک ده ساله‌ی شهر، شاخه‌ی معرفتی است.

The people there look at a wall as they would contemplate a fire ablaze or a pleasant dream. Their soil can hear the music of your senses and the wind carries the sound of mythical birds.

مردم شهر به یک چینه چنان می‌نگرند، که به یک شعله، به یک خواب لطیف. خاک، موسیقی احساس تو را می‌شنود، و صدای پر مرغان اساطیر می‌آید در باد.

Beyond the seas, there's a city where the sun is as wide as the eyes of dawn worshipers. The poets there are the inheritors of water, wisdom, and light. There's a city beyond the seas!

پشت دریاها شهری است، که در آن وسعت خورشید به اندازه‌ی چشمان سحرخیزان است. شاعران وارث آب و خرد و روشنی‌اند. پشت دریاها شهری است!

One must build a boat.

قایقی باید ساخت.

By Sohrab Sepehri
(October 7, 1928 – April 21, 1980)
A notable Iranian poet and a painter.

سهراب سپهری